

JOURNAL OF SCIENCE

PART A: ENGINEERING AND INNOVATION



Year / Yıl: 2021

Volume / Cilt: 8

Issue / Sayı: 1

e-ISSN 2147-9542



Owner | Sahibi

on behalf of Gazi University | Gazi Üniversitesi adına
Rector | Rektör
Prof. Dr. Musa YILDIZ

Publishing Manager

Prof. Dr. | Prof. Dr.
Cevriye GENCER
Gazi University | Gazi Üniversitesi

Chief Editor

Prof. Dr. | Prof. Dr.
Sema Bilge OCAK
Gazi University | Gazi Üniversitesi

Managing Editors

Prof. Dr. | Prof. Dr.
Mustafa Gürhan YALÇIN
Akdeniz University | Akdeniz Üniversitesi

Prof. Dr. | Prof. Dr.
Selim ACAR
Gazi University | Gazi Üniversitesi

Assoc. Prof. Dr. | Doç. Dr.
Uğur GÖKMEN
Gazi University | Gazi Üniversitesi



Editorial Board / Editörler Kurulu

Prof. Dr. Prof. Dr. Adnan SÖZEN	Gazi University - Energy Systems Engineering Gazi Üniversitesi - Enerji Sistemleri Mühendisliği
Prof. Dr. Prof. Dr. Ali KESKİN	Çukurova University - Automotive Engineering Çukurova Üniversitesi - Otomotiv Mühendisliği
Prof. Dr. Prof. Dr. Ali Osman SOLAK	Ankara University - Chemistry Ankara Üniversitesi - Kimya
Prof. Dr. Prof. Dr. Atila BIYIKOĞLU	Gazi University - Mechanical Engineering Gazi Üniversitesi - Makine Mühendisliği
Prof. Dr. Prof. Dr. Burçin BAYRAM	Miami University - Physics Miami Üniversitesi - Fizik
Prof. Dr. Prof. Dr. Çağlayan AÇIKGÖZ	Bilecik Şeyh Edebali University - Chemical Engineering Bilecik Şeyh Edebali Üniversitesi - Kimya Mühendisliği
Prof. Dr. Prof. Dr. Elif ORHAN	Gazi University - Physics Gazi Üniversitesi - Fizik
Prof. Dr. Prof. Dr. Erdal IRMAK	Gazi University - Electrical-Electronic Engineering Gazi Üniversitesi - Elektrik-Elektronik Mühendisliği
Prof. Dr. Prof. Dr. Hakan ATEŞ	Gazi University - Metallurgical and Materials Engineering Gazi Üniversitesi - Metalurji ve Malzeme Mühendisliği
Prof. Dr. Prof. Dr. Homer RAHNEJAT	Loughborough University - Electrical and Manufacturing Engineering Loughborough Üniversitesi - Elektrik ve İmalat Mühendisliği
Prof. Dr. Prof. Dr. Hüseyin Serdar YÜCESU	Gazi University - Automotive Engineering Gazi Üniversitesi - Otomotiv Mühendisliği
Prof. Dr. Prof. Dr. Meltem DOĞAN	Gazi University - Chemical Engineering Gazi Üniversitesi - Kimya Mühendisliği
Prof. Dr. Prof. Dr. Metin GÜRÜ	Gazi University - Chemical Engineering Gazi Üniversitesi - Kimya Mühendisliği
Prof. Dr. Prof. Dr. Murat KAYA	Aksaray University - Biotechnology Aksaray Üniversitesi - Biyoteknoloji
Prof. Dr. Prof. Dr. Nalan KABAY	Ege University - Chemical Engineering Ege Üniversitesi - Kimya Mühendisliği
Prof. Dr. Prof. Dr. Nuran AY	Eskişehir Technical University - Materials Science and Engineering Eskişehir Teknik Üniversitesi - Malzeme Bilimi ve Mühendisliği

Editorial Board / Editörler Kurulu

Prof. Dr. Prof. Dr. Nursel AKÇAM	Gazi University - Electrical-Electronic Engineering Gazi Üniversitesi - Elektrik-Elektronik Mühendisliği
Prof. Dr. Prof. Dr. Ömer ŞAHİN	Siirt University - Chemical Engineering Siirt Üniversitesi - Kimya Mühendisliği
Prof. Dr. Prof. Dr. Rob DWYER-JOYCE	The University of Sheffield - Mechanical Engineering Sheffield Üniversitesi - Makine Mühendisliği
Prof. Dr. Prof. Dr. Şükrü DURSUN	Konya Technical University - Environmental Engineering Konya Teknik Üniversitesi - Çevre Mühendisliği
Prof. Dr. Prof. Dr. Veli ÇELİK	Ankara Yıldırım Beyazıt University - Mechanical Engineering Ankara Yıldırım Beyazıt Üniversitesi - Makine Mühendisliği
Prof. Dr. Prof. Dr. Yücel ERCAN	TOBB University of Economics and Technology - Mechanical Engineering TOBB Ekonomi ve Teknoloji Üniversitesi - Makine Mühendisliği
Prof. Dr. Prof. Dr. Zafer EVİS	Middle East Technical University - Engineering Sciences Orta Doğu Teknik Üniversitesi - Mühendislik Bilimleri
Assoc. Prof. Dr. Doç. Dr. Alper BÜYÜKKARAGÖZ	Gazi University - Civil Engineering Gazi Üniversitesi - İnşaat Mühendisliği
Assoc. Prof. Dr. Doç. Dr. Çetin ÇAKANYILDIRIM	Hitit University - Chemical Engineering Hitit Üniversitesi - Kimya Mühendisliği
Assoc. Prof. Dr. Doç. Dr. Demet CANSARAN DUMAN	Ankara University - The Institute of Biotechnology Ankara Üniversitesi - Biyoteknoloji Enstitüsü
Assoc. Prof. Dr. Doç. Dr. Hacer KARACAN	Gazi University - Computer Engineering Gazi Üniversitesi - Bilgisayar Mühendisliği
Assoc. Prof. Dr. Doç. Dr. Mine TÜRKTAŞ ERKEN	Gazi University - Biology Gazi Üniversitesi - Biyoloji
Assist. Prof. Dr. Dr. Öğr. Üyesi Füsun YALÇIN	Akdeniz University - Mathematics Akdeniz Üniversitesi - Matematik
Assist. Prof. Dr. Dr. Öğr. Üyesi Senai YALÇINKAYA	Marmara University - Mechanical Engineering Marmara Üniversitesi - Makine Mühendisliği
Dr. Dr. Defne AKAY	Ankara University - Physics Ankara Üniversitesi - Fizik



Technical Editors / Teknik Editörler

Dr. Fatih UÇAR

Akdeniz University | Akdeniz Üniversitesi

Dr. Silver GÜNEŞ

Gazi University | Gazi Üniversitesi

Murat AKIN

Gazi University | Gazi Üniversitesi

Correspondence Address

Gazi University Graduate School of Natural and Applied Sciences
Emniyet Neighborhood, Bandırma Avenue, No:6/20B, 06560, Yenimahalle - ANKARA
B Block, Auxiliary Building

Yazışma Adresi

Gazi Üniversitesi Fen Bilimleri Enstitüsü
Emniyet Mahallesi, Bandırma Caddesi, No:6/20B, 06560, Yenimahalle - ANKARA
B Blok, Ek Bina

e-mail | e-posta

gujsa06@gmail.com

web page | web sayfası

<https://dergipark.org.tr/tr/pub/gujsa>

**Gazi University Journal of Science Part A: Engineering and Innovation
is a peer-reviewed journal.**

Gazi Üniversitesi Fen Bilimleri Dergisi Bölüm A: Mühendislik ve İnovasyon
hakemli bir dergidir.



INDEXING / DİZİNLENME



ACCESSIBILITY | ERİŞİLEBİLİRLİK



This work are licensed under a Creative Commons Attribution-ShareAlike 4.0 International License.

Bu eser Creative Commons Atıf-AynıLisanslaPaylaş 4.0 Uluslararası Lisansı ile lisanslanmıştır.

CONTENTS / İÇİNDEKİLER

Page / Sayfa	Articles / Makaleler
1-15	An Introduction to Software Testing Methodologies <i>A. Ziya AKTAŞ, Eray YAĞDERELİ, Doğa SERDAROĞLU</i> Review Article / Civil Engineering
16-23	Mathematical Modeling of a Diesel Electrical Locomotive <i>Mine SERTSÖZ, Mehmet FİDAN, Mehmet KURBAN</i> Research Article / Civil Engineering
24-34	Investigation of Manufacturing of a Pelton Turbine Runner of Composite Material on a 3D Printer <i>A. Murad GÜLLÜOĞLU, Oğuzhan BENDEŞ, Buğra YILMAZ, Adem YILDIZ</i> Research Article / Civil Engineering
35-42	Moisture Impact on Wind Density Power Seasonally <i>Zaid Ayad Jalal ALWINDAWI, Mehmet Y. GUNDOGDU</i> Research Article / Civil Engineering
43-57	Automated Sensor Data Validation and Correction with Long Short-Term Memory Recurring Neural Network Model <i>Abraham Sudharson PONRAJ, T. VIGNESWARAN, J. Christy JACKSON</i> Research Article / Civil Engineering
58-80	Wireless Signal Attenuation by Vegetation: Relationship Between Tree Characteristics and Signal Attenuation <i>Yusuf ABBA KYARI, James AGAJO</i> Research Article / Civil Engineering
81-93	Modal Analysis of Horizontal Axis Wind Turbine Rotor Blade with Distinct Configurations under Aerodynamic Loading Cycle <i>Aniekan Essienubong IKPE, Ekom Mike ETUK, Akanu-Ibiam Effiong NDON</i> Research Article / Civil Engineering

CONTENTS / İÇİNDEKİLER

Page / Sayfa	Articles / Makaleler
94-108	Modelling and Validation of The Production Parameters of Unalloyed Aluminium Sheets <i>Dickson David OLODU</i> Research Article / Civil Engineering
109-122	Application of Differential Transformation Method for Nonlinear Cutting Tool Vibration <i>İbrahim DEMİR, Mustafa Mehmet Fatih KARAHAN, Nizami AKTÜRK</i> Research Article / Civil Engineering
123-134	Failure Analysis of Hybrid Glass Reinforced Composites in Polymeric Industries <i>Dickson David OLODU</i> Research Article / Civil Engineering
135-145	Case Study for Thermo Mechanical Performance of an Integrated Optic Device via Equation-Based Modelling <i>Seval DÖNERTAŞ, Mutlu GÖKKAVAS, Ekmel ÖZBAY, Elif ÖZ ORHAN</i> Research Article / Civil Engineering
146-156	The Effects Welding Speed and Focal Length on Mechanical Characteristic of Fiber Laser-Welded Structures of DP600 Dual Phase Steel <i>Elif Selen ATMACA, Adem KURT</i> Research Article / Civil Engineering
157-165	The Dependence of The Nickel Concentration of ZnO Thin Films for Gas Sensors Applications <i>Baktiyar SOLTABAYEV, Irmak KARADUMAN ER, Memet Ali YILDIRIM, Aytunç ATEŞ, Selim ACAR</i> Research Article / Civil Engineering
166-188	Gümüşler (Niğde) Antimon (Sb) Cevherleşmesinin Mineralojik ve Jeokimyasal Araştırılması <i>Ali TÜMÜKLÜ, Okan TOSUNBAŞ</i> Research Article / Civil Engineering



An Introduction to Software Testing Methodologies

A. Ziya AKTAŞ^{1*} , Eray YAĞDERELİ¹ , Doğa SERDAROĞLU² 

¹Başkent University, Faculty of Engineering, Computer Engineering Department 06810, Ankara, Turkey

²Credit Suisse Poland - Szczytnicka 9, 50-382 Wrocław, Poland

Keywords	Abstract
PRISMA SDLC SW Testing Methodology TMMi	<p>It seems to the authors that ‘testing’ for many of the Computer Engineering or Software Engineering professionals or to laymen means the same as ‘code testing’ or ‘program testing’. Yet, recalling the SDLC (Software Development Life Cycle) steps such as Planning, Analysis, Design, Implementation or Construction and Maintenance, obviously will tell us that coding is just a piece of SDLC included in the Implementation. Therefore, unit testing, integration testing, black box testing or acceptance testing etc. would not cover the whole SDLC. One then needs any methodology, if available, to encompass all steps of SDLC.</p> <p>The major objective of this article has been to investigate the available methodologies applicable for software testing. During our research, we met TMMi (Test Maturity Model integration) and PRISMA (Product Risk Management) methodologies available in the professional arena. After understanding the characteristics of these methodologies, we attempted to propose a new methodology as a synthesis of these two methodologies.</p> <p>The details of these two methodologies are given in this article, while a newly proposed methodology described in the article will be applied on a web based problem to be reported later.</p>

Cite

Aktaş, A. Z., Yağdereli, E. & Serdaroglu, D., (2021). An Introduction to Software Testing Methodologies. *GU J Sci, Part A*, 8(1), 1-15.

Author ID (ORCID Number)

A. Z. Aktaş, 0000-0002-1829-7821
 E. Yağdereli, 0000-0002-5384-3912
 D. Serdaroglu, 0000-0001-5705-8551

Article Process

Submission Date 28.01.2019
Revision Date 18.12.2020
Accepted Date 24.03.2021
Published Date 29.03.2021

1. INTRODUCTION

1.1. Preliminaries

In the early years of digital computers, testing process had focused on hardware [Gelperin & Hetzel (1988) as an example]. The major concern was hardware reliability and software was then checked only for that concern. [“Once a programmer wrote a program, the differences between the concepts of program ‘checkout’, ‘debugging’, and ‘testing’ were not clear at that time. Baker distinguished in 1957 first, ‘testing’ from ‘debugging’”. This part is taken from the articles of Baker (1957) and Alam & Khan (2013) as an example].

As we all know now that computer applications have become an intrinsic part of our lives and virtually every business in every sector have depended on software. Software almost in all fields have increased in number, size and complexity and thus, testing has become more significant because of its greater economic risk. Software industry has been investing substantial effort and money to get higher quality products. In fact, software engineer is now defined as an engineer whose objective is to develop cost-effective and high quality software. However, software engineering field is still far from expected results. In addition to this problem, diversification of application platforms with mobile computing, customer demands to access their

data and applications from everywhere and competitive market pressures are facts to live with. Additionally, very high amount of data / information and knowledge that is shared between applications have made the problem worse (Aktaş, 1987; RTI, 2002).

Having a general introduction of software testing methodologies is the major objective of this article. After understanding the characteristics of the available methodologies and summarizing them, a new methodology is proposed briefly.

In the first Chapter, namely 1. INTRODUCTION, the article briefly introduces some preliminaries which is followed by subsections that deal with software-testing related concepts such as Risk Management, Capability Maturity Model Integration (CMMI), Test Maturity Model integration (TMMi), and Product Risk Management. Their elaborations are given in the Chapters 2-4 of the article. Chapter 5 has a proposed methodology for software testing. Article ends in Section 6: SUMMARY, CONCLUSIONS and FUTURE WORK.

1.2. Software Testing and Risk Management

As noted by Broadleaf Capital International PTY Ltd (2012) “Risk is not something new to human being. Yet, this knowledge is turned into a science only first in the last century”. This topic is elaborated in the next Chapter, Chapter 2.

1.3. Software Testing and CMMI (Capability Maturity Model Integration)

The software industry has often tried to improve its development methodologies in order to improve its product quality. A guideline that has been widely used for this purpose is known as the Capability Maturity Model (CMM). Black (2011) has claimed that “The CMM and the Capability Maturity Model Integration (CMMI) have often been regarded as a de-facto standard in the market for software development process improvement”. ICT (Information and Communications Technology) spending on quality assurance (QA) and testing has been rising steadily. ICT budget allocation for application quality and testing in software development field has grown from 18 percent to 35 percent between 2012 and 2015 and it is expected to be about 40 percent in the year 2018 (Capgemini, Sogeti & HP, 2015). Yet, CMM or CMMI has given only a limited attention to testing (van Veenendaal & Cannegieter, 2013). The CMMI has two dedicated process areas (Verification, VER and Validation, VAL). They provide more focus on testing at maturity Level 3 and they are summarized and presented in Table 1 (CMMI, 2010).

Therefore, testing community has created their own test process improvement models such as Test Maturity Model integration (TMMi) and Test Process Improvement (TPI) and other test methodologies.

Because risk and risk management are closely related concepts to software testing, the next Chapter, namely Chapter 2, is devoted to this topic, as noted earlier.

Table 1. CMMI Process Areas Related with Testing

Process Area	Description
Verification – VER	Aims to ensure that selected work products would meet the specified requirements of the product.
Validation – VAL	Incrementally validates products against customer’s requirements

1.4. Software Testing and TMMi (Test Maturity Model integration)

“TMMi (Test Maturity Model integration) was developed to serve as a guideline and a reference framework for test process improvement. It functions as a complementary model for CMMI to serve test managers, test engineers and software quality professionals” (CMMI, 2010; van Veenendaal, 2012a,b). TMMi is a

generic model and it is applicable to various life cycle models in various environments. One may also implement TMMi for test process improvement even for agile software development methodologies.

1.5. Software Testing and Risk-Based Testing (RBT) and PRISMA (Product Risk Management)

The British Standards Institute has produced the *BS 7925/2* standard which has two sections as test design techniques and test measurement techniques. One may round out the list of techniques as “Random Testing” and “Other Testing Techniques”. Random Testing (RT) has been the primary software-testing technique for decades. Its effectiveness in detecting software failures has been often controversial (Liu et al., 2011a,b; van Veenendaal, 2014). As a result of these concerns, Risk-based testing (RBT) concept has evolved from “good enough quality” and “good enough testing” concepts and “heuristic risk-based testing” (Bach, 1997; 1998; Liu et al., 2011a,b). Its fundamental principles can be listed as (Bach, 1999):

- Exhaustive testing (exercising every possible path and every combination of inputs and preconditions) is infeasible except for trivial cases;
- Selective testing techniques are needed to allocate test resources properly;
- The focus of testing has to be placed on features and aspects of software to reduce the failure risk and to ensure the quality of the applications.

As noted by Graham et al. (2008) “These can be achieved by applying the principle of risk-based prioritization of tests, known as Risk-Based Testing (RBT). The primary role of risk-based testing is to optimize available resources and time without affecting the quality of the product”.

The PRISMA model is a risk-based testing approach and developed in a bottom-up fashion (van Veenendaal, 2011, 2012a,b). It depends on:

- Identifying the areas that have the highest level of business and/or technical risk;
- Assessing the impact of possible defects and the likelihood of the occurrence of these defects;
- Visualizing product risks (test items) in a product risk matrix by assigning numeric values to both impact and likelihood.

2. SOFTWARE TESTING AND RISK MANAGEMENT

2.1. General

Due to lack of a common and comprehensive international standard, many varieties of standards or regulations have been developed during the last two decades. Finally, the first global risk management standard *ISO 31000:2009* (ISO, 2009a) was released. A list of important risk management standards were given by Ciocoiu & Dobrea (2010).

2.2. The Definition of Risk

As noted above, the first global risk management standard is *ISO 31000:2009* (ISO, 2009a). It is together with a revised set of definitions that are contained in *ISO/IEC Guide 73:2009* (ISO, 2009b).

The definition of risk in the *ISO 31000* standard is “the effect of uncertainty on objectives”. Guide 73 also states that “an effect may be positive, negative or a deviation from the expected, and that risk is often described by an event, a change in circumstances or a consequence” (ISO, 2009a).

Organizations often have to contend with internal and external factors and influences which they may not control and that generate uncertainty and thus risk. Such factors might assist or speed up the achievement of objectives; but also prevent or delay the organization achieving its objectives.

2.3. Risk Management Process (RMP)

According to *ISO 31000:2009*, risk management process is defined as: “systematic application of management policies, procedures and practices to the activities of communicating, consulting, establishing

the context, and identifying, analyzing, evaluating, treating, monitoring and reviewing risk” (ISO, 2009a). The main elements and overview of the risk management process are given as Figure 1.

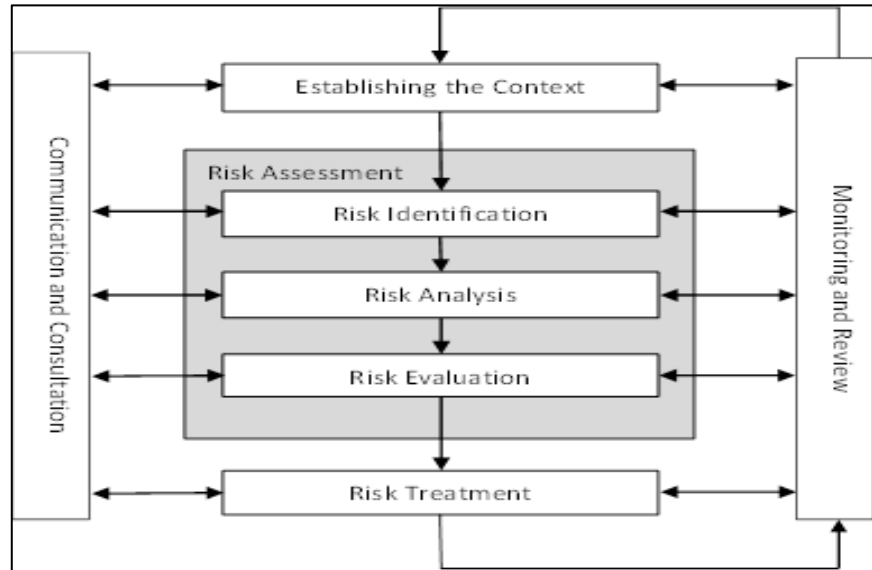


Figure 1. Main Elements of the Risk Management Process

2.4. Risk Characterization and Measurement

Risk analysis phase of risk management process involves consideration of the causes and sources of risk, their positive and negative consequences, and the likelihood that those consequences can occur. Fundamentally, risk is characterized and measured by considering consequences of what could happen and the likelihoods of those consequences. From the definition, risk is a function of both likelihood and a measure of consequence. In its simplest form risk can be defined as (Standards Australia/New Zealand, 2004):

$$\text{Risk} = A \text{ function of } (\text{Consequence and Likelihood}) \quad (1)$$

Consequences and their likelihoods are often combined to define a level of risk. The way in which consequences and likelihood are expressed and the way in which they are combined to reflect the type of risk and the purpose for which the risk assessment output is to be used. These should all be consistent with the risk criteria. Risk analysis can be qualitative, semi-quantitative or quantitative, or a combination of these, depending on the risk, the purpose of the analysis, and available data and resources.

Qualitative analysis is any method of analysis which uses description rather than numerical means to define a level of risk. This information may be brought together and summarized as simple descriptions of consequences and likelihoods of risks to use in a risk inventory table. However, criteria on which the ranking can be based must be decided and/or devised.

If it is taken that the level of risk is proportional to each of its two components (consequence or likelihood) the risk function simply becomes a product. As given in *AS/NZS 4360:2004*, this can be presented mathematically as (Standards Australia/New Zealand, 2004):

$$\text{Risk} = \text{Consequence} \times \text{Likelihood or } (R = C \times L) \quad (2)$$

If the level of risk is not linearly dependent on one or two of its components (consequence and likelihood), the risk function should include required weighting factor(s) and/or exponential operator for one or both of the components (Roy, 2004).

3. CAPABILITY MATURITY MODEL (CMM) AND CAPABILITY MATURITY MODEL INTEGRATION (CMMI)

As noted earlier, a methodology named TMMi (Test Maturity Model integration) has an objective of supporting test engineers in evaluating and improving their test processes. In developing this methodology two other methodologies, namely CMMI (Capability Maturity Model Integration) and TMM (Test Maturity Model) were used as guidelines (van Veenendaal & Cannegieter, 2013).

Capability Maturity Models are based on the premise of “the quality of a system or product is highly influenced by the quality of the process used to develop and maintain it” (van Veenendaal, 2012a,b). CMMs including CMMI focus on improving processes in an organization. They contain the essential elements of effective processes and describe an evolutionary improvement path (through capability/maturity levels) from ad hoc, immature processes to disciplined, mature processes with improved quality and effectiveness (van Veenendaal, 2012a,b).

In the context of software development, the capability maturity model is a group of related strategies for improving the software development process, irrespective of the actual software life-cycle model used. Capability/Maturity Levels are used in CMMI for (Software) Development to describe an evolutionary path recommended for an organization that wants to improve the processes it uses to develop software products or services. Maturity Levels of the CMMI for Development are given in the Figure 2 (CMMI, 2010).

In the context of software development, the capability maturity model is a group of related strategies for improving the software development process, irrespective of the actual software life-cycle model used. Capability/Maturity Levels are used in CMMI for (Software) Development to describe an evolutionary path recommended for an organization that wants to improve the processes it uses to develop software products or services. Maturity Levels of the CMMI for Development are given in the Figure 2 (CMMI, 2010).

4. SOFTWARE TESTING AND TMMi (TEST MATURITY MODEL INTEGRATION)

4.1. General

Testing process in the TMMi (Test Maturity Model integration) includes all software product quality-related activities. TMMi also uses the concept of maturity levels for process evaluation and improvement similar to the CMMI stages. Each TMMi maturity level also includes process areas, goals and practices. Thus, “the focus of testing changes from defect detection to defect prevention” (Capgemini, Sogeti & HP, 2015; CMMI Product Team 2010). “One also should note that the model is compliant with ISO 15504 standard, that is, Software Process Improvement and Capability Determination (SPICE) standard, for process assessment” (CMMI, 2010).

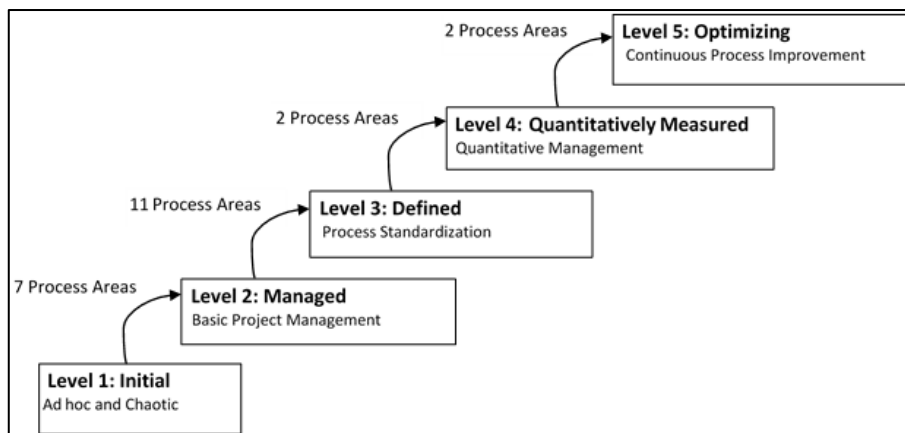


Figure 2. Maturity Levels of CMMI for Development

As noted earlier, TMMi similar to CMMI, has a leveled architecture for process improvement. There are five stages and/or levels in the TMMi architecture. Each level/stage has a set of process areas that an

organization needs to implement to achieve maturity at that level. Thus, they form a necessary foundation for the next level (van Veenendaal, 2012a,b). TMMi maturity levels and process areas as given in TMMi reference model are presented in Figure 3 (CMMI, 2010). In the following subsections, summary of five levels of TMMi are given (CMMI, 2010; Capgemini-Sogeti-HP, 2015).

4.2. Level 1: Initial

Level 1 of TMMi has no defined process areas. Testing at this level is an undefined process; it is often taken as part of debugging. In order to get the bugs out of the system, testing and debugging are interleaved. The objective of testing at this level is to show that the software runs without major failures. Level 1 of TMMi has no defined process areas. Testing at this level is an undefined process; it is often taken as part of debugging. In order to get the bugs out of the system, testing and debugging are interleaved. The objective of testing at this level is to show that the software runs without major failures.

4.3. Level 2: Managed

Testing becomes a managed process and it is clearly separated from debugging at this level. A company-wide or program-wide test strategy is now established. The process discipline of maturity Level 2 makes it possible that existing practices are made available during times of stress. The main objective of testing at this level is to verify that the product satisfies the specified requirements. Yet, many consider testing as being a project phase that follows coding.

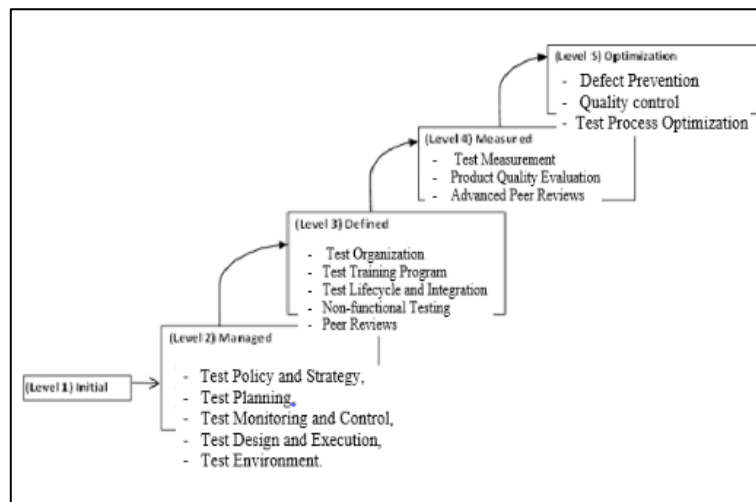


Figure 3. TMMi Maturity Levels and Process Areas of TMMi

The process areas at TMMi Level 2 are given as (CMMI, 2010; Capgemini-Sogeti-HP, 2015):

- Test Policy and Strategy,
- Test Planning,
- Test Monitoring and Control,
- Test Design and Execution,
- Test Environment.

4.4. Level 3: Defined

At TMMi Level 3, testing is not a lifecycle phase after implementation. Testing is now completely integrated into the development life-cycle and its associated milestones. Test planning is performed at an early stage of the project, usually during the requirements phase, and is documented by means of a master test plan. Organizations at TMMi Level 3 understand the importance of reviews for developing a quality product. A formal review program is implemented. At Level 3, test designs and techniques are expanded to include nonfunctional testing such as usability and/or reliability, depending on the business objectives,

although they focus mainly on functionality testing at TMMi Level 2. The process areas at TMMi Level 3 are given as (CMMI, 2010; Capgemini-Sogeti-HP, 2015):

- Test Organization
- Test Training Program
- Test Lifecycle and Integration
- Non-functional Testing
- Peer Reviews

4.5. Level 4: Management and Measurement

Testing is a thoroughly defined, well-founded and a measurable process at this level. An organization-wide test measurement program is used to evaluate the quality of the testing process, to assess productivity, and to monitor improvements. Measurements are incorporated into the organization's repository. Test measurement program also supports fact-based decision-making and predictions related to test performance and cost.

The presence of a measurement program allows an organization to implement a product- quality evaluation process by defining quality needs, quality attributes such as reliability, usability and maintainability and quality metrics. Product quality is understood in quantitative terms and is managed to the defined objectives throughout the lifecycle.

Reviews and inspections are considered as parts of the test process at this level. The process areas at TMMi Level 4 are given as follows (CMMI, 2010; Capgemini-Sogeti-HP, 2015):

- Test Measurement
- Product Quality Evaluation
- Advanced Peer Reviews

4.6. Level 5: Optimization

An organization has continuous focus on process improvement and fine-tuning at this level. The organization is capable of continually improving its processes depending on a quantitative understanding of statistically controlled processes. Test process performance is improved through incremental and innovative process and technological improvements. The testing methods and techniques are continuously optimized.

The three process areas at TMMi Level 5 are given as follows (CMMI, 2010; Capgemini-Sogeti-HP, 2015):

- Defect Prevention
- Quality control
- Test Process Optimization

5. SOFTWARE TESTING, RISK-BASED TESTING AND PRISMA APPROACH

5.1. General

Risk management has been the subject of research in software engineering since the works of Boehm (1989) and Charette (1989). Many risk management models and frameworks such as, SERIM (Software Engineering Risk Index Management), SERUM (Software Engineering Risk Understanding and Management), SEI-SRE (Software Engineering Institute - Software Risk Evaluation), Riskit, ProRisk, etc. have been proposed after two studies by Stern & Arias (2011) and Roy (2004). All these studies took risk management in the context of software development and did not address supervising testing activities according to risk management principles. In this respect, James Bach's "heuristic risk-based testing" proposal (1999) which was evolved from "good enough quality" and "good enough testing" concepts (1997-1999), were the first studies applying risk management concepts to testing activities.

The risk-based testing depends on the intuitive idea of to focus (identify and prioritize) test activities on those scenarios that trigger the most critical situations for a software system and ensure that these critical situations are both effectively mitigated and sufficiently tested (Roy, 2004; Wendland et al., 2012). In its first form, the way proposed by Bach (1998), risk-based testing fundamentally depends on heuristic risk analysis which can be performed by using one of two approaches: inside-out or outside-in. Inside-out begins with details about the situation and identify risks associated with them, also known as bottom-up approach. Outside-in begins with a set of potential risks and match them to the details of the situation, a more general top-down approach. According to Bach (1998), risk-based testing aims at testing the right things of a system at the right time and each test process is actually carried out in a risk-based way due to its sampling characteristics. He further states that in most cases, the consideration of risk is rather made implicitly.

After Bach's proposal, Amland's (2000) work was the first study utilizing risk analysis fundamentals and metrics to manage the test process by intelligent assessment by identifying the probability and the consequences of individual risks. In this study, he defined a risk-based testing approach based on Karolak's risk management process (Karolak, 1995). Risk-based testing approach as defined and diagrammed by Amland (2000) is given as Figure 4. Oval boxes in Figure 4 explain how his risk-based testing model fits in with the Karolak's (1995) risk management process. In this regard, Amland's study was considered to be the first to introduce a systematic risk-based testing approach (Felderer & Ramler, 2014).

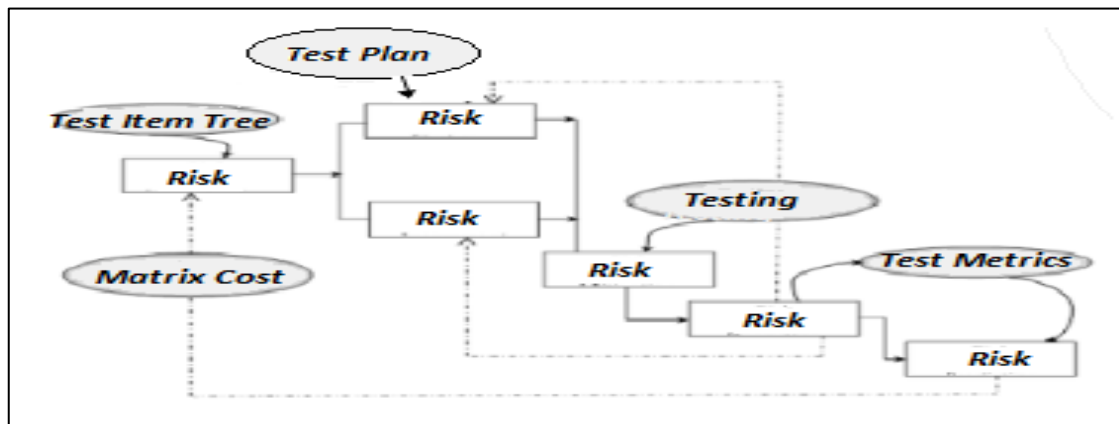


Figure 4. Risk-Based Testing

5.2. Related Work on Risk-Based Testing (RBT)

After these two pioneering works (Bach, 1998; Amland, 2000), many risk-based testing approaches have been proposed by academia and industry due to its practical relevance and importance. Because of the growing number of available risk-based testing approaches and its ever increasing usage in industrial test processes there is a need about surveying, comparing and categorizing of all these studies. There are three valuable articles that we identified serving this purpose. The first one is the article by Erdogan et al. (2014). This article presented “a systematic literature review on risk-based testing approaches.” They identified a total of 32 peer-reviewed articles. The articles were then grouped into 24 approaches of which only two approaches were found out about test-based risk assessment, while the remaining 22 were classified as addressing various aspects of risk-based testing.

The second article was given by Felderer & Schieferdecker (2014). In this article, “the taxonomy of risk-based testing has been developed by analyzing the works presented by 23 articles and it has been applied to four selected works on risk-based testing.”

The third article was given by Felderer et al. (2014, 2015). “This article has focused on how risk estimation is performed in different risk-based testing approaches, since risk estimation determines the importance of the risk values assigned to tests and consequently the quality of the overall risk-based testing process.”

5.3. PRISMA (Product Risk Management Approach)

The PRISMA model is a risk-based testing approach developed in bottom-up fashion. It can work at every level of testing (Graham et al., 2008; van Veenendaal, 2011). PRISMA approach utilizes a risk quantification method defined in (ISO 2009b) and in principle similar to the Barry Boehm's concept of "risk exposure". According to Boehm (1989), "Risk exposure is defined as the relationship where the probability of an unsatisfactory outcome and the loss due to the unsatisfactory outcome determine the valence of the risk event (the expected value of the risk)" (Standards Australia/New Zealand, 2004). The innovative aspect of the PRISMA approach is its assessment of every risk item from the point of many impact factors and likelihood factors. It groups and calls impact factors as "business risks" (on x axis) and likelihood factors as "technical risks" (on y axis) as shown in Figure 5.

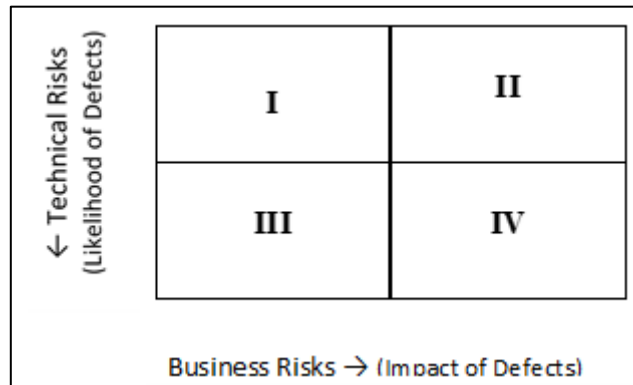


Figure 5. Product Risk Matrix

The standard risk matrix is divided into four areas (quadrants I, II, III and IV) as shown in Figure 5. Each represents a different risk level and type. A different risk level/type most likely will lead to a different test approach as documented in a test plan. The product risk matrix provides a general preview of the product risks to the stakeholders and the decision makers. It is much easier to understand a visual overview than a list of numbers.

Although there may be different impact and likelihood factors for every product, common impact factors that are usually utilized to determine and quantify (assess) impact of risk (test) items in PRISMA approach are given as follows (Graham et.al., 2008; van Veenendaal, 2012a,b):

- Critical areas (cost and consequences of failure);
- Visible areas;
- Mostly used areas;
- Importance to business;
- Cost of rework.

Likelihood factors that are often utilized to determine and assess importance of risk (test) items in PRISMA approach are given as (Graham et.al., 2008; van Veenendaal, 2012a,b):

- Complex areas;
- Changed areas;
- New technology and methods;
- People involved ;
- Time pressure;
- Optimization;
- Defect history;
- Geographical spread.

Other likelihood factors to be considered are new development versus re-use, size of application and number of entities interfaced.

The standard PRISMA process consists of the following activities as given in Figure 6 (Graham et.al., 2008; van Veenendaal, 2012a,b).

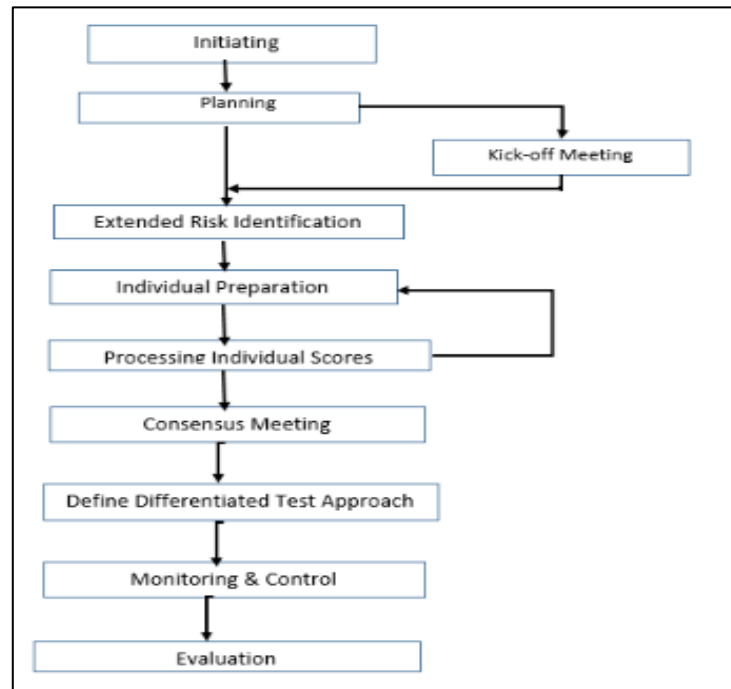


Figure 6. PRISMA Process Overview

Each step is outlined briefly in the following subsections:

a) Initiating

The main objectives in the initiating step are definition of the PRISMA process and setting of rules, factors, value ranges and weights for factors. Initiating step includes the following tasks:

- Definition of the PRISMA process to be used in the organization and its documentation;
- Define impact and likelihood factors;
- Determine scoring ranges for factors;
- Define a weight for each factor;
- Scoring rules.

While implementing the PRISMA approach a standard process is defined. Process variations can be implemented for different situations. This process shall be documented and disseminated as a handbook within the organization. The likelihood and the impact factors shall be defined in a comprehensive way for all stakeholders. The scoring range can be defined as 1 – 3 (low as 1, intermediate as 2 and high as 3), or the range of 1 - 5 or 1 - 9. The experiences show that the best range suitable to most cases for scoring is the 1 - 5 range which is divided as low (1-2), intermediate (3-4) and high (5).

b) Planning

In the planning step, scope, stakeholders and product risks are identified and defined. The planning step is essentially carried out by the test manager and includes the following tasks:

- Definition of scope;
- Select stakeholders;
- Gathering input documents;
- Identifying risk items;
- Review of impact and likelihood factors and rules;
- Assignment of factors to stakeholders.

The determined product risk items should be tagged uniquely and expressed in a comprehensive way for the stakeholders. This will help the stakeholders follow the risk items in the future easily. Stakeholders can be chosen among the project managers, developers, software architects, marketers, consumers, business managers. The stakeholders are those who install, use the product and affected by it. The factors are assigned to the stakeholders according to interests and roles of the stakeholders for scoring. Generally, the impact factors are assigned to business-related stakeholders and the likelihood factors to stakeholders on the technical side and they should be explained clearly to stakeholders.

c) Kick-off Meeting

After that all assignments are done, the first meeting with all the stakeholders is held and the test manager explains the product evaluation to all the stakeholders. The purpose of the kick-off meeting is to inform all the stakeholders about the process, risk assessment and the purpose of the activities, and to get their commitments. The kick-off meeting is optional but it is highly recommended. The risk items and factors should be explained in detail to stakeholders.

d) Extended Risk Identification

Main objectives of this step are to extend identified risk set, to verify risk set determined in planning step, to identify inconsistencies between requirements and risks. During this step, brainstorming sessions are used to verify and extend the initial risk set.

e) Individual Preparation

During the individual preparation step, participants score and register the impact and likelihood factors for each registered risk item. The values assigned by the stakeholder are based on perceived risks which are stakeholder's expectation that something could go wrong (likelihood of defects) and importance for the business (impact of defects). For the stakeholders not to be affected by the other stakeholders, the scoring process should be performed independently.

As a result of this step, "documents containing the scoring values of the assigned factors of each participant will be obtained."

f) Processing Individual Scores

The purpose of this step is summarized as follows:

- To verify and confirm that every participant scored factors assigned to him/her;
- To input and update draft product risk matrix with individual scores;
- To check whether scorings have been done correctly and identify violation of rules;
- To prepare an item list to be discussed later in the consensus meeting.

The test manager gathers the individual results of the stakeholders, controls them and puts them in process. The average value for each risk item is calculated for all of its likelihood and impact factors. A weighted sum of average values of likelihood and impact factors for each product risk item will be computed and a draft scoring total for the likelihood and impact factors will be gathered. After this calculation, each risk item is to be positioned in the product risk matrix.

g) Consensus Meeting

The resulting product risk matrix is analyzed by the stakeholders in the consensus meeting. During the meeting the items from the items list are discussed between stakeholders and test manager. At the end of the discussion final scores are determined and product risks are positioned in the resulting risk matrix as shown in Figure 7 (Serdaroğlu, 2015).

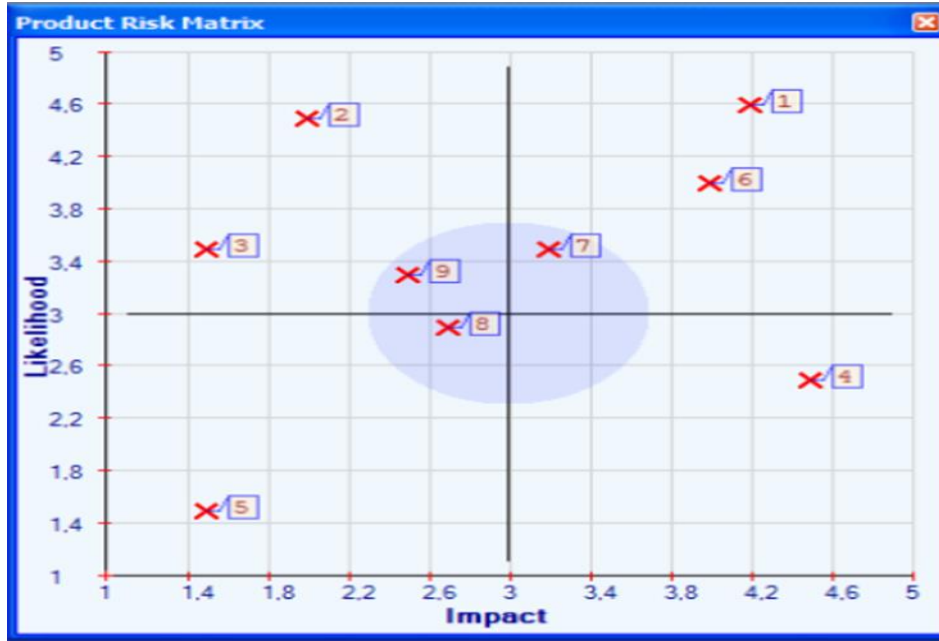


Figure 7. Example Product Risk Matrix

The resulting product risk matrix should always be validated with the stakeholders. If results are not according to the expectations of the stakeholders, they should be re-discussed to reach a consensus. If needed, a follow-up meeting or a specific discussion meeting in a smaller group could be organized (Serdaroğlu, 2015).

Some risk items are on the edges of the matrix. Items with low impact and low probability such as the risk item 5 are negligible. Items with a high impact and high probability such as the item 1 should be paid more attention in the test process. It is much harder to decide about the risk factors near the center of the matrix. Because it can be difficult to determine which area they belong to. Normally all the risk items within the circle are contained in the subject list of the test manager and they have to be discussed and analyzed. After the analysis, it should be decided into which quarter they are going to be placed.

h) Define Differentiated Test Approach

At this step a test approach is defined according to agreed product risk matrix (based on test items' position in the risk matrix). Main tasks of this step are defined as follows (Serdaroğlu, 2015):

- Make prioritization of test items;
- Identify test depth for each test item;
- Determine test design techniques.

A certain test approach is going to be determined for each quarter. It contains decisions about test design techniques to be applied, test and evaluation types to be held.

i) Monitoring & Control

Test monitoring and control, including reporting, should be organized around product risks. For technical risks (likelihood), technical reviews are more helpful, whereas for business risks (impact), it is more useful to determine the ways to be followed together with customer (Serdaroğlu, 2015).

j) Evaluation

Risks are not static and ever changing during test process. Therefore risk identification and assessment needs to be reviewed regularly and it has to be updated according to the results of tests. During the development of project and execution of the test, the test manager has to maintain the matrix, based on

lessons learned e.g. defects found or other measured indicators like DDP (Defect Detection Percentage), (changed) assumptions, updated requirements or architecture. “Changes in the projects’ scope, context or requirements will often require updates to the risk assessment” (Serdaroğlu, 2015).

Additionally, the test manager and the project manager can analyze product risk matrix together and use this information to determine the priorities of development, integration and the service schedule accordingly.

6. SUMMARY, CONCLUSIONS AND FUTURE WORK

6.1. Summary

This article includes an introductory study on the software testing methodologies. Two of the relevant methodologies, namely TMMi and PRISMA were studied in detail for developing another methodology as a synthesis of two, to apply on a real-world case study.

6.2. Conclusions

According to TMMi, testing becomes a managed process at Level 2, and testing approach is defined based on the result of a product risk assessment performed in the test policy and strategy process area of this level. The authors, therefore, have proposed incorporation of PRISMA approach into the TMMi framework at Level 2. The proposed incorporation of PRISMA to the TMMi model will augment efficiency and affectivity of testing process in terms of time and budget, since it allows allocation of valuable test resources on the areas that have the highest level of risk.

6.3. Future Work

The proposed hybrid methodology based on both TMMi and PRISMA will be applied on a web based real life problem and its results will be reported later.

Three of the recent publications such as Patrício et al. (2021) A Study on Software Testing Standard Using ISO/IEC/IEEE 29119-2: 2013. In: Al-Emran M., Shaalan K., Hassanien A. (eds) Recent Advances in Intelligent Systems and Smart Applications. Studies in Systems, Decision and Control, Vol 295. Springer, Cham.; Laksono et al. (2019) Assessment of Test Maturity Model: A Comparative Study for Process Improvement; and Hrabovská et al. (2019) Software Testing Process Models Benefits & Drawbacks: a Systematic Literature Review will be studied in detail and they will be added to the references of a next expected publication.

CONFLICT OF INTEREST

No conflict of interest was declared by the authors.

No fund support is received during this study.

ACKNOWLEDGEMENT

The authors express their wishes to acknowledge their cordial thanks and gratitude to the Editors and Anonymous Reviewers for their kind comments and supports on the article.

REFERENCES

- Aktaş, A. Z. (1987). Structured Analysis and Design of Information Systems, Prentice-Hall, USA.
- Alam, M., & Khan, A. I. (2013). Risk-Based Testing Techniques: A Perspective Study. *International Journal of Computer Applications*, 65(1), 33-41.
- Amland, S. (2000). Risk-Based Testing: Risk Analysis Fundamentals and Metrics for Software Testing Including a Financial Application Case Study. *Journal of Systems and Software*, 53(3), 287-295. doi:[10.1016/S0164-1212\(00\)00019-4](https://doi.org/10.1016/S0164-1212(00)00019-4)

- Bach, J. (1997). Good Enough Quality: Beyond the Buzzword. *IEEE Computer*, 30(8), 96-98. doi:[10.1109/2.607108](https://doi.org/10.1109/2.607108)
- Bach, J. (1998). A Framework for Good Enough Testing. *IEEE Computer*, 31(10), 124-126. doi:[10.1109/2.722304](https://doi.org/10.1109/2.722304)
- Bach, J. (1999). Risk-Based Testing: How to conduct heuristic risk analysis. *Software Testing and Quality Engineering Magazine*, November/December, 23-28. www.satisfice.com/articles/hrbt.pdf
- Baker, C. L. (1957). Review of "Digital Computer Programming, by D.D. McCracken". *Mathematical Tables and Other Aids to Computation*, 11(60), 298-305. doi:[10.2307/2001950](https://doi.org/10.2307/2001950)
- Black, R. (2011). *Advanced Software Testing*, Vol.1, Rocky Nook, USA.
- Boehm, B. W. (1989). *Tutorial: Software Risk Management*, IEEE Computer Society Press, New York.
- Broadleaf (2012). *A Simple Guide to Risk and Its Management*. Broadleaf Capital International Pty Ltd. (Accessed:21/02/2017) broadleaf.com.au/resource-material/a-simple-guide-to-risk-and-its-management/
- Capgemini, Sogeti & HP (2015). *World Quality Report 2015-16 Seventh Edition*.
- Charette, R. N. (1989). *Software Engineering Risk Analysis and Management*. McGraw-Hill, New York.
- Ciocioiu, C. N., & Dobrea, R. C. (2010). The Role of Standardization in Improving the Effectiveness of Integrated Risk Management. In: Nota, G. (Eds.) *Advances in Risk Management* (pp. 1-18). IntechOpen. doi:[10.5772/9893](https://doi.org/10.5772/9893)
- CMMI (2010). *CMMI for Development, Version 1.3*. (Technical Report: CMU/SEI-2010-TR-033). CMMI Product Team, Software Engineering Institute, Carnegie Mellon University. doi:[10.1184/R1/6572342.v1](https://doi.org/10.1184/R1/6572342.v1)
- Erdogan, G., Y. Li, Y., Runde, R. K., Seehusen, F., & Stølen, K. (2014). Approaches for the combined use of risk analysis and testing: a systematic literature review. *International Journal on Software Tools for Technology Transfer*, 16(5), 627-642. doi:[10.1007/s10009-014-0330-5](https://doi.org/10.1007/s10009-014-0330-5)
- Felderer, M., & Ramler, R. (2014). Integrating risk-based testing in industrial test processes. *Software Quality Journal*, 22(3), 543-575. doi:[10.1007/s11219-013-9226-y](https://doi.org/10.1007/s11219-013-9226-y)
- Felderer, M., & Schieferdecker, I. (2014). A taxonomy of risk-based testing. *International Journal on Software Tools for Technology Transfer*, 16(5), 559-568. doi:[10.1007/s10009-014-0332-3](https://doi.org/10.1007/s10009-014-0332-3)
- Felderer, M., Haisjackl, C., Pekar, V., & Brey, R. (2014). A Risk Assessment Framework for Software Testing. In: Margaria, T., & Steffen, B. (Eds.), *Leveraging Applications of Formal Methods, Verification and Validation. Specialized Techniques and Applications. Proceedings of the 6th International Symposium, ISO/LA 2014, Part II*, (pp. 292-308), October 8-11, Corfu, Greece. doi:[10.1007/978-3-662-45231-8_21](https://doi.org/10.1007/978-3-662-45231-8_21)
- Felderer, M., Haisjackl, C., Pekar, V., & Brey, R. (2015). An Exploratory Study on Risk Estimation in Risk-Based Testing Approaches. In: Winkler, D., Biffel, S., & Bergsmann, J. (Eds.), *Software Quality. Software and Systems Quality in Distributed and Mobile Environments. Proceedings of the 7th International Conference, SWQD 2015*, (pp. 20-23), January 20-23, Vienna, Austria. doi:[10.1007/978-3-319-13251-8_3](https://doi.org/10.1007/978-3-319-13251-8_3)
- Gelperin, D., & Hetzel, B. (1988). The Growth of Software Testing. *Communications of the ACM*, 31(6), 687-695. doi:[10.1145/62959.62965](https://doi.org/10.1145/62959.62965)
- Graham, D., van Veenendaal, E., Evans, I., & Black, R. (2008). *Foundations of Software Testing ISTQB Certification*. Cengage Learning Emea.
- Hrabovská, K., Rossi, B., & Pitner, T. (2019). Software Testing Process Models Benefits & Drawbacks: a Systematic Literature Review. arXiv:1901.01450. arxiv.org/abs/1901.01450
- ISO (2009a). *ISO 31000, Principles and Guidelines on Risk Management*.
- ISO (2009b.) *ISO/IEC Guide 73:2009, Risk Management -Vocabulary*.
- Karolak, D. W. (1995). *Software Engineering Risk Management*. Wiley-IEEE Computer Society Press.

- Laksono, M. A., Budiardjo, E. K., & Ferdinansyah, A. (2019). Assessment of Test Maturity Model: A Comparative Study for Process Improvement. In: Proceedings of the 2nd International Conference on Software Engineering and Information Management, ICSIM 2019, (pp. 110-118), January 10-13, Bali, Indonesia.
- Liu, H., Kuo, F-C., & Chen, T. Y. (2011a). Comparison of adaptive random testing and random testing under various testing and debugging scenarios. *Software: Practice and Experience*, 42(8), 1055-1074. doi:[10.1002/spe.1113](https://doi.org/10.1002/spe.1113)
- Liu, H., Xie, X., Yang, J., Lu, Y., & Chen, T. Y. (2011b). Adaptive Random Testing Through Test Profiles. *Software: Practice and Experience*, 41(10), 1131-1154. doi:[10.1002/spe.1067](https://doi.org/10.1002/spe.1067)
- Patrício, C., Pinto, R., & Marques, G. (2021) A Study on Software Testing Standard Using ISO/IEC/IEEE 29119-2: 2013. In: Al-Emran M., Shaalan K., & Hassanien A. (Eds) Recent Advances in Intelligent Systems and Smart Applications (pp. 43-62). doi:[10.1007/978-3-030-47411-9_3](https://doi.org/10.1007/978-3-030-47411-9_3)
- RTI (2002). Planning Report 02-3, The Economic Impacts of Inadequate Infrastructure for Software Testing. Prepared by Research Triangle Institute (RTI) for National Institute of Standards & Technology (NIST). (7007.011) (Accessed:20/02/2017) www.nist.gov/director/planning/upload/report02-3.pdf
- Roy, G. G. (2004). A risk management framework for software engineering practice. In: Strooper, P. (Eds.) Proceedings of the Australian Software Engineering Conference, ASWEC 2004, (pp. 60-67), April 13-16, Melbourne, Australia. doi:[10.1109/ASWEC.2004.1290458](https://doi.org/10.1109/ASWEC.2004.1290458)
- Serdaroğlu, D. (2015). Yazılım Test Süreci ve TMMi Modelinde Prisma Yaklaşımı Uygulaması. MSc. Thesis (in Turkish), Başkent Üniversitesi, Bilgisayar Mühendisliği Bölümü.
- Standards Australia/New Zealand (2004). Risk Management Guidelines Companion to AS/NZS 4360:2004 (HB 436:2004)
- Stern, R., & Arias, J. C. (2011). Review of Risk Management Methods. *Business Intelligence Journal*, 4(1), 59-78.
- van Veenendaal, E. (2011). Practical Risk-Based Testing Product Risk Management: The PRISMA Method. EuroSTAR 2011, November 21-24, Manchester, UK. (Accessed:08/03/2017) www.erikvanveenendaal.nl/NL/files/e-book%20PRISMA.pdf
- van Veenendaal, E. (2012a). Test Maturity Model integration (TMMi) Release 1.0. TMMi Foundation.
- van Veenendaal, E. (2012b). Practical Risk-Based Testing - The PRISMA Approach. UTN Publishers.
- van Veenendaal, E. (2014). Test Process Improvement and Agile: Friends or Foes?. *Testing Experience*, 27, 24-26. (Accessed:07/03/2017) www.erikvanveenendaal.nl/NL/files/testingexperience27_09_14_van_Veenendaal.pdf
- van Veenendaal, E., & Cannegieter, J. J. (2013). Test Maturity Model integration (TMMi) Results of the first TMMi benchmark - where are we today?. EuroSTAR. (Accessed:07/03/2017) www.erikvanveenendaal.nl/NL/files/e-book%20TMMi.pdf
- Wendland, M-F., Kranz, M. & Schieferdecker, I. (2012). A Systematic Approach to Risk-Based Testing Using Risk-annotated Requirements Models. In: The Seventh International Conference on Software Engineering Advances, ICSEA 2012 (pp. 636-642), Lisbon.



Mathematical Modeling of a Diesel Electrical Locomotive

Mine SERTSÖZ^{1*} , Mehmet FİDAN¹ , Mehmet KURBAN² 

¹Eskişehir Technical University, Transportation Vocational School, Eskişehir, Turkey

²Bilecik Şeyh Edebali University, Department of Electrical and Electronics Engineering, Bilecik, Turkey

Keywords	Abstract
<p>Transportation DE Locomotive Modeling Optimization LSM</p>	<p>Railway transportation has a huge share of energy consumption in the industry. The efficient power consumption is the most important issue for the minimization of the cost of railway transportation. The control strategy for efficient power consumption is varying due to the type of locomotive. Each type of locomotive needs its specific power model for this purpose. The range of the locomotives used in Turkey are full of diversity according to the type and size of the motor. In this research, DE 24000 type of locomotive is chosen for mathematically modeling of its required power under various load, speed, ramp, and curve conditions. Then a mathematical equation is produced according to these values with Least Square Method. The optimum efficient working point is found as 735.5-ton load and 38km/h speed with the aim of this produced equation.</p>

Cite

Sertsöz, M., Fidan, M., & Kurban, M. (2021). Mathematical Modeling of a Diesel Electrical Locomotive. *GU J Sci, Part A*, 8(1), 16-23.

Author ID (ORCID Number)	Article Process	
M. Sertsöz, 0000-0003-1641-9191	Submission Date	23.08.2019
M. Fidan, 0000-0003-2883-9863	Revision Date	24.12.2020
M. Kurban, 0000-0003-2618-2861	Accepted Date	04.03.2021
	Published Date	29.03.2021

1. INTRODUCTION

The cost components of a railway like other transportation projects can be classified to:

- The supplier costs. (Planning, Design, and Administrative; Right of way; Construction; Operating; Maintenance)
- The user costs. (Access time; Waiting time; Travel time in the train; Accident; Comfortable)
- The out of system costs. (Environmental, Social)

This study belongs to the second item, user costs. Because the goal is to help the user for efficient speeds and loads at a certain route. So, this will ensure efficient driving. Efficient driving is based on train resistance according to load, speed, and route information.

When it comes to the resistance of the train sets, and to examine the subject in more detail, the optimization process can be traced back to the oldest periods of development in the railways. Many researchers have made investigations in this field and have reached the empirical equations shared in the findings section. Studies in literature are mainly based on cruise resistance and their prediction models. Travel resistance was reported by Davis (1926) as follows:

$$R_s = AV^2 + BV + C$$

A is a constant which changes proportionally to the square of the speed and represents aerodynamic resistance caused by air pressure and friction.

B is a constant which is responsible for mechanical resistances and HVAC (Heating, Ventilating, and Air Conditioning).

C is a constant which is not fixed to the vehicle speed but is a function of weight.

In the past, detailed tests have been conducted to determine these constants. The cruise resistance coefficients of different trains were found for the Shinkansen. (Hara et al., 1967) Besides, different tests and cruise resistance tests were applied to the passenger cars and locomotives of Eurofim (Report ERRI C, 1993) However, since the tests are very costly, different empirical equations have been developed in the past for estimating the resistance of certain trains. An overview of the methods adopted by the main national railways (up to 2000) and a calculation tool, to calculate cruise resistance, in which the effects of various characteristics of the train's architecture can be taken into account, are presented; these results are compared with the results of other equations for calculating train resistance (Rochard & Schmid, 2000).

More recently, Lukaszewicz has proposed a method that allows the determination of train resistance coefficients by measuring only train speed and position from full-scale cruise tests (Lukaszewicz, 2007a). In this study, resistance was determined by the change in kinetic and potential energy of a train traveling between successful measurement points. Using this method (Lukaszewicz, 2007b), the same authors shared experimental results to determine the travel resistance of different trains and the effect of variables such as speed, number of axles, number of wagons, axle load, road type, and train length. Since 2005, a CEN (European Committee for Standardization) standard (EN 14067-4:2005+A1:2009) has described methodologies for evaluating the coefficients of Davis's formula starting from a predictive formula, numerical simulations, and reduced-scale tests from full-scale test measurements, but no strictly accepted methods have been obtained.

Cruise tests are performed to determine the speed-dependent terms (A and B) according to CEN Standards. There is a need for a special test for term C, which means that the train is traveling at a very low speed. To find the coefficients A and B in the CEN standard, the regression method and the velocity history identification method were used. The first cruise test is based on the combination of all available experimental data and the second is based on the combination of the equation of motion. Both methods require a very good knowledge of the test section properties (slopes and curve radiuses).

In another study in the literature, the standard methods for determining Davis's coefficients were compared to new methods. In particular, it has been shown that the three coefficients of the Davis's formula can be estimated by two tests only, the first is a very low-speed test on a high altitude slope section (without having to perform a traction test), and the second is a travel test starting at the train's maximum speed. It also proposed a regression method, which is a new method to define the A and B coefficients in the Davis equation. The main advantage of this method is that it does not need to know the characteristics and coefficient C of the railway line. Starting from experimental full-scale tests (characterized by a mass of 450 tonnes) scaled for a general ideal train; the entire procedure for determining travel resistance coefficients is described. The comparison of the results obtained by different methods for estimating the coefficients A and B of the Davis equation are presented and analyzed (Somaschini et al., 2016).

In this study, different from the above-mentioned studies, a single mathematical model was used to determine total resistance by using empirical equations that were accepted for all resistances. For this purpose, the Least Square Method (LSM) is used. Then, it was determined the optimum working point of the train according to load and speed with the aim of this mathematical model.

2. MATERIAL AND METHOD

The locomotive which is used in this study is DE 24000 locomotive. This locomotive has a diesel-electric motor on it, which is used in a loaded train. The approximate weight of the locomotive is 113 tonnes. It uses a 72V alternator and 600V_{RMS} generator. At the diesel part, the locomotive uses the Diesel V16 motor. The fuel capacity of the locomotive is 4.960 liters. The maximum speed of the locomotive can reach 144 km/h. The output power can reach 1760 kW. The tractive effort can reach 394-kilo newtons however, at the maximum speed it falls to 48-kilo newtons (Anonymous, 2016). These performance values of the locomotive can be obtained from the technical catalog of the locomotive.

On the other hand, the proposed mathematical model provides to obtain necessary load, speed, ramp, and curve values for any level of the power, which can not be obtained directly from the technical catalog. If the required power is taken as constant, the maximum speed is changing in the inverse direction of the change in the load and the ramp. Furthermore, speed has a more complex relationship with the curve. These relations can be expressed with a nonlinear mathematical model. The obtained values from the proposed model were used to present the performance curves of the locomotive in a railway in Turkey. These curves were also used to demonstrate the power efficiency of the locomotive.

The mathematical model is created using empirical equations shown below. The Pcon value in the formula stands for the power for the continuous regime, GL stands for the load of the locomotive, and the GV stands for the load to be carried, the P-value is axle press, N is axle numbers and A is the front viewing area that is 12 m² in all calculations. rl is cruising resistance of locomotive, rv is cruising resistance of cars, rk is the resistance force due to curve and rr is the resistance force due to the gradient. R is the total resistance which a locomotive must overcome to move (Urlu, 1999; Anonymous, 2018). The other resistances are neglected. (Other resistances that arise due to wind velocity, tunnels, or train marshaling and the acceleration resistance will not be discussed here)

This cruising resistance formula of locomotives is known as the Davis formula:

$$rl = 0,65 + \frac{13,15}{P} + 0,00932 * V + \frac{0,004526 * A * V^2}{P * N} \text{ (daN/ton)} \quad (1)$$

This cruising resistance formula of cars is known as the Strahi formula:

$$rv = 2 + 0,057 \frac{V^2}{100} \text{ (daN/ton)} \quad (2)$$

This curve resistance formula is known as the Röcki formula:

$$rk = \frac{650}{k - 55} \text{ (daN/ton)} \quad (3)$$

r is the ramp value in %. This value is taken as positive when climbing the ramp and negative when descending:

$$rr = r \quad (4)$$

All the resistances must be multiplied with train and carried load:

$$RL = rl * GL \quad (5)$$

$$RV = rv * GV \quad (6)$$

$$RK = rk * (GV + GL) \quad (7)$$

$$RR = rr * (GV + GL) \quad (8)$$

$$R = RL + RV + RK + RR \quad (9)$$

$$Pcon = \frac{R * V}{360} \text{ (daN)} \quad (10)$$

The proposed mathematical model of the locomotive is constructed by the application of the least-squares method. The least-squares method is a standard approach in regression analysis to approximate the solution of overdetermined systems, i.e., sets of equations in which there are more equations than unknowns. "Least squares" means that the overall solution minimizes the sum of the squares of the residuals made in the results of every single equation.

The most important application is in data fitting as this study. The best fit in the least-squares sense minimizes the sum of squared residuals (a residual being: the difference between an observed value, and the fitted value provided by a model). The details of the method are given below:

2.1. Least Square Method (LSM)

Y is the dependent variable, X_1 is the independent variable, β_1 is the unknown parameter of the X_1 variable and ϵ_i is error terms that can not be observed. It is possible to express one variable linear regression equation:

$$Y = \beta_0 + \beta_0 X_{1i} + \epsilon_i, i = 1, 2, \dots, n \quad (11)$$

One of the most commonly used methods to find $\beta_0 + \beta_1$ variables is the Least Squares Method. The finding values for $\beta + \beta_1$ are $\hat{\beta}_0$ and $\hat{\beta}_1$. In this case, the new equation can be written as follows:

$$Y = \hat{\beta}_0 + \hat{\beta}_0 X_{1i} + \epsilon_i, i = 1, 2, \dots, n \quad (12)$$

The basis of the used LSM to find the values of the are $\hat{\beta}_0$ and $\hat{\beta}_1$ terms in the equation rely on finding the values that will make the smallest sum of the squares of the total deviations. The error terms are the differences between the Y_i (observed values) and the \hat{Y}_i (expected values) (Ryan, 2008). This difference can be expressed as follows:

$$\hat{\epsilon}_i = Y_i - \hat{Y}_i \quad (13)$$

The sum of the differences between the value of estimation and that should be:

$$\sum_i^n \hat{\epsilon}_i = \sum_i^n (Y_i - \hat{Y}_i) = 0 \quad (14)$$

LSM determines the difference of $\hat{\beta}_0$ and $\hat{\beta}_1$ (the estimation parameters of $\hat{\beta}_0$ and $\hat{\beta}_1$) which will be smallest:

$$\text{the smallest } \sum_{i=1}^n \hat{\epsilon}_i^2 = \text{the smallest } \sum_{i=1}^n (Y_i - \hat{Y}_i)^2 \quad (15)$$

To obtain the LSM estimations of the regression coefficients, when the partial derivatives according to $\hat{\beta}_0$ $\hat{\beta}_1$ equation 6 are equalized to zero, Equation 17 and 18 normal equations are obtained. When the necessary analyzes are made through these equations, $\hat{\beta}_0$ and $\hat{\beta}_1$ which are the estimations of the β_0 and β_1 can be obtained from equations 19 and 20 (Gürünlü Alma & Vupa, 2008)

$$\sum_{i=1}^n (Y_i - (\hat{\beta}_0 - \hat{\beta}_1 X_{1i}))^2 = L \quad (16)$$

$$\sum_{i=1}^n Y_i = \hat{\beta}_0 n + \hat{\beta}_1 \sum_{i=1}^n X_i \quad (17)$$

$$\sum_{i=1}^n X_i Y_i = \hat{\beta}_0 \sum_{i=1}^n X_i + \hat{\beta}_1 \sum_{i=1}^n X_i^2 \quad (18)$$

$\hat{\beta}_0$, $\hat{\beta}_1$ and the calculation of the regression coefficient is as follows:

$$\hat{\beta}_1 = \frac{(n[\sum_{i=1}^n X_i Y_i] - (\sum_{i=1}^n X_i)(\sum_{i=1}^n Y_i))}{(\sum_{i=1}^n X_i^2) - (\sum_{i=1}^n X_i)^2} = \frac{\sum_{i=1}^n (X_{1i} - \bar{X}) - (Y_{1i} - \bar{Y})}{\sum_{i=1}^n (X_{1i} - \bar{X})^2} \quad (19)$$

$$\hat{\beta}_0 = \frac{\sum_{i=1}^n Y_i - \hat{\beta}_1 \sum_{i=1}^n X_i}{n} = \bar{Y} - \hat{\beta}_1 \bar{X} \quad (20)$$

$$R^2 = \frac{\sum_{i=1}^n (\hat{y}_i - \bar{y})^2}{\sum_{i=1}^n (y_i - \bar{y})^2} \quad (21)$$

3. CASE STUDY

Data to build a mathematical model are obtained from the Tülomsaş (locomotive producer company in Turkey). Then Matlab for LSM is used to find the optimum working point of locomotive according to a specific railway route. The railway line is a part of Konya (Turkey) conventional line between 282+969,130 km and 283+443,920 km. The mathematical model is used to find the optimum load and speed values for this route.

Mathematical model of DE 24000:

$$\begin{aligned} P_{con} = & (10^{-4} + 1.6x10^{-6}L)V^3 + 0.0029V^2 \\ & + \left((0.031 + 0.224x10^{-3}L)k^2 - (31 + 22.4x10^{-3}L)k \right. \\ & \left. + (6.34 + 5.66x10^{-3}L) + (0.2 + 3x10^{-4}L)(r - 1) \right) V \end{aligned} \quad (22)$$

Constraints:

$$10 \text{ km/h} \leq V \leq 140 \text{ km/h}$$

$$130 \text{ m} \leq k \leq 430 \text{ m}$$

$$0 \% \leq r$$

$$L \leq 1400 \text{ ton (include locomotive weight)}$$

$$P_{con} \leq 1760 \text{ kW}$$

Pcon: Power (kW)

L: Load (ton)

k: curve (meter)

r: ramp level (% ramp)

RMSE is about 0 for this novelty model for DE24000 locomotive. Then according to this model, some curves are obtained in this specific railway route. This route is shown in Table 1, the yellow part is used in this study (k=0).

Table 1. Line Data

Konya Conventional Line Between 277-284								
S.NO	Start	Level	Finish	Level	Distance	Level	Ramp %	Ramp ‰
1	277+521,61	795,293	278+149,320	794,660	627,710	-0,633	-0,00101	-1,01
2	278+149,320	794,660	279+140,000	794,496	990,680	-0,164	-0,00017	-0,17
3	279+140,000	794,496	279+669,790	792,516	529,790	-1,980	-0,00374	-3,74
4	279+669,790	792,516	281+190,830	791,333	1521,040	-1,183	-0,00078	-0,78
5	281+190,830	791,333	281+737,380	782,581	546,550	-8,752	-0,01601	-16,01
6	281+737,380	782,581	282+969,130	781,511	1231,750	-1,070	-0,00087	-0,87
7	282+969,130	781,511	283+443,920	789,108	474,790	7,597	0,01600	16,00
8	283+443,920	789,108	284+490,680	788,692	1046,760	-0,416	-0,00040	-0,40

3D figure can be drawn for power, load, and speed. Figure 1 is below.

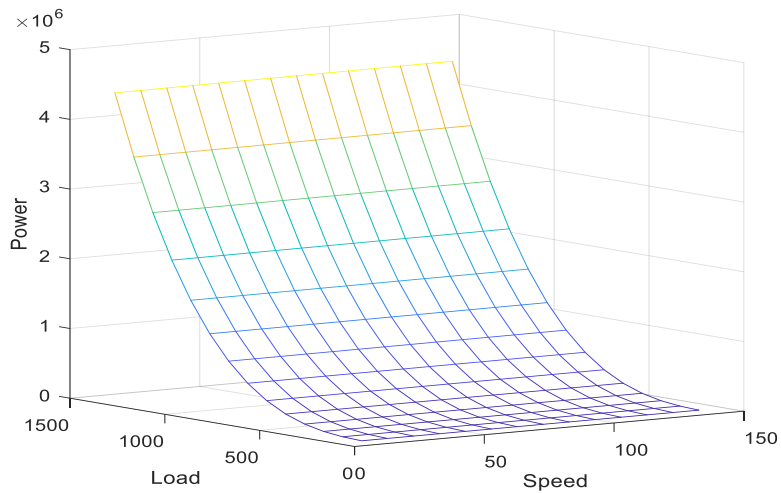


Figure 1. Power-Load-Speed Figure

L-S diagrams are very useful to obtain speed and load values. These values are obtained according to max power. Figure 2 is the Load-Speed diagram of the DE24000 below.

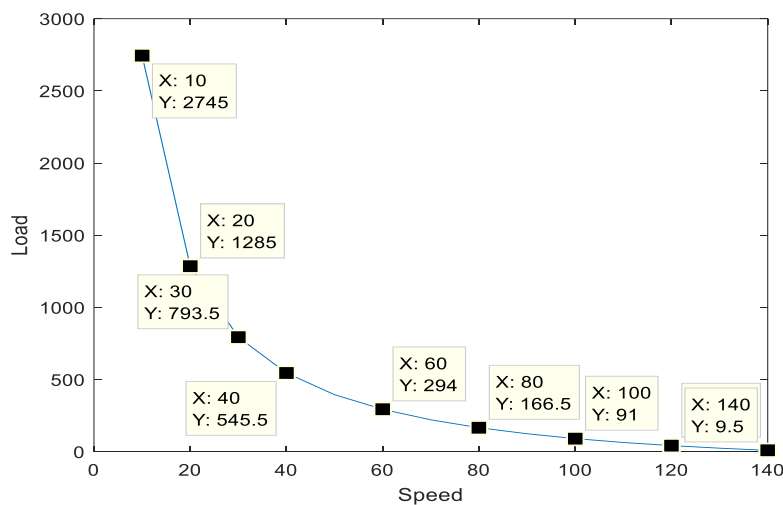


Figure 2. Load-Speed Diagram of The DE24000

There is an optimization problem here. In a certain power, load and speed have an intersection point. This point is the best working point for DE24000. Figure 3 shows this point.

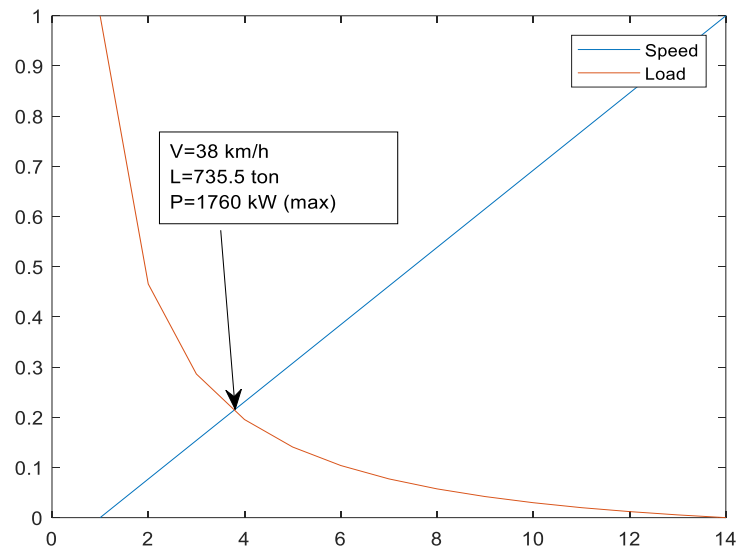


Figure 3. Optimum Speed and Load Values of The DE24000

The optimum point is found as 38 km/h and 735.5 tons for this railway route. This point is the value when both speed and load are equally important. If the arrival time is more important or the load to be carried is more important for the user, these points will be changed and these values can get easily from this novelty mathematical model. If the route will change these values will be changed too.

Previous studies generally are created with controlling dwell time, running time, and departure state for energy efficiency in railway systems. These systems are used in both regenerative braking and power supply systems but sometimes only power supply systems are used. (Albrecht, 2004; Chen et al., 2005; Kim & Oh, 2009).

4. RESULT

Differently previous studies, optimum speed, and load points are tried to be found in this study. There is no direct study similar to this study in the literature that can be given as an example.

The optimum point is found as 38 km/h and 735.5 tons according to the chosen route as previously mentioned. In this case, this calculation has been made considering that load and speed are the same effects on energy consumption (the locomotive was operated at full power).

There are two contributions to this study. The first contribution is that the power requirement of the locomotive can find easily with changing load, speed, curve, and ramp level of the railway. In this study, only one part of the railway is used but DE24000 can be used on all the railway's aims of this model. The customer of this locomotive will be able to see if the locomotive will work properly on the railway which is desired before planning.

Secondly, one more contribution is that the user can find the optimum working point of the locomotive according to a certain railway anywhere. Because efficiency speed and load values can change with the railway route and locomotive type. Some warning systems can be added to ensure that machinist can go on optimum energy conditions.

4. CONCLUSION

It is quite easy to set up warning systems by implementing some algorithms for energy efficiency in the railways. These systems can be prepared for locomotives and sold together with them. Ramp level, curve, length of the railway, and the load information are entered into the system. These systems will provide the

maximum speed information to the user when the maximum power value is limited. When this speed is exceeded, the system will alert. Such an application will help to use energy very economically.

Also, unhandled in this work, adding time knowledge to the model, the effect of time-saving on energy can be searched too. According to all information (ramp level, curve, length of the railway, and the load), how long time takes the journey and energy consumption can be found. This study is among the studies planned to be done in the future.

CONFLICT OF INTEREST

The authors declare that, there is no conflict of interest regarding the publication of this paper.

REFERENCES

- Albrecht, T. (2004). Reducing power peaks and energy consumption in rail transit systems by simultaneous train running time control. *Computers in Railways IX, WIT Press*, 885-894.
- Chen, J. F., Lin, R. L., & Liu, Y. C. (2005). Optimization of an MRT Trains schedule: reducing maximum traction power by using genetic algorithms. *IEEE Transactions on Power Systems*, 20(3), 1366-1372.
- Davis, Jr. W. J. (1926). The tractive resistance of electric locomotives and cars. *Gen. Electr. Rev.*, 29, 2-24.
- EN 14067-4:(2005)+A1:(2009). Railway applications - Aerodynamics - Part 4: Requirements and test procedures for aerodynamics on the open track.
- Gürünlü Alma, Ö., & Vupa, Ö. (2008). Regresyon analizinde kullanılan en küçük kareler ve en küçük medyan kareler yöntemlerinin karşılaştırılması. *SDÜ Fen Edebiyat Fakültesi Fen Dergisi (E-Dergi)*, 3(2) 219-229.
- Hara, T., Ohkushi, J., & Nishimura, B. (1967). Aerodynamic drag of trains. *Q. Rep. RTRI*, 8(4), 226-229.
- Kim, K. M., & Oh, S. M. (2009) A Model and Approaches for Smoothing Peaks of Traction Energy in Timetabling. *Journal of the Korean Society for Railway*, 12(6), 1018-1023.
- Lukaszewicz, P. (2007a). A simple method to determine train running resistance from full-scale measurements. *Proceedings of the Institution of Mechanical Engineers, Part F: Journal of Rail and Rapid Transit*, 221(3), 331-337.
- Lukaszewicz, P. (2007b). Running resistance - results and analysis of full-scale tests with passenger and freight trains in Sweden. *Proceedings of the Institution of Mechanical Engineers, Part F: Journal of Rail and Rapid Transit*, 221(2), 183-193.
- Report ERRI C 179/RP 9, Utrecht, (1993).
- Rochard, B. P., & Schmid, F. (2000). A review of methods to measure and calculate train resistances. *Proceedings of the Institution of Mechanical Engineers, Part F: Journal of Rail and Rapid Transit*, 214(4), 185-199.
- Ryan, T. P. (2008). Modern regression methods. 2nd Edition, John Wiley Sons, New York. ISBN: 978-0-470-08186-0.
- Somaschini, C., Rocchi, D., Tomasini, G., & Schito P. (2016). Simplified estimation of train resistance parameters: full-scale experimental tests and analysis. *Proceedings of the Third International Conference on Railway Technology: Research, Development and Maintenance*, Paper 58.
- Urlu, C. (1999). Demiryolu Araçlarının İleri Dinamiği. Ankara: TCDD Yayınları.
- Anonymous, (2016). Tülomsaş. (Accessed:22/11/2016) www.tulomsas.com.tr/main.php?kid=90
- Anonymous, (2018). (Accessed:22/11/2018) megep.meb.gov.tr/mte_program_modul/moduller_pdf/Trenlerin%20Dinami%C4%9Fi%20ve%20Tekerlek%20Kuvvetleri.pdf



Investigation of Manufacturing of a Pelton Turbine Runner of Composite Material on a 3D Printer

A. Murad GÜLLÜOĞLU¹ , Oğuzhan BENDEŞ^{2*} , Buğra YILMAZ¹ , Adem YILDIZ² 

¹TEMSAN, Turkish Electromechanics Industry Corp., General Directorate, Ankara, Turkey

²TEMSAN, Turkish Electromechanics Industry Corp., Directorate of R&D, Ankara, Turkey

Keywords	Abstract
<p><i>Pelton Turbine</i> <i>Additive Manufacturing</i> <i>Composite Turbine-Runner</i></p>	<p>Nowadays, different methods are used in manufacturing sector. One of these is the production technique on 3D printers, which is also described as additive manufacturing. In this study, Pelton turbine bucket was produced from composite material (carbon + thermoplastic) on a 3D printer and tested. Analytically, the special pelton turbine bucket designed at TEMSAN has a special form structure. Through additive manufacturing, the turbine runner was manufactured faster and more cost-effectively compared to production out of steel material. Tests were carried out in TEMSAN Hydraulic Test Laboratory at 5-7.5 bar pressure range and 26 l/s and 46 l/s flow rates. The highest breaking strength value was determined as 1775 N.</p>

Cite

Güllüoğlu, A. M., Bendeş, O., Yılmaz, B., & Yıldız, A. (2021). Investigation of Manufacturing of a Pelton Turbine Runner of Composite Material on a 3D Printer. *GU J Sci, Part A, 8(1)*, 24-34.

Author ID (ORCID Number)	Article Process	
A. M. Güllüoğlu, 0000-0002-5525-7132	Submission Date	10.01.2020
O. Bendeş, 0000-0002-2722-1212	Revision Date	22.03.2021
B. Yılmaz, 0000-0001-6799-4749	Accepted Date	24.03.2021
A. Yıldız, 0000-0001-6534-5737	Published Date	29.03.2021

1. INTRODUCTION

The 3D additive manufacturing method is used in different fields in the industry day to day. However, studies and product developments using different material types (polymer, composite, metal) do continue. For many years, products have been produced from polymer based materials by additive manufacturing method and used in many areas of the industry; automotive, medical, advertising and promotion sectors in particular. In the energy industry, too, various studies are carried out on the equipment produced on 3D metal printers. In addition to this, different designs and cost-reducing studies are effectively urged upon in connection with the equipment that generate power from renewable energy sources. Generation of energy from renewable energy sources increases in value with day to day due to low carbon emissions as well as environmental and climatic conditions. Approximately 15% of the world's energy demand is provided by hydraulic energy (Chouhan et al., 2017). In hydraulic energy, generation of energy is provided by using different turbine types depending on flow rate and head. Pelton turbine is preferred in projects with higher heads (pressure). In the study carried out by Takagi et al. (2014) it was conducted on a Pelton turbine that had been manufactured by means of additive manufacturing technique with nylon resin fibreglass matrix to accelerate the production time of the Pelton turbine and reduce the costs and it was stated that the design errors were detected earlier. In addition, it should be considered that the corrosion resistance of composite materials is higher and this will provide an advantage for use in micro turbine systems (Shirisha et al., 2014). In reducing the total weight, it is possible to manufacture lighter turbine runners with 1/7 composite materials, especially when compared to steel. Manufacturers can also reduce costs by reducing the processing rate and total production time on conventional machines (Albertani, 2013).

In this study, the turbine bucket of a Pelton Turbine, which is one of the hydraulic turbine types, was produced from composite material by 3D additive manufacturing technique and information about the tests carried out for the product manufactured is presented.

2. MATERIAL AND METHOD

While the products and materials used in engineering have physical, electrical, magnetic, chemical, mechanical and production properties, they should also possess properties such as material cost, product shape, environmental impact, usability, cultural aspects, aesthetics and recycling (Adhikary et al., 2013).

In hydroelectric power plants, the potential energy of water is stored in construction structures such as reservoirs and dams. This potential energy is transferred to the turbine-generator shaft as mechanical power by transmitting the potential and kinetic energy to the hydraulic turbine which is located at different heads by means of penstock pipes. The higher the potential energy of the water, the faster the water velocity when entering the turbine runner. Water that hits the turbine runner at high speeds causes wear on the turbine runner (Neopane et al., 2011). With this in mind, the material to be used in the turbine runner is designed to meet the incoming loads and withstand this abrasive and corrosive effect.

Today, hydraulic turbine runners are usually made of heat treated stainless steel (for example: X5CrNi13-4) through long processes such as casting, machining and welded manufacturing methods. In order to prevent erosion corrosion due to sediment in steel materials, special coating or paint systems need to be applied onto the materials made of metal (Gummer, 2009). These days, hydraulic turbine runners are endeavoured to be produced using different materials and production techniques. For instance, composite material that is a material system consisting of a mixture or combination of two or more micro or macro components provides the better material properties such as hardness, durability and toughness (Shirisha et al., 2014).

The use of 3D metal, polymer and composite printers is one of the new production techniques. While there are advantages in this method such as rapid prototyping, material wastage, easy production of complex parts, there are also disadvantages such as design and difficult dismantling of the supports, long manufacturing times, unexpected defects during manufacturing, high surface roughness and environmental conditions. Recently, methods called FDM (Fused Deposition Modelling) and SLS (Selective Laser Sintering) are used in 3D printers.

3D printers, referred to as FDM or FFF (Fused Filament Fabrication), are printers with similar characteristics. In these printers, the filament-shaped material wound on the reels is heated at a temperature that can be shaped, usually at 240-275°C, and passed through the sections called nozzle at certain thicknesses. Production is completed layer-by-layer, by adding filament to create part whose dimensions were previously defined on a solid modelling program on the printer table with a flat surface. In composite printers, as shown in Figure 1, additive manufacturing is performed by feeding different materials from two different nozzles. Generally, the basic matrix element is thermoplastic materials and is reinforced with materials such as carbon fibre, fiberglass and kevlar.

However, using only thermoplastic materials does not meet the mechanical strength requirements (Peng et al., 2018). Supporting with materials such as carbon, kevlar and fiberglass improves the strength properties of the product (Blok et al., 2018). Comparing the fiber reinforcing investigated, it was found that the nylon composite strength was in the following order: Carbon fiber > Glass fiber > Kevlar fiber (Dickson et al., 2017). Among the carbon, glass, and basalt fibers typically used in manufacturing of FRP (fiber-reinforced-polymer) bars, the carbon fibers were the strongest and most resistant to the various corrosive environments (Cousin et al., 2019). The effects of the type of reinforcement and fiber volume content on the impact damage performance of reinforced nylon specimens were of particular significance (Caminero et al., 2018). Kussmaul et al. (2017) in their study showed that carbon fiber reinforced polymers (CFRP) offered outstanding weight-specific properties and high design freedom.

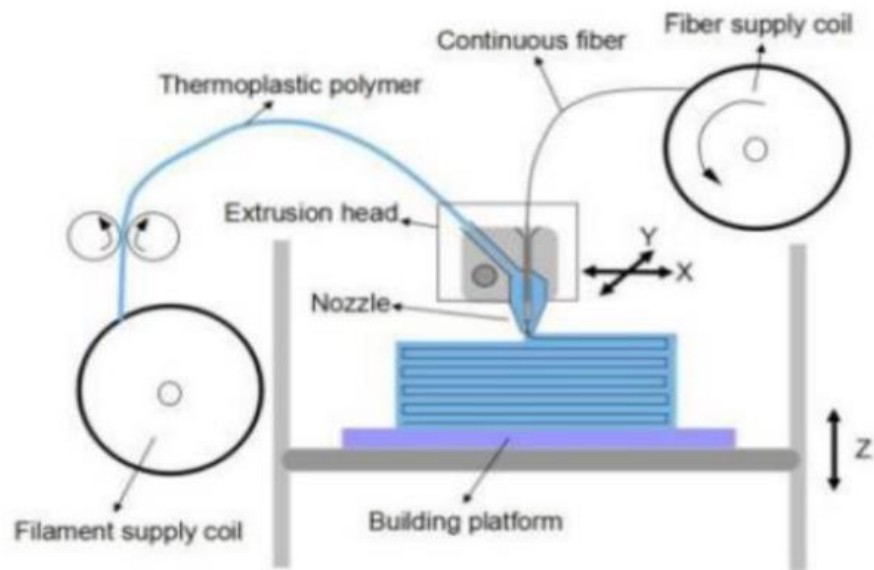


Figure 1. Schematic Representation of Composite Printer Operation (Zhao et al., 2019)

When making production on composite printers, first of all, software for preparation for printing that comes with the printer is used. To which layers the reinforcement materials (carbon fibre, fiberglass or kevlar) will be added is designated on this software and therefore all layers of the work piece are organised separately. In areas where stresses are critical, it is important to add the reinforcing materials at the right angle based on the density and direction of the stress formed. After the piece is prepared for printing, it is loaded onto the printer's memory for production and the production process begins. The printing process takes place on the printer thanks to composite and thermoplastic materials fed from two different nozzles. Figure 2 shows 3D printing process.

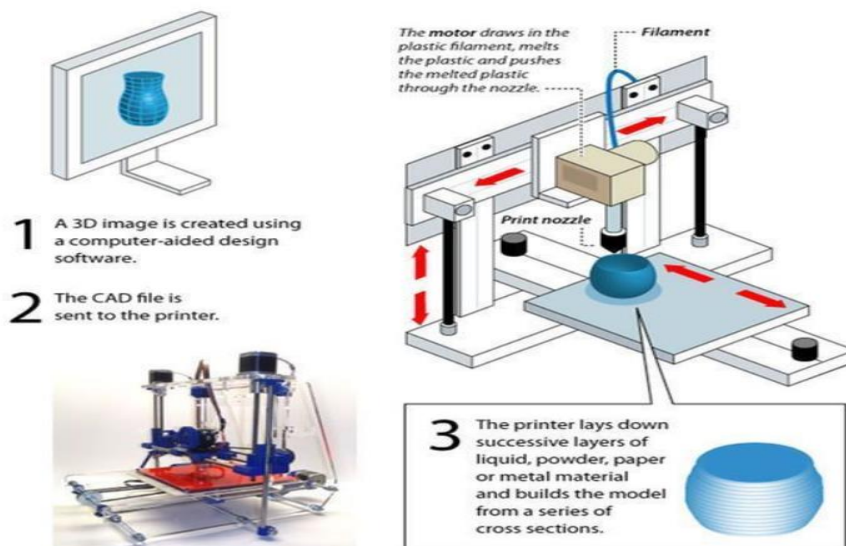


Figure 2. 3D Printer Design and Production Process (Dronesrate, 2021)

3. TEST STUDY AND RESULTS

In this study, Mark Two model printer of Markforged company was used. The plate dimensions are 320 mm x 132 mm x 154 mm. It is an FDM type printer with polymer matrix and supported by materials such as carbon fibre, kevlar and fiberglass. The pelton bucket developed, shown in Figure 3, by R&D Department of TEMSAN, whose dimensions are determined by analytical formulas, was produced out of composite materials with the help of this printer.

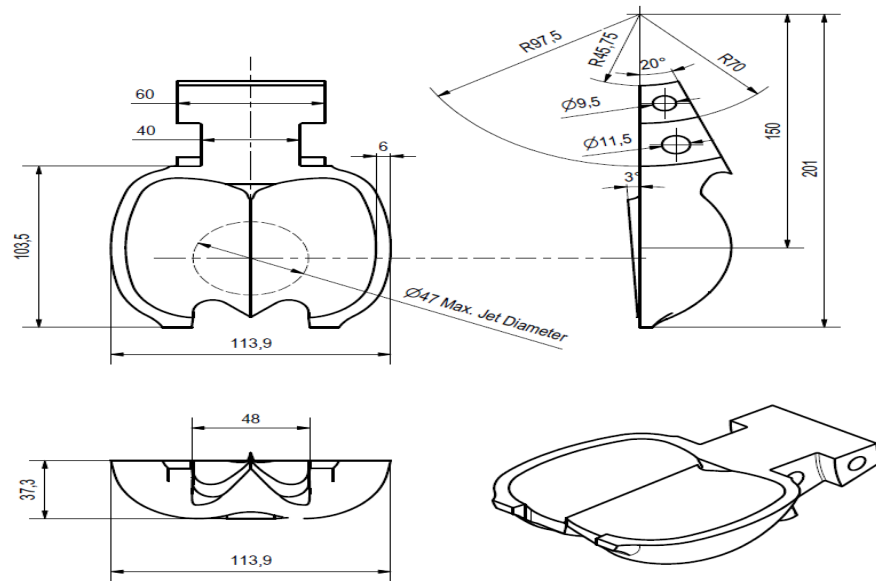


Figure 3. Dimensions of Pelton Bucket

In the production of Pelton bucket, the filament thermoplastic materials with a trade name of ONYX of the Markforged company were used as carbon reinforcement in the ratio of 22.9% initially and 36 % afterwards. In both test samples and production of the piece, the material fill rate was 100%. Test specimens containing 22.9% and 36% carbon (4 mm x 10 mm x 80 mm) were subjected to flexural strength test in the Mechanical Testing Department of METU Central Laboratory in accordance with ISO 14125 (2010) standard. The test results are given in Figure 4 and Figure 5.

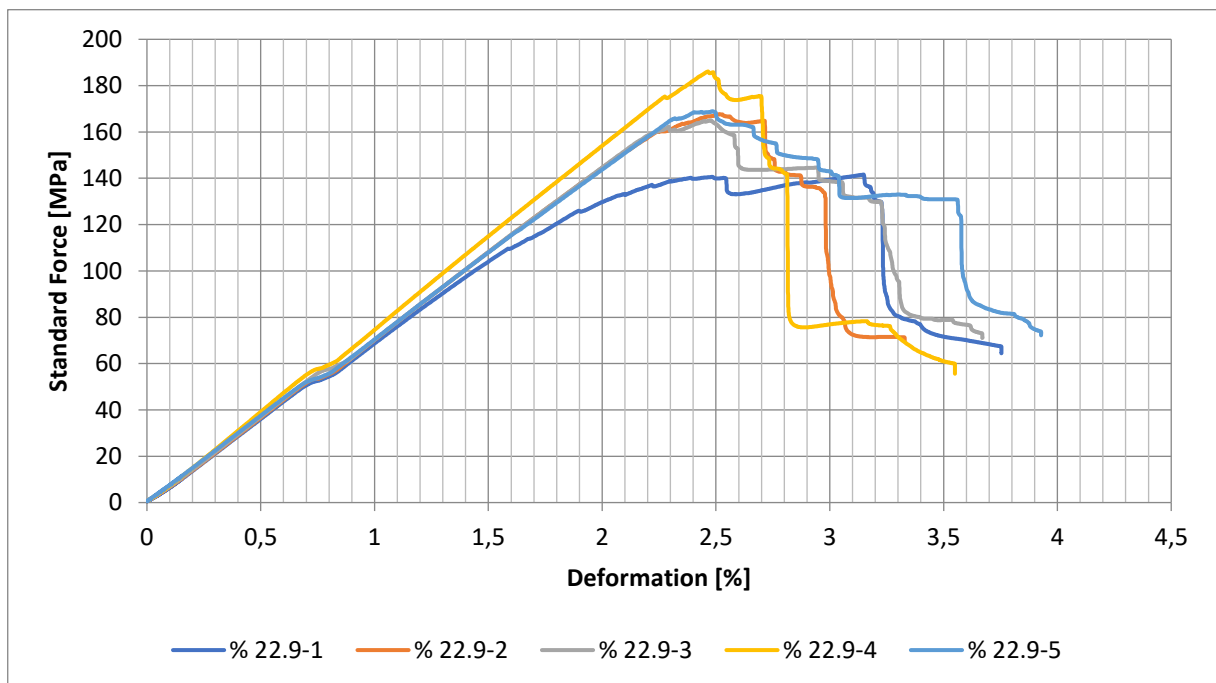


Figure 4. Flexural Strength - Deformation Graph of Samples Containing 22.9% Carbon

Flexural strength test at three points (ISO 14125, 2010) were performed on the universal Zwick brand testing machine as depicted in Figure 6. While the average value was 165.8 MPa (σ_m) in test samples containing 22.9% carbon filament, this value was 244.4 MPa for the samples containing 36% carbon. Table 1 and Table 2 show the average flexural strength (σ_m) tests for both carbon contents.

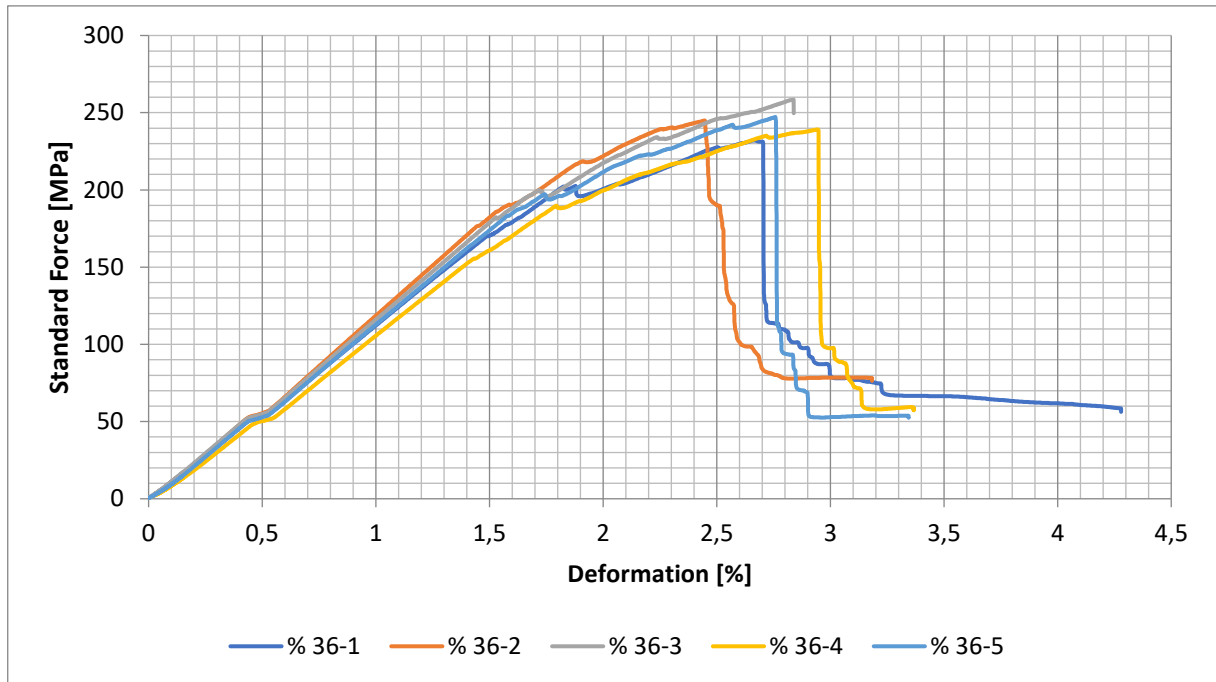


Figure 5. Flexural Strength - Deformation Graph of Samples Containing 36% Carbon

While a maximum flexural strength of 186 MPa was observed in samples containing 22.9% carbon, this value reached up to 258.5 MPa in samples containing 36% carbon. Fibre reinforced composites generally aim to improve weight strength and rigidity against weight ratios (Shirisha et al., 2014). When the test results are considered, it shows that the amount of deformation increases by only 10%, although the flexural strength value increases by 47.4% with the increase in the amount of carbon by volume. This shows that the material can be more rigid with increased carbon content.

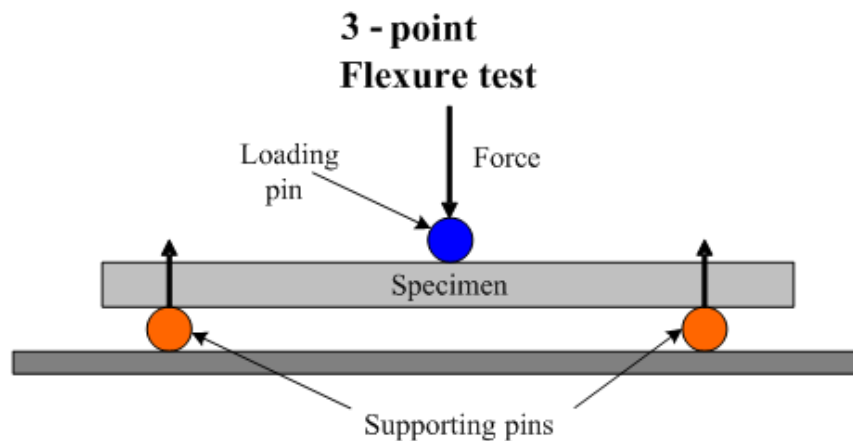


Figure 6. Schematic Representation of the 3 Point Flexural Strength Test (SubsTech, 2021)

Increasing the carbon content of the test samples by volume increases the flexural strength values. Pelton turbine buckets designed for 145 m head and 120 l/s flow rate for this study were subjected to a strength test after being produced as composite in additive manufacturing method to have the same amount of carbon rate by volume. A maximum of 3100 N force is generated on the Pelton bucket under the specified operating conditions. In the analyses carried out through finite elements method on the work piece, it was confirmed that the stress value was 145 MPa ($\sigma_{\text{Von-Mises}}$). When the flexural strength values of the samples containing 22.9% and 36% carbon are taken into consideration and the safety coefficients are calculated in the Equation (5); the values of 1.14 and 1.69 are obtained respectively.

Table 1. Flexural Strength Test Data for the Sample Containing 22.9% carbon

Series n=5	E _{mod} (MPa)	σ _m (MPa)	F _{max} (kg)	S ₀ (mm ²)
x	6948	165.88	30.6	42
s	260.9	15.91	2.73	0.25
v	3.76	9.59	8.93	0.60

Table 2. Flexural Strength Test Data for the Sample Containing 36% carbon

Series n=5	E _{mod} (MPa)	σ _m (MPa)	F _{max} (kg)	S ₀ (mm ²)
x	10600	244.42	45.9	42.37
s	813.2	9.79	1.93	0.36
v	7.67	4.01	4.21	0.85

The maximum force on the Pelton bucket was calculated by taking Equation (2) into consideration (Thake, 2000). Equation (1) and Equation (3) were used for A (water jet area) and σ_{flex} respectively.

$$d_{jet} = \sqrt{\frac{4}{\pi \cdot C_v \sqrt{2g}} \cdot \frac{1}{H_n^{0.25}} \cdot \sqrt{\frac{Q}{n_{jet}}}} \quad \text{m} \quad (1)$$

$$F_{jet} = \rho \cdot Q \cdot V_{jet} \quad \text{N} \quad (2)$$

$$\sigma_{flex} = F_{jet} / A \quad \text{MPa} \quad (3)$$

$$V_{jet} = C_v \cdot \sqrt{2gH} \quad \text{m/s} \quad (4)$$

$$S = \sigma_m / \sigma_{von-m} \quad (5)$$

It was decided to perform a tensile strength test taking into account the safety coefficients of samples containing 36% carbon prior to application tests. Samples containing 36% carbon were prepared in accordance with ISO 527-4 (2007) standard and tensile strength test was performed in the same laboratory. The graph for the tensile strength test results of five samples is given in Figure 7 and Table 3.

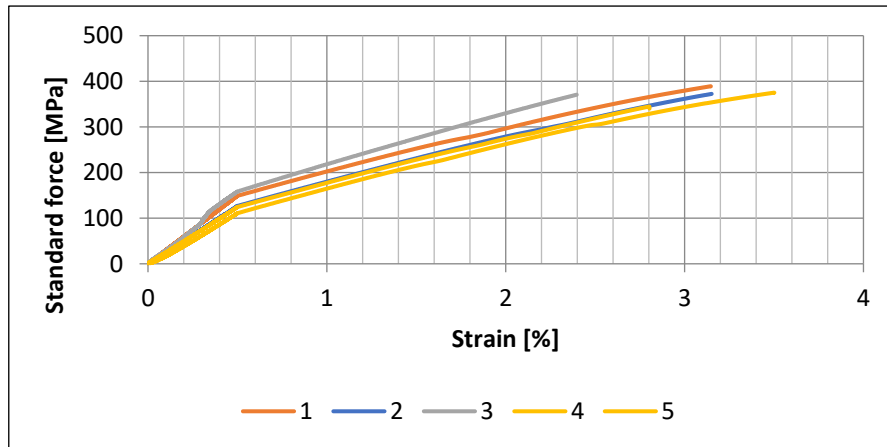
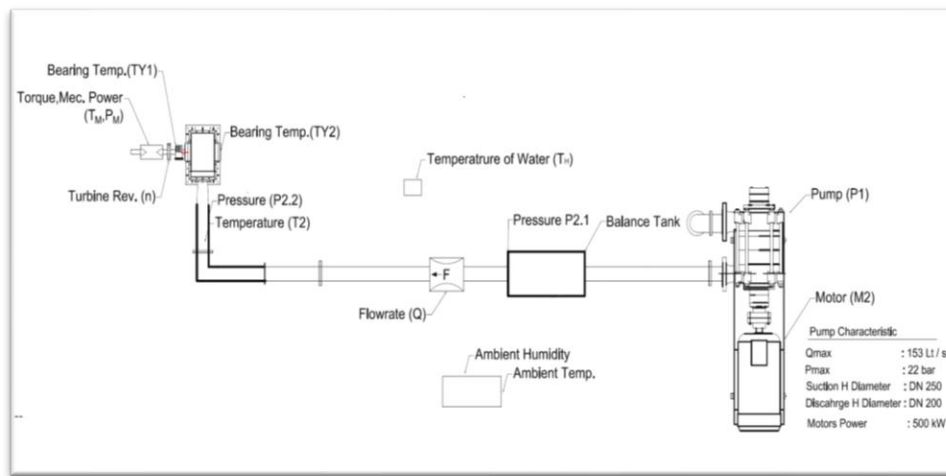
**Figure 7.** Graph for Tensile Strength Test Result of Samples Containing 36% Carbon

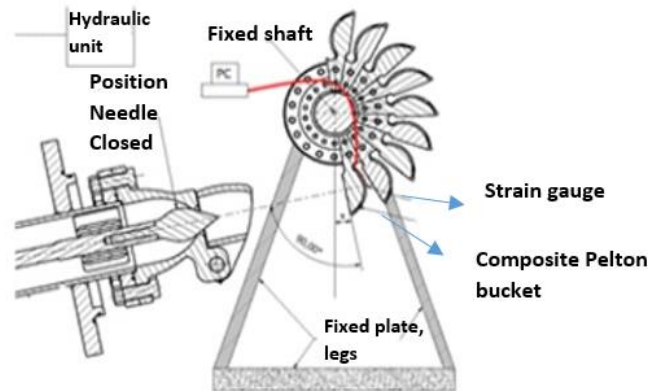
Table 3. Tensile Strength Test Data of the Sample Containing 36% Carbon

Series n=5	E_t (MPa)	σ_m (MPa)	ϵ_m (%)	b (mm)	h (mm)	A_0 (mm ²)
x	25500	370	3.0	25.04	2.714	67.95
s	3170	16.1	0.42	0.03271	0.0305	0.76
v	12.41	4.35	13.93	0.13	1.12	1.12

It was decided to produce five pieces of Pelton buckets in the dimensions given in Figure 3, with a carbon content of 36% (73.5 cm³) by volume. Application tests were performed in Hydraulic Test Centre of TEMSAN, which is shown schematically in Figure 8.

**Figure 8.** Schematic Drawing of Hydraulic Test Centre

These buckets were fixed to the shaft as shown in the schematic drawing in Figure 9 and subjected to maximum water jet force. With the help of Equations (2) and (4), breaking forces were managed to be determined. Flow rates applied in the hydraulic test centre were measured by Modmag magnetic flow meter and pressures were measured by Keller (PA-21Y) pressure transmitter. The needle opening can be adjusted automatically by means of a hydraulic cylinder and system having a measuring ruler sensor. Thanks to these highly accurate measuring elements, parameters such as flow rate, pressure and nozzle openings, which are considered to be the most significant factors affecting the operating conditions of a hydraulic turbine unit, can be controlled very precisely.

**Figure 9.** Application of Water Jet on Composite Pelton Bucket

The buckets used in the application are numbered as buckets 4, 5, 8, 10 and 11. The production of these buckets was carried out at a room temperature of (20°C) and an average relative humidity of 75%. Pelton

buckets consist of 337 layers containing thermoplastic and carbon. The production time lasted 35 hours. Post-production dimensions and weights of each bucket were inspected. 400 μm thick polymer material was used in the outer layers for smoother surface and dimensional accuracy.

During breaking tests, the test was halted at each pressure value until flow rate was stable. Pelton buckets were then kept under load for 10 minutes for each flow rate value. In addition to this, the buckets remained under load during the transition. Pressure transitions and stabilising of flow rate in the system lasted 10 min. In order to observe the breaking pressure and flow rate value of the bucket remotely, a strain gauge was attached to the buckets as shown in Figure 10. An Arduino-based program was composed to see the breaking value instantly. Thus, the breaking moments of the buckets were observed on the program without any problems. In order to prevent the turbine runner from rotating in the system, flanges were attached to both ends of the shaft and these flanges were mounted on a welded construction through an interconnection rod. Adjustment of flow rate was carried out with a needle driven by a hydraulic cylinder. The pressure of the system was controlled by a frequency controlled multistage pump.

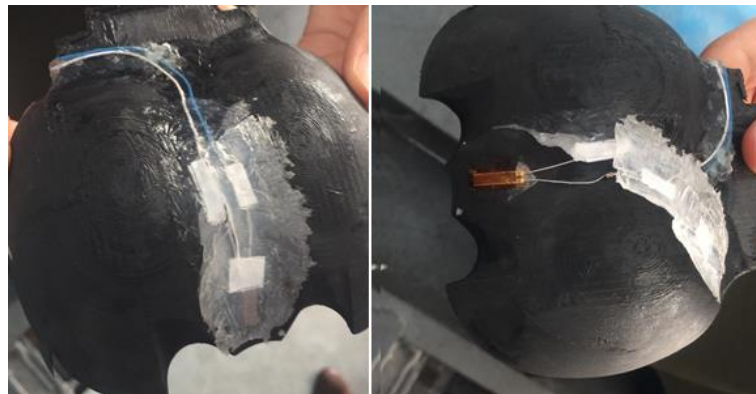


Figure 10. Connection of Strain Gauges on Pelton Buckets

The densities of carbon and thermoplastic (Onyx) materials used in production are 1.4 g/cm^3 and 1.2 g/cm^3 respectively. The weight of the buckets produced in additive manufacturing method is 200 g (± 10 g). The same bucket made of steel weighs 1338 grams. There is a 85% reduction in the weight of one turbine bucket.

When the graph in Figure 11 is examined, it is seen that Pelton buckets are broken at different flow rate and pressure values. The breakage of the buckets was observed to be in 2 ways; breaking by separating from their layers and breaking by bending. The bucket #11, on which breaking by bending was observed, has a breaking pressure of 7.44 bar, a breaking flow rate of 46 l/s and a breaking force of 1775 N. Similarly, the bucket #8, which was broken in a similar manner, was broken at a force of 7.52 bars, 44 l/s and 1746 N.

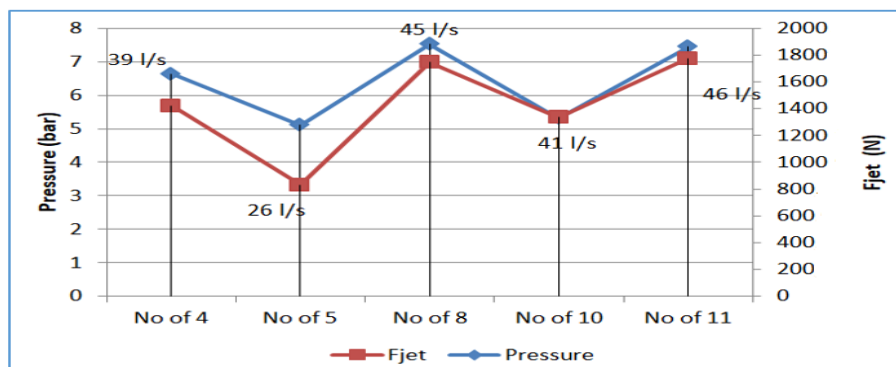


Figure 11. Pressure, Flow and Breaking Force Values Applied on Pelton Buckets

Breakage occurred in both pelton bucket samples in the regions where maximum stress was formed as seen in Figure 12. The remaining three samples were separated from the layers, as shown in Figure 13. These buckets were separated from their layers at lower forces.

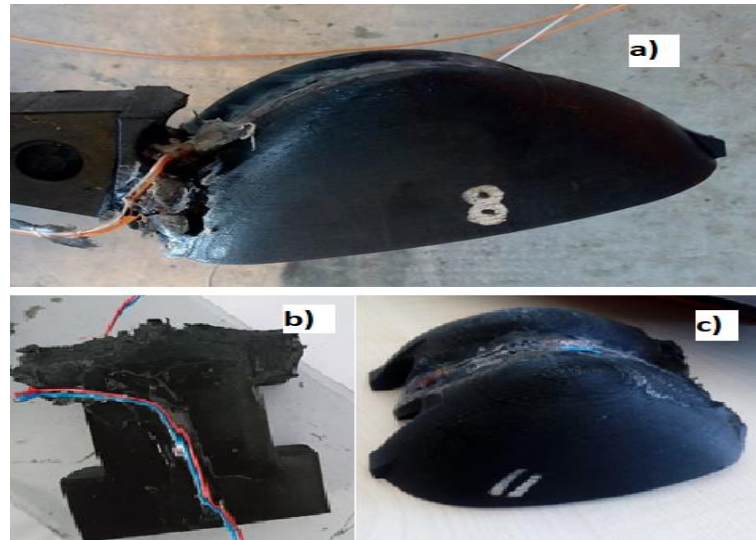


Figure 12. a) Broken bucket #8, b), c) Broken parts of bucket #11



Figure 13. Breaking photos of a) Bucket #4, b) Bucket #5, c) Bucket #10

The bucket #4 has the highest breaking strength out of the buckets separated from their layers and the bucket breaking pressure of this bucket is 6.64 bars, breaking flow rate is 39 l/s and breaking force is determined to be 1420 N. When the production follow-up schedules of these buckets are examined, it is seen that production stops at the 300th layer during the production of bucket #10 for about 10 hours. Therefore, it can be thought that the cooling of ambient and piece temperature that will occur during the pauses during production affects the adhesion strength of the layers (Ali et al, 2019). In the breaking tests applied, it is seen that none of the buckets can get close to the forces, working pressure and flow rate values designated in the design values. The main reason for this is that the acceptance of the safety coefficient of (> 1.5) designated at the design stage is suitable for steel materials but the same acceptance is not suitable for a composite material produced by additive manufacturing method. It is considered that if the additive

composite parts are to be used especially in machines subject to sudden load changes such as hydraulic turbines, the safety coefficient acceptance should be higher provided that the suitable production conditions are provided.

4. CONCLUSION AND DISCUSSION

The combination of different materials and the use of new production techniques (additive manufacturing) in the Pelton turbine bucket, which is one of the hydraulic turbine types, were investigated.

The Pelton turbine runner has a specially defined form. In this study, the Pelton runner produced as composite is 1/8 lighter than the steel material. This would provide the manufacturer with ease of application, such as transport and installation, as well as reduced radial forces from the turbine bearings, resulting in longer bearing life.

The composite material contains 36% C and 64% thermoplastic material (Onyx). In the mechanical tests carried out on the test specimen, the flexural strength value of 244.42 MPa and the tensile strength of 370 MPa were obtained. This value is very close to carbon steel mechanical values of 1.0037.

In breaking tests, some samples were separated from their layers and broke. Temperature and humidity are thought to be significant during additive manufacturing. It was also determined that any waiting or stopping during production affects the adhesion of the layers to each other. However, the breaking forces increased to 1775 N in two samples that demonstrated normal breaking behaviour. However, this result is considerably less than the expected value. The reason for this is that it is considered appropriate to select the safety coefficient acceptance at the design stage of the products with composite additive manufacturing in the machines with variable loads such as hydraulic turbines. In particular, testing for the safety coefficient value of >4 is recommended for further studies. However, this acceptance would not apply to all machinery equipment. For this reason, it will be appropriate to make security assumptions appropriate to the machine equipment in the production of composites with additive method.

Additive manufacturing is a new and rapidly expanding production technique. In our study, additive manufacturing technique provided the opportunity to quickly prototype and performs the tests related to the mathematically designed equipment such as turbine runners. Especially in the field of energy equipment, manufacturing method, acceptance of design and testing of different products such as fatigue will provide cost and time savings for project-based manufacturers. In this study, while the material cost of Pelton bucket produced as composite per unit was 200 €, the unit cost of the bucket made of metal is 301 €.

However, in the future, by changing the design assumptions such as the safety coefficient of the composite turbine runners produced in additive manufacturing method and increasing the carbon content, which is the support material, the use of hydraulic turbine runners manufactured by these methods can be realized in practice.

CONFLICT OF INTEREST

The authors declare that there is no conflict of interest regarding the publication of this paper.



REFERENCES

- Adhikary, P., Roy, K. P., & Mazumdar, A. (2013). Selection of hydro-turbine blade material: Application of fuzzy logic (MCDA). *International Journal of Engineering Research and Applications (IJERA)*, 3, 426-430.
- Albertani, R. (2013) Design and Manufacturing Study of Hydroelectric Turbines Using Recycled and Natural Fibre Composites” MSc Thesis, Oregon State University, Oregon.
- Ali, S. F., Malik, F. M., Kececi, E. F., & Bal, B. (2019). Optimization of Additive Manufacturing for Layer Sticking and Dimensional Accuracy. In: Kumar, K., Zindani, D., & Davim, J. P. (Eds.), Additive

- Manufacturing Technologies From an Optimization Perspective (pp. 185-198). IGI Global. doi:[10.4018/978-1-5225-9167-2.ch009](https://doi.org/10.4018/978-1-5225-9167-2.ch009)
- Blok, L. G., Longana, M. L., Yu, H., & Woods, B. K. S. (2018). An investigation into 3D printing of fibre reinforced thermoplastic composites. *Additive Manufacturing*, 22, 176-186. doi:[10.1016/j.addma.2018.04.039](https://doi.org/10.1016/j.addma.2018.04.039)
- Caminero, M. A., Chacón, J. M., García-Moreno, I., & Rodríguez, G. P. (2018). Impact damage resistance of 3D printed continuous fibre reinforced thermoplastic composites using fused deposition modelling. *Composites Part B: Engineering*, 148, 93-103. doi:[10.1016/j.compositesb.2018.04.054](https://doi.org/10.1016/j.compositesb.2018.04.054)
- Chouhan, K. S., Kisheorey, G. R., & Shah, M. (2017). Modelling, fabrication and analysis of pelton turbine for different head and materials. *International Journal of Computational Engineering Research (IJCER)*, 7(2), 2250-3005.
- Cousin, P., Hassan, M., Vijay, P., Robert, M., & Benmokrane, B. (2019). Chemical resistance of carbon, basalt, and glass fibres used in FRP reinforcing bars. *Journal of Composite Materials*, 53(26-27), 3651-3670. (2019). doi:[10.1177/0021998319844306](https://doi.org/10.1177/0021998319844306)
- Dickson, A. N., Barry, J. N., McDonnell, K. A., & Dowling, D. P. (2017). Fabrication of continuous carbon, glass and Kevlar fibre reinforced polymer composites using additive manufacturing. *Additive Manufacturing*, 16, 146-152. doi:[10.1016/j.addma.2017.06.004](https://doi.org/10.1016/j.addma.2017.06.004)
- Dronesrate (2021). Drone Infographics : How 3D Printers Work. (Accessed:17/03/2021) dronesrate.com/drones-infographic/drone-infographics-drone-infographics-how-3d-printers-work-infographic-maybe-something-for-3d-p
- Gummer, H. J. (2009). Combating Silt Erosion in Hydraulic Turbines. (Accessed:17/03/2021) <https://www.renewableenergyworld.com/2009/03/01/combating-silt-erosion-in-hydraulic-turbines>
- Kussmaul, R., Zogg, M., Weiss, L., Relea, E., Jacomet, R., & Ermanni, P. (2017). Carbon Fiber Reinforced Polymers for High-dynamic Testing Machines. *Procedia CIRP*, 66, 10-15. doi:[10.1016/j.procir.2017.03.300](https://doi.org/10.1016/j.procir.2017.03.300)
- Neopane, H. P., Dahlhaug O. G., & Cervantes, M. (2011). Sediment erosion in hydraulic turbines. *Global Journal of Researches in Engineering (Mechanical and Mechanics Engineering)*, 11(6), 17-26.
- Peng, Y., Wu Y., & Wang, K. (2018). Synergistic reinforcement of polyamide-based composites by combination of short and continuous carbon fibres via fused filament fabrication, structures. *Composite Structures*, 207, 232-239. doi:[10.1016/j.compstruct.2018.09.014](https://doi.org/10.1016/j.compstruct.2018.09.014)
- Shirisha, A., Vinod Kumar, V., Santosh Kumar, S., Varun, K., & Bhavana, A. (2014). Advanced composite micro-hydro turbine runner design and study its performance for power generation. *Advanced Materials Manufacturing & Characterization*, 4(1), 57-61. doi:[10.11127/ijammc.2014.03.09](https://doi.org/10.11127/ijammc.2014.03.09)
- SubsTech (2021). Flexural strength tests of ceramics, 3-point Flexure Test - Ceramics. (Accessed:17/03/2021) www.substech.com/dokuwiki/doku.php?id=flexural_strength_tests_of_ceramics
- Takagi, M., Watanabe, Y., Ikematsu, S., Hayashi, T., Fujimoto, T., & Shimatani, Y. (2014). 3D printed pelton turbine: how to produce effective technology linked with global knowledge. *Energy Procedia*, 61, 1593-1596. doi:[10.1016/j.egypro.2014.12.179](https://doi.org/10.1016/j.egypro.2014.12.179)
- Thake, J. (2000). Micro-Hydro Pelton Turbine Manual: Design, Manufacture and Installation for Small-scale Hydro-power. ITDG. ISBN-13: 9781853394607
- ISO (2007). Plastics - Determination of tensile properties - Part 4: Test conditions for isotropic and orthotropic fibre-reinforced plastic composites. TS EN ISO 527-4
- ISO (2010). Fibre-reinforced plastic composites - Determination of flexural properties. TS EN ISO 14125
- Zhao, H., Liu, X., Zhao, W., Wang, G., & Liu, B. (2019). An Overview of Research on FDM 3D Printing Process of Continuous Fiber Reinforced Composites. *Journal of Physics: Conference Series*, 1213(5), 052037. doi:[10.1088/1742-6596/1213/5/052037](https://doi.org/10.1088/1742-6596/1213/5/052037)



Moisture Impact on Wind Density Power Seasonally

Zaid Ayad Jalal ALWINDAWI^{1,*} , Mehmet Y. GUNDOGDU¹ 

¹Gaziantep University, Department of Mechanical Engineering, Gaziantep, Turkey

Keywords	Abstract
Moisture Wind Power Available Power in Wind Two-Phase Flow Wind Density Power	Increased carbon dioxide emissions in the atmosphere and their harmful effects on the atmosphere and humans in general, this increase leads to significant climate changes that continue to affect the coming years. There is an urgent need to develop and increase research on clean energy and find the impact of weather changes, on the turbine's efficiency as a result of density fluctuate. A two-phase flow homogeneous model used to find these changes. The study analyzed the effect of atmospheric conditions, including temperature, humidity and pressure on kinetic energy in the wind through its effect on air density and find the rate of change resulting from these conditions, the air is dry and when the air is humid so the increase or decrease of this energy will affect positively or negatively on the performance of the turbine. The city of Mersin was selected in Turkey for this analysis through the application of air conditions obtained from the General Directorate of Meteorology in Ankara and resolve for accurate and detailed for each season throughout the year 2017, where the temperature varies from 0 to 35 degrees Celsius and humidity of 15 to 99 percent, as well as air pressure from 966.95417 to 1025.9 hPa. The effect of moisture was studied mainly by using thermodynamic laws in this paper.

Cite

Alwindawi, Z. A. J., & Gundogdu, M. Y. (2021). Moisture Impact on Wind Density Power Seasonally. *GU J Sci, Part A*, 8(1), 35-42.

Author ID (ORCID Number)

Z. Alwindawi, 0000-0002-7658-7026
 M. Gundogdu, 0000-0001-5041-9529

Article Process

Submission Date 17.04.2020
Revision Date 05.11.2020
Accepted Date 19.03.2021
Published Date 29.03.2021

1. INTRODUCTION

The wind data analysis assessment is the key requirements to benefit the achievement of wind energy at any location. With the development in the economy and the rising population, human request for energy is increasing rapidly. Fossil energy such as coal and oil are non-renewable as they have to go through hundreds of millions of years of a geological procedure to be generated. The burning of fossil energy with the obstetrics of sulfur dioxide and dust leads to many environmental problems such as acid rain and photochemical smog problem. It also turnover underground solid carbon into gaseous carbon dioxide emitted into the atmosphere, which enhances the greenhouse effect, accelerates north and south polar ice to melt, and leads to a deadly threat to human civilization. There are several studies on wind energy potential and electricity generation (Karlsen, 2009; Carriveau, 2011; Giebel et al., 2011; Ragheb & Ragheb, 2011; Torenbeek, 2013; Salih & Majli, 2015; Clifton et al., 2016; Emeis, 2018). The previous paragraphs have assumed that the air was completely dry. In reality, it is in no way dry (Karlsen, 2009; Carriveau, 2011; Giebel et al., 2011; Ragheb & Ragheb, 2011; Torenbeek, 2013; Clifton et al., 2016; Emeis, 2018). Wind speed and energy maps of Turkey have been presented and the potential areas are identified with the emphasis on their significance, according to Ahmet Öztökal indicated that Along the Aegean and the Black Sea, coastal areas wind energy generation amounts are higher in winter than in summer (Karlsen, 2009). Wind power density is generally under the influence of relief (mountains, hills, valleys), ground thermic (thermal capacity of different soils and water); it is clear that in higher altitude wind is less influential by

*Corresponding author (Sorumlu Yazar), e-mail: zaidalwindawi@gmail.com

those parameters (Torenbeek, 2013). Wind energy potential assessment is critical factors for the suitable development of wind power application at a given location (Rotronic, 2005).

1.1. Factor Affecting on the Density

Air density is the mass of air molecules in a given volume so any more air mass flowing over wing allows to generate more lift and increasing wings performance. There are three factors are effective on-air density its pressure, temperature and Humidity. Pressure is a weight of column of air any increasing pressure means more air molecules in given volume. Temperature also affects density when temperature increase the air molecules have more energy, so they spread farther apart so when air warmer than stander it's less dense and performance decrease. Humidity also plays an important factor, air is made up of 78% Nitrogen, 21% Oxygen and 1% other gasses. The amount of water vapor in the air varies, but it can contribute up to 1%. Water vapor weighs less than the Nitrogen or Oxygen molecules that make up the rest of the air and, water vapor takes up about the same amount of space. So, when more water vapor in the air, the air has less mass which means it's less dense. thus, all factor affective on-air density also affective on-air power (available power).

2. MATERIAL AND METHOD

2.1. Theory

A mathematical description of the winds is most easily done by considering the momentum balance of the atmosphere thus, in this paper explain the theory for using homogeneous two-phase flow to find the kinetic energy by application the two-phase flow theory to find the density of air and then find the available power in wind, Also, the laws of thermodynamics the ideal gas laws is used to find the density of dry air and through it find the available energy hypothesis when it is dry air only and through these two scenarios the difference between them is found. Be-low is a guiding explanation of the mechanism of work in this research to find the available energy to prepare the laws and find the homogeneous air density and dry air and find the resulting difference in kinetic energy in terms of two conditions. Depending on this theory, was obtain accurate data on the impact of atmospheric changes on wind density power, as well as the extent of the variation of kinetic energy in the wind based on this theory.

2.2. Methodology

When air is wet it means that contains a quantity of water vapors so the atmospheric air in this condition is the two-phase case and considers there is no-slip velocity between air atomics, consider the air in this case a homogeneous state (Wills, 1967). Thus, a single-phase equation for continuity, momentum, and energy can apply by replacing the single-phase property with the mixture property. According to this condition using the weather data got from the General Directorate of Meteorology for Mersin city in 2017 (MGM, 2017), to calculates atmosphere density and other mix properties by using the following equation.

$$\rho_{\text{Atm}} = \alpha \rho_{\text{dry}} + [(1 - \alpha) \rho_v] \quad (1)$$

According to the ideal gas law the density of dry air is,

$$\rho_{\text{dry}} = \frac{P_{\text{dry}}}{R_a T_{\text{Atm}}} \quad (2)$$

from T_{Atm} find the saturation pressure of vapor from thermodynamics table and then from relative humidity and saturation pressure of vapor find the pressure of vapor,

$$\rho_{\text{dry}} = \frac{P_{\text{dry}}}{R_a T_{\text{Atm}}} \quad (3)$$

and from pressure of vapor and atmosphere pressure that obtained from metrology data find the pressure of dry air,

$$P_{\text{dry}} = P_{\text{Atm}} - P_v \quad (4)$$

then from recent equation find the density of air when R_a represent the constant of dry air. After calculating the density of dry air, it's necessary calculate the vapor density in atmosphere to obtained the density of mixture air (atmosphere) thus from pressure of vapor, temperature of atmosphere and constant of vapor R_v calculate the density of vapor,

$$\rho_v = \frac{P_v}{R_v T_{\text{Atm}}} \quad (5)$$

There are two way to find the humidity ratio ω the first way used psychrometric chart and second way used Colebrook-White Equation.

$$\omega = \frac{\text{mass of vapor}}{\text{mass of dry air}} \quad (6)$$

$$M_v = \frac{P_v V}{R_v T} \quad (7)$$

$$M_{\text{dry}} = \frac{P_{\text{dry}} V}{R_a T} \quad (8)$$

$$\frac{R_a}{R_v} = 0.622$$

$$\omega = 0.622 \frac{P_v}{P_{\text{dry}}} \quad (9)$$

Find volumetric concentration from two phase flow equation α The volumetric concentration is defined as the ratio between volumetric vapor flow and total volumetric flow in a given cross-section.

$$\alpha = \frac{Q_v}{Q_v + Q_{dry}} \quad (10)$$

From humidity ratio ω find the ratio between volume flow rate of vapor and dry and substituted it in volume concentration equation.

$$\omega = \frac{\rho_v Q_v}{\rho_{dry} Q_{dry}} \quad (11)$$

$$\frac{Q_v}{Q_{dry}} = \frac{\rho_{dry} \omega}{\rho_v} \quad \text{Substitute in Eq (10)}$$

So, the volume concentration equation is valid now then calculate density of mixture from equation (1).

The power available in the wind can be found from the following equation:

$$P_{in} = \frac{1}{2} A \rho V^3 \quad (12)$$

Where ρ is the density of the air, A is the swept area, and V is the wind speed. So, through this equation extract the power available in the wind in the first use the density of dry air and in the second use the density of the mixture and through them are extracted the power deviation as rate of change in the kinetic energy from dry air density to the mixture (atmosphere) density according metrology condition

$$P_{in\ dry} = \frac{1}{2} A \rho_{dry} V^3 \quad (13)$$

$$P_{in\ atm} = \frac{1}{2} A \rho_H V^3 \quad (14)$$

$$\lambda = \frac{P_{in\ dry} - P_{in\ atm}}{P_{in\ atm}} \quad (15)$$

The variability of wind power will be an increasing challenge for the power system as wind penetration grows and thus needs to study, thus from Equation (13) find the deviation of kinetic power of wind when supposition the wind is dry and when the wind is atmospheric according to the homogeneous flow.

3. RESULTS AND DISCUSSION

The statistical characteristics of the wind power have been analyzed by using meteorology data recorded by the General Directorate of Meteorology in Ankara for Mersin city in Turkey for the 2017 year. To decide the best suitable site for installing a wind farm as well as to select the turbine model suited for any site, it is necessary to carry out a careful wind energy resource evaluation. The meteorology data in the Excel program was analyzed by using the equations that were it was concluded in methodology section schedule explaining the change in the rate wind power.

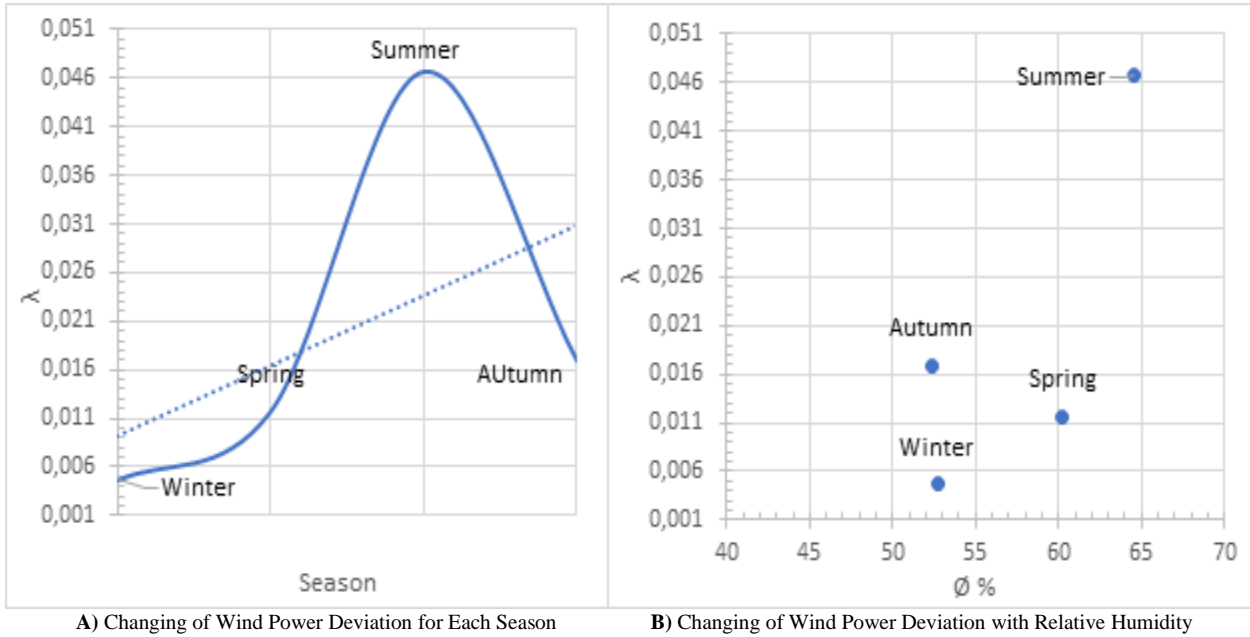


Figure 1. Wind Power Deviation Change Seasonally

Table 1. Wind Power Deviation Seasonally for 2017

Season	Temp (°C)	Ø %	V (m/s)	P _{atm} (Pa)	P _g (Pa)	P _{dry} (Pa)	P _v (Pa)	G	ρ _{dry}	ρ _v	α	ρ _H	λ
Winter	12.054	52.67	1.065	101978	1470.186	101216.801	752.324	0.00469	1277.56	5.7758	0.0000471	1277.50	0.0046
Spring	18.675	60.25	1.465	101282	2211.742	99971.901	2376.355	0.00824	1233.19	9.7160	0.000110	1233.04	0.0116
Summer	28.679	64.52	1.478	100573	3974.871	98032.900	2557.061	0.01623	1169.54	18.2312	0.000516	1169.03	0.0466
Autumn	22.620	52.32	1.056	101341	2876.303	99815.387	1504.923	0.00941	1215.38	10.8248	0.000170	1215.18	0.0169
Average	20.507	57.44	1.266	101293	2633.280	99759.200	1797.670	0.00964	1223.92	11.1370	0.000215	1223.69	0.0199

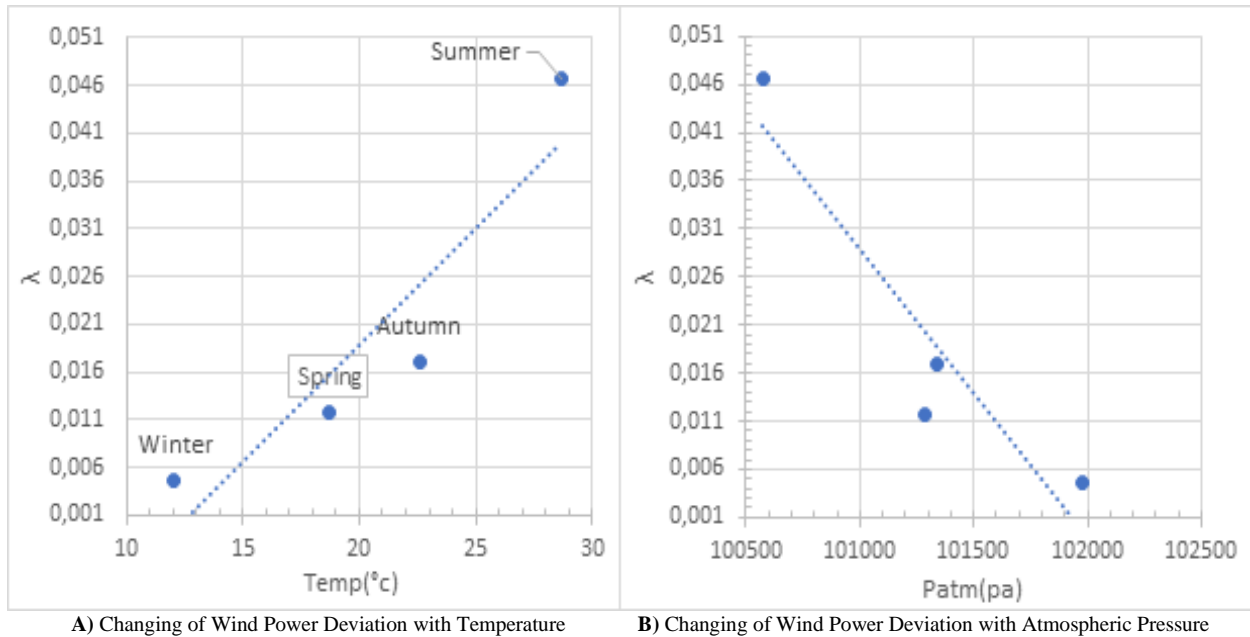


Figure 2. Changing of Wind Power with Meteorology Data

Table 1 represents a sensitive analysis of the 2017 seasonal wind energy deviation according to a two-phase flow homogeneous model for Mersin, Turkey. Figure 1A shows that the minimum deviation occurs in winter while the maximum power deviation appears in Summer. The deviation of the wind power increases gradually from the winter season through the spring to reach its highest value in the summer and then begins to decrease significantly in the autumn season. Any rising in deviation means decreasing in available wind power in atmospheric. This increasing and decreasing in deviation due to rising or dropping in temperature and relative humidity and atmospheric pressure, during winter the temperature is at low value 12.054°C and relative humidity at 52.6% that makes the moisture content at a low value at 5.77 g/m³ while in the summer the average temperature is 28.6°C and relative humidity at 64.5% makes an in-crease in water vapor content to 18.23 g/m³ which make the air more moisture content in air as known the water vapor has less weight from other content as shown in Figure 2.

4. CONCLUSIONS

Wind energy is important energy globally as it is clean energy used to produce electricity through the turbines. As it is known that a formula used to find the available energy in the air is $P=0.5V^3\rho$, the previous studies im-posed that the air density is constant and took it as dry air, this is a mistake because the atmospheric air density is changeable and depends on the temperature, humidity, and air pressure all of these factors change for every season throughout the year which causes losses are not few in available power if predicate as dry. The current study indicates that there is an energy deviation along each season, and throughout the year. When the temperature and relative humidity increases with decreasing in atmospheric pressure the power deviation increase which leads to a drop in available power.

ACKNOWLEDGEMENTS

I would like to express my special appreciation and gratitude to my supervisors, Prof. Dr Mehmet Yasar GUNDOGDU and Dr. Fuat YILMAZ, for all their help, patience, valuable advice, always providing and guiding me in the right direction. I'm very grateful and proud to work under their academic guidance. A special thanks to the General Directorate of Meteorology in Ankara for offering the meteorology data of Mersin city.

CONFLICTS OF INTEREST

No conflict of interest was declared by the authors.

NOMENCLATURE

λ : Power deviation between the available power for dry air and for atmospheric air

A : Area m^2

ρ_{Atm} : Density of atmospheric air g/m^3

ρ_{dry} : Density of dry air g/m^3

α : Volume void fraction between vapor area and total area

ρ_v : Density of water vapor g/m^3

P_{dry} : Pressure of dry air pascal

P_v : Pressure of water vapor pascal

P_g : Saturation vapor pressure (Pa)

R_a : Dry air gas constant $J/(kg.K)$

R_v : Vapor gas constant $J/(kg.K)$

T_{Atm} : Temperature of atmospheric air $^{\circ}C$

\emptyset : Relative humidity

ω : Humidity ratio

M_v : Mass of vapor

M_{dry} : Mass of dry air

Q_v : Volumetric vapor flow

Q_{dry} : Volumetric dry flow

REFERENCES

Carriveau, R. (2011). Fundamental and advanced topics in wind power. BoD-Books on Demand.

Clifton, A., Smith, A., & Fields, M. (2016). Wind plant preconstruction energy estimates. current practice and opportunities (No. NREL/TP-5000-64735). National Renewable Energy Lab.(NREL), Golden, CO (United States).

Emeis, S. (2018). Wind energy meteorology: atmospheric physics for wind power generation. Springer.

Giebel, G., Draxl, C., Brownsword, R., Kariniotakis, G., & Denhard, M. (2011). The state-of-the-art in short-term prediction of wind power. A literature overview, 2nd Edition, Technical Report.

Karlsen, J. A. (2009). Performance calculations for a model turbine. MSc Thesis, Institutt for energi-og prosessteknikk.

MGM (2017) Republic of Turkey Ministry of Agriculture and Forestry, Turkish State Meteorological Service.

Ragheb, M., & Ragheb, A. M. (2011). Wind turbines theory-the betz equation and optimal rotor tip speed ratio. In: Carriveau, R. (Eds.), *Fundamental and Advanced Topics in Wind Power* (pp. 19-38).

Rotronic (2005). *The Rotronic Humidity Handbook*. Rotronic Instrument Corp.

Salih, A. K. M., & Majli, A. S. (2015). *Fundamentals of Renewable Energy and Applications*. Journal of Fundamentals of Renewable Energy and Applications ISSN: 2090, 4541.

Torenbeek, E. (2013). *Synthesis of subsonic airplane design: an introduction to the preliminary design of subsonic general aviation and transport aircraft, with emphasis on layout, aerodynamic design, propulsion and performance*. Springer Science & Business Media.

Wills, G. B. (1967). *One-dimensional two-phase flow*, McGraw Hill.



Automated Sensor Data Validation and Correction with Long Short-Term Memory Recurring Neural Network Model

Abraham Sudharson PONRAJ^{1*}, T. VIGNESWARAN¹, J. Christy JACKSON²

¹School of Electronics Engineering, Vellore Institute of Technology, 600127, Chennai, India

²School of Computer Science Engineering, Vellore Institute of Technology, 600127, Chennai, India

Keywords	Abstract
Data Validation LSTM SARIMA Reference Evapotranspiration ETo Weather Data	Proper irrigation planning by matching reference evapotranspiration (ETo) with active crop growth requirement leads to an improved water usage efficiency and thereby improving the crop yield. ETo is primarily influenced by the following weather parameters the air temperature, relative humidity, wind speed and solar radiation. To make the ETo estimation system fault tolerant it is important to validate the real time data from the weather station, since the sensors used in these weather stations are prone to error due to influence of various environmental factors. A Recurring Neural Network (RNN) based Data Validation and Correction (DVC) algorithm was proposed to identify the faulty data and to correct them. Long Short-Term Memory (LSTM) RNN model is used to forecast the weather data such as temperature, solar radiation, wind speed and relative humidity. It uses statistical significance test to identify faulty data and isolate them. Then the DVC approach corrects the faulty data by replacing them by LSTM forecasted data. The performance evaluation of this approach showed better forecasting ability when compared with Seasonal Autoregressive Integrated Moving Average (SARIMA) based DVC and thereby improving overall performance of the DVC approach.

Cite

Ponraj, A. S., T. Vigneswaran, T., & Jackson, J. C. (2021). Automated Sensor Data Validation and Correction with Long Short-Term Memory Recurring Neural Network Model. *GU J Sci, Part A*, 8(1), 43-57.

Author ID (ORCID Number)

A. S. Ponraj, 0000-0002-3044-0985

T. Vigneswaran, 0000-0002-0478-6739

J. C. Jackson, 0000-0001-9468-7672

Article Process

Submission Date 05.07.2020

Revision Date 21.03.2021

Accepted Date 26.03.2021

Published Date 29.03.2021

1. INTRODUCTION

Global water intake doubles each 20 years, nearly twofold the rate of population increase. According to a Food and Agriculture Organisation (FAO) forecast, irrigation will have to meet 70-80% of the increase in food consumption between 2000 and 2030 (OECD, 2008). Though the practice of irrigation in agricultural farm is only around 300 million hectares or 20% of the cultivable land, but contributes significantly to over 40% of world food production (Fischer et al., 2012). Irrigation can mitigate the risk involved with rain-fed agriculture in dry regions. This helps protect farming from water shortages that are expected to occur more often. Efficient water use can maximize the diversity of agricultural crop, increase the yield, improve the economy and provide food at reduced price (Tiwari & Dinar, 2002). In view of the important role played by irrigation of agricultural farm in worldwide water usage, which significantly increase water availability for other human and environmental uses by better farm management practices that improve irrigation water production (Watson & Burnett, 2017).

A precise estimate of the amount of water lost to the atmosphere by combined evaporation and transpiration cycle called evapotranspiration (ET) is fundamentally mandatory for effective farm water management in order to improve agricultural crop water usage (Martin & Gilley, 1993; Tomar & Ranade, 2001). Reference evapotranspiration (ET_0) plays a vital role in solving the issues like soil water balance, irrigation system and water supply in the agro-ecosystem by providing a sustainable water management in these water starved regions. Hence proper irrigation planning by matching ET_0 with active crop growth requirement leads to an improved water usage efficiency and thereby improving the crop yield (Allen et al., 1998) ET_0 can be calculated by many empirical and non-empirical equation which depends on large amount of weather data (Cobaner, 2011). However, ET_0 is primarily influenced by the following weather parameters the air temperature, relative humidity, wind speed and solar radiation (Allen et al., 1998; Ponraj & Vigneswaran, 2019). This research work contributes by creating a fault tolerant model for predicting the reference evapotranspiration ET_0 using the daily weather data like the temperature, relative humidity, wind speed and solar radiation. There is a greater chance that the weather data used to estimate ET_0 is incorrect.

With weather data easily available these days and with data driven technologies used to estimate or predict ET_0 makes it even more vulnerable. The data used to develop these models and further for real time prediction with local sensor weather data or weather data from different source can be wrong or may contain spurious values. Mostly, sensors are subject to extreme environment condition and inherent sensor faults are the main drivers to these spurious data. This work aims at developing autonomous data validation and correction mechanism with weather data, which can be further used in creating a fault tolerant ET_0 prediction system. This is accomplished by identifying anomalies with statistical methods for each data value. Anomalies can be effectively identified in the input data variable by using long short-term memory recurring neural network (LSTM) model. The incorrect data value is removed when the data error has been identified. The faulty data is corrected by replacing it with the reliable forecasted value. This paper is organized as follows: section 2 describes the related work, section 3 outlines the methodology followed, section 4 discusses the results and section 5 concludes the work.

2. REVIEW OF RELATED WORK

Exhaustive data causes serious issues for a security mechanism in data analytics to identify all irregularities in real-time. The detection of anomalies and outliers from sensor data and other sources can no longer be considered human work. Hence, a need to simplify and automated the anomaly detection process. Automatic anomaly detection based on machine learning, statistics, etc. has been investigated in various areas, including network intrusion detection, authentication, medical data validation, sensor fault detection and more (Chandola et al., 2009). Given the number of such analyses in recent years, many anomaly detection methods still have not been able to minimize abnormalities in certain conditions (Sharma et al., 2010; O'Reilly et al., 2014). It is not the only threat, but as several sensors produces different type of data which may or may not be time dependent, in a single system. For IoT devices with multiple sensors, it is ineffective to use independent faulty data detection algorithms for each sensor.

Presently time series approach has gained popularity among other data-driven approaches to analyses data with periodical trend. For instance, one can find this approach used in various applications like electricity load forecast, market analysis to predict air ticket demand, battery health, etc (Venugopal & Vigneswaran, 2019). All these application exhibits periodical trend and may include seasonality as well, which are the temporal correlation of time series model (Box et al., 1994). A time- approach is capable to interpret the weather data or the observed sensor data as a structure of time-invariant parameters and this is their advantage. Further, this invariance is the key to any prediction model and thereby providing vital information to enhance the model. Furthermore, their efficacy for both linear and nonlinear models contributes to their competency for data fault analysis. Such facts reflect their need for improving the effectiveness of fault diagnostic application (Chatfield, 2000).

There have been several studies on various time series forecasting methods. The variable data is known to choose independent random step series in the random walk RW model (Simmons, 1986). This approach suggests that previous knowledge of data is not relevant and only new observations are valuable. The simple exponential smoothing method (SES model) has been widely applied in seasonal data for forecasting

applications (Gardner, 2006). The autoregressive integrated moving average (ARIMA) model is a most commonly used approach for forecasting in the last two decades amongst the other time series forecasting approaches (Mondal et al., 2014). The Sensor Fault Detection and Faulty Data Accommodation (SFDFDA) method were used in sewage monitoring system. It combines seasonal autoregressive moving average (SARIMA) system with a statistical significance test to allow correction of faulty temperature sensor data with forecasted temperature sensor data (Thiyagarajan et al., 2018). ADSaS (Anomaly Detection system using SARIMA and STL) combines SARIMA and Seasonal and Trend decomposition using Loess (STL) for improved performance in anomaly detection (Lee & Kim, 2018). It can be used for both periodic and non-periodic data.

SARIMA based model for forecasting has shown lesser accuracy and is capable of generating inconsistent forecast, though it is largely a flexible model. A recurring neural network (RNN) models is used to predict weather parameters, like the wind speed, air temperature and pressure and wind speed. Its flexibility enables the designer to update the network work design with ease (Roesch & Günther, 2019). An approach based RNN self-learning optimization for rain forecasting using weather dataset was successfully developed (Salman et al., 2015). ConvLSTM is a LSTM version, which comprises a convolution function within the LSTM cell. A model with the help of weather radar data is used for predicting rainfall by convLSTM data. It further reveals that its version of ConvLSTM decreased the RMSE by 23.0% when compared to linear regression models (Kim et al., 2017). LSTM based RNN has proven particularly effective for time series based faulty data identification (Malhotra et al., 2015). A new anomaly detection system was successfully developed to identify cyber-attacks using the Recurrent Neural Network (Goh et al., 2017). RNN and LSTM find its application in medical data and have been investigated in identifying anomalies in them (Chauhan & Vig, 2015).

3. METHODOLOGY

Forecasting is a method to predict future data trends with the help of mathematical model, based on past and historical data trends collected. The weather data measured by the sensor from the local automatic weather station are interpreted as time series data. The future results of the respective weather parameters may be estimated by a correct mathematical model using the historical dynamics of the various weather parameters. These data serve as a substitute sensor data to the actual sensor data and used to detect abnormalities and possible system failures by comparing both the data. Fault data detection: Data anomalies are abnormalities in data that do not align with typical behavioural patterns, which indicated fault in the data. So if the weather data unexpectedly deviates from or has any unusual occurrence in the usual behaviour pattern is labeled as anomalies. Identifying and correcting these anomalies are very vital. Finally, once the data is forecasted and anomaly detection is completed, it's essential to correct the weather data which seems to be incorrect. If not corrected, the entire system will be deemed a failure. Therefore, the forecasted data of that instant replaces the faulty data. Many more simultaneous instants of abnormalities can be termed as sensor failure in the system. The proposed approach is neatly described in Figure 1.

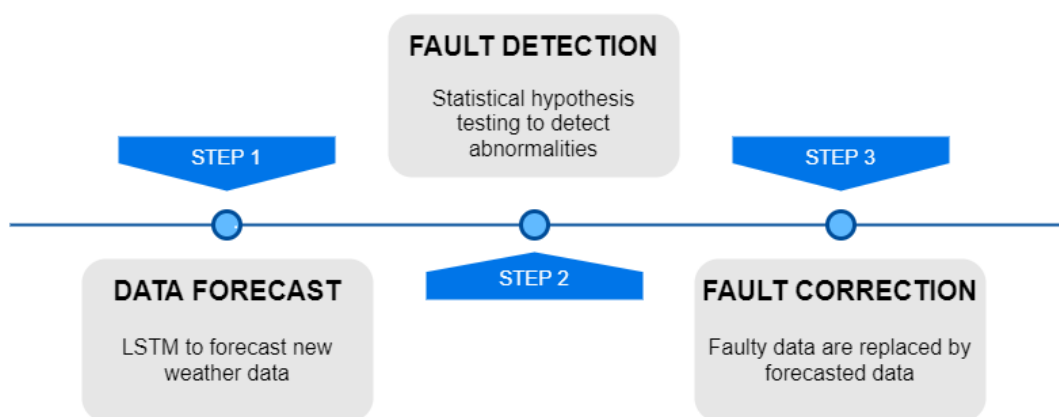


Figure 1. Data Correction and Validation Methodology

Step 1: Data forecast

The first step is to forecast weather data with the help of historical weather data. This step is vital as it sets the tone for the data validation and correction (DVC) model. This model makes use of the LSTM or SARIMA model to forecast the new weather data. The new forecasted data is used to replace the faulty data if an abnormality is detected in the data.

Step 2: Fault Detection

This step helps in identifying the faulty data. In this model, statistical method, like the hypothetical significance test, is used to validate the correctness of the data. The abnormalities detected by this test are classified as faulty data, and the faulty data are isolated. This is a simple but very effective approach.

Step 3: Fault Correction

The third and the final step is faulty data correction. When dealing with real time data, it is inevitable to have a faulty data because of various well known reasons as the harsh environmental condition or system failures. This step is an essential approach, as it contributes to making the system fault-tolerant. Once the faulty data is detected they are replaced by the forecasted weather data from step 1. A prolonged exhibition of faulty data ends in classifying it as a system failure.

3.1. Data Description

Localized weather data from the Tamil Nadu Agriculture University (TNAU), Coimbatore automated weather station were used for the study. It is located at 11.01°N latitude and 79.93°E longitude with an elevation of 431m above sea level. TNAU is in the city of Coimbatore located in Tamil Nadu. Coimbatore has a tropical wet and dry climate with an average maximum temperature of 31.5°C and minimum temperature of 22.13°C. The test data for the model was considered from the 1st of January 2017 to the 31st of December 2018. Similar weather parameters such as minimum air temperature AT_{\min} in °c, maximum air temperature AT_{\max} in °c, wind speed U_2 in km/hr, relative humidity RH in % and solar radiation in cal/cm²/day are used. Table 1 provides the statistical data parameters of the TNAU weather data.

Table 1. Statistical Parameter of the TNAU Coimbatore Weather Dataset

Dataset	Statistics	AT_{\max} in °C	AT_{\min} in °C	U_2 in km/h	SR in cal/cm ² /day	RH_{\max} in %	RH_{\min} in %
Training	Minimum	23.5	13.5	1.6	60.2	59	15
	Maximum	37.5	26.8	22.8	492	98	91
	Mean	31.88	22.39	6.53	344.72	85.70	54.05
	Std Deviation	2.51	2.20	3.47	78.34	5.03	12.27
	Skewness	-0.07	-1.09	1.62	-0.97	-1.58	0.10
Testing	Minimum	23.5	16	1.6	60.2	68	32
	Maximum	35	26	19.7	442.5	96	88
	Mean	30.47	22.43	7.17	317.52	86.59	60.59
	Std Deviation	2.00	1.58	4.21	82.33	4.69	11.04
	Skewness	-0.59	-1.23	1.17	-1.08	-1.57	0.08

3.2. Weather Data Forecast

For forecasting the weather data SARIMA and LSTM models were used in this study. To make the ARIMA even more effective, the seasonality parameter was included to model a wide range of seasonal data. It is termed as the SARIMA model with the order $(p,d,q)(P,D,Q)m$ where the new P,Q and D are the parameter for seasonality and the m is periods per season as shown in Equation (3) (Box et al., 2015). For example, if monthly data are modeled then the value of m will be 12. The predicted value for an instant t can be obtained just by taking the product of the seasonal and non-seasonal parameters.

$$(1 - \phi_1 B)(1 - \Phi_1 B^{12})(1 - B)(1 - B^{12})z_t = (1 + \theta_1 B)(1 + \Theta_1 B^{12})e_t \quad (1)$$

RNN's problem of the vanishing gradient was tackled with the introduction of LSTM, which stands for Long Short Term Memory, introduced by Hochreiter and Schmidhuber in the year 1997 (Hochreiter & Schmidhuber, 1997). LSTMs retain information for a longer time and allow for RNNs to learn more efficiently from the past data. A LSTM consists of recurrently connected memory block each consisting of an input cell, a forget gate and an output gate. At first the input x_t is processed with the previous state h_{t-1} in the input gate and passed over to the forget gate. Then, the output s_t of the forget gate is passed through a tanh activation function. Finally, again an element-wise multiplied is done by output o of an output gate, which is similar to the input gate and the final output h_t is produced (Husein & Chung, 2019). The final output h_t is described in Equation (2).

$$h_t = \tanh(s_t) \cdot o \quad (2)$$

3.3. Statistical Hypothesis Testing

The statistical hypothesis test is used to determine the fault in the observed data and the predicted sensor in this study. The probability value (p-value) is nothing but the probability of getting the actual value of a test, when the null-hypothesis is true. Here, it is determined with the help of the chi-square test. It is clearly described in Equation (3).

$$X^2 = \sum_{i=1}^{i=W_L} \frac{[(A_t)_i - (P_{t+f})_i]^2}{(P_{t+f})_i} \quad (3)$$

Where, X^2 is the chi-square, i is the instantaneous time, W_L is the width of the window, A_t is the actual observed or actual weather value, and P_{t+f} is the predicted output from LSTM model.

The goodness of fit for the LSTM model depends in the chi-square distribution of X_{df}^2 of the X^2 . Degree of freedom df , it is the total number of the data points at a given window W_L minus one ($df = W_L - 1$) and it influence the distribution X_{df}^2 . The width of the window remains constant for the analysis but it keeps moving with the time t . The significance value often denoted by α is a value which is chosen beforehand. It is used to estimate the p-value at a given instant in a particular window. The significance value is determined by the confident interval value (Sedgwick, 2014). If the confident interval is 95% then the significance value α will be 5% or 0.05. With the df and α value available the p-value can be determined by the following relationship shown in Equation (3).

$$p - value = P(X_{df,\alpha}^2 \geq X^2) \quad (4)$$

From Equation (4) it can be said that a p-value less than the chosen significance value rejects the null hypothesis. The value is considered to be significant only if the above case is met, that is X_{df}^2 should be greater than the X^2 .

3.4. Data Validation and Correction

The data validation and correction approach heavily depends on the LSTM forecast model and the statistical significance test, to detect or identify and correct any sensor faults or abnormalities. The first and foremost in this approach is to forecast the weather parameter with the help of the time series model LSTM. The parameters like the epochs, activation, optimiser, hidden layers and learning rate should be chosen appropriately.

The next step is to validate the sensor data or any given data to detect any possible abnormalities. The significance test is used in the approach to detect the abnormalities. The first step here is to determine the chi-square value X^2 , it in turn help in determining the p-value. The pre-chosen critical significance value α is 0.05. Hence in the DVC algorithm the p-value is compared against the value 0.95. Such that, p-value greater than 0.95 indicates a significant value and a value less than 0.95 indicates a fault. The significant values can be used further to train and develop the forecasting model.

The final step is to replace the value. The actual value or the observed sensor value is compared with the forecasted value to check it lies with the predictive limit. If it lies within the predictive limit then there is no need to disturb the value. But when the value lies outside the predictive limit then there arises a concern to correct the value at that particular instant. The forecasted value from the LSTM model is inserted in the place of the actual or observed value at that particular instant. A warning is signaled by the system if there are three or more consecutive faulty data. Algorithm 1 neatly describes the DVC approach to fault detection and replacement. In algorithm 1 both SARIMA based and LSTM based weather prediction is given, however the DVC approach with LSTM is preferred since it has better accuracy.

4. RESULTS AND DISCUSSION

The TNAU, Coimbatore weather data collected from January 2017 to December 2018 were used to develop the forecasting model using LSTM. Mean absolute error (MAE), root mean square error (RMSE) and mean absolute percentage error (MAPE) are used to evaluate the performance of the algorithm. They are given Equation (5), (6) and (7) respectively.

$$MAE = \frac{1}{N} \sum_{i=1}^N |P_i - A_i| \quad (5)$$

$$RMSE = \sqrt{\frac{1}{N} \sum_{i=1}^N (P_i - A_i)^2} \quad (6)$$

$$MAPE = \frac{1}{N} \sum_{i=1}^N \frac{|P_i - A_i|}{A_i} \times 100 \quad (7)$$

Where, P_i is the predicted value at instant i , A_i is the actual observed value and N is the maximum number of data points.

Algorithm 1 Data Validation and Correction (DVC)**1. LSTM_RNN for weather prediction**

```

for all  $i \in 1 : \text{length}[A(t)_i]$  do
    predicting [  $P_{t+f}$  ] $i$ 
    estimate predictive limit [  $P_{t+f}(-)$ ] $i$  and [  $P_{t+f}(+)$ ] $i$ 
     $i = i + 365$ 
end

```

(or) SARIMA for weather prediction

```

for all  $i \in 1 : \text{length}[A(t)_i]$  do
    determine (p, d and q) and (P, D and Q)
    predicting [  $P_{t+f}$  ] $i$ 
    estimate predictive limit [  $P_{t+f}(-)$ ] $i$  and [  $P_{t+f}(+)$ ] $i$ 
     $i = i + 365$ 
end

```

2. Calculate CHI square

$$X^2 = \sum_{i=1}^{i=W_L} \frac{[(A_t)_i - (P_{t+f})_i]^2}{(P_{t+f})_i}$$

Calculate p-value

$$\text{p-value} = P(X_{df,\alpha}^2 \geq X^2)$$

Faulty Data Detection

```

if p-value > 0.95,
    | Actual data is error free and can be used for training the model further
End
if p-value < 0.95,
    | Possibility of abnormalities in the actual data and has to be investigated
End

```

3. Faulty Data Correction

```

if [( $P_{t+f}(-)$ ) $i$  < ( $A_t$ ) $i$  < ( $P_{t+f}(+)$ ) $i$ ] then
    | no correction
end
if ( $A_t$ ) $i$  lie outside ( $P_{t+f}(-)$ ) $i$  and ( $P_{t+f}(+)$ ) $i$  then
    | value is replaced with forecasted value of that instant
end
if more than 3 ( $A_t$ ) $i$  lie outside ( $P_{t+f}(-)$ ) $i$  and ( $P_{t+f}(+)$ ) $i$  then
    | WARNING is indicated by the system and
    | value is replaced with forecasted value of that instant
end

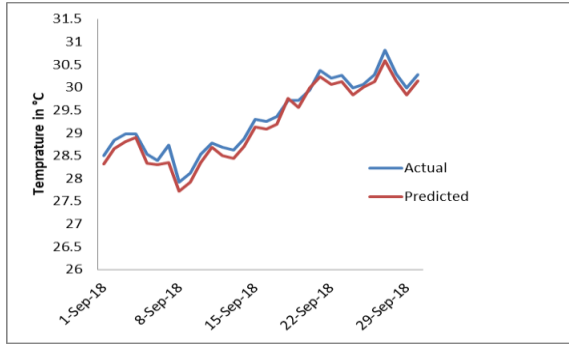
```

The weather parameters used in this study were the air temperature AT, relative humidity RH, wind speed U_2 and solar radiation SR. Further, one month of data was selected to validate the DVC algorithm. Random errors were introduced in the selected one month data and using statistical hypothesis test the errors were identified. Once they were identified they were subsequently replaced by the forecasted data of that particular time instant. Table 2 shows the performance evaluation of the model for all the four weather parameter.

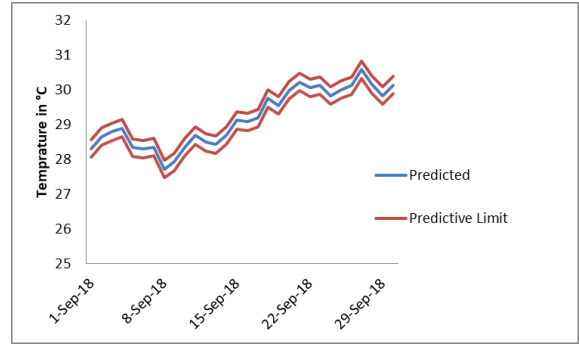
Table 2. The Performance Values Obtained from the Data Validation Correction Model

Weather Parameter	DVC with LSTM			DVC with SARIMA		
	MAE	RMSE	MAPE	MAE	RMSE	MAPE
Temperature	0.15	0.16	0.51	0.26	0.26	0.91
Relative Humidity	1.45	1.66	2.11	3.1	3.43	4.46
Wind Speed	0.45	0.72	7.18	0.66	0.92	10.89
Solar Radiation	21.99	25.68	6.56	42.25	46.75	12.33

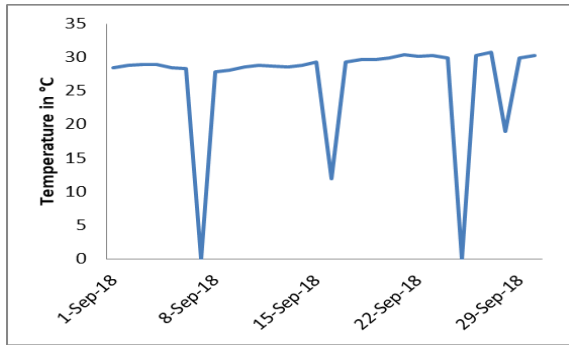
For the air temperature, the first step was to forecast the new temperature at instant i with the LSTM model. From the Table 2, MAE for temperature prediction is 0.15, RMSE is 0.16 and the MAPE obtained a value of 0.51. It is also clear that LSTM based approach shows better performance when compared to SARIMA based approach. The next step was to determine the predictive limit $(P_{t+f}(-))_i$ and $(P_{t+f}(+))_i$. After which random temperature values as error were introduced and then the p-value was determined for each instant. Then the p-values were compared with the critical value, which is set as 0.95 in this approach. Figure 2 (a) shows the plot of actual and the predicted temperature value, Figure 2 (b) is the predicted temperature values with predictive limit of the LSTM approach. In Figure 2 (c) introduced random temperature error values can be seen and in Figure 2 (d) p-value for the temperature value with induced error were plotted with the critical value for the LSTM based DVC. So anything below the critical value is considered a faulty data. Similarly the Figure 3 (a) shows the plot of actual and predicted temperature values using the SARIMA based DVC model. Figure 3 (b) is plot of the predicted temperature with predictive limit. Figure 3 (c) and (d), shows the temperature with induced temperature and plot which shows the p-value and critical limit respectively. Figure 2 (a) and Figure 3 (a) indicated the performance of the forecast of the LSTM and SARIMA model but it is the LSTM that performance better. Hence, the LSTM based DVC outshines the SARIMA based DVC in finding the faulty data and replacing them.



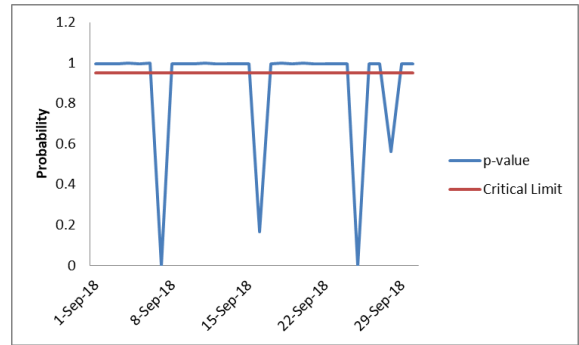
(a) Predicted temperature by LSTM model



(b) Predicted temperature with predictive limit

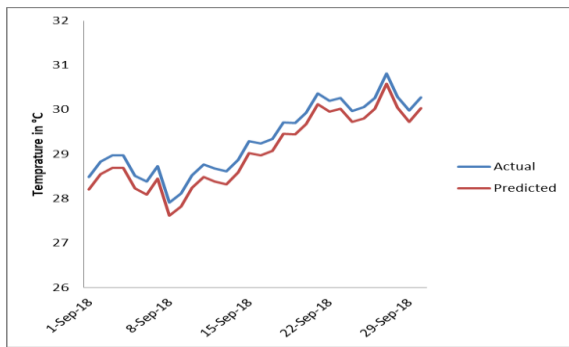


(c) Induced error value in temperature data



(d) p-value of the error induced

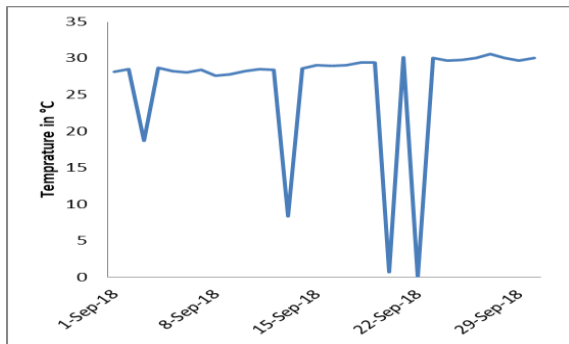
Figure 2. LSTM Based DVC Model for Temperature Data



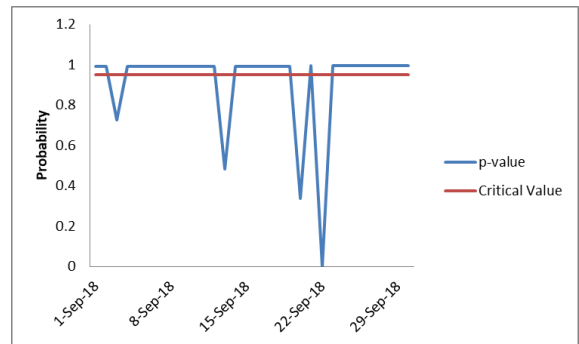
(a) Predicted temperature by SARIMA model



(b) Predicted temperature with predictive limit



(c) Induced error value in temperature data



(d) p-value of the error induced DVC SARIMA

Figure 3. SARIMA Based DVC Model for Temperature Data

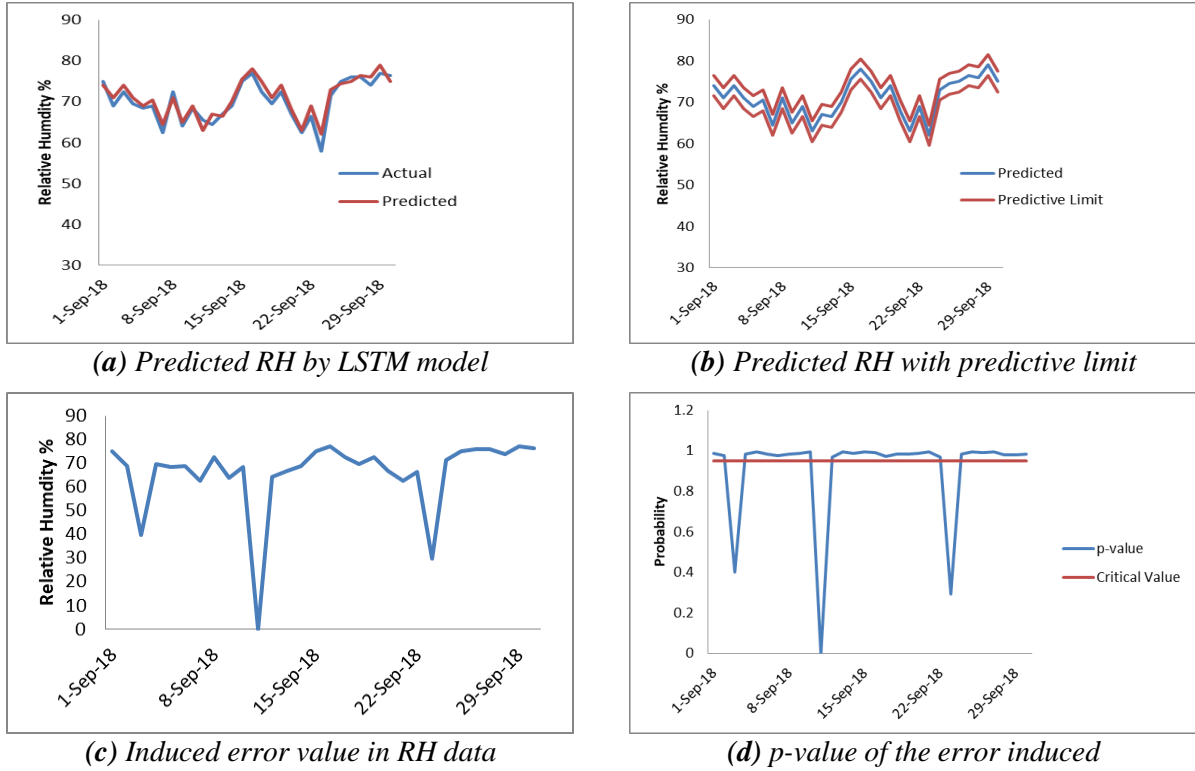


Figure 4. LSTM Based DVC Model for Relative Humidity (RH) Data

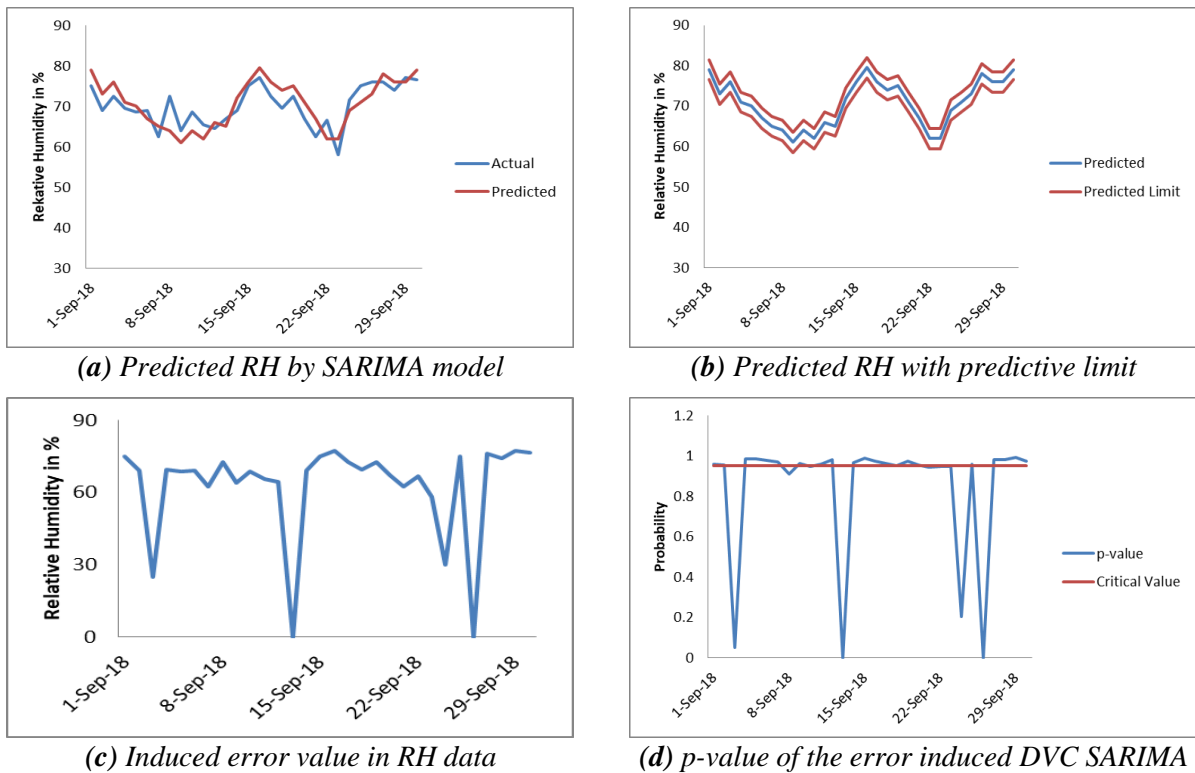


Figure 5. SARIMA Based DVC Model for Relative Humidity (RH) Data

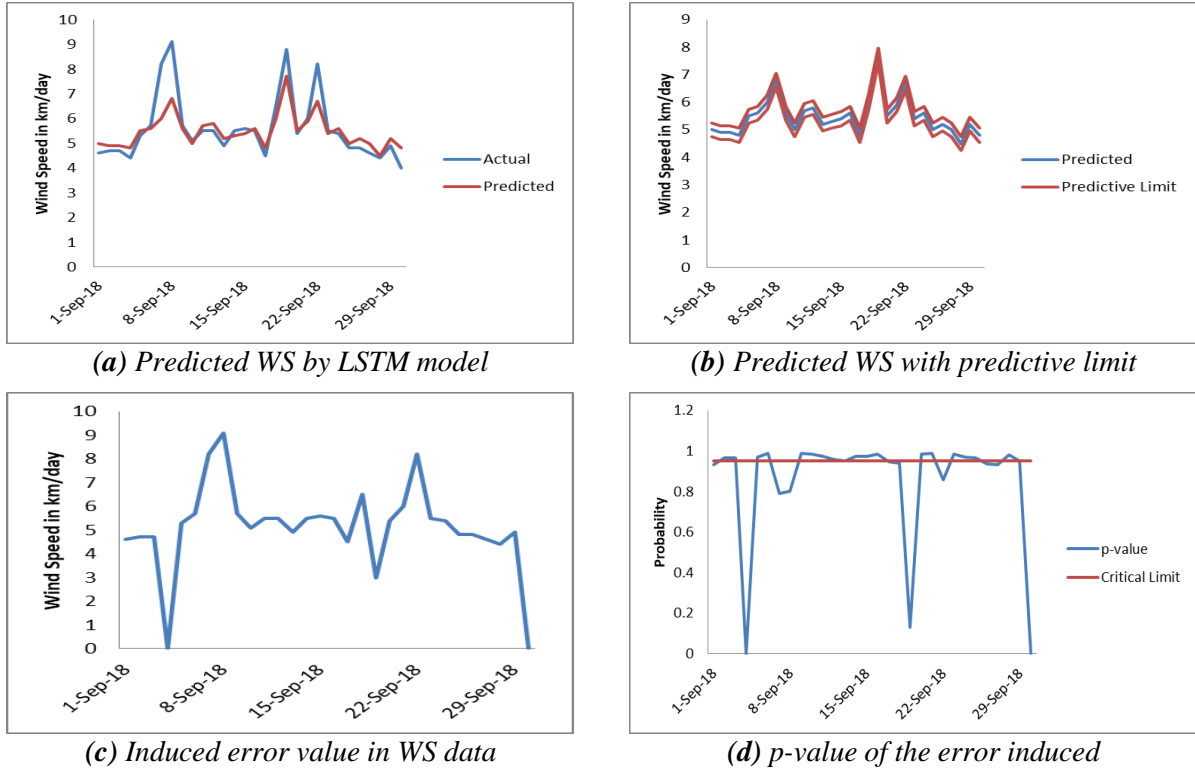


Figure 6. LSTM Based DVC Model for Wind Speed (WS) Data

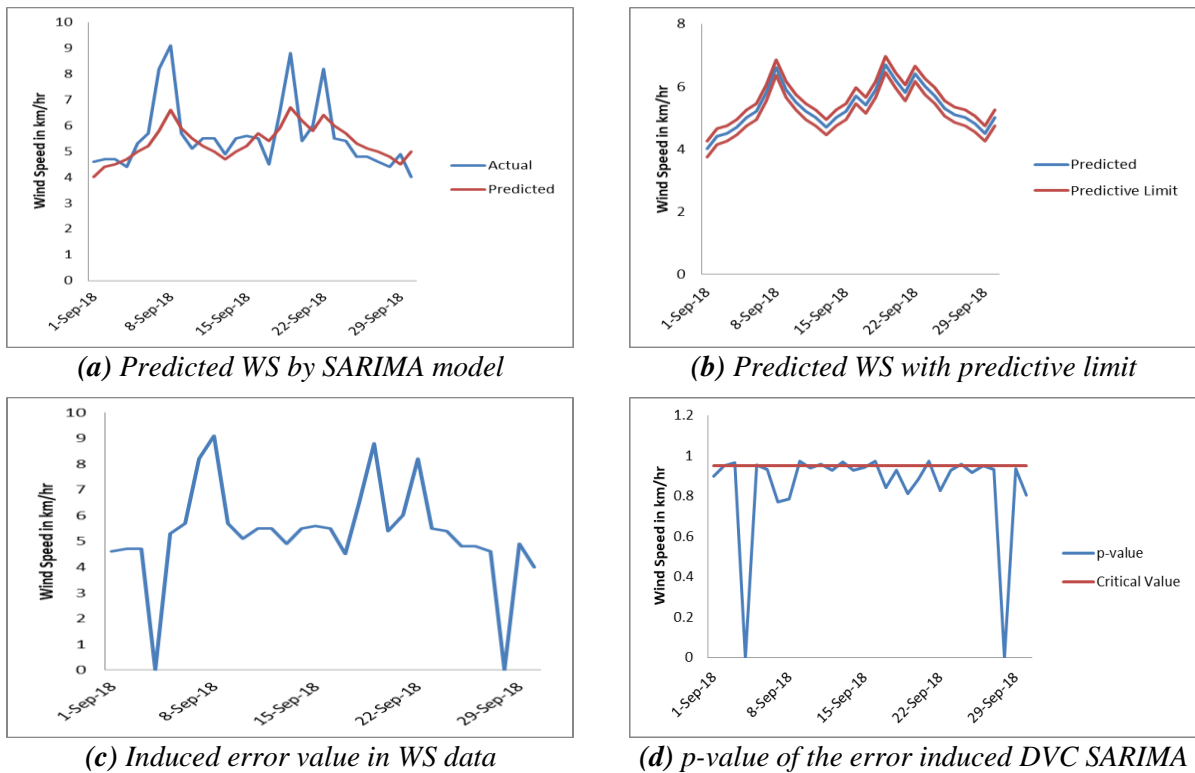


Figure 7. SARIMA Based DVC Model for Wind Speed (WS) Data

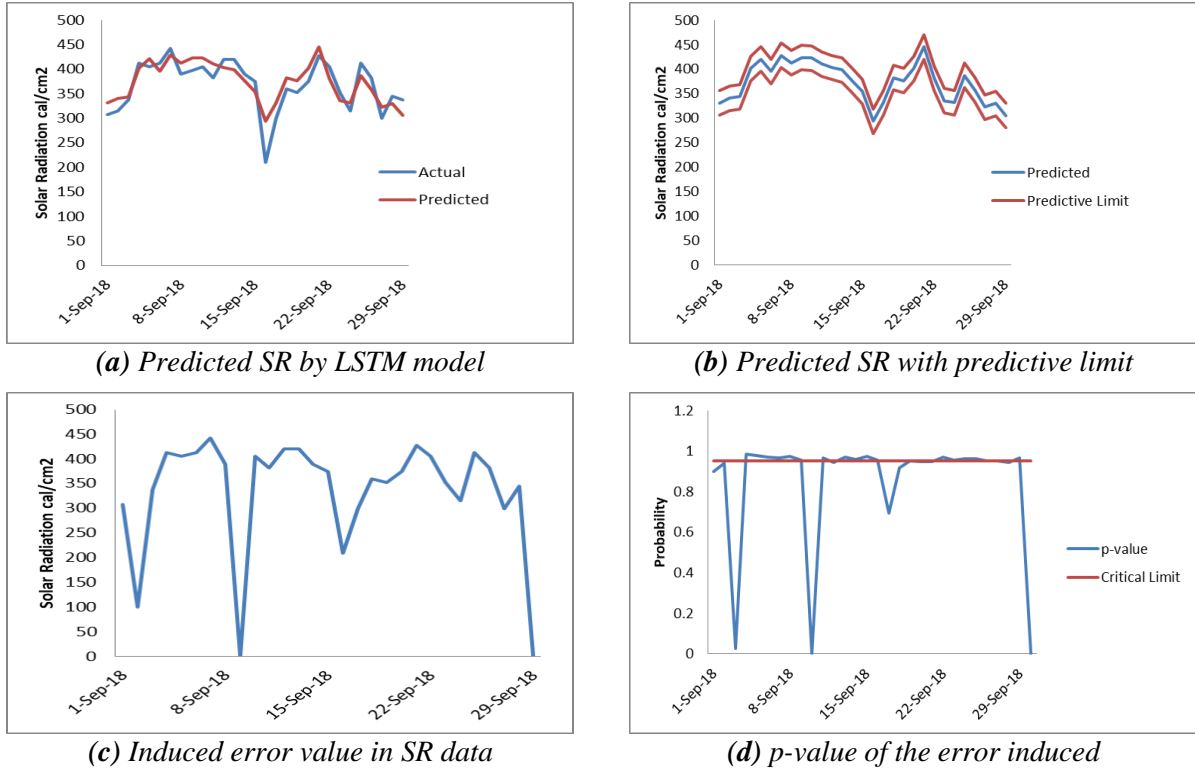


Figure 8. LSTM Based DVC Model for Solar Radiation (SR) Data

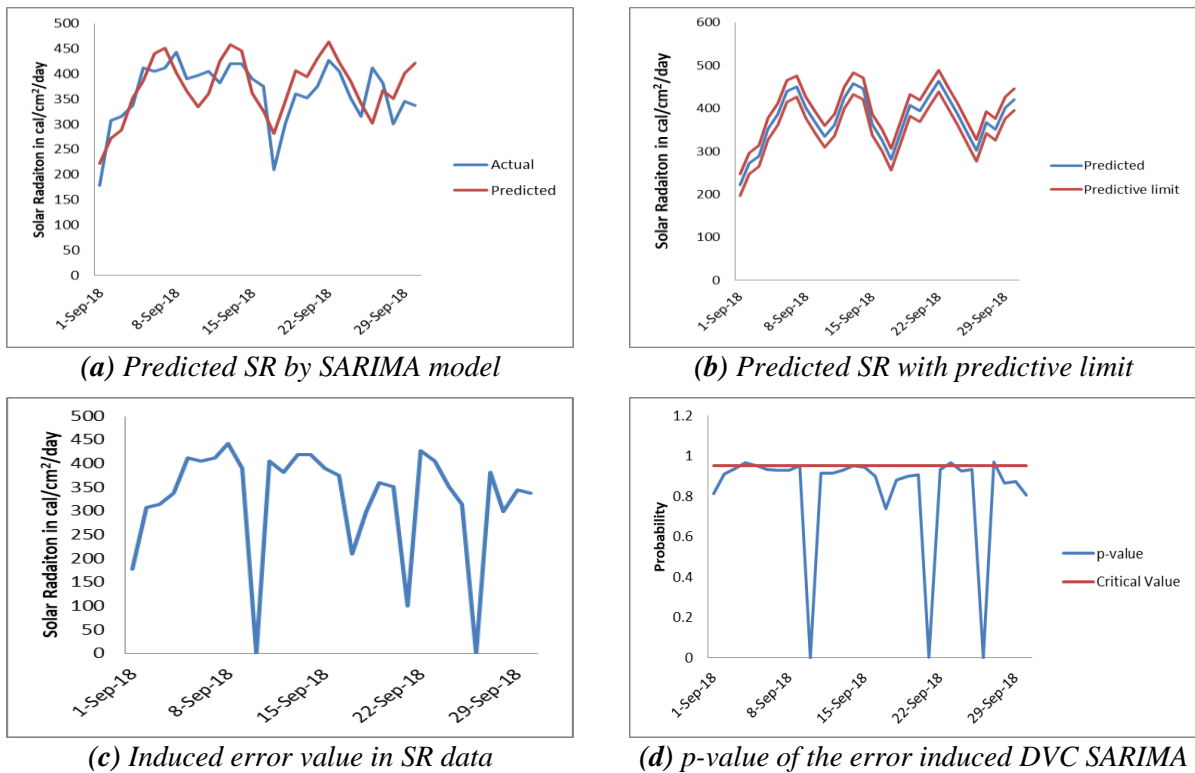


Figure 9. SARIMA Based DVC Model for Solar Radiation (SR) Data

Similar steps were followed for the other three parameters. From Table 2 the MAE, RMSE and MAPE for relative humidity, wind speed and solar radiation for DVC with LSTM shows better performance than DVC with SARIMA. Figure 4, 5, 6, 7, 8, and 9 shows performance of LSTM based DVC and SARIMA based DVC. It is clear that in all the four parameter LSTM based DVC performs better.

The Data Validation Correction (DVC) algorithm not only identifies the faulty data, it corrects the faulty ones with the predicted input data. It also can warn the user of system failure. With the help of the p-value and critical significance values this faulty data are identified. Once they are identified they are replaced by the predicted data or the substitute weather data. Continuous or prolonged detection of abnormalities that is, a consecutive occurrence of three values beyond the predictive limit will be classified as warning to the system. After identifying the error values with the help of p-value and critical value, error values are corrected by replacing them with forecasted values of that instant Figure 10 illustrates the replacement of error values with corrected values using the LSTM based DVC approach.

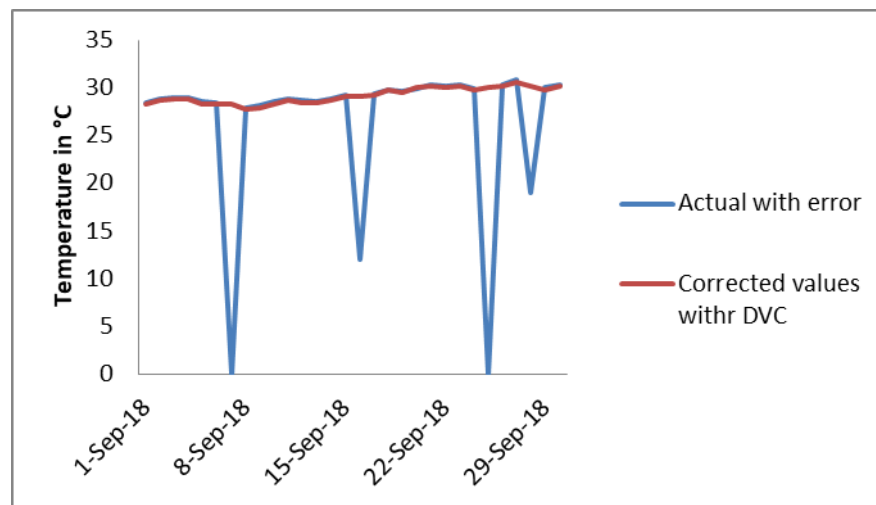


Figure 10. Corrected Values with LSTM Based DVC Approach

5. CONCLUSION

The contribution of ET_0 in water balance calculation, irrigation planning and estimating yield prediction is immense it very important to accurately predict it. Therefore, accurate prediction is possible if the input weather data is fault free and of high quality. This lead to the development of data validation and correction algorithm to find faulty weather inputs from the sensor or any other source. To predict the input data or the weather data in the DVC approach, first SARIMA based prediction was used. SARIMA based approach though it boast of flexibility and less memory usage, low accuracy in predicting weather output data and difficulty in developing a single model to predicted multiple weather data stands against. Secondly the LSTM time series prediction model was used to improve the DVC algorithm. When using LSTM-RNN in DVC approach accuracy of the predicted weather data improved though at cost of increasing memory usage and longer computation time. The data fault detection was effectively done using statistical approach and then the faulty data was replaced by the predicted data. The prediction value of weather inputs like the temperature, relative humidity, solar radiation and wind speed yielded root mean square error (RMSE) value of 0.16, 1.66, 0.72 and 25.68 respectively. The proposed DVC approach works only with time series data and it's basically a forecast based approach to detect and replace abnormalities in data. An approach for both time dependent and time independent data would increase the effectiveness of fault detection and correction.

CONFLICTS OF INTEREST

No conflict of interest was declared by the authors.

REFERENCES

- Allen, R. G., Pereira, L. S., Raes, D., & Smith, M. (1998). Crop Evapotranspiration, guidelines for computing crop water requirements, FAO Irrigation and Drainage Paper No. 56. Food and Agriculture Organization of the United Nations, Rome, 300p.
- Box, G. E., Jenkins, G. M., & Reinsel, G. C. (1994). Time Series Analysis, Forecasting and Control. Englewood Cliffs, 598p.
- Box, G. E. P., Jenkins, G. M., Reinsel, G. C., & Ljung, G. M. (2015). Time series analysis: forecasting and control, 5th Edition. John Wiley & Sons, 712p.
- Chandola, V., Banerjee, A., & Kumar, V. (2009). Anomaly detection: A survey. ACM Computing Surveys (CSUR), 41(3), Article No:15, 1-58.
- Chatfield, C. (2000). Time-Series Forecasting. CRC Press, 280p.
- Chauhan, S., & Vig, L. (2015). Anomaly detection in ECG time signals via deep long short-term memory networks. In: Proceedings of the IEEE International Conference on Data Science and Advanced Analytics (DSAA 2015), 1-7.
- Cobaner, M. (2011). Evapotranspiration estimation by two different neuro-fuzzy inference systems. Journal of Hydrology, 398(3-4), 292-302.
- Fischer, G., Nachtergaele, F. O., Prieler, S., Teixeira, E., Tóth, G., van Velthuisen, H., Verelst, L., & Wiberg, D. (2012). Global Agro-ecological Zones (GAEZ v3. 0) - Model Documentation. (IIASA: Laxenburg, Austria; FAO: Rome, Italy) pure.iiasa.ac.at/13290
- Gardner, Jr, E. S. (2006). Exponential smoothing: The state of the art-Part II. International Journal of Forecasting, 22(4), 637-666.
- Goh, J., Adepun, S., Tan, M., & Lee, Z. S. (2017). Anomaly Detection in Cyber Physical Systems Using Recurrent Neural Networks In: Proceedings of the 18th International Symposium on High Assurance Systems Engineering (HASE 2017), 140-145.
- Hochreiter, S., & Schmidhuber, J. (1997). Long short-term memory. Neural computation, 9(8), 1735-1780.
- Husein, M., & Chung, I. Y. (2019). Day-ahead solar irradiance forecasting for microgrids using a long short-term memory recurrent neural network: A deep learning approach. Energies, 12(10), 1856, 1-22.
- Kim, S., Hong, S., Joh, M., & Song, S. K. (2017). DeepRain: ConvLSTM Network for Precipitation Prediction using Multichannel Radar Data. In: Proceedings of the 7th International Workshop on Climate Informatics. arxiv.org/abs/1711.02316
- Lee, S., & Kim, H. K. (2018). ADSaS: Comprehensive Real-time Anomaly Detection System. 19th World International Conference on Information Security and Application (WISA 2018), Revised Selected Papers, 29-41, Springer.
- Malhotra, P., Vig, L., Shroff, G., & Agarwal, P. (2015). Long Short Term Memory Networks for Anomaly Detection in Time Series. In: Proceedings of the European Symposium on Artificial Neural Networks, Computational Intelligence and Machine Learning. (ESANN 2015), vol. 89, 89-94.
- Martin, D. L., & Gilley, J. (1993). Irrigation Water Requirements, Chapter 2, Part 623 of the National Engineering Handbook, United States Department of Agriculture - Soil Conservation Service.
- Mondal, P., Shit, L., & Goswami, S. (2014). Study of effectiveness of time series modeling (ARIMA) in forecasting stock prices. International Journal of Computer Science, Engineering and Applications, 4(2), 13-29.
- O'Reilly, C., Gluhak, A., Imran, M. A., & Rajasegarar, S. (2014). Anomaly detection in wireless sensor networks in a non-stationary environment. IEEE Communications Surveys & Tutorials, 16(3), 1413-1432.
- OECD (2008). Environmental outlook to 2030, The Organisation for Economic Co-operation and Development, 1-10.

- Ponraj, A. S., & Vigneswaran, T. (2019). Daily evapotranspiration prediction using gradient boost regression model for irrigation planning. *The Journal of Supercomputing*, 76, 5732-5744.
- Roesch, I., & Günther, T. (2019). Visualization of Neural Network Predictions for Weather Forecasting. *Computer Graphics Forum*, 38(1), 209-220.
- Salman, A. G., Kanigoro, B., & Heryadi, Y. (2015). Weather forecasting using deep learning techniques. In: *Proceedings of the International Conference on Advanced Computer Science and Information System (ICACSIS 2015)*, 281-285.
- Sedgwick, P. (2014). Understanding statistical hypothesis testing. *BMJ*, 348.
- Sharma, A. B., Golubchik, L., & Govindan, R. (2010). Sensor faults: Detection methods and prevalence in real-world datasets. *ACM Transactions on Sensor Networks (TOSN)*, 6(3), Article No:23, 1-39.
- Simmons, L. F. (1986). M-competition-A closer look at NAIVE2 and median APE: A note. *International Journal of Forecasting*, 2(4), 457-460.
- Thiyagarajan, K., Kodagoda, S., Van Nguyen, L., & Ranasinghe, R. (2018). Sensor failure detection and faulty data accommodation approach for instrumented wastewater infrastructures. *IEEE Access*, 6, 56562-56574.
- Tiwari, D., & Dinar, A. (2002). Balancing future food demand and water supply: The role of economic incentives in irrigated agriculture. *Quarterly, Journal of International Agriculture*, 41(1), 77-97.
- Tomar, A. S. & Ranade, D. H. (2001). Pan coefficient determination for evapotranspiration at Indore, Madhya Pradesh. *Indian J. Soil Conserv.*, 29, 173-175.
- Watson, I., & Burnett A. D. (2017). *Hydrology: An Environmental Approach*, Routledge, 722p.
- Venugopal, P., & Vigneswaran, T. (2019). State-of-Health Estimation of Li-ion Batteries in Electric Vehicle Using IndRNN under Variable Load Condition. *Energies*, 12(22), 4338, 1-29.



Wireless Signal Attenuation by Vegetation: Relationship Between Tree Characteristics and Signal Attenuation

Yusuf ABBA KYARI^{1*} , James AGAJO² 

¹Faculty of Technology, School of Engineering, University of Portsmouth, Anglesea Building, PO1 3DJ, Portsmouth, United Kingdom

²Department of Computer Engineering, Federal University of Technology Minna, Minna, Niger State, Nigeria

Keywords	Abstract
Wireless Signal Attenuation Vegetation Modelling Trees	Vegetation is a significant factor that affects the Quality of Service of radio waves. Several measurement campaigns have been conducted to predict the effect of trees on a radio wave at the micro and millimetre wavelengths. The experiments show that depth of vegetation is a major factor that contribute to signal attenuation. Furthermore, different components of the vegetation cause different behaviours of the radio wave. The empirical models did not put into to consideration the characteristics of the trees in the vegetation. The analytical approaches using wave theory have considered the vegetation characteristics, density and the geometry. This paper focuses on using existing models to characterise a vegetation based on measured parameters of a tree stand with a view to estimating the density of the foliage within a vegetation accurately. The foliage density will be used as the vegetation parameter in the wave theory model. Simulation of the signal attenuation will be conducted based on the density of the vegetation that will be estimated. The tree species selected for simulation are Pinus, Ash and Silver Birch tree species.

Cite

Abba Kyari, Y., & Agajo, J. (2021). Wireless Signal Attenuation by Vegetation: Relationship Between Tree Characteristics and Signal Attenuation. *GU J Sci, Part A, 8(1)*, 58-80.

Author ID (ORCID Number)	Article Process
Y. Abba Kyari, 0000-0002-3970-6161	Submission Date 17.07.2020
J. Agajo, 0000-0001-5773-4249	Revision Date 15.02.2021
	Accepted Date 21.03.2021
	Published Date 29.03.2021

1. INTRODUCTION

Trees existing on the path of a communication link was found to play a significant role in the radio signal's quality of service (QoS). They have been classified as an obstruction to the Line of Sight (LOS) between the transmitter and the receiver for many years (Al-Basheir et al., 2006; Meng & Lee, 2010; Adegoke & Siddle, 2012). This causes research on the interaction between radio waves and trees to be ongoing for several decades (Ghoraishi et al., 2013). Trees have a very complex structure composed of randomly oriented stems, branches, twigs and leaves, which causes scattering, absorption and diffraction of radio waves. The result of this causes signals to follow a different path to transmit signals to the receiver that causes the signal degradation.

Investigative studies about the effects of vegetation on radio waves showed that several factors can contribute to signal attenuation. These include; vegetation type, density, leaf state, the size of the foliage and frequency of propagation (Rogers et al., 2002; Savage et al., 2003; Ndzi et al., 2005; Al-Basheir et al., 2006; Helhel et al., 2008). Wet trees cause extra attenuation and absorption while evergreen trees have more effect on radio signals than deciduous trees (Helhel et al., 2008). Furthermore, coniferous trees are worse than broad-leaved evergreens as reported in (McLarnon, 1997; BBC & ITC, 1998). Single isolated trees may not cause major problems, but in a dense forest, the attenuation level is high. The attenuation

level within a density of a forest per unit area depends on the distance in which the radio signal will penetrate through the forest. The shape of the Leaves and the thickness of the stems have less significant effects on radio waves at lower frequencies as the wavelength of the radio wave is larger than the thickness of the vegetation which makes easy penetration through medium. According to the CCIR report stated by (McLarnon, 1997) and the investigation carried out by (Savage et al., 2003) showed that signal attenuation by vegetation has a high dependency on frequencies. In general, trees can exist as a single or group of trees, and they can be either homogeneous or mixed tree types. This will result in the different effects they will have on radio waves even at the same frequency due to the different tree types and the geometry of the link (Ndzi et al., 2012). The different effects have become a constraint on the design of modern wireless communication systems. Figure 1 shows different modes of signal propagation through vegetation (Adegoke & Siddle, 2012)

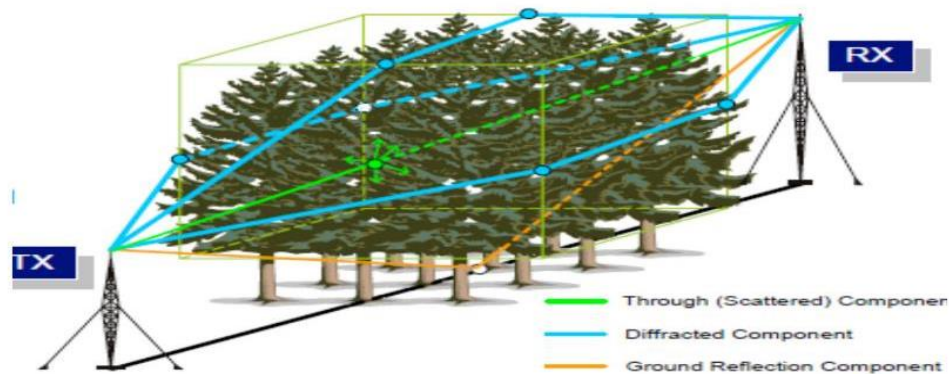


Figure 1. Different Modes of Signal Propagation Through Vegetation (Adegoke & Siddle, 2012)

Since the 1960s, significant research has been done with a view to developing models that will be used to predict excess attenuation of radio waves as they pass through a vegetation. Several measurement campaigns were conducted to evaluate these models. Accurate modelling of radio waves through vegetation requires a proper description of the tree geometry and foliage distribution that will be valid for wide frequency range (Ghoraishi et al., 2013). However, each measurement that has been conducted so far was based on specific tree type, climate conditions and experimental setup. Empirical and semi-empirical models have been proposed for the prediction of signal attenuation by vegetation because of their simplicity. The measurement geometry of the vegetation was not taken into account, and they do not distinguish between the modes of propagation. Most of the models proposed did not take into account the density of the vegetation (Ndzi et al., 2005; Ghoraishi et al., 2013). The major drawback of the empirical models is that they were developed based on existing data that was measured on specific tree types and in predominantly trees that grow in temperate climates. Parameters in these models are frequency, incident angles, direct-path length through vegetation. Other parameters associated with the particular environment under which measurements were performed usually computed through regression curves fitted to the measurement data (Ghoraishi et al., 2013). These measurements yielded different results when applied to different species of trees. Therefore, the performance of the models appear to be inconsistent when different link setup is being used (Ndzi et al., 2012). Mean attenuation or link budget calculation are usually what the empirical models provide (Ndzi et al., 2005). This drawback has attracted more experimental campaigns with the view of developing a generalized model to predict signal attenuation in later years.

2. REVIEW OF EXISTING MODELS

2.1. Existing Attenuation by Vegetation Prediction Models

Path losses can be modelled experimentally based on the given equation (Sabri et al., 2018), where the depth of vegetation (d_f) and frequency (f) are the parameter of path loss (PL_{veg}). A , B , and C are constant empirically determined fitting parameters.

$$PL_{veg}(dB) = A \cdot f^B \cdot d_f^C \quad (1)$$

2.1.1. Modified Exponential Decay Model (MED)

The most frequently cited prediction model was the Exponential Decay (EXD) given as;

$$L = 0.26f^{0.77}d_f \quad (2)$$

However, a large discrepancy was observed. Therefore, the MED model was presented to overcome some of the problems with the EXD expressed as;

$$L = \begin{cases} 1.33f^{0.284}d^{0.588}, & \text{if } 14 < d \leq 400 \\ 0.45f^{0.284}d, & \text{if } 0 < d \leq 14 \end{cases} \quad (3)$$

2.1.2. COST 235 and FITU-R

Cost 235 model was proposed in 1996 based on measurements conducted on grove trees at different frequencies on different tree species (COST, 1996). An improvement on the EXD model was obtained by changing the value of the fitting parameters to produce the COST 235 model.

$$L = 15.6f^{-0.009}d^{0.26}[dB] \quad \text{In-leaf} \quad (4)$$

$$L = 26.6f^{-0.2}d^{0.5}[dB] \quad \text{Out-of-leaf} \quad (5)$$

Further optimisation of the three numerical values in EXD has resulted in the Fitted ITU-R model. The measurement data by (Stephens & Al-Nuaimi, 1995) at frequencies 11.2 GHz and 20 GHz resulted in the development of the FITU-R model

$$L = 0.39f^{0.39}d^{0.25}[dB] \quad \text{In-leaf} \quad (6)$$

$$L = 0.39f^{0.18}d^{0.59}[dB] \quad \text{Out-of-leaf} \quad (7)$$

Where **f** is in MHz and **d** is in meters.

The experiment concluded the COST235 should be used when planning a Wireless Sensor Network (WSN).

The models mentioned above are exponential forms of expressions to predict excess attenuation as a function of operating frequency and length of propagation (Goldhirsh & Vogel, 1998), without considering other mechanisms that may be involved in the propagation of the signal such as, refraction and ground reflection.

2.1.3. Maximum Attenuation Model (MA)

Further investigation showed that at higher frequencies, attenuation decreased as vegetation depth increases and the gradient becomes shallower. This indicated that the scattering of the signal from tree to tree becomes a significant mode of propagation. The scattering contributes to the received signal and, therefore, reduces the effective attenuation. The measured 38 GHz data led to the suggestion that an improved model of attenuation to be given in the form (Seville & Craig, 1995);

$$A_m = A_m \quad (8)$$

Where **A_m** is the maximum attenuation and **γ** is specific attenuation for very short vegetative paths (dB/m). **d** is the path within the vegetation. Specific attenuation due to vegetation, **γ** dB/m, depends on the density and species of the vegetation. This model became the ITU-R recommendation for cases where the transmitter is located outside the vegetation, and the location of the receiver is inside the vegetation for

frequencies ranging from 30MHz – 30GHz (ITU, 2013). The parameter **A_m** has a frequency dependency of the form

$$A_m = A_1 f^\alpha \quad (9)$$

Different values of **A₁** and **α** have been used as fitting parameters depending on the species of the vegetation, frequency applied and the location.

These measurements indicate a limitation to the use of the model. Another limitation is the fixed attenuation gradient that prove not to be the desired model to be used. Therefore, the measurement geometry and methodology need to be taken into account.

2.1.4. Non Zero Gradient (NZG)

The Non-Zero Gradient (NZG) model was proposed to overcome the zero final gradient problems of the MA model for frequencies above 5GHz (Ndzi et al., 2012). The NZG model uses the initial (**R₀**), the final gradient (**R_∞**), and the offset of the final gradient (**k**) of the attenuation curve. The model also suffers from the problems associated with using values of parameters obtained from fitting curves to experimental data (Savage et al., 2003). The NZG model can be expressed in the form (Ndzi et al., 2012);

$$Att_{NZG} = R_\infty d + k \left\{ 1 - \exp \left(\frac{-R_0 - R_\infty}{k} d \right) \right\} \quad (10)$$

The values of these parameters were obtained based on estimates carried out by Stephens in 1998. However, as pointed out by (BBC & ITC, 1998), the values of the parameters may vary with measurement sites due to propagation anomalies that are not existing in all locations (Ghoraishi et al., 2013).

2.1.5. Dual Gradient Model (DG)

The operating frequency and the beamwidth of the antenna were proposed to be taken into account in the DG model. The site geometry is taken into consideration, which considers the extent of illumination of the vegetation medium. This is characterised by the illumination width, **W**, the maximum effective coupling width resulting from the interaction between the transmitting and receiving antenna beamwidths inside the vegetation medium (Rogers et al., 2002). However, the DG model was not recommended because, as the frequency increases, the inverse relationship with frequency suggests a decreasing attenuation. This appears to contradict both the anticipated behaviour and that observed in the measured data (Ghoraishi et al., 2013). Therefore, the DG model proposed has proved to have several inaccuracies (Savage et al., 2003). It was concluded that further work on this model is needed to eliminate these inconsistencies. Figure 2 shows the depiction of Vegetation measurement Geometry (Rogers et al., 2002)

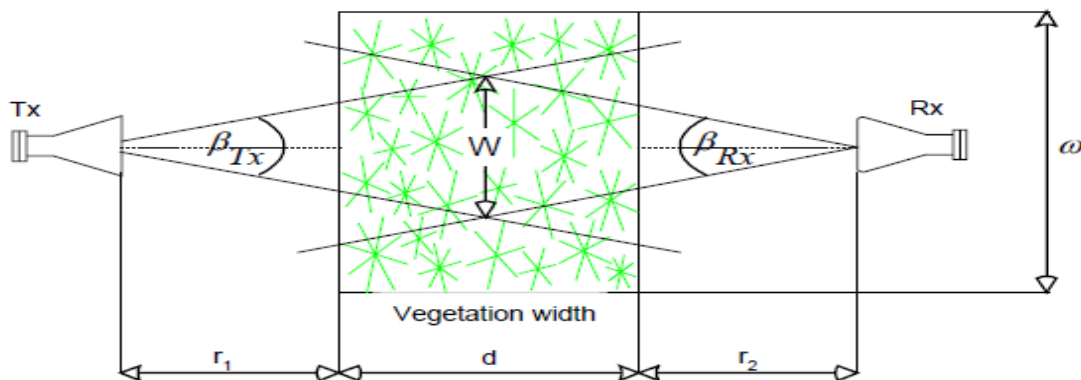


Figure 2. Vegetation Measurement Geometry (Rogers et al., 2002)

$$L = \frac{R_{\infty}}{f^a W^b} d + \frac{k}{W^c} \left(1 - e^{\left(\frac{-(R_0 - R_{\infty}) W c d}{k} \right)} \right) \quad (11)$$

Where $\mathbf{a}, \mathbf{b}, \mathbf{c}, \mathbf{k}, \mathbf{R}_0$ and \mathbf{R}_{∞} are constants described in (Al-Naimi & Hammoudeh, 1993) \mathbf{W} is illumination width of the vegetation medium.

2.1.6. Radiative Energy Transfer Theory (RET)

RET is one of the later approaches in predicting signal attenuation by vegetation using physics-based analysis.

The RET has been adopted in the current ITU recommendation for modelling attenuation through a vegetation for frequencies above 1 GHz, which is given by the expression below. The values of the input parameters used for different tree specimen have been summarized in the ITU recommendations (ITU, 2013).

$$L_{scat} = -10 \log_{10} \left(\begin{array}{l} e^{-\tau} + \frac{\Delta Y_R^2}{4} \cdot \{ [e^{-\hat{\tau}} - e^{-\tau}] \cdot \bar{q}_M + e^{-\tau} \cdot \sum_{m=1}^M \frac{1}{m!} (\alpha W \tau)^m [\bar{q}_m - \bar{q}_M] \} \\ + \frac{\Delta Y_R^2}{2} \cdot \{ e^{-\hat{\tau}} \cdot \frac{1}{P_N} + \sum_{k=\frac{N+1}{2}}^N [A_k e^{\frac{\hat{\tau}}{s_k}} \cdot \frac{1}{1 - \frac{\mu_N}{s_k}}] \} \end{array} \right) \quad (12)$$

2.1.7. Wave Theory Based Model

The wave theory-based model is believed to be more accurate for presenting the coherence effects and phase information and it has proven to have no limitation on whether the medium is homogenous or not. Coherent wave propagation models based on Monte Carlo simulation of scattering from a realistic looking fractal trees are successfully used to obtain the statistics of wave propagation through foliage (Meng & Lee, 2010). Physical and structural parameters, such as the height, mean stem diameter, and tree density were computer generated for the estimation of the foliage attenuation. Full wave numerical technique, Method of Moments was applied by (Koh et al., 2003) to calculate the scattering from a cluster of leaves or needles. Foldy's approximation with the single scattering theory was used, and it overestimates the forward scattering as high as 3-4dB at 35GHz as stated in the report. Based on this approach, a forest wave propagation model known as Fractal-Based Coherent Scattering Model (FCSM) has been implemented and verified successfully for a number of applications (Wang & Sarabandi, 2007).

Multiple scattering is an important factor in long distance propagation through vegetation which give drawback to the wave theory model because it is essentially a single-scattering model that has been shown (Al-Naimi & Hammoudeh, 1993) to overestimate the attenuation at high frequencies or long distances. To include high order multiple-scattering in the wave theory model, the mathematical complexity will be increased which will make it less time efficient.

2.1.8. Statistical Wave Propagation (SWAP) Model

Computing excess attenuation over long distances using wave theory even at single scattering could be time-consuming. To simplify the computation, the forest is considered as a homogenous medium along the radio wave direction and then the forest will be treated as blocks of forest as can be seen in Figure 3 (Ghasemi et al., 2013). The computation will be done on a single block and then the result will be applied to corresponding blocks. Based on this methodology, the SWAP model was developed.

The SWAP model is built on the function of wave propagation behaviour on a single block of forest, such as the relationship between the field distributions, fluctuation, attenuation on the input and output surfaces. It uses an existing FCSM model and applies to a representative block of the forest to pre-compute the

propagation parameters. Network approach is used on the parameters of each block to calculate the total power at the receiver.

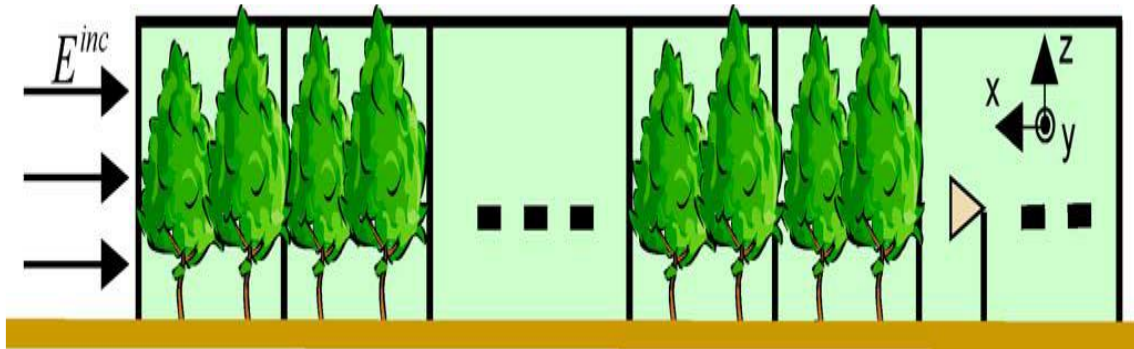


Figure 3. A Forest Divided into Blocks of Small Similar Forests (Ghasemi et al., 2013)

The model is evaluated on by conducting measurement on red pine stand which indicated good accuracy between the measured and simulated data (Wang & Sarabandi, 2007). They concluded that the SWAP model is quite complex and may not appeal to ordinary users. However, it can serve as the computation engine to develop a macro-model which features a simple mathematical expression relating the foliage path-loss to the foliage and radio system parameters of the specific wave propagation scenario.

2.2. Vegetation Characteristics

Understanding how trees grow in an environment is an important aspect to assess the condition of the tree. The vertical growth rate of trees allows some trees to dominate other plants.

Trees grown in urban areas are subjected to different stresses such as; compacted soil, limited space and intense pruning which affect their growth rate. The environment affects the shape and form of the trees, which makes it difficult to predict the tree height, biomass and crown dimensions than with forests where trees are much more homogenous in their growth and form for a particular environment and species (Shrestha & Wynne, 2012; Hong, 2015).

2.2.1. Tree Growth Modelling

The dimensions of tree height and crown are important tree characteristics used in many growth and yield models. Measurement of diameter at breast height of a tree is used to estimate the height of trees by using height-diameter relationship, and to determine the dominant height for measuring site productivity (Petrauskas & Rupšys, 2010; Rupšys & Petrauskas, 2010). Several pieces of research have been made to develop a reliable relationship between crown size and stem diameter, and the density of trees in a stand (Hemery et al., 2005; Vanclay, 2009). Because of the low market value of the crown, not too much attention has been put on the study of tree crowns. However, crown size is an important parameter in the studies of the growth of trees because the size of the crown determines the photosynthetic capacity of a tree (Hemery et al., 2005; Arzai & Aliyu 2010). While the crown of a tree represents the potential growth of a tree, the measurement of a tree's crown is difficult to obtain (Lockhart et al., 2005).

2.2.2. Crown Diameter Prediction Models Using Diameter at Breast Height

Close correlation exists in principle between crown diameter and stem characteristics, such as diameter and stem characteristics.

Crown growth modelling systems are used to predict adequately the recovery from competition among trees where competition indices are not available. It is also used as a variable for stem diameter and height growth equations (Vanclay, 1994). The equations for predicting crown width of open-grown trees are known as Maximum Crown Width (MCW) equations while for stand-grown trees are called Largest Crown Width (LCW) equations. Figure 4 shows close correlation between the linear prediction model and the measure data (Hemery et al., 2005).

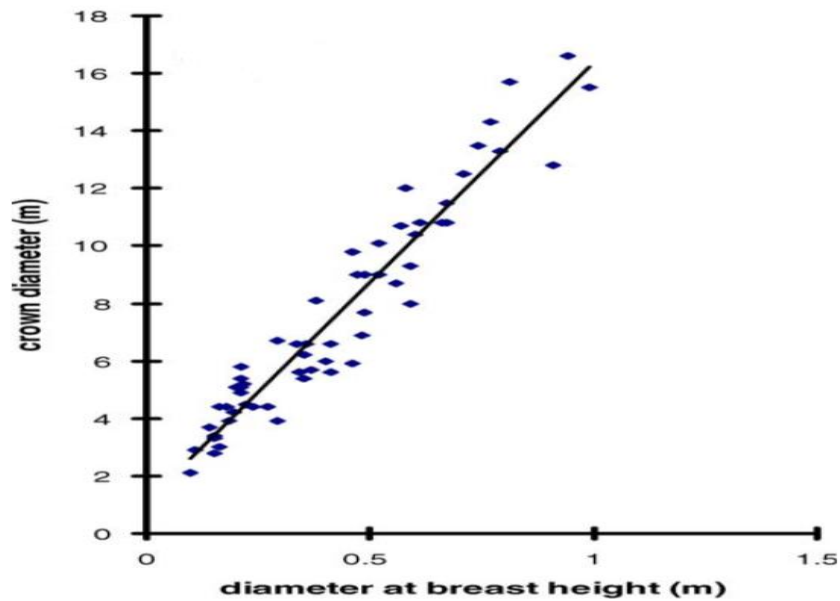


Figure 4. Crown Diameter- Stem Diameter Relationship for Beech Tree (Hemery et al., 2005)

Simple linear model between crown width and diameter at breast height is often adequate when modelling crown diameter equations (Hemery et al., 2005; Arzai & Aliyu, 2010; Ibrahim et al., 2014). Power functions and the monomolecular functions are used to model crown width that are nonlinear (Bragg, 2001).

Table 1 shows the summary of different prediction models developed and used to estimate crown diameter given the Stem Diameter at Breast Height (DBH) in different tree stands within a range of conditions of the stands (Burgin et al., 2011).

Table 1. Summary of Model Equations for Estimation of Crown Diameter (width) Using DBH (Burgin et al., 2011)

No.	Model Equation	Function type
1.	$Cw = a + b \times dbh$	Linear
2.	$Cw = a + b \times dbh + c \times dbh^2$	Quadratic
3.	$Cw = a \times dbh^b$	Power
4.	$Cw = a \times b^{dbh}$	Power
5.	$Cw = a \times (1 - e^{-b \times dbh})$	Monomolecular
6.	$Cw = \frac{dbh}{(a + b \times dbh)^2}$	Hossfeld 1

Where; **Cw**; crown width (diameter), **dbh**; stem diameter at breast height, **a**, **b**, **c**; fitting parameters.

The fitting parameters are estimated for values generated by measurements conducted on different tree species. The parameters can be applied to similar species and models have proven to be applicable for a wide range on of species.

2.2.3. Tree Height Prediction Models Using Diameter at Breast Height

Tree height to DBH relationship is an important component to estimate yield, landscape appraisal and growth of trees and it is the most commonly used measurement for tree size (Sumida et al., 2013; Hong, 2015). In growth and yield modelling, height-DBH relationships are used to estimate tree's height and the tree volume can be estimated from the relationship. Many height-diameter equations have been developed for various species as can be seen in Table 2.

Table 2. Summary of Model Equations for Estimation of Tree Height Using DBH as a Parameter

No.	Model Equation	Source
1.	$H = 1.3 + \exp(a+b \times dbh)^c$	(Eng, 2012)
2.	$H = 1.3 + a(1 - \exp(b \times dbh)^c)$	(Eng, 2012)
3.	$H = 1.3 + \exp(a+b \times dbh^c)$	(Wang & Hann, 1988)
4.	$\ln(H) = a + b \times dbh^{-0.2} + c \times \ln(1.3)$	(Oyebode et al., 2012)
5.	$H = 1.3 + a(1 - \exp(-b \times dbh))^c$	(Corral-Rivas et al., 2014)
6.	$\ln(H - 1.3) = a + b/dbh$	((Schreuder & Hafley, 1977)

Where; **H**; tree height, **dbh**; stem diameter at breast height, **a**, **b**, **c**; fitting parameters.

2.2.4. Branch Diameter and Stem Diameter Relationship

Researchers have theorized, observed and inferred that the relationship between the branch and the stem may relate to the strength of the attachment between them (Gilman, 2003), but only a few studies testing the ratio between the branch and stem diameter has been performed especially on shade tree species. In his paper, (Strickland & Goddard, 1965) observed that the greater the angle between the stem and the branch, the shorter and smaller the branch length and the diameter respectively.

It was not feasible to measure Maximum Branch Diameter (MBD) of a tree when taking forest inventories in the past. But remote sensing approaches have been ongoing to develop the relationships between the MBD with other features such as tree height, crown radius and measures of competitive status. Due to the ease in measuring the DBH of a tree, Table 3 shows different models that were developed to predict the MBD using independent variables such as DBH, crown radius, and tree height.

Table 3. Equations for Predicting Maximum Branch Diameter

No.	Model Equation	Source
1.	$MBD = a \times R^b \times H^c \times L^d + \varepsilon$	(Groot & Schneider, 2011)
2.	$MBD = a \times R^b \times H^c \times BA^d + \varepsilon$	(Groot & Schneider, 2011)
3.	$MBD = a \times R^b \times H^c \times BA^d \times (1 + BAL)^e + \varepsilon$	(Groot & Schneider, 2011)
4.	$\ln(DBG) = p - a \times e^{-b \times GUH} + \varepsilon$	(Loubère et al, 2004)

Where; **MBD**; maximum branch diameter (cm). **R**; crown radius (m). **H**; stem height (m). **L**; crown length (m). **BA**; plot basal area (m²/ha). **BAL**; competition index, defined as the basal area of the stems larger than that of the stem in view. **DBG**; living branch diameter. **GUH**; branch insertion counted from stem apex. **a**, **b**, **c**, **d**, **e**, **ε**, **p**; fitting parameters.

The increase in MBD with height can be due to exposure of taller trees to the wind speed. Wind increases the deflection and sizes of branches (Eloy, 2011).

2.2.5. Predicting The Number of Foliage in a Tree

Trees are important components in forest ecosystems, and to understand and adequately describe such systems, quantifying various aspects of trees is necessary. There are some probability sampling strategies, particularly applicable to tree characteristics that have been used but rarely in ecological field studies (Gregoire et al., 1995). It's hard to measure the total foliar area or mass of a tree. However, a variety of sampling methods are proposed, and estimators are presented based on the probability sampling methods (Jessen, 1955; Shinozaki et al., 1964).

Randomized Branch Sampling (RBS) is an application of multistage probability sampling, which was developed by (Jessen, 1955) to estimate the number of fruits on an individual tree. This method of sampling provides an efficient means to estimate many characteristics of trees (El-Shaarawi & Piegorsch, 2002). It can be used to estimate foliar area and mass, number of leaves, surface area of a tree and the average stem length from the butt of the main stem to a terminal bud (Gregoire et al., 1995). The RBS estimator makes use of inverse probability weighting in a way that there is no bias. Furthermore, if a random selection of branches is made with probability roughly proportional to the amount of the tree characteristic of interest (foliage, area) borne by respective branches, the estimation is very precise too (El-Shaarawi & Piegorsch, 2002).

The tree diagrammed in Figure 5a contains 27 possible paths extending from the butt of the main stem to a terminal shoot. The four branch segments of one possible path are shown in Figure 5b. RBS can be stopped after selection of a branch at any node, in which case the entire branch (3 in Figure 5c) is treated as the terminal segment of the path. RBS can also be started from the butt of any branch on a tree (Figure 5d), in which case the resultant estimates pertain only to the entire starting branch (encircled), not the entire tree (Gregoire et al., 1995).

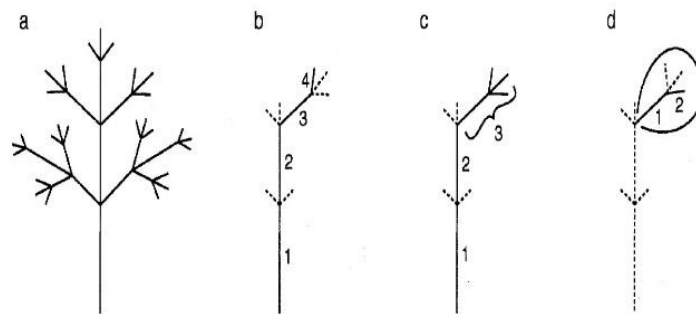


Figure 5. Sampling of Branches in RBS (Gregoire et al., 1995)

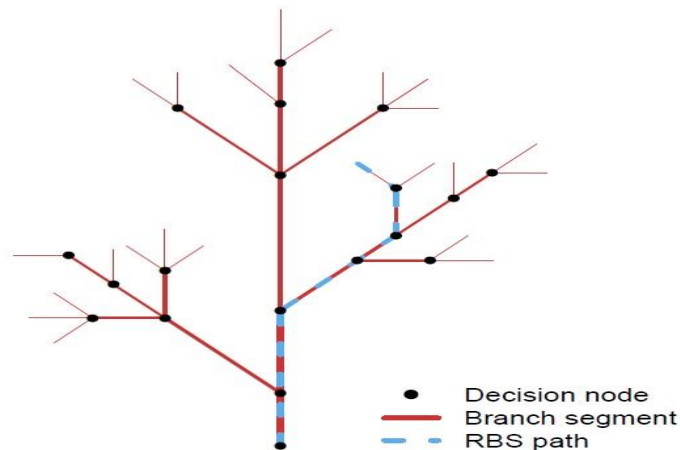


Figure 6. Simplified Diagram of a Tree Showing One Possible RBS Path.
There are 23 Terminal Branches in This Diagram (Schlecht, 2011)

3. INVESTIGATION AND SIMULATION SETUP

3.1. Estimation of Components

In this section, the most widely used prediction models will be adopted to estimate the components and the characteristics of trees. The tree species selected for simulation are Pinus, Ash and Silver Birch species. The foliage density of a tree stand will be used as the foliage parameter to predict the attenuation of a

wireless signal due to vegetation. The plot area will be 100m². The attenuation prediction model adopted will be the electromagnetic wave theory using single scatterer.

3.1.1. Crown Width Estimation Using DBH

The commonly used prediction model is the linear model given by the expression below.

$$Cw = a + b \times DBH \quad (13)$$

3.1.2. Tree Height Estimation Using DBH

As the crown width of a tree can be estimated using DBH, the height of a tree can also be estimated using the correlation between the DBH and tree height. The prediction model to estimate the height of a tree is given in the expression below.

$$H = 1.3 + a \times (1 - \exp(-b \times DBH))^c \quad (14)$$

Where **1.3** is the breast height.

To predict the maximum branch diameter of a tree, the basal area of a tree is calculated. Basal area is a term used to estimate the average area occupied by trees in a given plot (usually in acres or hectares). It is defined as the total cross-sectional area of all stems in a stand measured at breast height and express as per unit plot area (e.g. m²/ha) (Anonymous, 2015). Tree stems are usually cylindrical shape. Therefore, the cross-sectional area of stem is the same as the area of circle that which calculated as;

$$BA = \pi \times (DBH/2)^2 \quad (15)$$

Where BA is the basal area, DBH is the diameter at breast height. $\pi = 3.142$.

The crown height of a tree can be estimated using the estimated values of the CW and the tree height. The length of and width of a crown determines the photosynthetic capacity of a tree.

3.1.3. Maximum Branch Diameter Estimation (MBD)

The branch diameter of a tree decreases as from the crown base up to the tree apex (Loubère et al., 2004). To predict the diameter of the largest branch, crown radius, tree height, and the tree basal area can be used as parameters in the expression below;

$$MBD = a \times R^b \times H^c \times BA^d + \varepsilon \quad (16)$$

Where, **R**, **H**, **BA** are the crown radius, tree height and basal area respectively. **a,b,c,d** and ε are the estimated fitting parameter values.

3.1.4. Number of Branches and Leaves on a Tree

Randomized Branch Sampling is used to estimate different characteristics of a tree. In RBS, the main stem is also considered as a branch. Therefore, the entire above-ground component of the tree is considered as a branch comprising of several segments. A 'path' is defined as the sequence of the connected branch segments. The number of possible paths equals to the number of terminal shoots (Jessen, 1955). The starting point of a path can be from any butt of a branch segment (Figure 5b, c, d). RBS provides an estimate for the number of branches (or characteristics of interest). Figure 7 illustrates RBS (Anonymous, 2019).

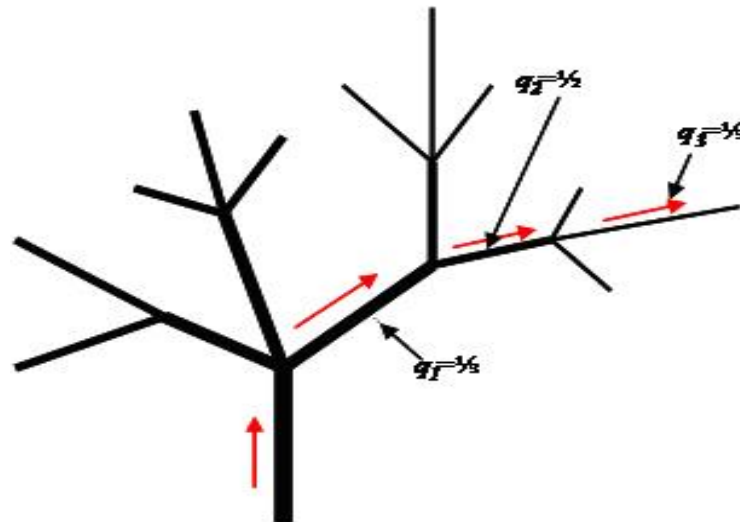


Figure 7. Illustration of Randomised Branch Sampling (Anonymous, 2019)

From the above diagram, $Q_r = q_1 \times q_2 \times q_3$

The unconditional probability of the r^{th} branch segment selection of a path is

$$Q_r = \prod_{k=1}^r q_k \quad (17)$$

Where Q_r is the unconditional probability of the of the branch segment. If f_r is the number of branches in the r^{th} branch of the path, then the total number of branches can be estimated using;

$$\hat{f} = \sum_{r=1}^R \frac{f_r}{Q_r} \quad (18)$$

To estimate the number of branches on a tree, the first branch segment will be the main stem and the probabilities of each segment will be computed to give the overall number of branches. The drawback of the RBS is that at least one path must be counted manually by observing the branching system of the tree. Tree branches are formed using the phenomenon called fractal-based theory. Tree formation depends on the species, the density and the environment. The structures of tree forms can be categorized into three forms, which are; columnar, decurrent, and excurrent as can be seen in Figure 8 (Lin & Sarabandi, 1999) and Figure 9 (Anonymous, 2021).



Figure 8. Examples of Decurrent and Excurrent Types of Trees (Lin & Sarabandi, 1999)

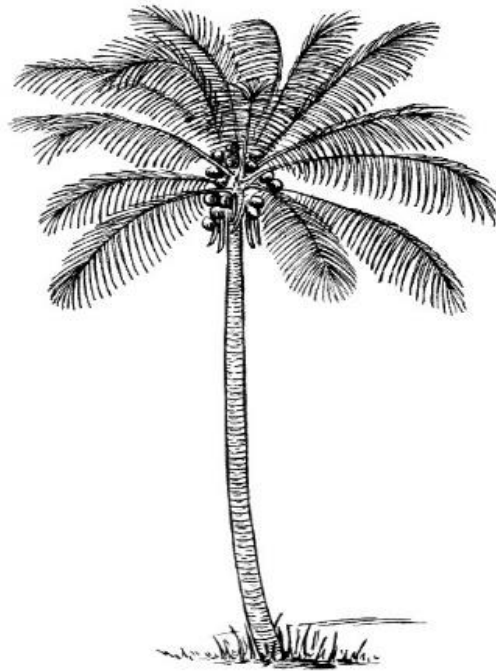


Figure 9. Example of a Columnar Tree (Anonymous, 2021)

The correlation of the ages between the branches (**B**) and the stems (**T**) in different tree forms can be expressed as

$$\mathbf{T} = \mathbf{a} + \mathbf{bB} \quad (19)$$

Where **a** is the intercept parameter and **b** is the regression slope measured for different species of particular tree forms (Eloy, 2011). The intercept is usually greater or equal to zero. A high intercept means a tree that current twigs develop from the older stems.

Decurrent trees are usually deciduous trees while excurrent trees are usually coniferous trees. In deciduous trees, the lateral branches grow faster than or sometimes as fast as the terminal shoot that give rise to the growth habit of the tree, thereby the main stem eventually disappears and forming a large crown. In conifer trees, the main stem out grows the branches giving the tree crown a cone shape.

The relationship between the radiuses of the branches formed from the main branch shows that branches become smaller than the main branch as they split to form new branches (Eloy, 2011). Another relationship is between the length of the old and the new branches given a growth rate function of the tree expressed as

$$L_b = \frac{l_a}{g} \quad (20)$$

Where **L_b** is the length of the old branch (in this case the stem) and **L_a** is the length of the new branch. **g** is the growth rate of the tree which is dependent on the species and environment (Kirtley, 2013).

To estimate the total number of branches and leaves on a particular tree using RBS, the conditional probabilities of each segment on the path should be obtained. Taking into account the growth rate of the three tree species selected for this paper, and assuming the branch formation starts at height **I_a**, the total number of branch splits will be "**H-I_a / g**" which will give the total number of splits in relation to the height of the tree where **H** is the breast height. Likewise, the total number of branch segment can then be estimated using "**CW / g**".

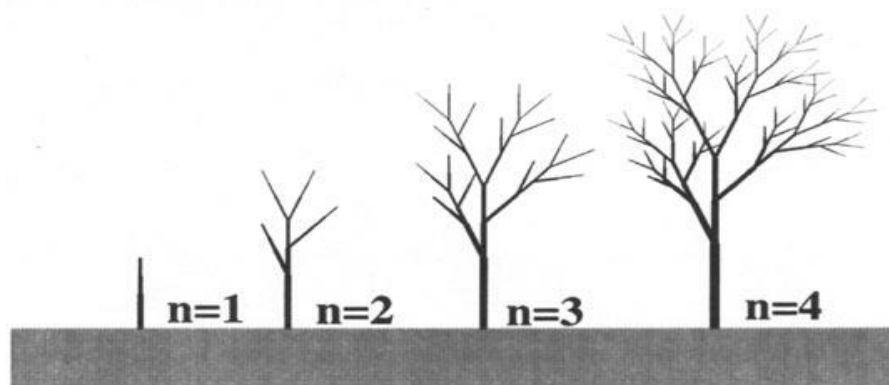


Figure 10. Example of Fractal Branch Formation (Wang & Sarabandi, 2007)

The leaf orientation on a twig of a tree can be examined to assume how the branches split from the main branch. The orientation angle of the branch of a tree is usually formed at 45 degrees from the main branch for broadleaves and 60 degrees angle for conifer trees (Wang & Sarabandi, 2007). Figure 11 shows examples of leaf structure of birch (a), ash (b) and pine trees (c) (Anonymous, 2020a,b,c). From Figure 11 the probability of each segment from the stem will be $\frac{1}{2}$ for birch, $\frac{1}{3}$ for ash and $\frac{1}{3}$ for pine trees.

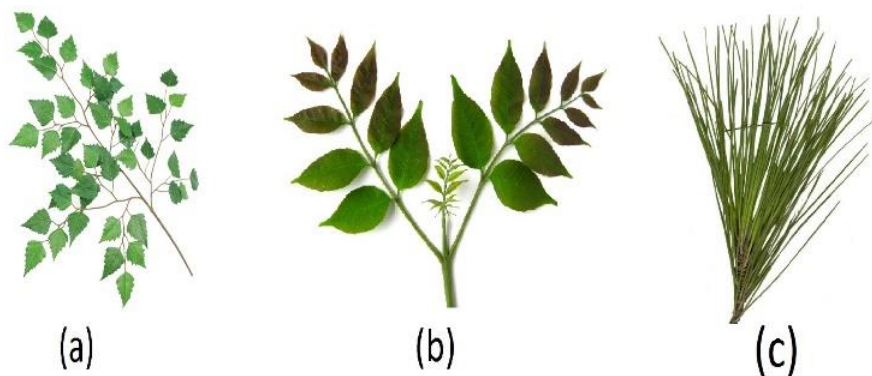


Figure 11. Examples of Leaf Structure of (a) Birch, (b) Ash and (c) Pine Trees (Anonymous, 2020 a,b,c)

Most leaves grow at the end of the twigs (the smallest branch on the tree), forming a canopy. Ash trees are broadleaved trees having a compound leaf. Meaning a leaf consisting multiple leaflets. These leaves occur in opposite pairs with the exception of the terminal leaflet (Figure 11b). The arrangement of the leaflets are typically 4-6 pairs, making a total of 9-13 leaflets (Kirtley, 2013). On each twig, there are 4 compound leaves which in total gives 36-52 leaflets on each twig. Birch leaves are similar to Ash trees, but they have larger leaflets that make four leaflets on a compound leaf and 3-4 compound leaves on each twig. Pine trees, on the other hand, have needle-like leaves 2-5 inches long. They are formed in groups of 2-5, and each group has a bundle of 2-3 needles, and each twig has average of 3-7 groups.

3.1.5. Signal Propagation Based on Wave Theory Model

The physics based FCSM model has proven to be the ideal model to predict vegetation loss due its accuracy in capturing incoherent power that is contributed by the scattering of the tree particles. A Monte Carlo simulation of scattering using computer generated fractal trees was successfully used in obtaining the propagation of a signal through vegetation (Lin & Sarabandi, 1999). The approach in the computation of the FCSM is based on Distorted Born Approximation (DBA) (Lin & Sarabandi, 1999; Wang & Sarabandi, 2005; 2007). The tree stands were generated using parameters such as trunk diameter, height, density, etc., to form a physical structure of a tree. The tree components (leaves, branches, and stem) are considered to be a group of dielectric scatterers. The scatterers are illuminated inside the forest by coherent mean-field, and the scattered fields are coherently added. The forest medium attenuates the scattered fields and likewise the illuminating field. Single scattering among the branches is computed at lower frequencies. However, at

micro and millimetre wave frequencies, multiple scattering cannot be ignored (Wang & Sarabandi, 2005; 2007). In this model, the trees are categorised into deciduous or evergreen conifer trees. The only difference is the extension of the trunk into the canopy (crown) layer for evergreen trees, and either disk is used for deciduous or cylinders for conifer evergreen trees to represent the leaves and needles as depicted in Figure 12 (Burgin et al., 2011).

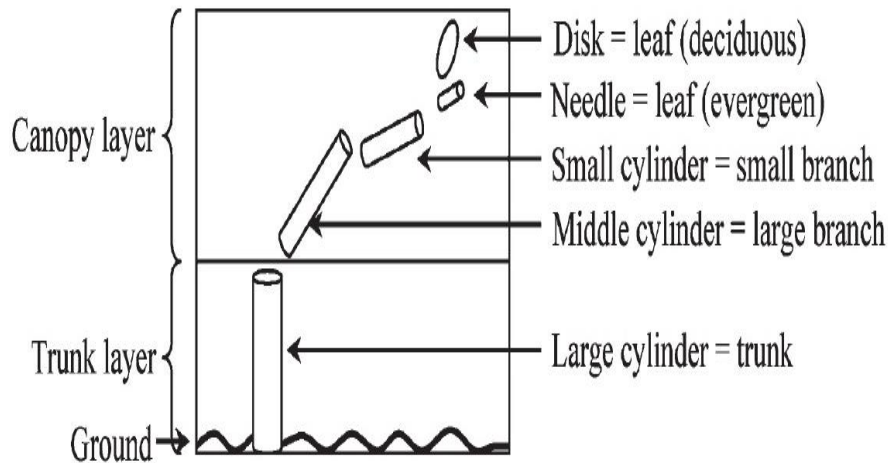


Figure 12. Building Blocks of Scatterers for Wave Theory Model (Burgin et al., 2011)

The boundary between the stem and the crown layer, for most trees, can be set at the first branching point where the stem divides into multiple large branches, even though the boundary is not explicitly defined. The stems are modelled as single dielectric cylinder populating the lower vertical layer. Two categories of branches are modelled as a collection of small and large dielectric cylinders in the crown layer. Depending on the type of tree, dielectric needles or disks are used to model the leaves. By obtaining the densities of the stems, branches, and leaves, lateral homogeneity is implemented over a modelling unit. The scatterers of a particular species inside each vertical layer are considered homogenous, with stationary statistics as seen in Figure 13 (Burgin et al., 2011).

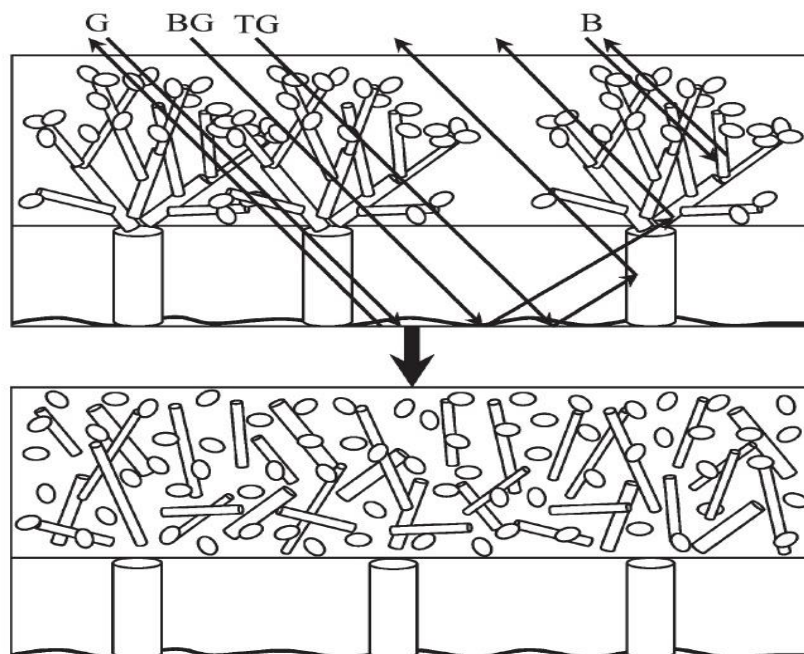


Figure 13. Realistic Geometry of Tree Stands with Four Scattering Mechanisms (top) and the Model Realization (Burgin et al., 2011)

Using the components of trees estimated, they are treated as a cluster of scatterers with a specific position, orientation and geometric shape and sizes (Figure 13). The entire tree is assumed to be illuminated by a plane wave with a propagation direction of unit vector \mathbf{k}_i that is given by;

$$E^i(r) = E_0^i e^{ik_0 \mathbf{k}_i \cdot r} \quad (21)$$

The scattered field is calculated for individual trees since the relative position of the trees are uncertain with respect to other trees and is usually of the order of many wavelengths. Therefore, the total scattered power is determined by adding the incoherent scattered power of individual trees. To total scattered power from a tree can be computed by adding the single scattered field from each scatterer and neglecting the effect of multiple scattering among the scatterers. The propagation constant of a forest medium can be estimated using Foldy's approximation \mathbf{M}_{pq} denoted by

$$M_{pq} = \frac{j2\pi n}{k_0} \langle S_{pq} \rangle \quad (22)$$

Where $\mathbf{j} = \sqrt{-1}$, \mathbf{n} is the number of scatterers in a tree, \mathbf{k}_0 is the wave number in free space. S_{pq} is the amplitude of the single scatterer given by

$$\bar{E}_p^s = \frac{e^{jk_0 R}}{R} S_{pq} \cdot \bar{E}_q^i \quad (23)$$

Where \bar{E}_p^s and \bar{E}_q^i Are the incident and scattered fields respectively. \mathbf{R} is the distance from a scatterer to a receiver that detects the scattered field. $\langle \rangle$ represent the average of the forward scattering amplitudes of all the scatterers in a tree. Because of the inhomogeneous nature of the tree components in the vertical direction, the tree stand can be divided into different layers in the horizontal direction, for which \mathbf{M}_{pq} will be different depending on the respective geometry of the function. In conifer trees, the layers are divided into three while, in deciduous trees, the level is undefined. Figure 14 shows layer division of a pine stand (Wang & Sarabandi, 2007).

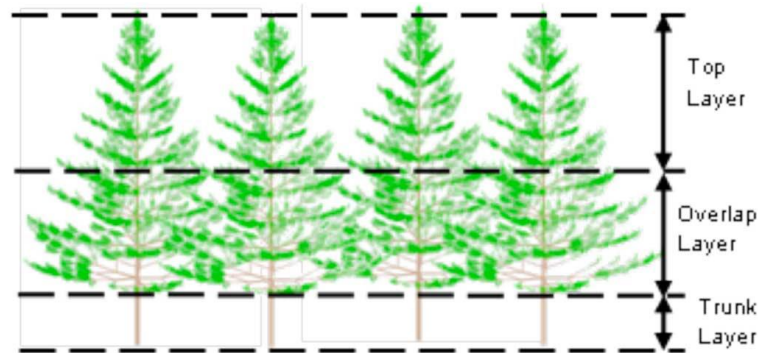


Figure 14. Layer Division of a Pine Stand (Wang & Sarabandi, 2007)

The scattered field is then computed from each scatterer to the receiver using equations given, with both incident and scattered field modified by Foldy's propagation constant together with free space counterparts using;

$$E = T \times E_0 \quad (24)$$

Where

$$E = \begin{pmatrix} E^v \\ E^h \end{pmatrix}, E_0 = \begin{pmatrix} E_0^v \\ E_0^h \end{pmatrix} \quad (25)$$

and

$$T = \begin{pmatrix} e^{jM_{vv}R} & 0 \\ 0 & e^{jM_{hh}R} \end{pmatrix} \quad (26)$$

\mathbf{E} and \mathbf{E}_0 are the polarised electric field vectors of the radio signal propagating inside the forest medium and in free space. \mathbf{v} and \mathbf{h} are the representation of vertical and horizontal propagation. \mathbf{T} is the transmissivity matrix of the effective medium with the constant of propagation $\mathbf{M}_{\mathbf{v}\mathbf{v}}$ and $\mathbf{M}_{\mathbf{h}\mathbf{h}}$, \mathbf{R} is the travelled distance by the incident wave before arriving the receiver. In forest structures, the azimuthal symmetry is mostly assumed thereby making the averaged transmissivity of the depolarized components is approximately zero $\mathbf{M}_{\mathbf{v}\mathbf{h}} \approx \mathbf{0}$, $\mathbf{M}_{\mathbf{h}\mathbf{v}} \approx \mathbf{0}$.

Four different mechanisms of wave propagation inside forest environments occur, which are; scattered field with the scatterer illuminated by the direct incident wave, the reflected scattered field with the scatterer illuminated by the direct incident wave, the direct scattered field with the scatterer illuminated by the reflected incident wave, and the reflected scattered field with the scatterer illuminated by the reflected incident wave. The ground effect is an important feature in FCSM which the roughness of the ground is accounted for by using Fresnel reflection coefficient (Figure 15).

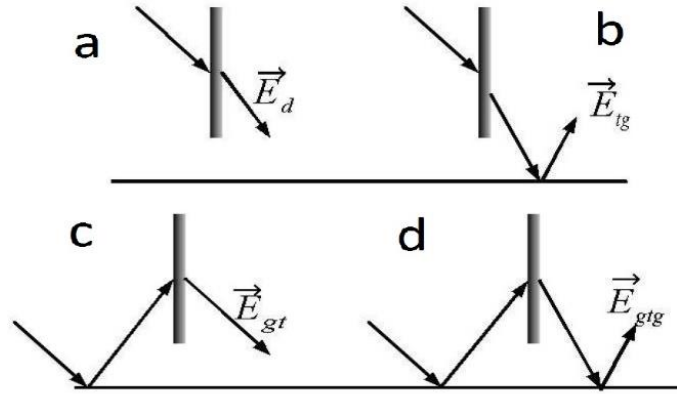


Figure 15. Components of Scattered Field Above Ground Plane Responding to Four Wave Propagation Scenarios, (a) Direct-Direct, (b) Direct-Reflected, (c) Reflected-Direct and (d) Reflected-Reflected (Burgin et al., 2011)

The polarization of the incident and scattered waves is a dependent point in the computation formulation of scattering from a single scatterer. The two polarizations are the horizontal and vertical polarization. Vertical polarization is assumed for this experiment where

$$\hat{\phi} = \hat{h} \times \hat{h} \quad (27)$$

and

$$\hat{h} = \frac{\hat{z} \times \hat{k}}{|\hat{z} \times \hat{k}|} \quad (28)$$

\hat{z} and \hat{k} are unit vectors of the direction of the incident or scattered wave. The total scattered field at the receiver is obtained by adding all the scattered fields of the scatterers. The same process can be followed using the given expression to calculate for leaves, branches and stems of other trees.

4. RESULTS AND DISCUSSION

The correlation between crown diameter and stem **DBH** are known to be high, so the crown diameter can be estimated using linear prediction equation. The results obtained from estimating crown width using **DBH**

as the independent parameter is shown in Table 4. The density of the stand does not affect the ratio between the **CW** and the **DBH**, and the linear model is the most commonly used model because of its simplicity. From the Regression Coefficients available in literature, more data can be obtained for wide range of species as can be found in (Hemery et al., 2005; Sánchez-González et al., 2007; Arzai & Aliyu, 2010; Ibrahim et al., 2014). The results give similar correlation between Height and **DBH**. However, linear models did not yield accurate estimates (Arzai & Aliyu, 2010). This is because, the density of the stand changes the growth pattern of the tree due to the competition amongst the trees (Martínez-Vilalta et al., 2006; Sánchez-González et al., 2007; Rupšys & Petrauskas, 2010). Furthermore, at larger DBH, the estimation using linear model did not yield good correlation. Hence, the exponential model is the most ideal (Wang & Hann, 1988; Peper et al., 2001).

Predicting the diameter of the branch has not been conducted in most species. This is because the branches in a tree have no economic value, but it is used to estimate the biomass of the crown that other parameter such as the crown dimensions can be used. However, the information obtained from the results can help guide the development of pruning strategies, and likewise in radio communications, the thickness of branches is important as it also affects radio signals at high frequencies. The basal area of a tree was easily obtained. The basal area is important in estimating the branch diameter because of the gravitational force and wind force that are acting on the tilted branch angle from the stem.

Randomised Branch sampling is an effective and time efficient method of sampling tree components density compared to the conventional methods. The path selection is sampled at the longest path on the largest branch. Should the sample path selected at smaller branches, more than one path should be selected, and then the average of the sampled result is estimated. Given the higher branch segments based on the sizes of the crown, the foliage density increased as the path length increase. The variance between the estimate and the actual measured characteristic (fruits, Biomass, Foliage), it suggests that RBS can give less than ten percent (10%) variance (Jessen, 1955; Gregoire et al., 1995). The pipe Model theory (Shinozaki et al., 1964) has been used to estimate the number of leaves or branches of trees. In the model, it is viewed that each leaf is supported by a single pipe connecting the leaf through the branches and the stem to the root hairs. The pipe handles the transportation of water and other nutrients. The summary of the different parameters estimated from DBH and RBS are given in Table 4.

The FCSM model is a wave theory model aimed at predicting the path loss by considering the vegetation components as a cluster of dielectric scatterers. The input parameters for the FCSM model are in two parts;

- 1) The vegetation parameters and
- 2) The radio system parameters.

Table 4. Summary of Different Tree Characteristics Estimated from Existing Prediction Models

species	DBH(cm)	CW (m)	H (m)	BA (cm ²)	$MBD = a * R^b * H^c * BA^d + \epsilon$ (cm)	Number of branch segment(s)	Total numbe of Branches in a tree	Average leaves/needles per twig	total numbe of leaves/needles in a tree
Pine	10	1.2896	8.1234	78.55	2.3524	5	135	84	11340
	20	1.5886	13.6903	314.2	2.8018	6	405	84	34020
	30	1.8876	18.1725	706.95	3.1471	7	1215	84	102060
Ash	10	2.7938	9.9269	78.55	4.0067	6	32	36	1152
	20	4.8294	18.0708	314.2	6.0053	10	512	36	18432
	30	6.8651	24.3179	706.95	7.4983	14	8192	36	294912
Birch	10	2.5904	5.0986	78.55	2.5813	4	8	12	96
	20	4.2055	7.4878	314.2	3.2815	6	32	12	384
	30	5.8206	9.4298	706.95	3.8761	7	64	12	768

Table 5 give details of the input parameters for the FCSM. In the vegetation parameters, the Specie is not significant while the orientation of the foliage in the propagation direction is specified. However, the species determine how many likely layers the vegetation can be split into. The moisture content of the foliage is significant for determining the permittivity of the dielectric components. The crown width parameter calculates the vegetation depth along the path. In the case where multiple species are present, each species will be estimated individually.

Table 5. Input Parameters for FCSM Wave Theory

Vegetation Parameters			Radio System Paramter
Forest Stand	Tree Structure Prameter	Dielectric Prameter	
Area of the Plot	Tree height		Signal Frequency
Tree density	DBH		Tx and RX disatance
Specis type	Crown width and depth	Leaf Moisture content	Tx and RX height
	Leaf Form (needle/leaf)	Wood moisture content	Tx and Rx Polarisation
	Leaf Dimensions (cross sectional area)	Soil moisture content	
	Leaf Density		
	Tilt angle		

NB: the values in the table are estimated values which will be as vegetation parameters to predict signal loss as it passes through the vegetation

As described in the previous sections, attenuation rate corresponds to scattering of the coherent mean field by the tree components along the direction of the signal propagation. Scattering of signal through foliage also provide the advantage of redirecting part of the incident wave towards the receiver.

MATLAB R2015a was used for the simulation of the signal propagation. As predicted by researchers, Vegetation density and type are one of the major factors that affect signal propagation through vegetation. For Pinus trees, the excess attenuation is higher due to the density of components within the tree. The attenuation due to frequency does not make a significant loss at frequencies above 10GHz. This is due to the wavelength of the frequencies are at the millimetre range. Figures 16-18 show the simulation results of the attenuation levels of signals when transmitted through pinus tree, ash tree and birch tree respectively.

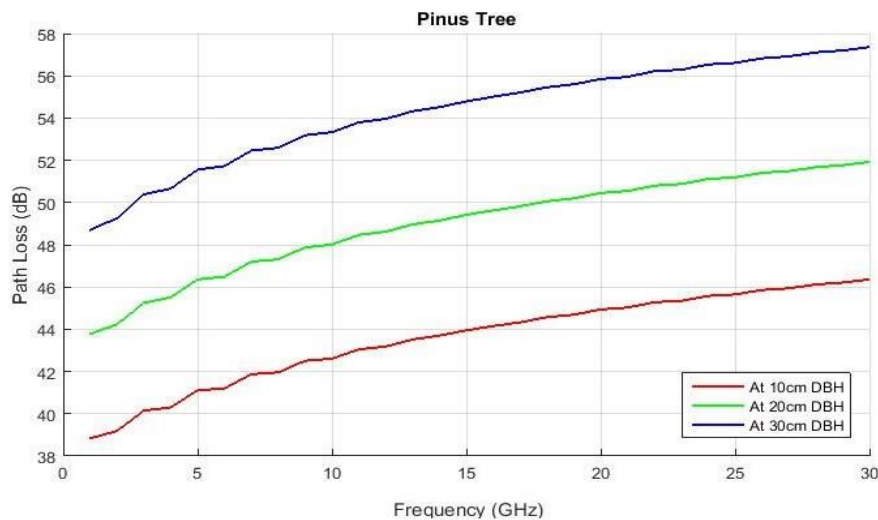


Figure 16. Excess Attenuation of Signal in a Stand of $0.05/m^2$ Density for Pinus Tree with Estimated Foliage Densities at Tree Diameter at Breast Height (DBH)

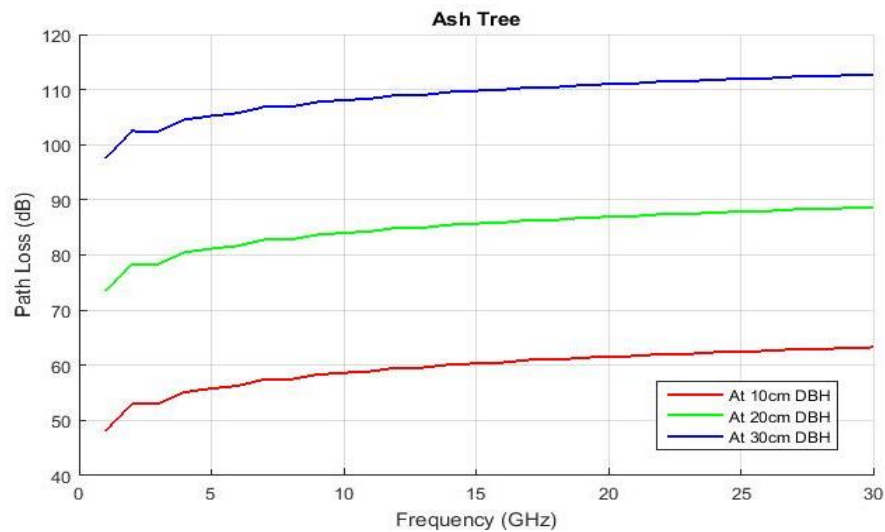


Figure 17. Excess Attenuation of Signal in a Stand of $0.05/m^2$ Density for Ash (*Fraxinus Excelsior*) Tree with Estimated Foliage Densities at Tree Diameter at Breast Height (DBH)

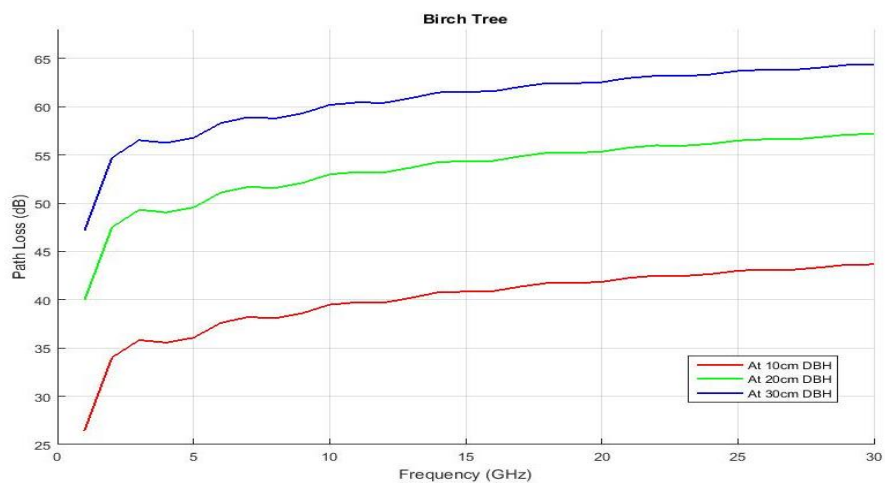


Figure 18. Excess Attenuation of Signal in a Stand of $0.05/m^2$ Density for Silver Birch Tree with Estimated Foliage Densities at Tree Diameter at Breast Height (DBH)

The types of leaf and the size also has a significant role in signal attenuation in the sense that larger leaves produce higher attenuation as can be seen in Figure 17. Even though Ash tree has less foliage density than the Pinus tree, the path loss is higher due to the size of the dielectric scatterers. This suggests the importance of the cross-sectional area of the leaves in calculating the extent of scattering within the leaves indicating that, the larger the leaf size, the higher the attenuation. Birch trees have lower attenuation because it does not produce dense foliage as can be produced by the Pine and Ash trees.

Most of the scattering of the radio wave at the micro and millimetre waves are caused by the leaves because the thickness of the leaves is approximately equal to the wavelength. However, scattering occurs at the branch level due to the angle orientation of some of the branches, whereby causing the signal to bounce when in contact with the branch surface.

5. CONCLUSIONS

This paper includes two main parts. The first part is the study of vegetation characteristics and estimation of vegetation density components using existing models. The second part is the application of wave theory model for the prediction of signal attenuation through an estimated vegetation density.

Diameter at breast height has shown to be the strongest estimator for crown width, tree height and basal area in most tree species. Randomised branch sampling is an efficient and unbiased sampling method which was used to estimate foliage density.

Fractal-Based Coherent Scattering Model (FCSM) which is a wave theory model was adopted for the application of wave propagation through foliage. The initial model uses computer generated forest environment that in the end cannot give the actual characteristic of the foliage geometry. The coherent mean field is attenuated before hitting individual particles of the foliage by the effective medium. After the scattered field from each particle is being attenuated by the medium, they are then added by at the receiver. This in turn gives the total scattered field been attenuated by the vegetation.

The vegetation input parameter for the FCSM was replaced by the exact estimate of the vegetation using the vegetation models introduced. The experiment showed that wave theory model can be adopted as a more efficient model for wireless signal attenuation through several vegetation densities.

6. FUTURE WORK

This project work is a study work based on secondary data. The future work involves more data acquisition either secondary or measurement campaign for the vegetation modelling of more species that can satisfy a broad range of environments.

FCSM model applied, even though it provides good estimations, it is rather complex, and it is not attractable to radio link designers. Therefore, some simple formula, based on simulation results need to be developed.

Future experimental investigation should be conducted to compare the predicted path loss through a realistically measured vegetation density with the simulated path loss in an environment.

CONFLICT OF INTEREST

No conflict of interest was declared by the authors.

REFERENCES

- Adegoke, A. S., & Siddle, D. (2012, May). *Investigation into vegetation effects on propagating radio waves*. Conference on Applied Radio System Research (ARSR-SWICOM), University of Manchester, United Kingdom.
- Al-Basheir, M. S., Shubair, R. M., & Sharif, S. M. (2006). Measurements and analysis for signal attenuation through date palm trees at 2.1 GHz frequency. *Sudan Engineering Society Journal*, 52(45), 17-22.
- Al-Naimi, M. O., & Hammoudeh, A. M. (1993). Influence of Vegetation on Attenuation of Radio wave Signals in the X-Band Frequency Region. COST 235 TD, CP 149.
- Arzai, A., & Aliyu, B. (2010). The relationship between canopy width, height and trunk size in some tree species growing in the Savana zone of Nigeria. *Bayero Journal of Pure and Applied Sciences*, 3(1), 260-263. doi:[10.4314/bajopas.v3i1.58808](https://doi.org/10.4314/bajopas.v3i1.58808)
- BBC & ITC (1998). The Effect of Trees on Television Reception. Arboricultural Advisory & Information Service, Arboriculture Research Note: 146/98/TV. (Accessed: 06/07/2015) www.users.globalnet.co.uk/~skellern/download/tv_reception.pdf
- Bragg, D. C. (2001). A local basal area adjustment for crown width prediction. *Northern Journal of Applied Forestry*, 18(1), 22-28.
- Burgin, M., Clewley, D., Lucas, R. M., & Moghaddam, M. (2011). A Generalized Radar Backscattering Model Based on Wave Theory for Multilayer Multispecies Vegetation. *IEEE Transactions on Geoscience and Remote Sensing*, 49(12), 4832-4845. doi:[10.1109/TGRS.2011.2172949](https://doi.org/10.1109/TGRS.2011.2172949)

- Corral-Rivas, S., Álvarez-González, J., Crecente-Campo, F., & Corral-Rivas, J. (2014). Local and generalized height-diameter models with random parameters for mixed, uneven-aged forests in Northwestern Durango, Mexico. *Forest Ecosystems*, 1(1), 6. doi:[10.1186/2197-5620-1-6](https://doi.org/10.1186/2197-5620-1-6)
- COST (1996). COST 235 – Radiowave propagation effects on next-generation fixed-services terrestrial telecommunications systems. European Commission, Luxembourg. ISBN:92-827-8023-6
- El-Shaarawi, A. H., & Piegorisch, W. W. (2002). *Encyclopaedia of Environmetrics*. John Wiley & Sons, Ltd. doi:[10.1002/9780470057339](https://doi.org/10.1002/9780470057339)
- Eloy, C. (2011). Leonardo's Rule, Self-Similarity, and Wind-Induced Stresses in Trees. *Physical Review Letters*, 107(25), 258101. doi:[10.1103/PhysRevLett.107.258101](https://doi.org/10.1103/PhysRevLett.107.258101)
- Eng, H. (2012). Tree Height Estimation in Redwood/Douglas-fir Stands in Mendocino County. In: *Proceedings of Coast Redwood Forests in a Changing California: A Symposium for Scientists and Managers* (pp. 649-654), Pacific Southwest Research Station, Forest Service, US Department of Agriculture: Albany, CA, USA.
- Ghasemi, A., Abedi, A., & Ghasemi, F. (2013). *Propagation Engineering in Radio Links Design*. New York, Springer. doi:[10.1007/978-1-4614-5314-7](https://doi.org/10.1007/978-1-4614-5314-7)
- Ghoraishi, M., Takada, J., & Imai, T., (2013). Radio Wave Propagation Through Vegetation. In: Y. Zheng (Eds.), *Wave Propagation Theories and Applications* (pp. 155-174). doi:[10.5772/52571](https://doi.org/10.5772/52571)
- Gilman, E. F. (2003). Branch-to-stem diameter ratio affects strength of attachment. *Journal of Arboriculture*, 29(5), 291-294.
- Goldhirsh, J., & Vogel, W. J. (1998). Handbook of propagation effects for vehicular and personal mobile satellite systems: overview of experimental and modelling results. Report jointly authored by The Johns Hopkins University Applied Physics Laboratory (APL: A2A-98-U-0-021) and The University of Texas at Austin Electrical Engineering Research Laboratory (EERL: EERL-98-12A).
- Gregoire, T. G., Valentine, H. T., & Furnival, G. M. (1995). Sampling Methods to Estimate Foliage and Other Characteristics of Individual Trees. *Ecological Society of America*, 76(4), 1181-1194. doi:[10.2307/1940925](https://doi.org/10.2307/1940925)
- Groot, A., & Schneider, R. (2011). Predicting maximum branch diameter from crown dimensions, stand characteristics and tree species. *The Forestry Chronicle*, 87(04), 542-551. doi:[10.5558/tfc2011-053](https://doi.org/10.5558/tfc2011-053)
- Helhel, S., Özen, Ş., & Göksu, H. (2008). Investigation of GSM signal variation depending weather conditions. *Progress In Electromagnetics Research B*, 1, 147-157. doi:[10.2528/PIERB07101503](https://doi.org/10.2528/PIERB07101503)
- Hemery, G. E., Savill, P. S., & Pryor, S. N. (2005). Applications of the crown diameter-stem diameter relationship for different species of broadleaved trees. *Forest Ecology and Management*, 215(1-3), 285-294. doi:[10.1016/j.foreco.2005.05.016](https://doi.org/10.1016/j.foreco.2005.05.016)
- Hong, B. (2015). Predicting the Growth in Tree Height for Building Sunshine in Residential District. *Open Journal of Forestry*, 5(1), 57-65. doi:[10.4236/ojf.2015.51007](https://doi.org/10.4236/ojf.2015.51007)
- Ibrahim, E. M., Osman, E. H. & Idris, E. A. (2014). Modelling the Relationship between Crown width and Diameter at Breast Height for Naturally grown Terminalia tree species. *J. Nat. Resour. Environ. Stud.*, 2(2), 42-49.
- ITU (2013). Attenuation in vegetation. Series of ITU-R Recommendations P.833-8. International Telecommunication Union, Geneva. (Accessed: 23/10/2019) https://www.itu.int/dms_pubrec/itu-r/rec/p/R-REC-P.833-8-201309-S!!PDF-E.pdf
- Jessen, R. J. (1955). Determining the Fruit Count on a Tree by Randomized Branch Sampling. *Biometrics*, 11(1), 99-109. doi:[10.2307/3001484](https://doi.org/10.2307/3001484)
- Kirtley, P. (2013). How To Identify An Ash Tree. (Accessed: 23/10/2019) <http://paulkirtley.co.uk/2013/how-to-identify-an-ash-tree/>

- Koh, I. S., Wang, F., & Sarabandi, K. (2003). Estimation of coherent field attenuation through dense foliage including multiple scattering. *IEEE Transactions on Geoscience and Remote Sensing*, 41(5), 1132-1135. doi:[10.1109/TGRS.2003.813552](https://doi.org/10.1109/TGRS.2003.813552)
- Lin, Y-C., & Sarabandi, K. (1999). A Monte Carlo coherent scattering model for forest canopies using fractal-generated trees. *IEEE Transactions on Geoscience and Remote Sensing*, 37(1), 440-451. doi:[10.1109/36.739083](https://doi.org/10.1109/36.739083)
- Lockhart, B. R., Weih, R. C., & Smith, K. M. (2005). Crown radius and diameter at breast height relationship for six bottomland hardwood species. *Journal of the Arkansas Academy of Science*, 59, 110-115.
- Loubère, M., Saint-André, L., Hervé J-C., & Vestøl, G. I. (2004). Relationships between stem size and branch basal diameter variability in Norway spruce (*Picea abies* (L.) Karsten) from two regions of France. *Annals of Forest Science*, 61(6), 525-535. doi:[10.1051/forest:2004047](https://doi.org/10.1051/forest:2004047)
- Martínez-Vilalta, J., Vanderklein, D., & Mencuccini, M. (2006). Tree height and age-related decline in growth in Scots pine (*Pinus sylvestris* L.). *Oecologia*, 150(4), 529-544. doi:[10.1007/s00442-006-0552-7](https://doi.org/10.1007/s00442-006-0552-7)
- McLarnon, B. (1997). *HF/UHF/Microwave Radio Propagation: A Primer for Digital Experimenters*. Proceedings of the American Relay Radio League (ARRL) Conference.
- Meng, Y. S., & Lee, Y. H. (2010). Investigations of foliage effect on modern wireless communication systems: A review. *Progress In Electromagnetics Research*, 105, 313-332. doi:[10.2528/PIER10042605](https://doi.org/10.2528/PIER10042605)
- Ndzi, D., Savage, N., & Stuart, K. (2005, Oct). *Wideband Signal propagation through Vegetation*. XVII GA of URSI.
- Ndzi, D. L., Kamarudin, L. M., Mohammad, E. A. A., Zakaria, A., Ahmad, R. B., Fareq, M. M. A., Shakaff, A. Y. M., & Jafaar, M. N. (2012). Vegetation attenuation measurements and modelling in plantations for wireless sensor network planning. *Progress In Electromagnetics Research B*, 36, 283-301. doi:[10.2528/PIERB11091908](https://doi.org/10.2528/PIERB11091908)
- Oyebade, B. A., Popo-ola, F. S., & Alex, A. (2012). Height–Diameter Equations for Eight Midwestern Rainforest Species in Nigeria using Monserud’s Model. *ARPJ Journal of Science and Technology*, 2(5), 480-486.
- Peper, P. J., McPherson, E. G., & Mori, S. M. (2001). Equations for predicting diameter, height, crown width, and leaf area of San Joaquin Valley street trees. *Journal of Arboriculture*, 27, 306-317.
- Petrauskas, E., & Rupšys, P., (2010) Age-Varying Bivariate Distribution Models for Growth Prediction. In: V. Mladenov, K. Psarris, N. Mastorakis, A. Caballero, & G. Vachtsevanos (Eds.), *Mathematical Models for Engineering Science* (pp. 250-255). International Conference on Mathematical Models for Engineering Science (MMES '10), November 30-December 2, Puerto De La Cruz, Tenerife, Spain. ISBN: 978-960-474-252-3
- Rogers, N. C., Seville, A., Richter, J., Ndzi, D., Savage, N., Caldeirinha, R. F. S., Shukla, A. K., Al-Nuaimi, M. O., Craig, K., Vilar, E., & Austin, J. (2002). A generic model of 1-60 GHz radio propagation through vegetation-Final report (QinetiQ Report No: QINETIQ/KI/COM/CR020196/1.0), UK Radiocommunications Agency (Contract Number: AY3880/510005719).
- Rupšys, P., & Petrauskas, E. (2010). The bivariate Gompertz diffusion model for tree diameter and height distribution. *Forest Science*, 56(3), 271-280.
- Sabri, N., Mohammed, S. S., Fouad, S., Syed, A. A., Al-Dhief, F. T., & Raheemah, A. (2018). Investigation of Empirical Wave Propagation Models in Precision Agriculture. *MATEC Web of Conferences*, 150, 06020. doi:[10.1051/mateconf/201815006020](https://doi.org/10.1051/mateconf/201815006020)
- Sánchez-González, M., Cañellas, I., & Montero, G. (2007). Generalized height-diameter and crown diameter prediction models for cork oak forests in Spain. *Investigación Agraria: Sistemas y Recursos Forestales*, 16(1), 76-88.

- Savage, N., Ndzi, D., Seville, A., Vilar, E., & Austin, J. (2003). Radio wave propagation through vegetation: Factors influencing signal attenuation. *Radio Science*, 38(5), 1088. doi:[10.1029/2002RS002758](https://doi.org/10.1029/2002RS002758)
- Schlecht, R. (2011). Application of Randomized Branch Sampling to Conifer Trees: Estimating Crown Biomass. MSc Thesis, University of Montana.
- Schreuder, H. T., & Hafley, W. L. (1977). A Useful Bivariate Distribution for Describing Stand Structure of Tree Heights and Diameters. *Biometrics*, 33(3), 471-478. doi:[10.2307/2529361](https://doi.org/10.2307/2529361)
- Seville, A., & Craig, K. H. (1995). Semi-empirical model for millimetre-wave vegetation attenuation rates. *Electronics Letters*, 31(17), 1507-1508. doi:[10.1049/el:19951000](https://doi.org/10.1049/el:19951000)
- Shinozaki, K., Yoda, K., Hozumi, K., & Kira, T. (1964). A Quantitative Analysis of Plant Form - The Pipe Model Theory: I. Basic Analyses. *Japanese Journal of Ecology*, 14(3), 97-105. doi:[10.18960/seitai.14.3_97](https://doi.org/10.18960/seitai.14.3_97)
- Shrestha, R., & Wynne, R. (2012). Estimating Biophysical Parameters of Individual Trees in an Urban Environment Using Small Footprint Discrete-Return Imaging Lidar. *Remote Sensing*, 4(2), 484-508. doi:[10.3390/rs4020484](https://doi.org/10.3390/rs4020484)
- Stephens, R. B. L., & Al-Nuaimi, M. O. (1995). Attenuation measurements and modelling in vegetation media at 11.2 and 20 GHz. *Electronics Letters*, 31(20), 1783-1785. doi:[10.1049/el:19951215](https://doi.org/10.1049/el:19951215)
- Strickland, R. K., & Goddard, R. E. (1965). Inheritance of branching and crown characteristics in slash pine. Proceedings of the 8th Southern Conference on Forest Tree Improvement (pp. 57-63), Savannah, Georgia. June 16-17.
- Sumida, A., Miyaura, T., & Torii, H. (2013). Relationships of tree height and diameter at breast height revisited: analyses of stem growth using 20-year data of an even-aged *Chamaecyparis obtusa* stand. *Tree Physiology*, 33(1), 106-118. doi:[10.1093/treephys/tps127](https://doi.org/10.1093/treephys/tps127)
- Vanclay, J. K. (1994). Modelling forest growth and yield: applications to mixed tropical forests. CAB International, Wallingford, UK. ISBN: 0-85198-913-6
- Vanclay, J. K. (2009). Tree diameter, height and stocking in even-aged forests. *Annals of Forest Science*, 66(7), 702. doi:[10.1051/forest/2009063](https://doi.org/10.1051/forest/2009063)
- Wang, C-H., & Hann, D. W. (1988). Height-diameter equations for sixteen tree species in the central western Willamette Valley of Oregon. Forest Research Laboratory, Oregon State University, Corvallis. Research Paper: 51.
- Wang, F., & Sarabandi, K. (2005). An enhanced millimeter-wave foliage propagation model. *IEEE Transactions on Antennas and Propagation*, 53(7), 2138-2145.
- Wang, F., & Sarabandi, K. (2007). A physics-based statistical model for wave propagation through foliage. *IEEE Transactions on Antennas and Propagation*, 55(3), 958-968. doi:[10.1109/TAP.2007.891841](https://doi.org/10.1109/TAP.2007.891841)
- Anonymous (2015). Basal Area, A guide for understanding the relationships between pine forests and wildlife habitat. MS Wildlife, Fisheries, & Parks. (Accessed: 20/08/2015) www.mdwfp.com/media/4194/basal_area_guide.pdf
- Anonymous (2019). Randomized branch sampling. AWF-Wiki. (Accessed: 29/10/2019) wiki.awf.forst.uni-goettingen.de/wiki/index.php/Randomized_branch_sampling
- Anonymous (2020a). Silk Birch Tree Branches Elegant Birch 24" Long x42 Leaves | Birch tree leaves, Birch leaf, Plant leaves. (Accessed: 25/03/2021) www.pinterest.com/pin/163044448994027412/
- Anonymous (2020b). Ash Tree Leaves. (Accessed: 24/03/2021) line.17qq.com/articles/ogmcopv.html
- Anonymous (2020c). Longleaf Pine01, Wikimedia Commons. (Accessed: 25/03/2021) commons.wiki-media.org/wiki/File:Longleaf_Pine01.jpg
- Anonymous (2021). Coconut Tree BW, WPclipart. (Accessed: 25/03/2021) wpclipart.com/plants/trees/food_trees/coconut_tree_BW.png.html



Modal Analysis of Horizontal Axis Wind Turbine Rotor Blade with Distinct Configurations under Aerodynamic Loading Cycle

Aniekan Essienubong IKPE^{1*}, Ekom Mike ETUK², Akanu-Ibiam Effiong NDON³

¹University of Benin, Department of Mechanical Engineering, Benin City, PMB 1154, Nigeria

²University of Benin, Department of Production Engineering, Benin City, PMB 1154, Nigeria

³Akwa Ibom State University, Department of Civil Engineering, Mkpato Enin, PMB 1167, Nigeria

Keywords	Abstract
Wind Turbine Rotor Blade Modal Analysis Bending Eigenfrequencies Failure	Q-Blade simulation tool was employed in modal analysis of horizontal axis wind turbine blade with three distinct configurations (with spar, no spar and solid) to determine the configuration with adequate structural integrity under aerodynamic loading conditions. The blade configurations were analysed in four different modes based on the flapwise and edgewise response of the blade to aerodynamic loads/forces, and the corresponding modal eigenfrequencies were evaluated. Bending due to combined effects of flapwise and edgewise modal frequencies on the blade were also evaluated at different rotor blade speeds ranging from 2-8m/s. It was observed that the solid blade configuration had the least modal eigenfrequencies for both flapwise and edgewise response in all the four modes as follows: 22.03 and 62.60 Hz in mode 1, 58.0 and 212.8 Hz in mode 2, 122.6 and 600.6 Hz in mode 3, 194.4 and 1118.9 Hz in mode 4. The rotor blade configuration with No spar had the highest modal eigenfrequencies for both flapwise and edgewise response in all the four modes followed by the blade configuration with spar. Bending of the rotor blade due to combined effects of flapwise and edgewise modal frequencies at the aforementioned blade speeds were also highest in blade configuration with No spar and lowest in the solid blade configuration. The low modal eigenfrequencies and low bending values on the solid blade configuration imply high stiffness and strength but with additional mass, which is why 6000 series aluminium was selected in order to minimize the extra weight.

Cite

Ikpe, A. E., Etuk, E. M., & Ndon, A. E. (2021). Modal Analysis of Horizontal Axis Wind Turbine Rotor Blade with Distinct Configurations under Aerodynamic Loading Cycle. *GU J Sci, Part A*, 8(1), 81-93.

Author ID / (ORCID Number)

A. E. Ikpe, 0000-0001-9069-9676

E. M. Etuk, 0000-0002-1866-9349

A. E. Ndon, 0000-0002-2637-6546

Article Process

Submission Date 10.08.2020

Revision Date 20.12.2020

Accepted Date 04.03.2021

Published Date 29.03.2021

1. INTRODUCTION

Different number of blades is typically used in designing the horizontal axis wind turbines, depending on the purpose of the wind turbine. However, turbines with two or three blades are mostly used for power generation. Therefore, the most common designs of modern wind turbines are based on the horizontal shaft structure (Soriano et al., 2013). Upon approaching the wind turbine, there is a decline in wind speed and increase in wind turbulence. Consequently, rotation of the wind turbine blades result in turbulence, manifesting in the form of rotational vertical wakes (Etuk & Ikpe, 2020a).

The wind axis rotor blades during operation are subjected to structural loading conditions characterized by aerodynamic effects (velocity deficit, pressure differential, flow expansion, rotation of the wake field and increased turbulence) driving the wind/air particles in the atmosphere. The flow field around a wind turbine may be characterized by two major mechanisms such as convection and turbulent diffusion (Vermeer et al., 2003). Generally, wind turbine blades during operation may be subjected to lightning strikes, physical

*Corresponding Author, e-mail: aniekan.ikpe@eng.uniben.edu

impacts and damaging surface erosion conditions particularly in hostile terrains where the wind is accompanied by heavy rainfall (Yasuda et al., 2012; Garolera et al., 2016). Depending on severity of the aerodynamic forces which is a function of wind speed, the turbine rotor blades may be exposed to some degree of vibration which can be classified as forced vibration and resonant vibration. Forced vibration may occur due to external loads, internally generated forces/loads, unbalances and ambient excitation while resonant vibration is majorly caused by natural modes of vibration of the body (Brain & Mark, 1999).

An inherent property of any structure as related to vibration is the natural frequency of the structure. If a given structure vibrates at frequencies higher or closer to its natural frequency, the vibration may be exceptionally high (Ivan et al., 2014). It is therefore necessary to regularly evaluate the natural frequency of high load bearing structures such as the wind turbine blade to avoid unforeseen failure in service condition. The natural frequencies are thus said to be fundamental properties that are not dependent on the choice of coordinates. The mode shapes are often determined by finding the eigenvalues and the eigenvectors of the system. The operating deflection shape is defined as any forced motion of two or more points on the structure while the shape is defined by specifying the motion of two or more points, noting that motion is a vector quantity which signifies that it possesses magnitude and direction (Owunna et al., 2016).

Ikpe et al. (2018) reported that High Cycle Fatigue (HCF) due to repeated cyclic loading on rotor blades in service condition is a major cause of blade failure. Ikpe et al. (2019) employed three finite element solvers such as CATIA 2017 version, ANSYS R15.0 2017 version and HYPERMESH 2016 version in the modelling process of 0.40 mm x 0.40 mm plate. The corresponding mode shapes (Chladni patterns) as well as the modal frequencies were simulated using Finite Element Method (FEM). Result of modal frequency obtained from the experimental analysis agreed with the FEM simulated results, with HYPERMESH generated results being the closest to the experimental values. It was observed that the modal frequencies obtained from the FEM and experimental approach increased as the excitation time increased.

Finite element method (FEM) was employed by Efe-Ononeme et al. (2018) to determine the natural frequency of two turbine blade materials applicable to Trans-amadi power plant in Port Harcourt, Nigeria. Comparing the two gas turbine blade materials, the fundamental frequency under the same load conditions was 751 Hz for IN 738 and 896 Hz for U500 turbine blade material. This implies that the natural frequencies obtained for both materials were much higher than the operational frequency of 85Hz for resonance to occur. Therefore, resonance would be delayed across the blade materials in service condition, indicating that gas turbine blades designed with both materials would be dynamically stable under operational frequency approaching 745 Hz.

Etuk et al. (2020b) investigated the normal, radial, axial and tangential loading cycles undergone by wind turbine rotor blades and their effects on the displacement of the blade structure using QBlade finite element sub module. Geometry of the deformed blades were characterized by twisting and bending configuration at maximum strain deformation at frequencies up to 200 Hz. From the deflection values obtained, it was found that normal loading cycle would cause the highest level of structural damage on the rotor blade followed by radial, axial and tangential loading. To increase the reliability of a wind turbine blade, Mouhsine et al. (2018) developed an airfoil structure to calculate the optimum blade geometry for the procedure. The optimum efficient geometry was complex, consisting of airfoils sections of increasing width, thickness and twist angle towards the hub. At a nominal wind speed of 12 m/s, 0.045 m was obtained as the tip displacement of the blade.

Studies have shown that turbine rotor blades in recent times are manufactured from composite materials because, they satisfy complex design constraints such as light weight and high stiffness while also providing adequate resistance to the static and aerodynamic loads (Bagherpoora & Xuemin, 2017). The failure analysis of two sandwich composite wind turbine rotor blade with 1 and 2.5m length subjected to wind load was carried out by Chen & Kam (2011), through theoretical and experimental approaches. The skin and core of the turbine blade were made of Glass fibre/epoxy composite laminae and PVC foam while the handle at the blade root was made of aluminium alloy. Stresses in the turbine blade were determined through finite element code ANSYS while the skin and the core of the blade were modelled using shell and solid

elements. A phenomenological failure criterion was employed in predicting the first-ply failure strength of the blade. The measured ultimate load of the rotor blade was used to validate the results which was found to be accurate in predicting fairly good ultimate failure load and failure location of 1m long when compared to the experimental results.

Okokpujie et al. (2020) implemented a multi-criteria decision method (MCDM) to select the best material for developing a horizontal wind turbine blade, considering aluminium alloy, stainless steel, glass fibre, and mild steel as alternative materials. Quantitative research approach using AHP and TOPSIS multi-criteria decision method was employed. The result revealed a consistency index of 0.056 and a consistency ratio of 0.062 obtained via the AHP method. 78%, 43%, 67%, and 25% were the performance scores, and aluminium alloy was selected as the best material, followed by glass fibre.

Operational modal analysis to extract the modal parameters before failure and operational modal analysis on the damaged structure of the 6.4 m length turbine blade made of glass fibres combined with epoxy resin was conducted by Marulo et al. (2014). The Experimental results revealed a decrease in the natural frequencies and an increase of the estimated modal damping of the structure. The reduction in natural frequencies was due to decrease in the stiffness of the structure. Results of the operational modal analysis were compared with numerical ones and correlation was found between them. Hence, it was concluded that structural integrity of a structure can be monitored by using modal parameters, like natural frequencies, damping characteristics and mode shapes.

Pedersen & Kristensen (2003) compared the results from two experiments, i.e. frequency, damping and the mode shapes. The orientation of the blade some effects on the measured results obtained by modal analysis. There were variations in the measured frequency up to 1.6% at 1 edgewise and 3 flapwise natural frequencies. The damping results had variations up to 56%, at 3 flapwise natural frequency. The uncertainty on the damping was due to smaller quantities of the damping characteristics.

A comparative study was conducted by Taware et al. (2016), using Glass Fibre Reinforced Plastic (GFRP) blade and GFRP blade with steel wire mesh to determine the natural frequencies and deformation of mode shape. It was observed that natural frequencies for the first three modes of the GFRP blade with steel mesh increased by 2-3% more than only the GFRP blade. Also, the mode shapes for the first three modes indicated that there was less variation in deformation of the GFRP blade than the GFRP blade with steel wire mesh. The obtained natural frequencies gave the resonant condition frequencies for both blades.

In this study, modal analysis of horizontal axis wind rotor blade with distinct configurations was carried to determine the structural integrity of each blade configuration under aerodynamic loading conditions.

2. MATERIAL AND METHOD

Wind turbine blades are composed of two faces (the suction face and the pressure face), bound together and stiffened either by one or more integral (shear) webs connecting the upper and lower section of the blade shell or by a box beam (box spar with shell fairings) (Brøndsted & Nijssen, 2013). The shells are adhesively joined together to the spars. The flapwise load is as a result of the wind pressure while the edgewise load is due to gravitational forces and torque load acting on the blade. The flapwise bending is resisted by the spar, internal webs or spar inside the blade, while the edges of the profile carry the edgewise bending. From the loading points on material, one of the main laminates in the main spar is subjected to cyclic tension-tension loads (pressure side) while the other (suction side) is subjected to cyclic compression-compression loads. The laminates at the leading and trailing edges that carry the bending moments related to the gravitation loads are subjected to tension-compression loads (Mishnaevsky et al., 2017). Figure 1 represents detailed illustration of the rotor blade section. QBlade is a Blade Element Moment Method (BEM), Double Multiple Streamtube (DMS) and nonlinear lifting line theory (LLT) design and simulation software for vertical and horizontal axis wind turbine. QBlade incorporates a number of tools such as QFEM to setup and simulate the internal blade structure and perform structural blade design, modal analysis, static deflection as well as stress analysis.

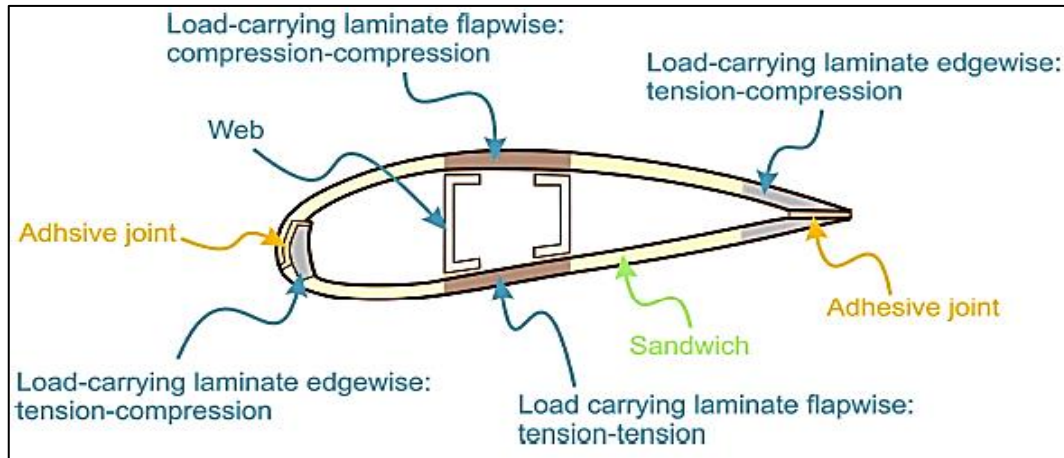


Figure 1. Illustration of the Rotor Blade Section

In this study, QBlade v0.8 was employed in the modal analysis of different blade configurations using the isotropic tapered Euler Beam elements in order to evaluate the modal eigenfrequencies and associated bending effects to determine the most suitable blade configuration that can withstand structural failure due to aerodynamic loads/forces from the wind and the bending stresses resulting thereof. The respective chord lengths and angle of twist of each section is shown in Figure 2. The total length of the blade was 2.2 m, total number of sections was 15 while the number of blades employed in the simulation process was 3. The blade was divided into 15 sections. The first three sections had the circular foil applied at the blade section while the remaining 12 sections had NACA 4610 airfoil applied on them. The blade geometry/root coordinates is presented in Figure 2.

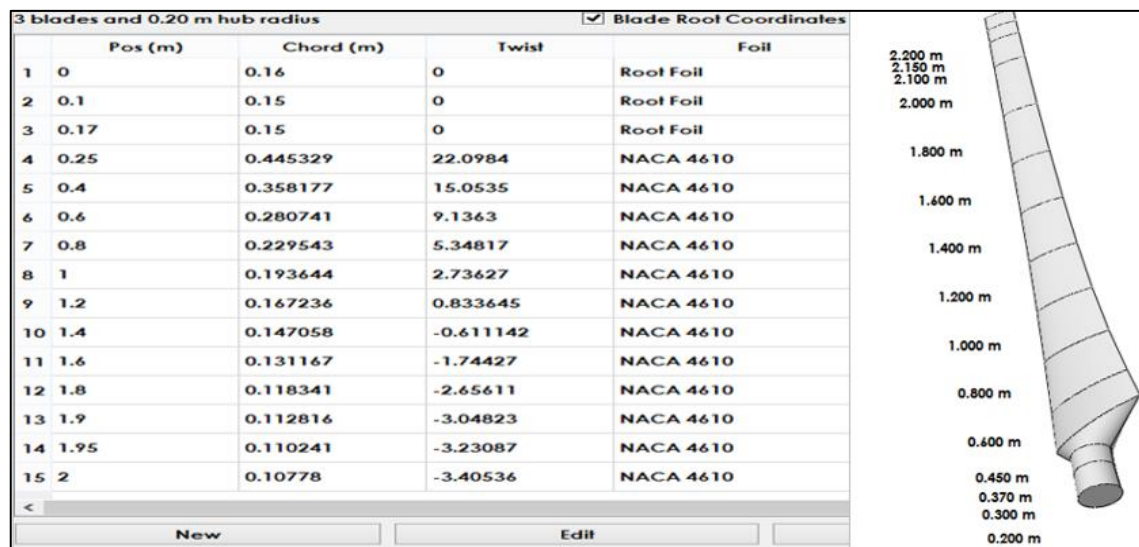


Figure 2. Blade Geometry/Root Coordinates

Loading data was imported from a previously simulated turbine that uses the same rotor. In the structural blade design module, a simple structural model was defined for the rotor blade inside the Structural Blade Design/Modal Analysis tab. The model was defined and simulated using isotropic material properties only. After defining the structural model, sectional blade properties were computed and a modal analysis had been performed. The resulting mode shapes and frequencies were visualized and changed from the dock window. At this stage, the structural properties can be plotted in graphs, by changing to Graph View in the toolbar. This study was carried out using three horizontal wind turbine blade configurations such as hollow with spar, hollow without spar and the solid configuration. Properties of the rotor blade analyzed in this study are presented in Table 1. Longer blades are prone to high deflections, making structural stiffness (to ensure tip clearance, i.e., to avoid the blade from hitting the tower) a significant factor in the blade design, but stiffness-to-weight ratio is of major importance from the material perspective (Ikpe et al., 2016a,

2016b). The various frequency eigenmodes are to determine structural integrity of the rotor blade under aerodynamic loading conditions. The three blade configurations employed in this study are presented in Figure 3.

Table 1. Material Properties of the 6000 Series Aluminium Rotor Blade

Properties	Shell Material specifications	Internal Material specifications
	6000 Series Aluminium	Polyurethane 20GF 6SD
Density (kg/m^3)	2740	1360
Elastic Modulus (MPa)	7e+04	1.72e+03
Mass (kg)	Hollow with Spar: 13.2465 Hollow no Spar: 12.1003 solid: 31.535	
Section No.	Rotational Speed	119(1/min)
	Shell Thickness (m)	Spar Thickness (m)
1	0.00320	0.01280
2	0.0030	0.01200
3	0.0030	0.01200
4	0.00961	0.03844
5	0.00773	0.03092
6	0.00606	0.02423
7	0.00495	0.01981
8	0.00418	0.01671
9	0.00361	0.01444
10	0.00317	0.01269
11	0.00283	0.01132
12	0.00255	0.01021
13	0.00243	0.00974
14	0.00238	0.00952
15	0.00233	0.00930

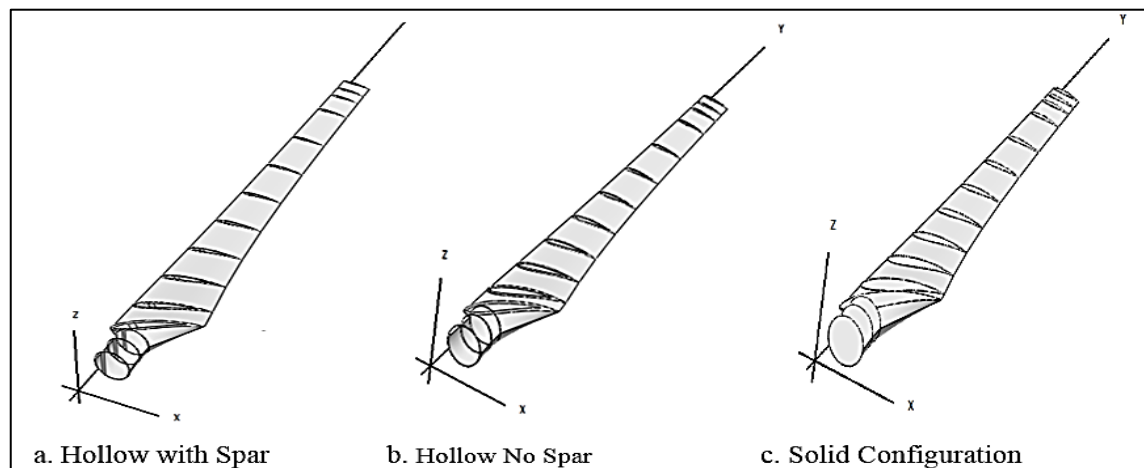


Figure 3. The Three Blade Configurations Employed in This Study

Figure 3 represents typical rotor blade configurations for horizontal wind turbine application. It can be observed in the above rotor blade configurations that some of the blades are configured with a hollow pattern reinforced with spar (see Figure 3a), some of them are configured with just a hollow pattern with no spar (see Figure 3b) while some of them are configured without spar and hollow pattern (see Figure 3c). The hollow pattern is simply a configuration in which a center hole or trench is made at the mid-section of the blade. This is sometimes applicable to high density rotor blades where the mid-section are made hollow

in order to reduce the blade density. In such case, the trench can extend fully or partially along the blade length (i.e., span-wise direction).

The term “spar” is a beam-like structural member that supports the ribs in an airfoil, aircraft wing or wind rotor blades, and running span-wise at right angles to the blade leading edge. In other words, spars which serves as a reinforcing members of a wind turbine rotor blade increases the structural strength and stiffness of the blade to prevent tower strikes in the event of sudden wind gusts, forms the structural framework upon which reduction in axial fatigue, improvement of compressive strain, buckling resistance as well as resistance to gravitational and aerodynamic loads are well assured. Spars are usually “L or T” shaped member installed within the hollow section of the rotor blade. It consist of upper and lower members known as spar caps and vertical sheet members known as shear webs which spans the distance between the spar caps of which the spar caps are welded or riveted to the top and bottom of the vertical member to prevent buckling.

The third rotor blade configuration as shown in Figure 3c is the solid configuration which neither has spars nor hole in the mid-section of the blade. The solid blade in this case is densely rigid with no internal holds, solid in cross section with both interior and exterior part uniformly filled with the same material. Like every other rotor blades, the leading and trailing edges are properly streamlined to meet aerodynamic specifications for wind turbine rotor blades.

3. RESULTS AND DISCUSSION

When the direction of wind flows along a cambered airfoil/wind rotor blade which has some degree of curvature, the wind velocity and acceleration continues to change along the blade radius, producing aerodynamic forces that acts on the blade as the wind speed changes. Different force components were observed at different sections of the curved blade. One of the force components is normal to the tangent or towards the center of curvature of the rotor blade. This component is known as normal force which is acting at that point. Normal loading or forces are those forces acting perpendicularly to the direction of motion. In other words, normal component of force does not change the magnitude of the flow velocity but changes the direction of velocity at that point. Values obtained for normal loads and tangential loads acting along the turbine rotor blade sections at wind speeds ranging from 2-8 m/s are presented in Table 2.

Table 2. Normal and Tangential Loads Along Blade Sections at Different Wind Speeds

Blade Radius (m)	Normal Loading at different Wind speeds				Tangential Loading at different Wind speeds			
	2m/s	4m/s	6m/s	8m/s	2m/s	4m/s	6m/s	8m/s
0.00	0.44	1.30	2.66	4.53	-0.86	-1.43	-2.29	-3.40
0.10	0.62	1.71	3.39	5.68	-1.32	-1.88	-2.70	-3.74
0.17	1.16	2.79	4.44	6.84	-1.94	-2.17	-3.11	-4.42
0.25	1.06	8.47	19.14	32.19	-0.33	2.83	9.02	19.57
0.40	2.00	11.90	26.39	42.93	0.35	3.92	11.99	24.72
0.60	3.69	15.98	32.56	44.06	0.41	3.91	12.55	20.39
0.80	5.69	20.43	38.45	42.61	0.34	3.78	12.70	14.48
1.00	8.25	25.21	44.27	43.99	0.21	3.63	12.58	12.14
1.20	11.58	30.23	49.97	48.10	0.06	3.50	12.33	12.18
1.40	15.34	35.13	55.28	53.77	-0.10	3.36	11.96	13.31
1.60	19.59	40.02	60.00	61.05	-0.29	3.19	11.23	14.90
1.80	23.56	43.54	62.57	68.41	-0.45	2.87	9.82	15.61
1.90	24.75	41.92	58.32	67.77	-0.43	2.43	7.42	13.97
1.95	26.61	33.83	47.75	57.61	-0.32	1.93	5.42	10.76
2.20	8.47	18.15	26.76	32.56	0.17	1.12	2.95	5.49

The other component of force is in the direction tangential to the blade at a given point. This component is known as the tangential force acting at that point. Tangential loading or forces are those forces acting along the direction of motion. In other words, the said tangential force does not change the direction of motion but changes the velocity magnitude. Values obtained for tangential loads/forces acting along the turbine rotor blade sections at different wind speeds are presented in Table 2. Table 3 indicates radial and axial loads/forces acting along the blade sections at different wind speeds. Etuk et al. (2020b) classified the loading conditions as normal load due to vibration of the rotor blade, axial load due to wake losses, tangential load or point load on different sections of the blade due to wind direction and radial load due to cyclic motion of the blade within the wind field domain. Table 2 and 3 indicates that the loading cycles increase as the blade radius increases. This is because the trailing edge of the blade towards the tip becomes slender and more streamlined against drag and wake forces. This in turn serves as advantage to the rotor which then rotates with increased speed, but at higher loading cycle in attempt to overcome the associated aerodynamic loads in the wind field domain.

Table 3. Normal and Tangential Loading Along Blade Sections at Different Wind Speeds

Blade Radius (m)	Radial Loading at different Wind speeds				Axial Loading at different Wind speeds			
	2m/s	4m/s	6m/s	8m/s	2m/s	4m/s	6m/s	8m/s
0.00	0.40	1.24	2.31	3.34	-0.62	-1.34	-2.03	-3.24
0.10	0.56	1.62	3.02	4.28	-1.14	-1.63	-2.30	-3.42
0.17	1.12	2.50	3.54	5.72	-1.53	-2.02	-2.58	-4.26
0.25	1.04	7.45	17.17	26.16	-0.28	2.19	7.21	17.73
0.40	1.08	10.52	24.28	37.42	0.30	2.29	9.32	22.12
0.60	2.46	13.18	28.16	40.26	0.38	2.41	11.15	18.36
0.80	4.52	18.47	33.35	38.61	0.28	2.56	11.34	13.85
1.00	6.25	23.30	38.37	39.99	0.19	2.64	11.50	12.10
1.20	8.53	28.24	42.63	44.80	0.03	2.58	11.16	12.15
1.40	12.24	31.12	48.18	47.27	-0.07	3.22	10.52	13.02
1.60	15.45	34.06	54.40	53.62	-0.24	3.03	10.19	14.20
1.80	17.61	39.14	57.62	58.54	-0.41	2.52	8.12	13.61
1.90	20.87	35.92	61.26	62.31	-0.39	2.24	6.75	11.97
1.95	23.36	29.72	40.27	52.11	-0.28	1.64	3.52	8.76
2.00	6.84	16.08	23.40	47.58	0.14	1.06	2.10	3.49

3.1. Modal Analysis Results

Result obtained for the modal analysis is a representation of how the blade will response to aerodynamic loads (see Table 2 and 3) in the flapwise and edgewise direction. Flapwise response of the rotor blade shows the blade response along the z-axis or deflection of the blade towards the blade flap, which is at the surface along the trailing edge. However, edgewise response of the rotor blade indicates response along the x-axis or deflection towards the edges of the rotor blade. In other words, aerodynamic forces/loads are parallel to the rotor edges for the edgewise deflection and perpendicular to the local chord or rotor plane for the flapwise deflection. eigenfrequency also known as natural frequency is a certain discrete frequency at which the rotor blade tends to vibrate (Bhatt, 2009). When vibrating at certain eigenfrequency, the rotor blade deforms into a corresponding shape known as eigenmodes. According to Larsen et al. (2002), modes are inherent properties of a given structure, and are determined by the properties of the material (density, stiffness, and damping behaviour) and boundary conditions of such structure. Each mode is characterized mainly by natural frequency, modal damping and mode shapes also known as modal parameters. As shown in Figure 4a-7a, eigenfrequency analysis only provides the shape of the mode not the amplitude of any physical vibration of the rotor blade (Higham et al., 2008). Figure 4b-7b represents the plots for flapwise eigenfrequency and edgewise eigenfrequency for the three (3) blade configuration considered in this study.

The solid blade has the lowest eigenfrequency values of 22.03 Hz at flapwise direction and 62.60 Hz at edgewise direction for mode 1, compared to the hollow blade configuration with no spar which has the highest eigenfrequency values followed by hollow blade configuration with spar. Deformation of modal shape in mode 1 is barely observed for flapwise deflection and observed at the mid-span of the blade for edgewise deflection, causing slight bending on the mode shape as shown in Figure 4a.

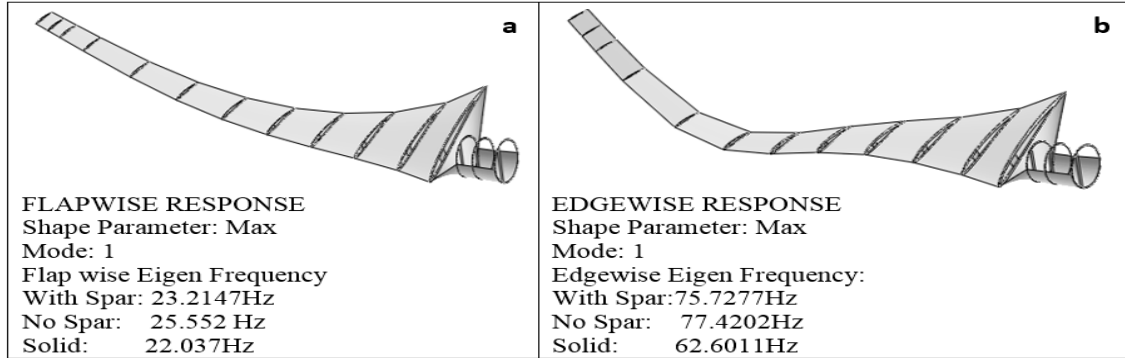


Figure 4a. Flapwise and Edgewise Response of Rotor Blade Modal Shape 1

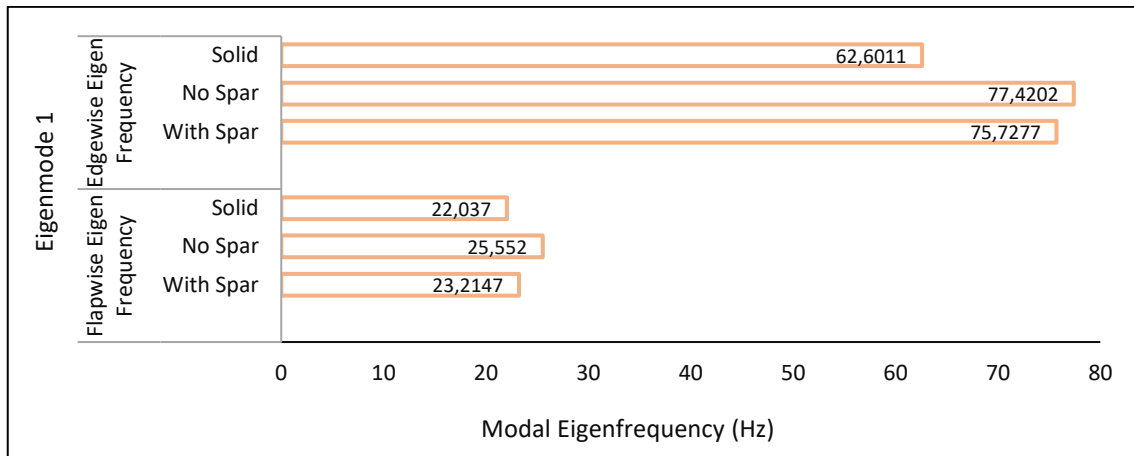


Figure 4b. Corresponding Modal Eigenfrequencies for Modal Shape 1

Similarly in mode 2, the solid blade has the lowest eigenfrequency value of 58.0 Hz at flapwise direction and 212.8 Hz at edgewise direction compared to the hollow blade configuration with no spar which has the highest eigenfrequency values followed by hollow blade configuration with spar. The blade response to aerodynamic loads (see Table 2 and 3) in mode 2 is observed at the mid-span of the blade for the flapwise deflection and observed to extend from the mid-span of the blade to the blade for the edgewise deflection, causing significant bending on the mode shape as shown in Figure 5a.

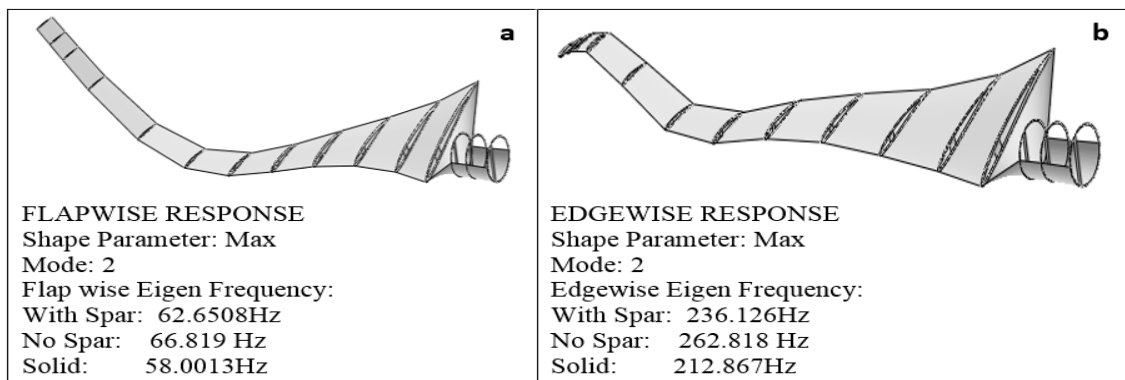


Figure 5a. Flapwise and Edgewise Response of Rotor Blade Modal Shape 2

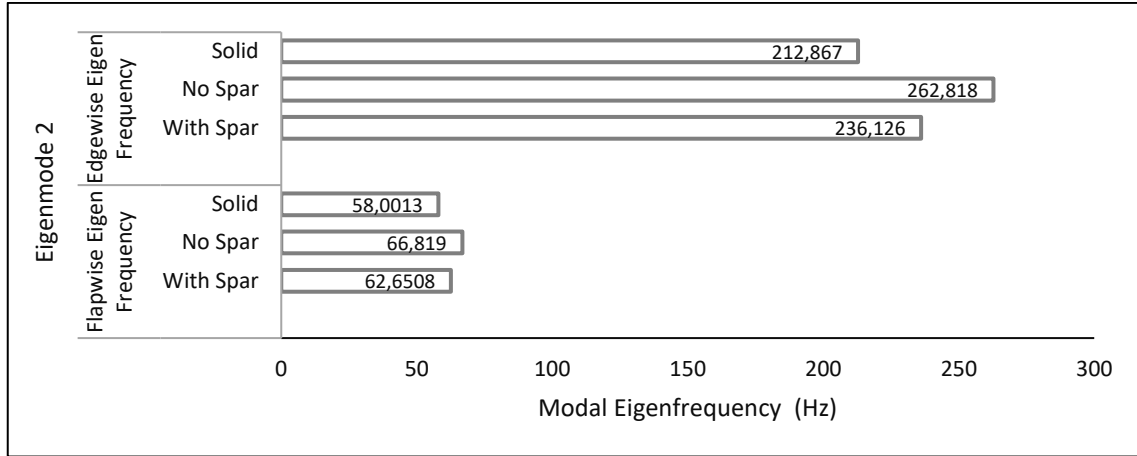


Figure 5b. Corresponding Modal Eigenfrequencies for Modal Shape 2

In mode 3, the solid blade has the lowest eigenfrequency values of 122.6 Hz at flapwise direction and 600.6 Hz at edgewise direction compared to the hollow blade configuration with no spar which has the highest eigenfrequency values followed by hollow blade configuration with spar. The blade response to aerodynamic loads (see Table 2 and 3) in mode 3 is observed to extend from the mid-span of the blade to the trailing edge for the flapwise deflection and observed to extend from the mid-span of the blade to the blade tip and slightly to the blade leading edge for edgewise deflection, causing significant deformation and distortion on the blade modal shape as shown in Figure 6a.

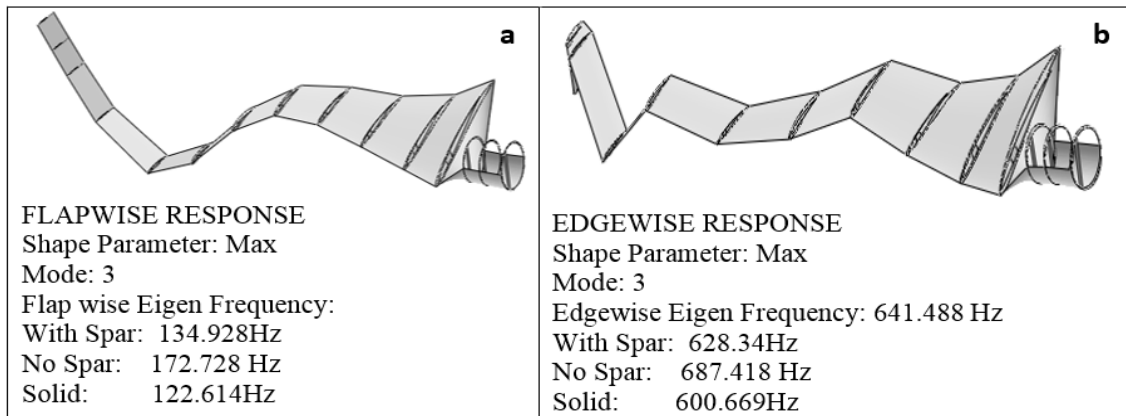


Figure 6a. Flapwise and Edgewise Response of Rotor Blade Modal Shape 3

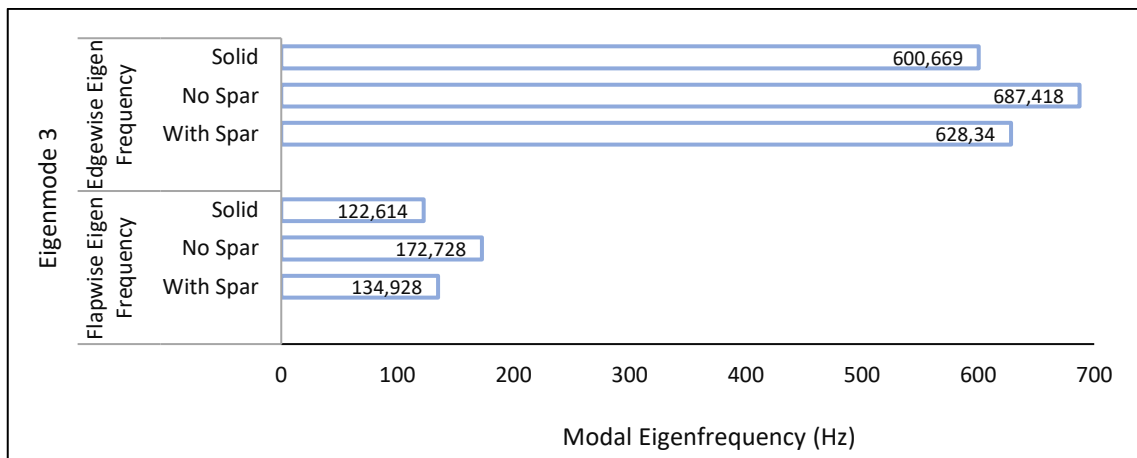


Figure 6b. Corresponding Modal Eigenfrequencies for Modal Shape 3

Finally in mode 4, solid blade configuration also has the lowest eigenfrequency values of 194.4 Hz at flapwise direction and 1118.9 Hz at edgewise direction compared to the hollow blade configuration with

no spar which has the highest eigenfrequency values followed by hollow blade configuration with spar. The blade response to aerodynamic loads (see Table 2 and 3) in mode 4 caused damage from the mid-span, across the trailing edge of the blade and towards the blade tip for flapwise response. The blade was observed to deflect towards the tip. For edgewise response, the aerodynamic loads were observed to affect the entire blade except for some parts between the leading edge and the blade root, causing significant deformation and distortion on the blade characterised by twisting modal shape as shown in Figure 7a.

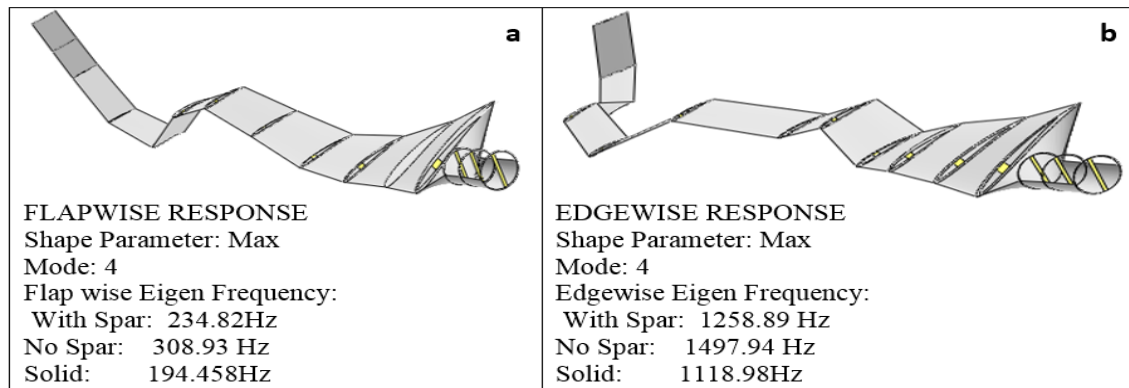


Figure 7a. Flapwise and Edgewise Response of Rotor Blade Modal Shape 4

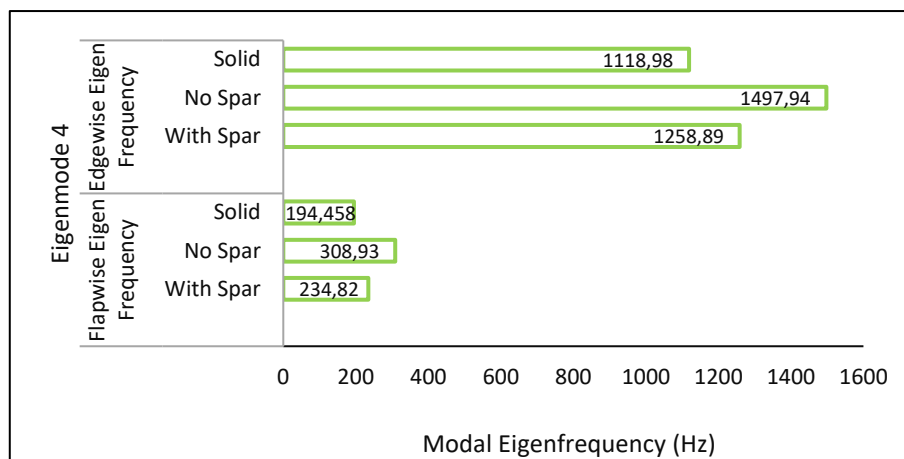


Figure 7b. Corresponding Modal Eigenfrequencies for Modal Shape 4

Figure 8-11 represents bending on the turbine rotor blade for different eigenmodes ranging from 1-4 at various wind speeds ranging from 2-8m/s. The bending values plotted for each eigenmodes indicate that the eigenmodes are characterised by different modal frequencies and rotational speeds resulting in bending effects of the blade. The bending effect is as a result of natural frequencies at each revolution speed of the blade which is at increasing order. Modal analysis carried out by Chaudhari (2014) on horizontal wind turbine blade at rotational speeds of 5 and 10m/min revealed that natural frequency of the turbine blade increases as the rotor speed also increase. On the other hand, Tartibu et al. (2012) in their investigation found that the blade natural frequency increased as the eigenmodes progressed. It can be observed in Figures 8-11 that bending due to the combined effects of natural frequency or modal eigenfrequency at the flapwise and edgewise direction of the rotor blade increased correspondingly with increase in the eigenmodes and rotor blade speeds. This in turn resulted in the bending effects on the blade which increased gradually as the rotor speeds and its eigenmodes increased. It should be noted that each mode is defined by a natural (modal or resonant) frequency, modal damping and a mode shape. As represented on each plot in Figures 8-11, the highest bending effect on each configuration of the blade at various rotor speeds (2, 4, 6 and 8m/s) considered in the analysis is observed on the rotor blade configuration with no spar. This is followed by the rotor blade configuration with spar while the lowest bending effects on the blade configurations at various rotor speeds considered in the analysis is observed on the solid blade configurations. There is no standard to determine if the bending values will have deleterious effects that may result in failure of the wind turbine blade. However, judging from the bending values which are all less than one (1), the blade may not

obviously fail during operation. Aerodynamic loads/forces exerted by the wind on turbine rotor blades depend on blade configurations which in turn influences the blade aerodynamics. Large deflections on the blade can result in bending stresses and cause significant vibrations which consequently reduce clearance between the turbine shaft and the blade. However, with blades having the capacity to bend to some extent, advantage can be drawn from aerodynamic effects such that, the wind that gets slide over the blade results at increased area of contact, thereby, exerting more force on the blade for effective rotation and power recovery.

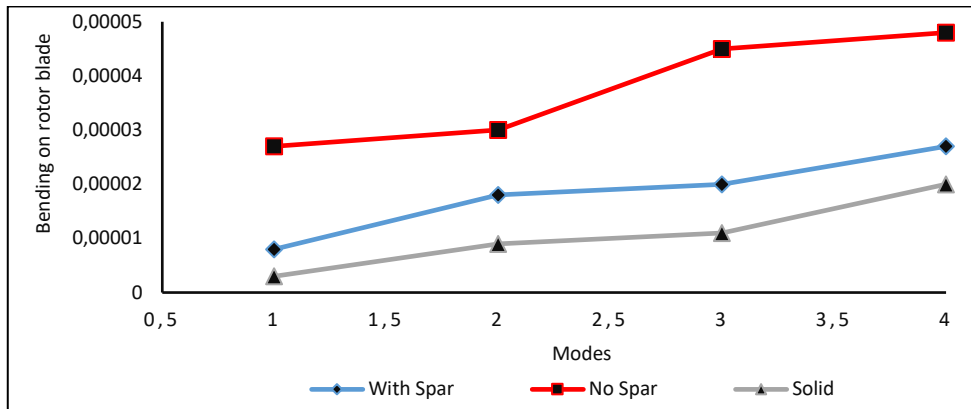


Figure 8. Bending on Rotor Blade for Different Mode Cycles at Rotation Speed of 2m/s

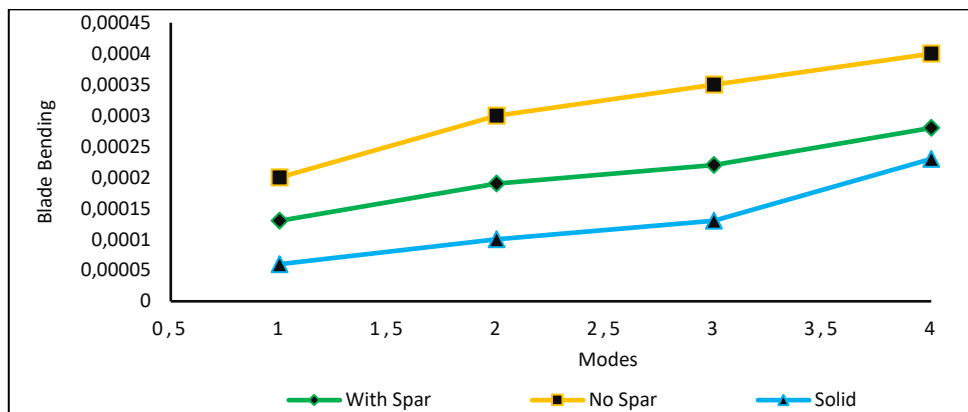


Figure 9. Bending on Rotor Blade for Different Mode Cycles at Rotation Speed of 4m/s

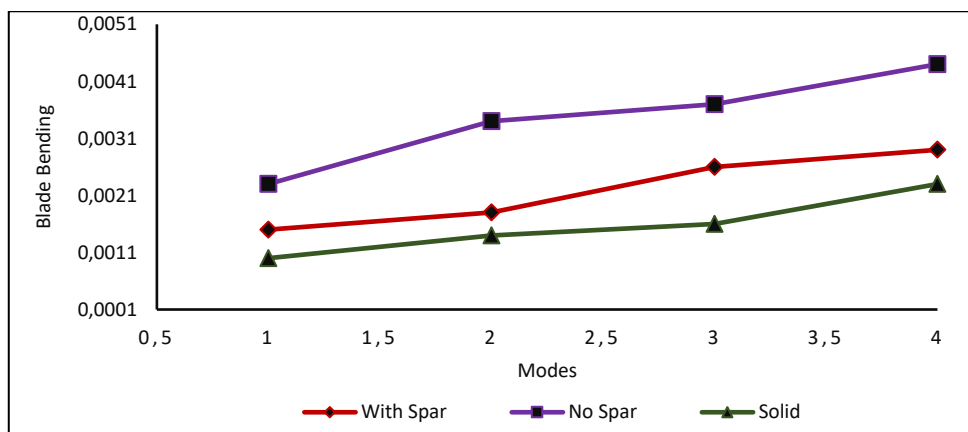


Figure 10. Bending on Rotor Blade for Different Mode Cycles at Rotation Speed of 6m/s

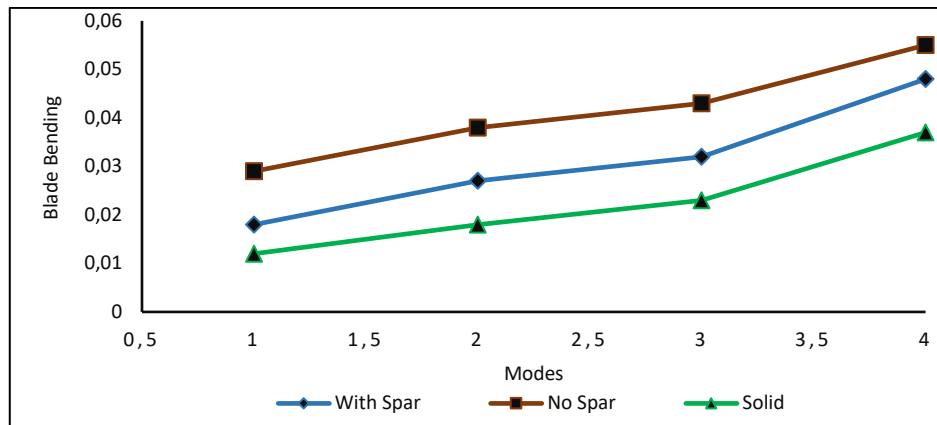


Figure 11. Bending on Rotor Blade for Different Mode Cycles at Rotation Speed of 8m/s

4. CONCLUSION

In this study, modal analysis was successfully carried out on horizontal axis wind turbine blade with distinct configurations under aerodynamic loading cycle. The results reveal that the aluminium solid blade is more preferred due to lower eigenvalues which offers advantage against bending stress at all rotor blade speeds as can be seen from the above analysis. The solid blade incurs additional weight but it is easy to model to specification using simple forming techniques. In actual case scenario, the additional weight can be minimized by selecting lightweight materials like the 6000 series aluminium employed in this study. Thus, for longevity and resistance against aerodynamic loads acting on wind turbine blades in duty cycle, the solid blade configuration is acclaimed to be more suitable particularly in areas with very high wind speeds.

CONFLICT OF INTEREST

There is no conflict of interest associated with the publication of this paper.

REFERENCES

- Bagherpoora, T., & Xuemin, L. (2017). Structural Optimization Design of 2MW Composite wind turbine blade. *Energy Procedia* 105, 1226-1233.
- Bhatt, P. (2009). *Maximum Marks Maximum Knowledge in Physics Class X*, Second Edition. Allied Publishers Private Limited, New Delhi, ISBN: 978-81-8424-444-1.
- Brain, J. S., & Mark, H. R. (1999) *Experimental Modal Analysis*. Vibration Technology Inc, Jamestown, California, 95327.
- Brøndsted, P., & Nijssen, R. (2013). *Advances in Wind Turbine Blade Design and Materials*. Woodhead Publishing, Oxford, UK, pp. 484.
- Chaudhari, N. B. (2014). Dynamic Characteristics of Wind Turbine Blade. *International Journal of Engineering Research and Technology*, 3(8), 1-6.
- Chen, C. P., & Kam, T. Y. (2011). Failure Analysis of Small Composite Sandwich Turbine Blade Subjected to Extreme Wind Load. *Procedia Engineering*, 14, 1973-1981.
- Efe-Ononeme, O. E., Ikpe, A. E., & Ariavie, G. O. (2018). Modal Analysis of Conventional Gas Turbine Blade Materials (UDIMET 500 and IN738) For Industrial Applications. *Journal of Engineering Technology and Applied Sciences*, 3(2), 119-133.
- Etuk, E. M., & Ikpe, A. E. (2020a). 3D Modelling of the Wind Flow Trajectories and Its Characteristic Effects on Horizontal Axis Wind Turbine at Different Wind Regimes. *Journal of International Environmental Application and Science*, 15(2), 68-80.
- Etuk, E. M., Ikpe, A. E., & Adoh, U. A. (2020b). Design and Analysis of Displacement Models for Modular Horizontal Wind Turbine Blade Structure. *Nigerian Journal of Technology*, 39(1), 121-130.

- Garolera, A. C., Madsen, S. F., Nissim, M., Myers, J. D., & Holboell, J. (2016). Lightning Damage to Wind Turbine Blades from Wind Farms in the US. *IEEE Transactions on Power Delivery*, 31(3), 1043-1049.
- Higham, N. J., Mackey, D. S., Tisseur, F., & Garvey, S. D. (2008). Scaling, Sensitivity and Stability in the Numerical Solution of Quadratic Eigenvalue Problems. *International Journal for Numerical Methods in Engineering*, 73, 344-360.
- Ikpe, A. E., Owunna, I., Ebunilo, P. O., & Ikpe, E. (2016a). Material Selection for High Pressure (HP) Compressor Blade of an Aircraft Engine. *International Journal of Advanced Materials Research*, 2(4), 59-65.
- Ikpe, A. E., Owunna, I., Ebunilo, P. O., & Ikpe, E. (2016b). Material Selection for High Pressure (HP) Turbine Blade of Conventional Turbojet Engines. *American Journal of Mechanical and Industrial Engineering*, 1(1), 1-9.
- Ikpe, A. E., Efe-Ononeme O. E., & Ariavie, G. O. (2018). Thermo-Structural Analysis of First Stage Gas Turbine Rotor Blade Materials for Optimum Service Performance. *International Journal of Engineering and Applied Sciences*, 10(2), 118-130.
- Ikpe, A. E., Ndon, A. E., & Etuk, E. M. (2019). Response Variation of Chladni Patterns on Vibrating Elastic Plate under Electro-Mechanical Oscillation. *Nigerian Journal of Technology*, 38(3), 540-548.
- Ivan, B., Marco, A., & Mathias, L. (2014). Physically and Geometrically Non-linear Vibrations of Thin Rectangular Plates. *International Journal of Non-Linear Mechanics* 58, 30-40.
- Larsen, G. C., Hansen, M. H., Baumgart, A., & Carlen, I. (2002). *Modal Analysis of Wind Turbine Blades*. Denmark, Forsknings center Risoe, Risoe-R, 1181, ISBN: 87-550-2697-4.
- Marulo, F., Petrone, G., Alessandro, V. D., & Lorenzo, E. D. (2014). Operational modal analysis on a wind turbine blade. *Proceedings of ISMA2014 and USD2014*, 783-798.
- Mishnaevsky, L., Branner, K., Petersen, H. N., Beauson, J., McGugan, M., & Sørensen, B. F. (2017). Materials for Wind Turbine Blades: An Overview. *Materials*, 10(1285), 1-24.
- Mouhsine, S. E., Oukassou, K., Ichenial, M. M., Kharbouch, B., & Hajraoui, A. (2018). Aerodynamics and Structural Analysis of Wind Turbine Blade. *Procedia Manufacturing*, 22, 747-756.
- Okokpuije, I. P., Okonkwo, U. C., Bolu, C. A., Ohunakin, O. S., Agboola, M. G., & Atayero, A. A. (2020). Implementation of multi-criteria decision method for selection of suitable material for development of horizontal wind turbine blade for sustainable energy generation. *Heliyon*, 6, e03142.
- Owunna, I., Ikpe, A. E., Satope, P., & Ikpe E. E. (2016). Experimental Modal Analysis of a Flat Plate Subjected to Vibration. *American Journal of Engineering Research*, 5(6), 30-37.
- Pedersen, H. B., & Kristensen, O. J. D. (2003). Applied modal analysis of wind turbine blades: Modal analysis on loaded and unloaded blade, Denmark. Forsknings center Risoe, Risoe-R, 1388(7), 41-46.
- Tartibu, L. K., Kilfoil, M., & Vandermerwe, A. J. (2012). Vibration Analysis of a Variable Length Blade Wind Turbine. *International Journal of Advances in Engineering and Technology*, 4(1), 630-639.
- Taware, G. B., Mankar, S. H., Ghagare, V. B., Bharambe, G. P., & Kale, S. A. (2016). Vibration Analysis of a Small Wind Turbine Blade. *International Journal of Engineering and Technology*, 8(5), 2121-2126.
- Soriano, L. A., Yu, W., & Rubio, J. J. (2013). Modelling and Control of Wind Turbine. *Mathematical Problems in Engineering*, 982597, 1-13.
- Vermeer, L., Sorensen, J., & Crespo, A. (2003). Wind Turbine Wake Aerodynamics. *Progress in Aerospace Sciences*, 39, 467-510.
- Yasuda, Y., Yokoyama, S., Minowa, M., & Satoh, T. (2012). Classification of Lightning Damage to Wind Turbine Blades. *IEEE J. Trans*, 7, 559-566.



Modelling and Validation of The Production Parameters of Unalloyed Aluminium Sheets

Dickson David OLODU^{1*}

¹Department of Mechanical Engineering, Faculty of Engineering, Benson Idahosa University, PMB 1100, Benin City, Edo State, Nigeria

Keywords	Abstract
Mechanical Properties Modelling Process Parameters Unalloyed Aluminium Validation of Model	Modelling of process parameters and its validation in Aluminium production industries poses great challenges in the production of Aluminium sheets in Aluminium Manufacturing companies. This research therefore focused on the modelling and validation of production parameters of unalloyed Aluminium sheets in Aluminium manufacturing industries. The process parameters investigated were temperature (T), pressure (P) and percentage by volume of Aluminium (A_p) used. The effects of these process parameters on the mechanical properties of the developed unalloyed Aluminium sheets were modelled to ease Aluminium manufacturing processes in Aluminium industries. From the plots obtained, it was observed that the optimal tensile strength, young modulus of elasticity, shear modulus and Brinell hardness number were 621MPa, 69GPa, 25.5GPa, and 61 at temperature of 1921°C, 1610°C, 1442°C and 1800°C respectively. In comparison with pressure, the obtained values for optimal tensile strength, young modulus of elasticity, shear modulus and Brinell Hardness Number were 562MPa, 68GPa, 26.2GPa and 61 at pressure of 72GPa, 69.5GPa, 69.5GPa and 69.5GPa respectively. Moreover, empirical Models were also developed for predicting the mechanical properties such as tensile strength, young modulus of elasticity, shear modulus and hardness for the produced unalloyed Aluminium sheets. The models were validated using coefficient of determination (R^2) and mean absolute percentage error (MAPE). The coefficient of determination (R^2) obtained ranges from 0.9213 (92.13%) to 0.9911 (99.11%) which indicates that a substantial good fit was achieved by the regression models developed. The mean absolute percentage error of the developed models also ranges from 0.46% to 3.38% which was below 10% recommended. The values obtained from the validation of these models were therefore found to be satisfactory, and shows good predictability of the model and its adequacy. Finally, the results obtained show that temperature and pressure had great effects on the mechanical properties of the produced unalloyed Aluminium sheets.

Cite

Olodu D. D., (2021). Modelling and Validation of The Production Parameters of Unalloyed Aluminium Sheets. *GU J Sci, Part A*, 8(1), 94-108.

Author ID (ORCID Number)

Dickson David Olodu, 0000-0003-3383-2543

Article Process

Submission Date	22.10.2020
Revision Date	31.12.2020
Accepted Date	11.03.2021
Published Date	29.03.2021

1. INTRODUCTION

The research and development of new materials together with its design is the engine that drives economic progress. That is to say, today, technology depends greatly on scientific research of materials, and this contributes to economic growth of any nation. Moreover, there are inadequate empirical and interactive models to predict mechanical properties and determine the interaction of some process variables of the manufacturing processes in Aluminium production industries. This had resulted to most failure in the manufacture of these materials as a roofing material and other engineering applications. The utilization of process control and process monitoring are rarely fully implemented for the production of Aluminium sheets. This may be due to a poor scientific understanding of the manufacturing processes based on the

complexities of the process containing multiple variables affecting the final products (Olodu and Osarenmwinda, 2018).

Kok (2005) examined the mechanical properties of Al_2O_3 particle reinforced 2024 Al alloy composites produced through vortex method. It was noted that optimum conditions of the production process were 700°C for pouring temperature, 550°C for preheated mold temperature, 900 rev/min for stirring speed, 5 g/min for particle addition rate, 1 min for stirring time and 6MPa for applied pressure respectively. Kumar et al. (2013) stated that the hardness and tensile strength of A359/ Al_2O_3 MMC increases as temperature increased. In their study, it was also observed that electromagnetic stirring action adopted during the fabrication resulted in smaller grain size and good particulate matrix interface bonding. Venkatesh and Harish (2015) examined Al/SiC composites produced through the powder metallurgy route to achieve the desired properties and also to improve the mechanical properties of Aluminium. According to Nieh and Chellman (1984); Friend (1987), they observed that reinforcement of aluminium improves its strength, fatigue, modulus, wear resistance and creep. Studies on trimodal aluminium metal matrix composites and the factors affecting their strength were reported by Yao et al. (2010), they noted that among these factors, tensile strength was the most convenient and widely quoted measurement which is of central importance in many applications. Saravanan et al. (2015) observed that there is an increase of 30% in hardness and an increase in tensile strength that is almost twice that of base aluminum alloy for TiB_2 particulate reinforced composites. The influence of stirring speed and stirring time on the distribution of particles in SiC AMC has been analyzed by Prabu et al. (2006). Nieh et al. (1985) also observed that in the early stages of processing a non-uniform distribution of reinforcement, which persists to the final product in the forms of streaks or clusters of reinforcement with their attendant porosity all of which lowered the strength, ductility, and toughness of the Aluminium material. Furthermore, for a given matrix alloy, the elongation to failure is reduced by increasing volume fraction (Crowe et al., 1985). Rozovsky et al. (1973) reported that the compression of a short cylinder between anvils is a much better test for metal working applications. The deformation behavior of solid cylinders of an aluminum alloy metal matrix composite under dry condition was estimated by Joardar et al. (2012). Orbulov and Ginzler (2012) observed that engineering factors such as the aspect ratio (height/diameter ratio) of the specimens and the temperature of the tests have significant effect on the compressive strength and properties of Aluminium. The effect of reinforcing particle shape and interface strength on the deformation and fracture behavior of an Al/ Al_2O_3 composite was investigated by Romanova et al. (2009), they observed that interface debonding and particle cracking were the two mechanisms for a particle fracture.

This study therefore, focuses on the modelling and validation of production process parameters of unalloyed Aluminium sheets.

2. MATERIALS AND METHODS

The material used in this study is unalloyed Aluminium sheet obtained from Differential Aluminium Company located in Benin City, Edo State, Nigeria. This material was subjected to various temperatures and pressures ranging from 670°C to 2400°C and from 20 Gpa to 78 GPa respectively. These materials produced at various temperatures and pressures were evaluated for mechanical properties after cooling.

2.1. Method of Data Collection

The various samples of the developed unalloyed Aluminium sheets that were produced at various temperature and pressure were tested according to American Society for Testing and Materials (ASTM) using the tensometer and Charpy Impact Test machines respectively. The data obtained were further evaluated for mechanical properties for the developed Unalloyed Aluminium sheets. Furthermore, Samples were also tested on a 10 ton DAK tensile testing machine at a constant cross head speed of 1 mm/min. Standard samples of tensile specimens ASTM-E8M are prepared for testing. A total of 6 samples were tested in each case and average values were obtained.

2.2. Evaluation of Developed Unalloyed Aluminium Sheets for Mechanical Properties at Various Temperatures and Pressures

The developed unalloyed Aluminium sheets samples were evaluated for mechanical strength (tensile strength, young modulus of elasticity, Brinell hardness and shear modulus) using Equation 1 to 4 respectively (Idicula et al., 2009).

$$\text{Tensile strength} = \frac{\text{Maximum Load}}{\text{Original Cross - Sectional Area}} \quad (1)$$

$$\text{Young's modulus of Elasticity} = \frac{\text{Stress}}{\text{Strain}} = \frac{FL_o}{L_m - L_o} \quad (2)$$

Where, F = Applied force, L_o = Original length; L_m = Final length

$$\text{shear modulus} = \frac{\text{shear stress}}{\text{shear strain}} = \frac{\frac{F}{A}}{\frac{x}{y}} \quad (3)$$

Where, F = Applied force, A = Cross-sectional area; x = Extension; y = Original length

$$\text{Brinell Hardness Number (BHN)} = \frac{2P}{\pi D[D - \sqrt{D^2 - d^2}]} \quad (4)$$

Where P is the load in kilogram, D is the steel ball diameter in millimeter, and d is the depression diameter or indentation diameter.

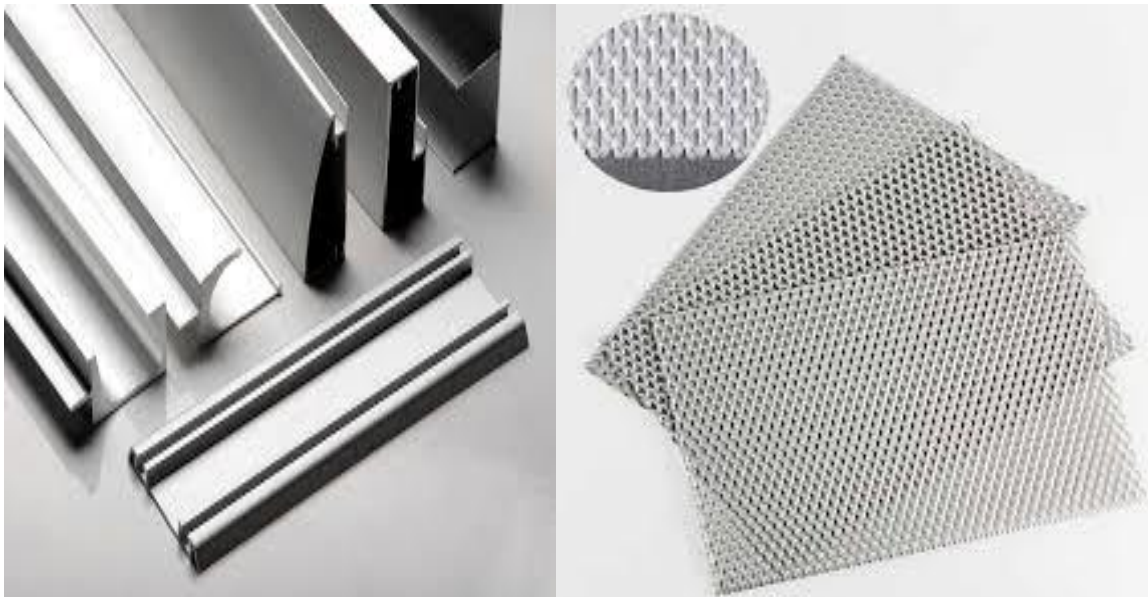


Figure 1. Developed Aluminium Sheets

2.3. Empirical Model Development of the Manufacturing Process of Unalloyed Aluminium Sheets

In this research work, all empirical models were developed using experimental values (E) obtained from the produced unalloyed Aluminium sheets using tensile strength, modulus of elasticity, shear modulus and Brinell hardness number results. The empirical model was used to predict the mechanical properties of the unalloyed Aluminium sheet material (tensile strength, modulus of elasticity, shear modulus and Brinell hardness number) by taking the inputs as percentage by volume of Aluminium, Pressure, percentage by volume of impurities and temperature respectively. The objective of the experiment is to allow an estimation of interactive and quadratic effects and therefore provide a predictive model that will find an

improved, as well as represent the experimental observations as an empirical mathematical function. This is expressed in the form shown in equation 5 and 6.

$$Y = \text{Constant} + \alpha_1 T + \alpha_2 M + \alpha_3 A_p + \alpha_4 TM + \alpha_5 TA_p + \alpha_6 MA_p + \alpha_7 T^2 + \alpha_8 M^2 + \alpha_9 A_p^2 \quad (5)$$

$$Y = \text{Constant} + \alpha_1 P + \alpha_2 M + \alpha_3 A_p + \alpha_4 PM + \alpha_5 PA_p + \alpha_6 MA_p + \alpha_7 P^2 + \alpha_8 M^2 + \alpha_9 A_p^2 \quad (6)$$

Where, M= Percentage by volume of other impurities present in unalloyed Aluminium sheets (%)

A_p = percentage by volume Aluminium (%)

T = Temperature (°C)

P = Pressure (MPa)

Y = Output (Mechanical Properties)

and $\alpha_1, \alpha_2, \alpha_3, \alpha_4, \alpha_5, \alpha_6, \alpha_7, \alpha_8,$ and α_9 are the coefficient of T, M, A_p , TM, TA_p , MA_p , T^2 , M^2 , and A_p^2 or P, M, A_p , PM, PA_p , MA_p , P^2 , M^2 , and A_p^2 respectively.

The output was obtained through the interaction between M, A_p and T or M, A_p and P. A quadratic model of second order regression was obtained for unalloyed Aluminium sheets for mechanical strength (tensile strength, modulus of elasticity, shear modulus and Brinell hardness number). A code was written in a MATLAB program (MATLAB software, version 7.5.0 (R2007b) to investigate the interactions of the various parameters of the developed empirical model.

2.4. Validation of the Models Developed

The mean absolute percentage error, and coefficient of determination was to validate the model. They were determined using equation 7 and equation 8 respectively.

$$\text{Absolute percentage error} = \frac{\text{Experimental value} - \text{Predicted Value}}{\text{Experimental Value}} \quad (7)$$

$$\text{Coefficient of Determination, } R^2 = \left[1 - \frac{\sum(Y_i - \hat{Y})^2}{\sum(Y_i - \bar{Y})^2} \right] \quad (8)$$

Where Y_i = Experimental value

\hat{Y} = Predicted values

3. RESULTS AND DISCUSSION

The Empirical Model Developed for unalloyed Aluminium sheets (tensile strength, modulus of elasticity, shear modulus and Brinell hardness number) is shown in equation 9-16 respectively.

$$\begin{aligned} &\text{Tensile Strength of Unalloyed Aluminium Sheet with Respect to Temperature } (6_T) \\ &= -93.4725 - 0.0629T + 0.5717M + 0.8493A_p + 0.0069TM + 0.0105TA_p \\ &\quad - 0.0376MA_p - 0.0014T^2 + 0.0204M^2 - 0.0356T^2 \end{aligned} \quad (9)$$

$$\begin{aligned} &\text{Tensile Strength of Unalloyed Aluminium Sheet with Respect to Pressure } (6_p) \\ &= -61.6083 - 0.0264P + 0.4261M + 0.2420A_p + 0.0044PM + 0.0070TA_p \\ &\quad - 0.0213MA_p - 0.0010P^2 + 0.0124M^2 - 0.0192P^2 \end{aligned} \quad (10)$$

$$\begin{aligned} &\text{Modulus of Elasticity of Unalloyed Aluminium Sheet with Respect to Temperature } (E_T) \\ &= -24.3775 - 0.0130T + 0.1316M + 0.1362A_p + 0.0018TM + 0.0028TA_p \\ &\quad - 0.0083MA_p - 0.0004T^2 + 0.0050M^2 - 0.0085T^2 \end{aligned} \quad (11)$$

$$\begin{aligned} &\text{Modulus of Elasticity of Unalloyed Aluminium Sheet with Respect to Pressure } (E_p) \\ &= -26.8877 - 0.0596P + 0.5647M + 0.4228A_p + 0.0033PM + 0.0055PA_p \\ &\quad - 0.0212MA_p - 0.0007P^2 + 0.0071M^2 - 0.0116P^2 \end{aligned} \quad (12)$$

$$\begin{aligned} &\text{Shear Modulus of Unalloyed Aluminium Sheet with Respect to Temperature } (\partial_T) \\ &= -172.4409 - 0.0460T + 0.7486M + 0.4670A_p + 0.0137TM + 0.0274TA_p \\ &\quad - 0.0445MA_p - 0.0033T^2 + 0.0291M^2 - 0.0768T^2 \end{aligned} \quad (13)$$

$$\begin{aligned} &\text{Shear Modulus of Unalloyed Aluminium Sheet with Respect to Pressure } (\partial_p) \\ &= -172.4409 - 0.0460T + 0.7486M + 0.4670A_p + 0.0137TM + 0.0274TA_p \\ &\quad - 0.0445MA_p - 0.0033T^2 + 0.0291M^2 - 0.0768T^2 \end{aligned} \quad (14)$$

$$\begin{aligned} &\text{Brinell Hardness Number of Unalloyed Aluminium Sheet with Respect to Temperature } (BHN_T) \\ &= -3.3481 + 0.0010T + 0.0295M - 0.0123A_p + 0.0003TM + 0.0006TA_p \\ &\quad - 0.0007MA_p - 0.0001T^2 + 0.0005M^2 - 0.0017T^2 \end{aligned} \quad (15)$$

$$\begin{aligned} &\text{Brinell Hardness Number of Unalloyed Aluminium Sheet with Respect to Pressure } (BHN_p) \\ &= -65.3512 - 0.3944P + 1.3150M + 1.2742A_p + 0.0007PM + 0.0053PA_p \\ &\quad + 0.0059MA_p + 0.0004P^2 + 0.0012M^2 + 0.0074P^2 \end{aligned} \quad (16)$$

Table 1. Effect of Temperature on Tensile Strength for Unalloyed Aluminium Sheets, Experimental (E), Predicted (P), Absolute Percentage Error and Coefficient of Determination

Temperature (°C)	Tensile Strength (MPa) Experimental (E)	Tensile Strength (MPa) Predicted (P)	Absolute Percentage Error (%)
1024	342	345	0.87
1200	469	472	0.64
1442	543	546	0.55
1610	452	455	0.66
1800	600	600	0.00
1921	621	624	0.48
2001	612	614	0.33
2112	602	604	0.33
2200	594	596	0.34
Mean Absolute Percentage Error (%)			0.47
Coefficient of determination = 0.9536			

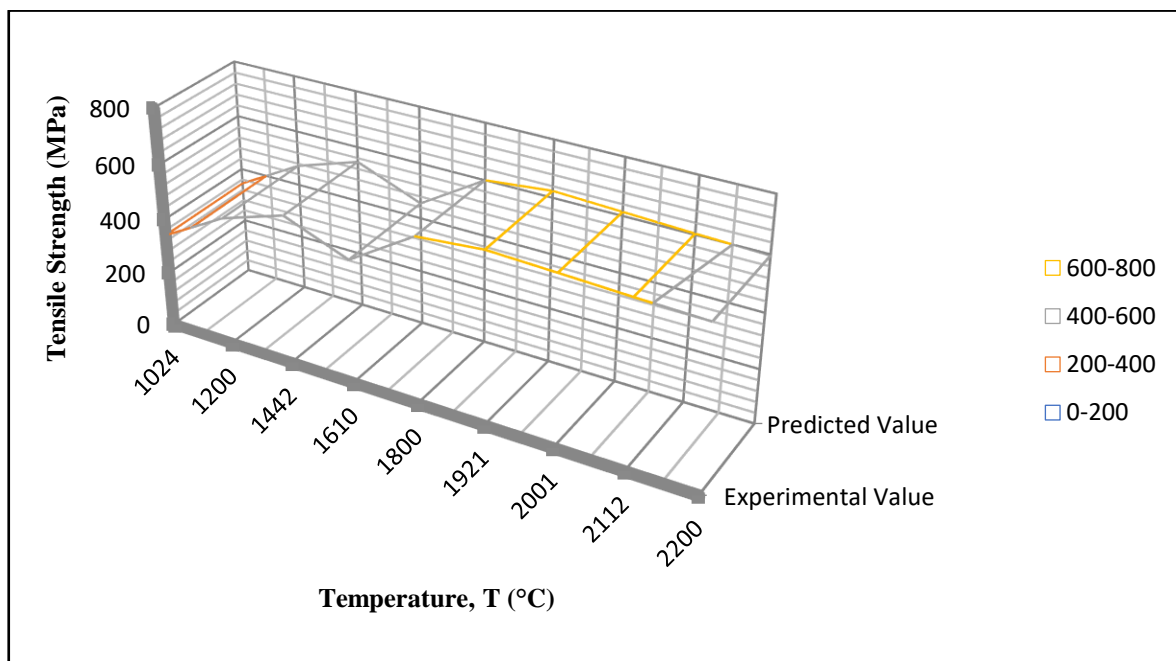


Figure 2. Graph of Effects of Temperature on the Tensile Strength of Unalloyed Aluminium Sheet, Experimental (E) and Predicted (P) Values

Table 2. Effect of Pressure on Tensile Strength for Unalloyed Aluminium Sheets, Experimental (E), Predicted (P), Absolute Percentage Error and Coefficient of Determination

Pressure (GPa)	Modulus of Elasticity (MPa) Experimental (E)	Modulus of Elasticity (MPa) Predicted (P)	Absolute Percentage Error (%)
40	342	343	0.29
56	480	483	0.63
62	510	511	0.20
65	452	455	0.66
69.5	543	545	0.37
72	562	568	1.07
74	555	554	0.18
76	548	550	0.37
78	546	548	0.37
Mean Absolute Percentage Error (%)			0.46
Coefficient of determination = 0.9531			

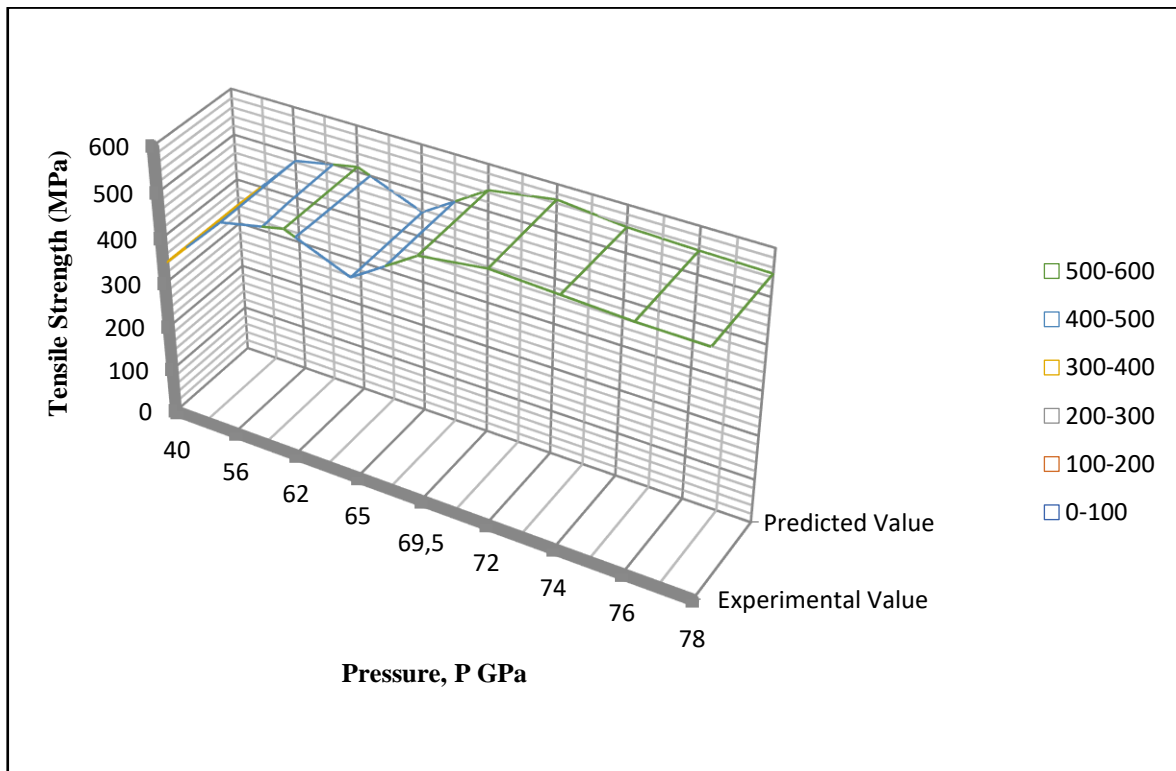


Figure 3. Graph of Effects of Pressure on the Tensile Strength of Unalloyed Aluminium Sheet, Experimental (E) and Predicted (P) Values

Table 3. Effect of Temperature on Modulus of Elasticity for Unalloyed Aluminium Sheets, Experimental (E), Predicted (P), Absolute Percentage Error and Coefficient of Determination

Temperature (°C)	Modulus of Elasticity (GPa) Experimental (E)	Modulus of Elasticity (GPa) Predicted (P)	Absolute Percentage Error (%)
1024	42	41	2.38
1200	47	46	2.13
1442	52	51	1.92
1610	69	68	1.45
1800	62	61	1.61
1921	59	58	1.69
2001	63	63	0.00
2112	64	63	1.56
2200	54	53	1.85
Mean Absolute Percentage Error (%)			1.62
Coefficient of determination = 0.9536			

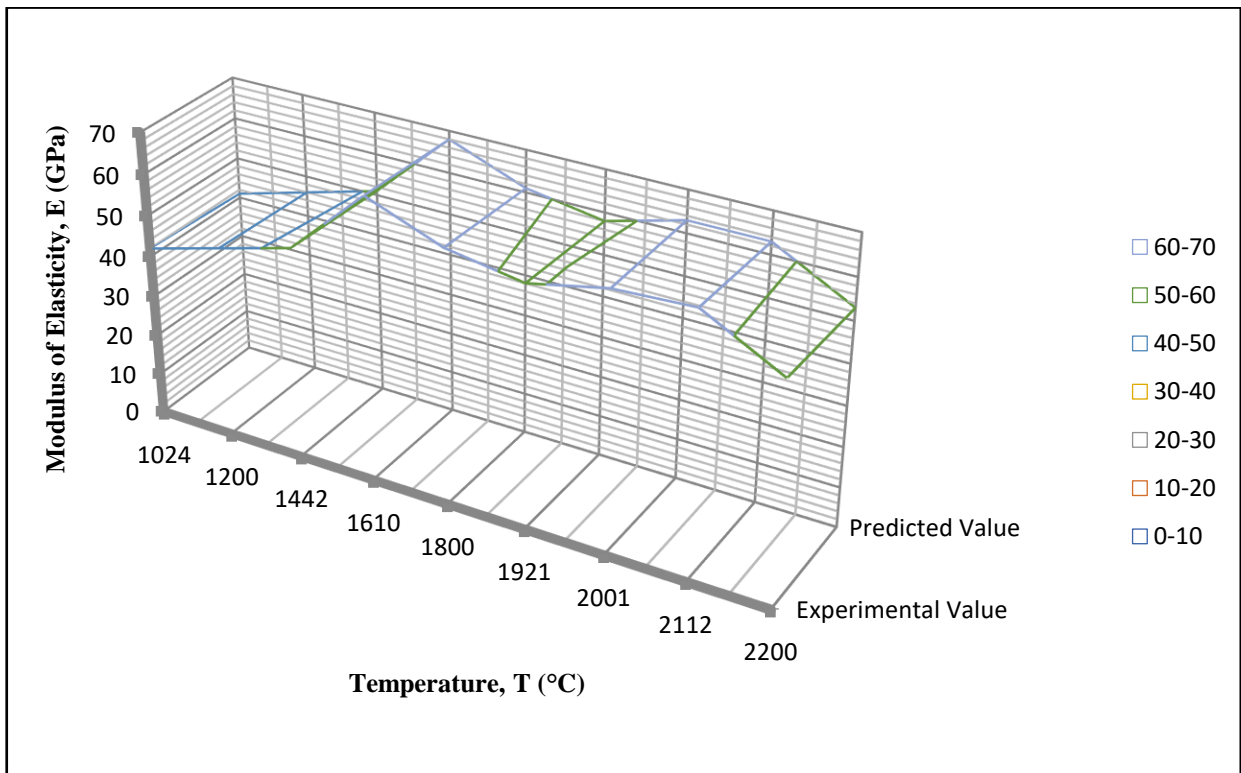


Figure 4. Graph of Effects of Temperature on the Modulus of Elasticity of Unalloyed Aluminium Sheet, Experimental (E) and Predicted (P) Values

Table 4. Effect of Pressure on Modulus of Elasticity for Unalloyed Aluminium Sheets, Experimental (E), Predicted (P), Absolute Percentage Error and Coefficient of Determination

Pressure (GPa)	Modulus of Elasticity (GPa) Experimental (E)	Modulus of Elasticity (GPa) Predicted (P)	Absolute Percentage Error (%)
40	42	41	2.38
56	47	46	2.13
62	52	51	1.92
65	60	58	3.33
69.5	68	66	2.94
72	59	57	3.89
74	63	61	3.17
76	64	62	3.13
78	60	56	6.67
Mean Absolute Percentage Error (%)			3.38
Coefficient of determination = 0.9411			

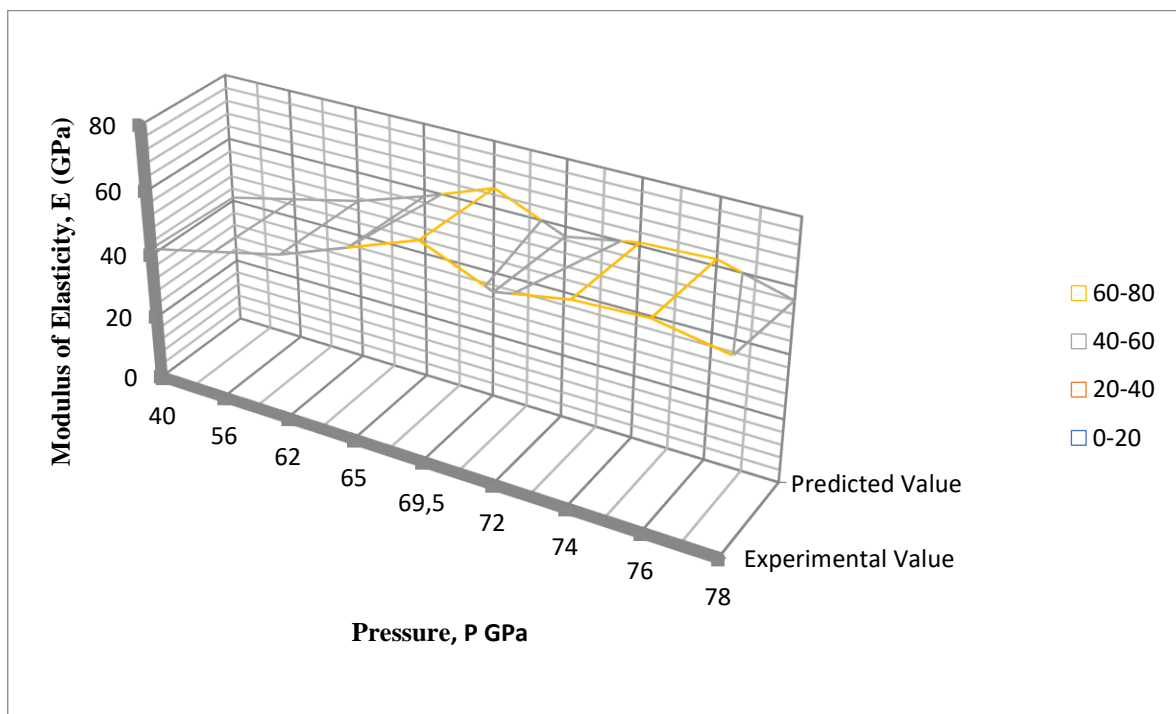


Figure 5. Graph of Effects of Pressure on the Modulus of Elasticity for Unalloyed Aluminium Sheet, Experimental (E) and Predicted (P) Values

Table 5. Effect of Temperature on Shear Modulus for Unalloyed Aluminium Sheets, Experimental (E), Predicted (P), Absolute Percentage Error and Coefficient of Determination

Temperature (°C)	Shear Modulus (GPa) Experimental (E)	Shear Modulus (GPa) Predicted (P)	Absolute Percentage Error (%)
1024	19	18	5.26
1200	23	24	4.35
1442	25.3	26	2.77
1610	23.4	24	2.56
1800	20.6	21.5	4.37
1921	19.8	20	1.01
2001	21.4	23	7.47
2112	21.6	22	1.85
2200	22	22	0.00
Mean Absolute Percentage Error (%)			3.29
Coefficient of determination = 0.9536			

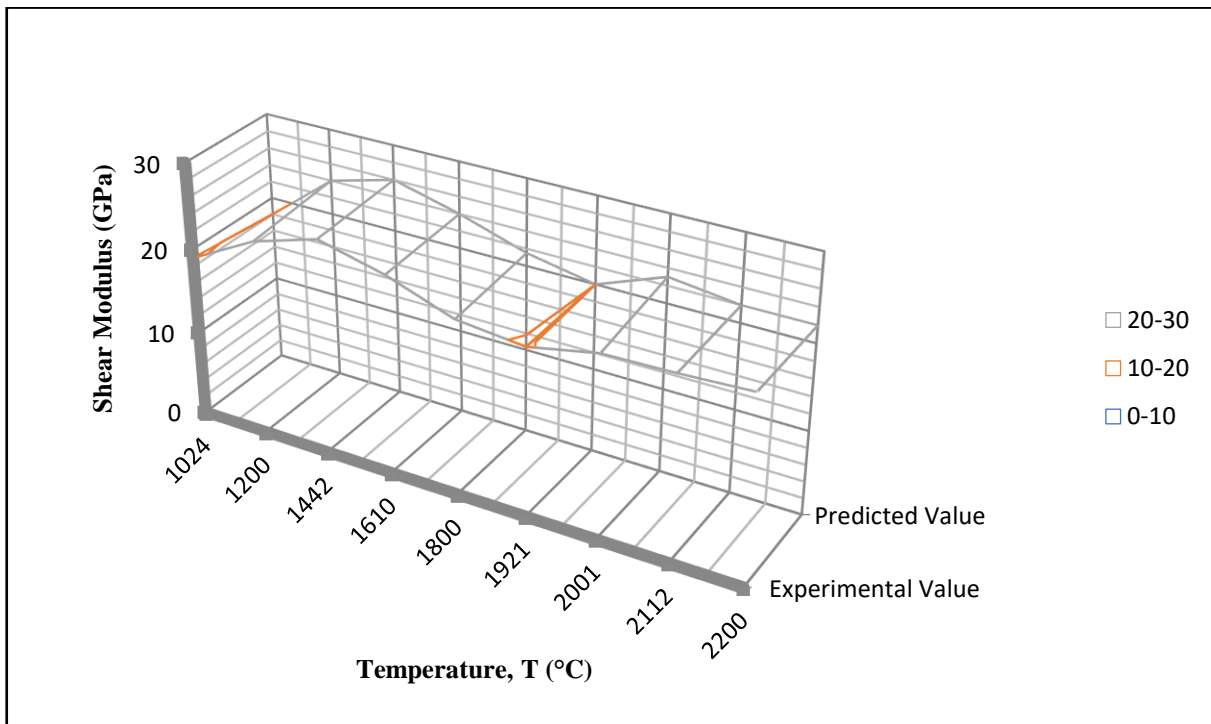


Figure 6. Graph of Effects of Temperature on the Shear Modulus of Unalloyed Aluminium Sheet, Experimental (E) and Predicted (P) Values

Table 6. Effect of Pressure on Shear Modulus for Unalloyed Aluminium Sheets, Experimental (E), Predicted (P), Absolute Percentage Error and Coefficient of Determination

Pressure (GPa)	Shear Modulus (GPa) Experimental (E)	Shear Modulus (GPa) Predicted (P)	Absolute Percentage Error (%)
40	19	18	5.26
56	23.8	22	7.56
62	24.5	26	6.12
65	24.9	25	0.40
69.5	26.2	25	4.58
72	19.8	20	1.01
74	22.5	23	2.22
76	22.8	23	0.88
78	23	23	0.00
Mean Absolute Percentage Error (%)			3.11
Coefficient of determination = 0.9531			

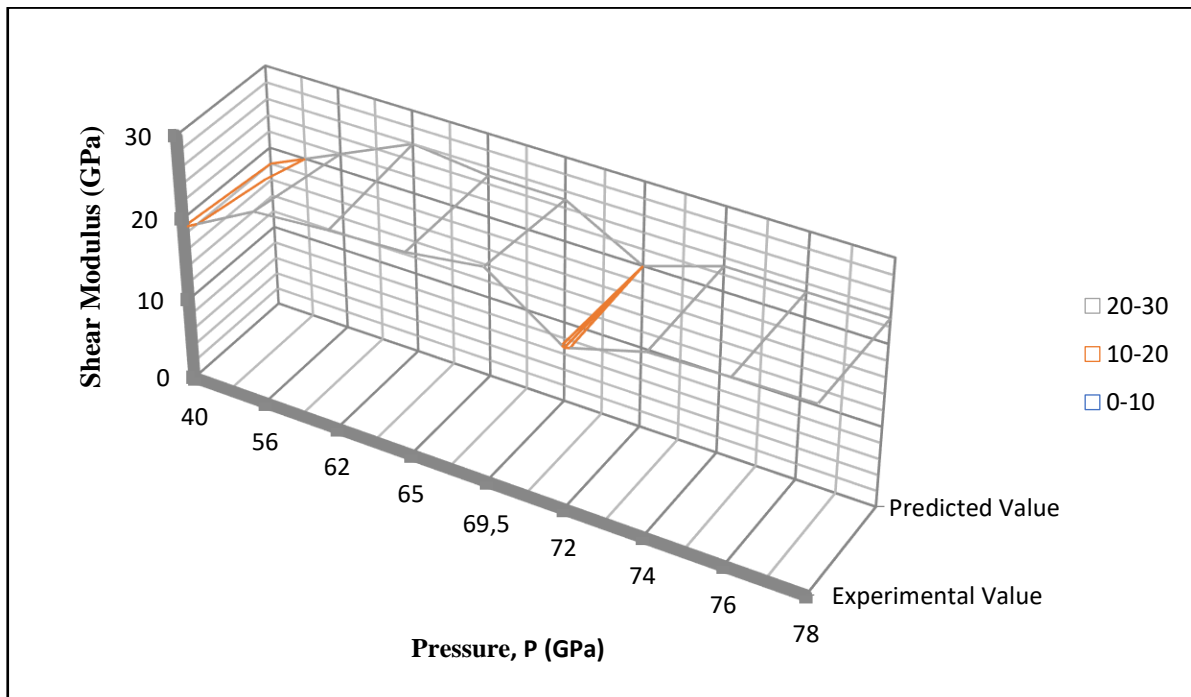


Figure 7. Graph of Effects of Pressure on the Shear Modulus of Unalloyed Aluminium Sheet, Experimental (E) and Predicted (P) Values

Table 7. Effects of Temperature on the Hardness of Unalloyed Aluminium Sheets, Experimental (E), Predicted (P), Absolute Percentage Error and Coefficient of Determination

Temperature (°C)	Brinell Hardness (N/mm ²) Experimental (E)	Brinell Hardness (N/mm ²) Predicted (P)	Absolute Percentage Error (%)
1024	39.00	40.00	2.56
1200	57.00	56.00	1.75
1442	62.00	62.00	0.00
1610	64.00	65.00	1.56
1800	68.00	69.50	2.21
1921	70.00	72.10	3.00
2001	75.00	74.20	1.07
2112	75.00	76.00	1.33
2200	72.00	73.00	1.39
Mean Absolute Percentage Error (%)			1.65
Coefficient of determination = 0.9828			

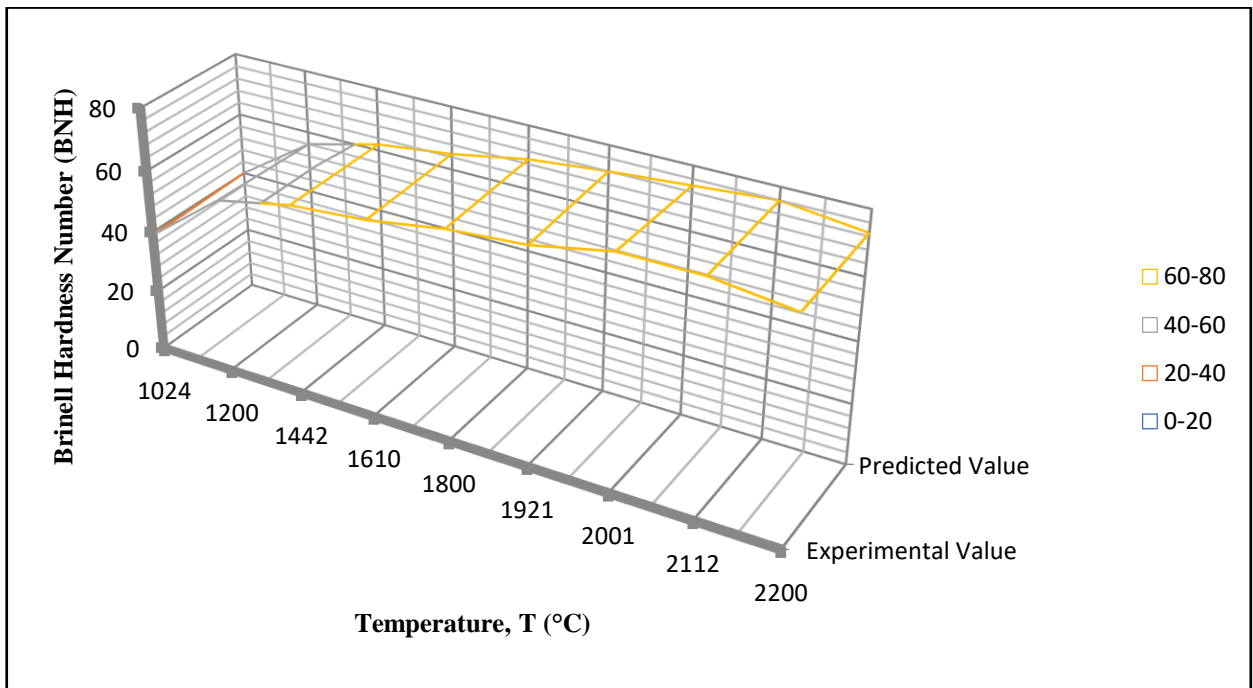


Figure 8. Graph of Effects of Temperature on the Hardness of Unalloyed Aluminium Sheet, Experimental (E) and Predicted (P) Values

Table 8. Effect of Pressure on the Hardness of Unalloyed Aluminium Sheets, Experimental (E), Predicted (P), Absolute Percentage Error and Coefficient of Determination

Pressure (GPa)	Brinell Hardness Number Experimental (E)	Brinell Hardness Number Predicted (P)	Absolute Percentage Error (%)
40	30	29	3.33
56	35	36	2.87
62	40	38	5.00
65	45	44	2.22
69.5	61	63	3.28
72	58	56	3.45
74	56	56	0.00
76	53	52	1.89
78	46	45	2.22
Mean Absolute Percentage Error (%)			2.70
Coefficient of determination = 0.9232			

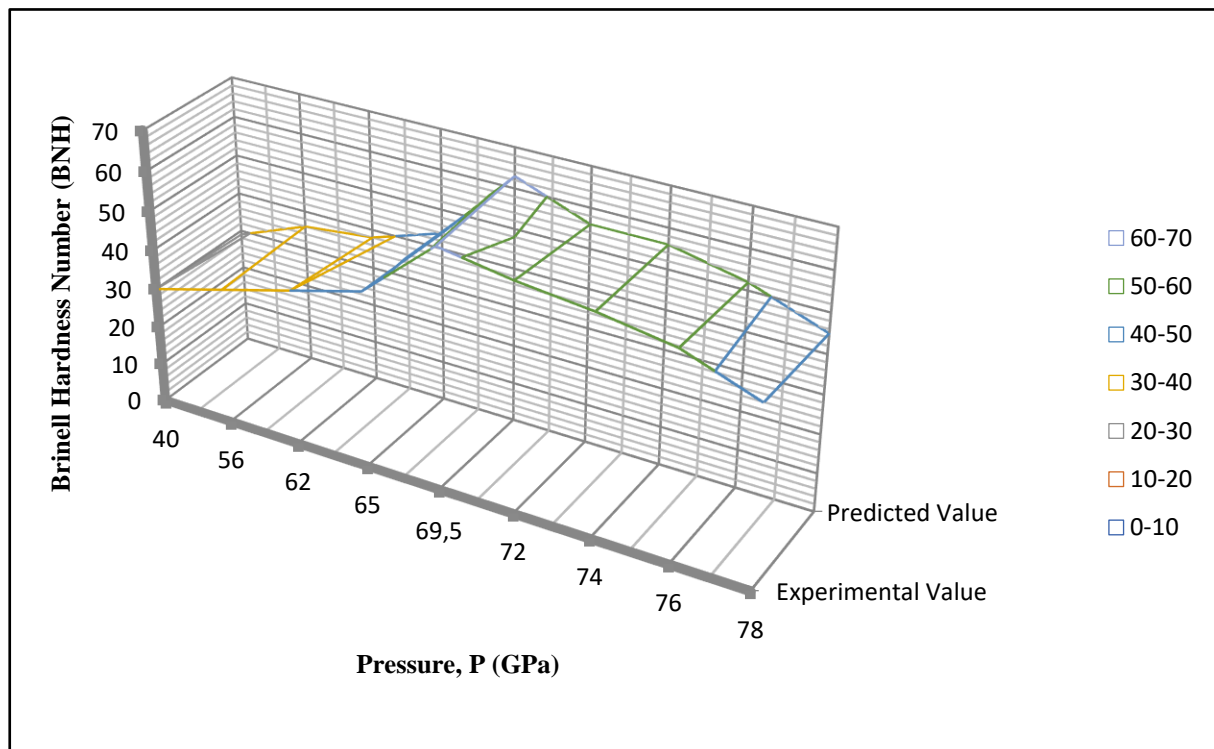


Figure 9. Graph of Effects of Pressure on the Hardness of Unalloyed Aluminium Sheet, Experimental (E) and Predicted (P) Values

3.1. Discussion of Results

3.1.1. Validation of Model for Unalloyed Aluminium Sheets

From the plots obtained in Figure 2-9, it was observed that the optimal tensile strength, young modulus of elasticity, shear modulus and Brinell hardness number were 621MPa, 69GPa, 25.5GPa, and 61 at temperature of 1921°C, 1610°C, 1442°C and 1800°C respectively. In comparison with pressure, the obtained values for optimal tensile strength, young modulus of elasticity, shear modulus and Brinell Hardness Number (BHN) were 562MPa, 68GPa, 26.2GPa and 61 at pressure of 72GPa, 69.5GPa, 69.5GPa and 69.5GPa respectively. The predicted values for the mechanical properties (tensile strength, modulus of elasticity, shear modulus and Brinell hardness number) of unalloyed Aluminium sheets were obtained using Equation 9-16 while the absolute percentage error and coefficient of determination was determined using Equation 7 and 8 respectively. The mechanical properties (tensile strength, modulus of elasticity, shear modulus and hardness), Experimental (E), Predicted (P), absolute percentage error values were presented in Table 1-8 and Figure 2-9.

The model was validated by comparing the predicted values from empirical models with experimental data. The predicted values were found to compare favourably with measured values. The absolute percentage error and coefficient of determination were calculated based on equation 7 and 8 respectively. The mean absolute percentage error and coefficient of determination of unalloyed Aluminium sheets is shown in in Table 1-8 and Figure 2-9 for tensile strength, modulus of elasticity, shear modulus and Brinell hardness number respectively. The models were validated using coefficient of determination (R^2) and mean absolute percentage error (MAPE). The coefficient of determination (R^2) were determined to be 0.9828 (98.28%) for tensile strength, 0.9385 (93.85%) for modulus of elasticity, 0.9787 (97.87%) for shear modulus, and 0.9847 (98.47%) for Brinell hardness number respectively which indicates that a substantial good fit was achieved by the regression model developed. Moreover, the mean absolute percentage error of predicted values from model when compare with the experimental values were determined to be 0.46% and 0.47% for tensile Strength, 1.62% and 3.38% for modulus of elasticity, 3.11% and 3.29% for shear modulus and 1.65% and 2.70% for Brinell hardness number respectively. These values are significantly small and below the maximum error of 10% proposed by Liping and Deku (1992) and Osarenmwinda and Nwachukwu (2010). These values were therefore found to be satisfactory and show good predictability of the model and its adequacy.

4. CONCLUSION

The modeling and validation of production process parameters of unalloyed Aluminium sheets had been achieved. Empirical Models were developed for predicting the mechanical properties (tensile strength, modulus of elasticity, shear modulus and hardness) for the produced unalloyed Aluminium sheets. The models were validated using coefficient of determination (R^2) and mean absolute percentage error (MAPE). The coefficient of determination (R^2) obtained ranges from 0.9213 (92.13%) to 0.9911 (99.11%) which indicates that a substantial good fit was achieved by the regression model developed. The mean absolute percentage error of the developed models ranges from 0.46% to 3.38% which was below 10% recommended. The values obtained from the validation of these models were therefore found to be satisfactory, and shows good predictability of the model and its adequacy. In addition, the developed models and the determined interactions will serve as a guide to assist researchers, industrialist and small scale manufacturers to estimate the properties of unalloyed Aluminium sheets to be produced.

CONFLICT OF INTEREST

There is no conflict of interest in this research article.

REFERENCES

Crowe, C. R, Gray, R. A, & Hasson, D. F. (1985). Microstructure Controlled Fracture Toughness of SiC/Al Metal Matrix Composites. Proceedings of the Fifth International Conference on Composite Materials, 843-66.

- Friend, C. M. (1987). The Effect of Matrix Properties on Reinforcement is Short Al₂O₃ Fiber-Al MMCs. *Journal of Materials Science*, 22(8), 3005-3010.
- Idicula, M., Joseph, K., & Thomas, S. (2009). Mechanical Performance of Short Banana/Sisal Hybrid Fibre Polyester Composite. *Journal of Reinforced Plastics and Composites*, 29(1), 12-29.
- Joardar, H., Sutradhar, G., & Das, N. S. (2012). FEM Simulation and Experimental Validation of Cold Forging Behavior of LM6 Base Metal Matrix Composites. *Journal of Minerals and Materials Characterization and Engineering*, 11(10), 989-994.
- Kok, M. (2005). Production and Mechanical Properties of Al₂O₃ Particle-Reinforced 2024 Aluminium Alloy Composites. *Materials Processing Technology Journal*, 161(3), 381-387.
- Kumar, A., Lal, S., & Kumar, S. (2013). Fabrication and Characterization of A359/Al₂O₃ Metal Matrix Composite using Electromagnetic Stir Casting Method. *Journal of Materials Research and Technology*, 2(3), 250-254.
- Liping, G., & Deku, M. S. (1992). Production of Sawdust-Plastic Composite Using Compression Moulding. *International Journal of Material Science*, 2, 87-92.
- Nieh, T. G., & Chellman, D. J. (1984). Modulus Measurements in Discontinuous Reinforced Aluminum Composites. *Scripta Metallurgica*, 18, 925-938.
- Nieh, T. G., Raninen, R. A., & Chellman, D. J. (1985). Microstructure and Fracture in SiC Whisker Reinforced 2124 Aluminum Composite. Proceedings of the Fifth International Conference on Composite Materials. Metallurgical Society, Inc., 825-842.
- Olodu, D. D & Osarenmwinda, J. O. (2018). Empirical Modelling of Injection Moulded High Density Polyethylene-Grass Composite. *American Journal of Engineering Research (AJER)*, 7(12), 245-250.
- Orbulov, I. N, Ginsztler, J. (2012). Compressive Behaviour of Metal Matrix Syntactic Foams. *Acta Polytechnica Hungarica*, 9(2), 43-56.
- Osarenmwinda, J. O, Nwachukwu, J. C. (2010). Development of Composite Material from Agricultural Waste. *International Journal of Engineering Research in Africa*, 3, 42-48.
- Prabu, S. B., Karunamoorthy, L., Kathiresan, S., & Mohan, B. (2006). Influence of Stirring Speed and Stirring Time on Distribution of Particles in Cast Metal Matrix Composite. *Journal of Materials Processing Technology*, 171(2), 268-73.
- Romanova, V. A., Balokhonov, R. R., & Schmauder, S. (2009). The Influence of the Reinforcing Particle Shape and Interface Strength on the Fracture Behavior of a Metal Matrix Composite. *Acta Materialia*, 57(1), 97-107.
- Rozovsky, E., Hahn, W. C., & Avitzur, B. (1973). The Behavior of Particles During Plastic Deformation of Metals. *Metallurgical Transactions*, 4(4), 927-30.
- Saravanan, C., Subramanian, K., Ananda Krishnan, V., & Sankara Narayanan, R. (2015). Effect of Particulate Reinforced Aluminium Metal Matrix Composite. *Mechanics and Mechanical Engineering*, 19(1), 23-30.
- Venkatesh, B., & Harish, B. (2015). Mechanical Properties of Metal Matrix Composites (Al/SiCp) Particles Produced by Powder Metallurgy. *International Journal of Engineering Research and General Science*. 3(1), 1277-1284.
- Yao, B., Hofmeister, C., Patterson, T., Sohn, Y., van den Bergh, M., Delahanty, T., & Cho, K. (2010). Microstructural Features Influencing the Strength of Trimodal Aluminum Metal-matrix-Composites. *Composites Part A: Applied Science and Manufacturing*, 41(8), 933-941.



Application of Differential Transformation Method for Nonlinear Cutting Tool Vibration

İbrahim DEMİR^{1,2*}, Mustafa Mehmet Fatih KARAHAN², Nizami AKTÜRK¹

¹Gazi University, Faculty of Engineering, Department of Mechanical Engineering, 06570, Ankara, Turkey

²Manisa Celal Bayar University, Faculty of Engineering, Department of Mechanical Engineering, 45140, Manisa, Turkey

Keywords	Abstract
Vibration Differential Transformation Method Delayed Differential Equation Chatter	This article aims to solve the mathematical model developed for machine tool vibrations by employing Differential Transformation Method (DTM). Multi-step differential transformation method is used as it has been shown to have good accuracy in physical applications. Nondimensionalization (scaling) technique is used in order to fully understand the physical effects of each varying parameter. Transformed function of delayed nonlinear velocity terms are explained. MatLab® software is used for DTM solutions. The equation of motion is solved with the DDE23 function in MatLab® software as well as with MatLab®/Simulink® software to compare the results. The solution of the fundamental DTM which is obtained by using the constant transformed function values which differ from other methods after a certain time period. However, the results obtained with the transformed functions for different values at each sampling time (Multi-Step DTM) give very close results to Simulink® and DDE23.

Cite

Demir, İ., Karahan, M. M. F., & Aktürk, N. (2021). Application of Differential Transformation Method for Nonlinear Cutting Tool Vibration. *GU J Sci, Part A*, 8(1), 109-122.

Author ID (ORCID Number)	Article Process
İ. Demir, 0000-0002-2128-3949	Submission Date 28.10.2020
M. M. F. Karahan, 0000-0001-9040-5041	Revision Date 15.02.2021
N. Aktürk, 0000-0003-1398-8145	Accepted Date 04.03.2021
	Published Date 29.03.2021

1. INTRODUCTION

Vibration is a phenomenon that is rarely desired and generally untoward in engineering applications. In addition to the obtaining the mathematical model of vibrating systems, the solution of the established model also requires an effort. Analytical solutions of mathematical models of engineering problems are generally very challenging as models are established to be more realistic. Hence, various semi-analytical and numerical methods are employed to obtain the solution. The differential transformation method (DTM), a semi-analytical method, is employed in this paper for investigating machine tool vibrations as it is quite complicated in nature. Differential Transformation Method, based on Taylor Series, was first used by Zhou (1986) for electrical circuit (Hatami et al., 2017). Jang et al. (2000) promoted an adaptive grid size mechanism. Abdel & Hassan (2002) suggested DTM to obtain eigenvalues, eigenfunctions and to find out a solution the partial differential equations. Ayaz (2004) offered three-dimensional differential transformation method and defined the basic theorems. Varying grid size is employed by Kurnaz & Oturanç (2005) to boost the accuracy of the DTM solutions.

Arikoğlu & Özkol (2005) introduced DTM to solve integro-differential equations. Difference equations are carried out by utilizing DTM by Arikoğlu & Özkol (2006a). Arikoğlu & Özkol (2006b) presented theorems related to DTM for the solution of differential-difference equations (DDEs). Application of DTM on integro-differential and integral equations systems was also discussed by Arikoğlu & Özkol (2008).

Momani & Ertürk (2008) designed a modified DTM for the good accuracy of non-linear oscillatory system solutions. A different DTM technique worked by El-Shaded (2008) for non-linear oscillatory systems. Karakoç & Bereketoğlu (2009) used DTM in the solution of delay differential equations. Kuo & Lo (2009) utilized DTM to explore the response of a physical system. Chen & Chen (2009) adopted DTM to the non-linear physical system solution. Thongmoon & Pusjuso (2010) compared DTM with the Laplace transform method for a system of differential equations.

Mirzaee (2011) applied DTM to the solution of linear and nonlinear DDEs. Süngü & Demir (2012) compared DTM with Adomian Decomposition Method for the solution of linear and nonlinear differential equations. Villafuerte & Chen-Charpentier (2012) developed the random DTM to solve random differential equations.

Gokdogan et al. (2012) compared numerical results obtained by DTM with analytical solution for the DDE. Šmarda et al. (2013) presented theorems related to DTM for the solution of nonlinear differential and integro-differential equations with proportional delays. Bozdoğan & Ozturk (2014) apply differential transform method to investigate the free vibration analysis of an orthotropic beam model. Tabatabaei & Gunerhan (2014) solved Duffing equations by means of DTM. DTM is also used by Bozdogan & Aydin (2016) in stability analysis for multistory structure that is modeled as a continuous system. Benhammouda & Leal (2016) proposed an analytical solution for the nonlinear delay differential equations by using DTM. Rebenda & Šmarda (2017) presented semi-analytical DTM approach for the solution of functional differential equations with multiple delays. Hatemi et al. (2017) explained DTM on some physical problems.

In this current study, the solution of a mathematical model in cutting tool vibrations is investigated. DTM is applied to the mathematical model presented for the first time. The mathematical model is comprised of delayed, nonlinear differential equations. In this paper, a system of transformed equations is expressed in matrix form. The difficulty caused by the transformed nonlinear terms is overcome by using transformed functions which are found at previous cycle and sampling time. The results obtained by DTM which is a semi analytical method are in good agreement with the numerical methods, Simulink and DDE23 MatLab® function.

2. DIFFERENTIAL TRANSFORMATION METHOD

In this method, which is based on Taylor Series, the transformed function, $F(k)$ and inverse transform, $f(t)$ is defined as follows.

$$F(k) = \frac{1}{k!} \left[\frac{d^k f(t)}{dt^k} \right]_{t=t_0}, \quad f(t) = \sum_{k=0}^{\infty} F(k)(t-t_0)^k \quad (1)$$

The basic DTM theorems used in this article is below (Zhou, 1986; Arıkoğlu & Özkol, 2006).

$$x(t) = \frac{d^m f(t)}{dt^m}, \quad X(k) = \frac{(k+m)!F(k+m)}{k!} \quad (2)$$

$$x(t) = f(t)g(t), \quad X(k) = \sum_{l=0}^k F(l)G(k-l) \quad (3)$$

$$f(t) = g(t+a), \quad F(k) = \sum_{h_1=k}^N \binom{h_1}{k} a^{h_1-k} G(h_1) \quad (4)$$

3. SOLUTION TECHNIQUE

Multi-step differential transformation method is used in physical applications due to its high accuracy (Hatami et al., 2017). In this study, instead of using a single t_o value and the associated transformed function to obtain the function value at a specific time, t , different t_o values and different transformed functions are used in each step by keeping the step interval, $t - t_o = T_o$, constant.

$$F_{t_o}(k) = \frac{1}{k!} \left[\frac{d^k f(t)}{dt^k} \right]_{t=t_o} \quad f(t_{t_o+T_o}) = \sum_{k=0}^{\infty} F_{t_o}(k) T_o^k \quad (5)$$

4. PROBLEM FORMULATION

In cutting tool vibrations, the equation of motion defining the single degree of freedom and self-excited vibration, including flank wear caused by vibrations, is shown as follows:

$$\ddot{y}(t) + 2\xi\omega_n\dot{y}(t) + \omega_n^2 y(t) = -b \frac{\omega_n^2}{k} \left[K_1 (y(t) - y(t-T)) + K_2 VB_d(t) \right] \quad (6)$$

The relationship between the flank wear and the cutting velocity was expressed first by Taylor (1907) (Altintas, 2012). There is a connection between the relative velocity of the two materials and the wear rate (Maekawa et al., 1989; Chowdhury et al., 2011; Zanger & Schulze, 2013). The mathematical model proposed for the flank wear length which includes the lost material length, $G_m(t)$, depending on the vibration velocity, whose basic approach is based on the above studies is given in Eq 7.

$$VB_d(t+dt) = VB_d(t) + \frac{G_m(t)z_1}{z_2} = VB_d(t) + \frac{z_1}{z_2} p\dot{y}(t)^q \quad (7)$$

Eq. 7 is described with the idea that it will be easier to use previous values.

$$VB_d(t) = VB_d(t-dt) + \frac{z_1}{z_2} p\dot{y}(t-dt)^q \quad (8)$$

The terms in Eqs. 6 and 8 $y(t)$, cutting tool displacement in vibration motion, $\dot{y}(t)$, first derivative of displacement (velocity), $\ddot{y}(t)$, second derivative of displacement (acceleration), $y(t-T)$, displacement in the previous cycle of the workpiece, $VB_d(t)$, flank wear length caused by vibration, K_2 , hardness of work material, K_1 , specific cutting constant, b , deep of cut, k , cutting tool stiffness, ω_n , natural frequency, ξ , dimensionless damping ratio and the other terms are some process parameters. Initial conditions are $y(0) = 0$, $\dot{y}(0) = V$, $VB_d(0) = 0$. The term $bK_2VB_d(t)$ in Eq. 6 is the force on the flank face. It is assumed as $b(HB/3)VB_d(t)$ in this mathematical model based on the investigation by Astakhov (2004). HB is the Brinell hardness of the workpiece material. This force will only exist when the vibration velocity is positive due to physical acceptance. Similarly, the term related to velocity in Eq. 8 prevail when the vibration velocity is positive, otherwise it will be $VB_d(t) = VB_d(t-dt)$.

For the convenience and the understanding of the Eqs. 6 and 8, some dimensionless parameters are used as below.

$$u = y / VB_{do} \quad \tau = \omega_n t \quad \delta = \omega_n T \quad w = VB_d / VB_{do} \quad \delta_o = \omega_n T_o$$

Taking first and second derivative of y :

$$\frac{dy}{dt} = \frac{dy}{d\tau} \frac{d\tau}{dt} = VB_{do} \omega_n \frac{du}{d\tau} \qquad \frac{d^2y}{dt^2} = VB_{do} \omega_n^2 \frac{d^2u}{d\tau^2}$$

The above derivatives and dimensionless parameters are substituted in Eq. 6.

$$VB_{do} \omega_n^2 \frac{d^2u}{d\tau^2} + 2\xi VB_{do} \omega_n^2 \frac{du}{d\tau} + VB_{do} \omega_n^2 u = -b \frac{\omega_n^2}{k} VB_{do} \left[K_1 (u - u(\tau - \delta)) + \frac{HB}{3} w \right] \quad (9)$$

Eq. 10 is obtained by dividing Eq. 9 by the coefficient of the second dimensionless derivative.

$$\frac{d^2u}{d\tau^2} + 2\xi \frac{du}{d\tau} + u = -\frac{b}{k} \left[K_1 (u - u(\tau - \delta)) + \frac{HB}{3} w \right] \quad (10)$$

Dimensionless parameters are also substituted in Eq. 8.

$$VB_{do} w(\tau) = VB_{do} w(\tau - \delta_o) + \frac{z_1}{z_2} p (VB_{do} \omega_n)^q \left(\frac{du(\tau - \delta_o)}{d\tau} \right)^q \quad (11)$$

Eq. 12 is found by dividing Eq. 11 by VB_{do} .

$$w(\tau) = w(\tau - \delta_o) + \frac{z_1}{z_2} p (VB_{do})^{q-1} (\omega_n)^q \left(\frac{du(\tau - \delta_o)}{d\tau} \right)^q \quad (12)$$

The following abbreviations are used to make the Eq. 10 and 12 look simpler.

$$a_1 = 2\xi \qquad a_2 = b \frac{K_1}{k} \qquad a_3 = b \frac{HB}{3k} \qquad a_4 = \frac{z_1}{z_2} p \omega_n^q VB_{do}^{q-1}$$

After these operations, Eq. 13 and 14 and dimensionless initial conditions appear as follows.

$$u''(\tau) + a_1 u'(\tau) + (1 + a_2)u(\tau) - a_2 u(\tau - \delta) + a_3 w(\tau) = 0 \quad (13)$$

$$w(\tau) = w(\tau - \delta_o) + a_4 u'(\tau - \delta_o)^q \quad (14)$$

$$u(0) = 0 \qquad u'(0) = \frac{V}{VB_{do} \omega_n} = 1 \qquad w(0) = 0 \quad (15)$$

5. APPLICATION OF DIFFERENTIAL TRANSFORMATION METHOD

In this section, DTM is applied to solve the presented equation of motion. Eq. 13 and 14 will be solved in three cases where q is equal to 1, 2 and 3.

Case 1

In this case, Eq. 13 and 14 is handled for $q = 1$.

$$u''(\tau) + a_1 u'(\tau) + (1 + a_2)u(\tau) - a_2 u(\tau - \delta) + a_3 w(\tau) = 0 \quad (13)$$

$$w(\tau) = w(\tau - \delta_o) + a_4 u'(\tau - \delta_o) \quad (16)$$

Eq. 13 is transformed by means of the above fundamental transformations as follow. These transformed functions are renewed at each step.

$$\frac{(k+2)!U(k+2)}{k!} + a_1 \frac{(k+1)!U(k+1)}{k!} + (1+a_2)U(k) - a_2U(k)_{\tau_o-\delta} + a_3W(k) = 0 \tag{17}$$

The $\tau_o - \delta$ value in the lower right index of the term $U(k)_{\tau_o-\delta}$ in this transformed Eq. 17 represents the previous transformed function as δ . The final equation is organized as follows.

$$(k+2)(k+1)U(k+2) + a_1(k+1)U(k+1) + (1+a_2)U(k) - a_2U(k)_{\tau_o-\delta} + a_3W(k) = 0 \tag{18}$$

By adapting the above fundamental transformations to Eq. 16:

$$W(k) = \sum_{h_1=k}^N \binom{h_1}{k} (-\delta_o)^{h_1-k} W(h_1) + a_4(k+1) \sum_{h_1=k+1}^{N+2} \binom{h_1}{k+1} (-\delta_o)^{h_1-k-1} U(h_1) \tag{19}$$

is obtained. This equation is also expressed as:

$$0 = \sum_{h_1=k+1}^N \binom{h_1}{k} (-\delta_o)^{h_1-k} W(h_1) + a_4(k+1) \sum_{h_1=k+1}^{N+2} \binom{h_1}{k+1} (-\delta_o)^{h_1-k-1} U(h_1) \tag{20}$$

The equation system obtained by changing k from 0 to N to find the transformed functions, $U(k)$, in the Eq. 18 is shown as follows.

$$\begin{pmatrix} (2)(1) & 0 & 0 & 0 & 0 & 0 & 0 & 0 \\ a_1(2) & (3)(2) & 0 & 0 & 0 & 0 & 0 & 0 \\ (1+a_2) & a_1(3) & (4)(3) & 0 & 0 & 0 & 0 & 0 \\ 0 & (1+a_2) & a_1(4) & (5)(4) & 0 & 0 & 0 & 0 \\ 0 & 0 & (1+a_2) & a_1(5) & (6)(5) & 0 & 0 & 0 \\ 0 & 0 & 0 & \ddots & \ddots & \ddots & 0 & 0 \\ 0 & 0 & 0 & 0 & \ddots & \ddots & \ddots & 0 \\ 0 & 0 & 0 & 0 & 0 & (1+a_2) & a_1(N+1) & (N+2)(N+1) \end{pmatrix} \begin{pmatrix} U(2) \\ U(3) \\ U(4) \\ U(5) \\ U(6) \\ \vdots \\ \vdots \\ U(N+2) \end{pmatrix} + \begin{pmatrix} a_1(1)U(1) + (1+a_2)U(0) - a_2U(0)_{\tau_o-\delta} + a_3W(0) \\ (1+a_2)U(1) - a_2U(1)_{\tau_o-\delta} \\ -a_2U(2)_{\tau_o-\delta} \\ -a_2U(3)_{\tau_o-\delta} \\ -a_2U(4)_{\tau_o-\delta} \\ \vdots \\ \vdots \\ -a_2U(N)_{\tau_o-\delta} \end{pmatrix} + \begin{pmatrix} 0 & 0 & 0 & 0 & 0 & 0 & 0 & 0 \\ a_3 & 0 & 0 & 0 & 0 & 0 & 0 & 0 \\ 0 & a_3 & 0 & 0 & 0 & 0 & 0 & 0 \\ 0 & 0 & a_3 & 0 & 0 & 0 & 0 & 0 \\ 0 & 0 & 0 & a_3 & 0 & 0 & 0 & 0 \\ 0 & 0 & 0 & 0 & \ddots & 0 & 0 & 0 \\ 0 & 0 & 0 & 0 & 0 & \ddots & 0 & 0 \\ 0 & 0 & 0 & 0 & 0 & 0 & \ddots & 0 \\ 0 & 0 & 0 & 0 & 0 & 0 & 0 & a_3 \end{pmatrix} \begin{pmatrix} W(1) \\ W(2) \\ W(3) \\ W(4) \\ \vdots \\ \vdots \\ W(N) \end{pmatrix} = \begin{pmatrix} 0 \\ 0 \\ 0 \\ 0 \\ \vdots \\ \vdots \\ \vdots \\ 0 \end{pmatrix} \tag{21}$$

The equation system obtained by changing k from 0 to $N-1$ to find the transformed functions in the Eq. 20 is also shown as follows.

$$\begin{pmatrix} \binom{1}{0}(-\delta_o)^1 & \binom{2}{0}(-\delta_o)^2 & \dots & \dots & \binom{N}{0}(-\delta_o)^N \\ 0 & \binom{2}{1}(-\delta_o)^1 & \dots & \dots & \binom{N}{1}(-\delta_o)^{N-1} \\ 0 & 0 & \ddots & \dots & \vdots \\ 0 & 0 & 0 & \ddots & \vdots \\ 0 & 0 & 0 & 0 & \binom{N}{N-1}(-\delta_o)^1 \end{pmatrix} \begin{pmatrix} W(1) \\ W(2) \\ \vdots \\ W(N-1) \\ W(N) \end{pmatrix} + \\
 \begin{pmatrix} a_4(1)\binom{2}{1}(-\delta_o)^1 & a_4(1)\binom{3}{1}(-\delta_o)^2 & \dots & \dots & \dots & a_4(1)\binom{N+2}{1}(-\delta_o)^{N+1} \\ a_4(2)\binom{2}{2}(-\delta_o)^0 & a_4(2)\binom{3}{2}(-\delta_o)^1 & \dots & \dots & \dots & a_4(2)\binom{N+2}{2}(-\delta_o)^N \\ 0 & a_4(3)\binom{3}{3}(-\delta_o)^0 & \ddots & \dots & \dots & \vdots \\ 0 & 0 & \ddots & \ddots & \dots & \vdots \\ 0 & 0 & 0 & a_4(N)\binom{N}{N}(-\delta_o)^0 & \dots & a_4(N)\binom{N+2}{N}(-\delta_o)^2 \end{pmatrix} \begin{pmatrix} U(2) \\ U(3) \\ \vdots \\ \vdots \\ U(N+1) \\ U(N+2) \end{pmatrix} + \\
 \begin{pmatrix} a_4(1)\binom{1}{1}(-\delta_o)^0 U(1) \\ 0 \\ \vdots \\ 0 \\ 0 \end{pmatrix} = \begin{pmatrix} 0 \\ 0 \\ \vdots \\ 0 \\ 0 \end{pmatrix} \tag{22}$$

The equations in these last two matrices form are given in Eqs. 23 and 24.

$$\mathbf{A}_1\mathbf{U} + \mathbf{A}_2 + \mathbf{A}_3\mathbf{W} = \mathbf{0} \tag{23}$$

$$\mathbf{A}_4\mathbf{W} + \mathbf{A}_5\mathbf{U} + \mathbf{A}_6 = \mathbf{0} \tag{24}$$

After mathematical operations the transformed equations are found as below:

$$\mathbf{U} = (\mathbf{A}_1 - \mathbf{A}_3(\mathbf{A}_4^{-1}\mathbf{A}_5))^{-1}(-\mathbf{A}_2 + \mathbf{A}_3(\mathbf{A}_4^{-1}\mathbf{A}_6)) \tag{25}$$

$$\mathbf{W} = -\mathbf{A}_4^{-1}(\mathbf{A}_5\mathbf{U} + \mathbf{A}_6) \tag{26}$$

It should be noted here that there are no transformed function values $\mathbf{U}(0)$, $\mathbf{U}(1)$, $\mathbf{W}(0)$ in the \mathbf{U} and \mathbf{W} vectors. Because these values indicate the initial values in each step.

Case 2

In this case, Eqs. 13 and 14 is handled for $q = 2$. It is needed to make some mathematical operations to determine the transformed function of $u'(\tau - \delta_o)^q$ in Eq. 14. Let the function is $f(\tau) = u'(\tau - \delta_o)^2$ to be applied DTM. The mathematical operations to be done step by step to find the transformed function are as follows.

- $U_1(k) = \sum_{h_1=k}^N \binom{h_1}{k} (-\delta_o)^{h_1-k} U(h_1)$ transformed function of $u(\tau - \delta_o)$
- $U_2(k) = (k + 1)U_1(k + 1)$ transformed function of $u'(\tau - \delta_o)$
- $U_2(l)$ is found as $U_2(l) = (l + 1) \sum_{h_1=l+1}^N \binom{h_1}{l+1} (-\delta_o)^{h_1-l-1} U(h_1)$ by using $U_1(l)$
- $U_2(k-l)$ is $U_2(k-l) = (k-l+1) \sum_{h_2=k-l+1}^N \binom{h_2}{k-l+1} (-\delta_o)^{h_2-k+l-1} U(h_2)$

The transformed function of $f(\tau)$ is $F(k) = \sum_{l=0}^k U_2(l)U_2(k-l)$ due to the theorem in Eq. 3. After these operations

$$F(k) = \sum_{l=0}^k \sum_{h_1=l+1}^N \sum_{h_2=k-l+1}^N (l+1)(k-l+1) \binom{h_1}{l+1} \binom{h_2}{k-l+1} (-\delta_o)^{h_1+h_2-k-2} U(h_1)U(h_2) \tag{27}$$

is obtained. If DTM is applied to Eq. 14, the following transformed equation is found.

$$0 = \sum_{h_1=k+1}^N \binom{h_1}{k} (-\delta_o)^{h_1-k} W(h_1) + a_4 \sum_{l=0}^k \sum_{h_1=l+1}^N \sum_{h_2=k-l+1}^N (l+1)(k-l+1) \binom{h_1}{l+1} \binom{h_2}{k-l+1} (-\delta_o)^{h_1+h_2-k-2} U(h_1)U(h_2) \tag{28}$$

Since q is equal to 2, this last equation is quite different from Eq. 20. It is quite difficult to obtain equation system in $q = 1$ solution for $q = 2$. Instead, the transformed function at the previous sampling time is used for $f(\tau) = u'(\tau - \delta_o)^2$.

The transformed function of $f(\tau) = u'(\tau - \delta_o)u'(\tau - \delta_o)$

$$F(k) = \sum_{l=0}^k (l+1)(k-l+1)U_{\tau-\delta_o}(l+1)U_{\tau-\delta_o}(k-l+1) \tag{29}$$

Thus, Eq. 14 is transformed as follows.

$$0 = \sum_{h_1=k+1}^N \binom{h_1}{k} (-\delta_o)^{h_1-k} W(h_1) + a_4 \sum_{l=0}^k (l+1)(k-l+1)U_{\tau-\delta_o}(l+1)U_{\tau-\delta_o}(k-l+1) \tag{30}$$

Since functions $U_{\tau-\delta_o}$ are found in the previous step, there are no nonlinear terms in Eq. 30. Thus, a system of linear equations for Eq. 30 can be obtained as Eq. 31.

$$\begin{pmatrix} \binom{1}{0}(-\delta_o)^1 & \binom{2}{0}(-\delta_o)^2 & \cdots & \cdots & \binom{N}{0}(-\delta_o)^N \\ 0 & \binom{2}{1}(-\delta_o)^1 & \cdots & \cdots & \binom{N}{1}(-\delta_o)^{N-1} \\ 0 & 0 & \ddots & \cdots & \vdots \\ 0 & 0 & 0 & \ddots & \vdots \\ 0 & 0 & 0 & 0 & \binom{N}{N-1}(-\delta_o)^1 \end{pmatrix} \begin{pmatrix} W(1) \\ W(2) \\ \vdots \\ W(N-1) \\ W(N) \end{pmatrix} + a_4 \begin{pmatrix} F(0) \\ F(1) \\ \vdots \\ F(N-2) \\ F(N-1) \end{pmatrix} = \begin{pmatrix} 0 \\ 0 \\ \vdots \\ 0 \\ 0 \end{pmatrix} \quad (31)$$

Eq. 20 in the first solution is replaced by Eq. 30. Eq. 31 is below as more compact form.

$$\mathbf{A}_4 \mathbf{W} + \alpha_4 \mathbf{F} = \mathbf{0} \quad (32)$$

If \mathbf{W} in Eq. 32 is substituted in Eq. 23 equations below are found.

$$\mathbf{U} = -\mathbf{A}_1^{-1} \mathbf{A}_2 + \alpha_4 \mathbf{A}_1^{-1} \left(\mathbf{A}_3 \left(\mathbf{A}_4^{-1} \mathbf{F} \right) \right) \quad (33)$$

$$\mathbf{W} = -\alpha_4 \mathbf{A}_4^{-1} \mathbf{F} \quad (34)$$

Case 3

In this case, Eq. 13 and 14 is handled for $q = 3$. In this solution, the approach in solution $q = 2$ is repeated. Let the function is $f(\tau) = u'(\tau - \delta_o)^3$ to be applied DTM. Mathematical operations are included in the appendix and the transformed function is as follows.

$$F(k) = \sum_{l=0}^k \sum_{m=0}^l \sum_{h_1=m+1}^N \sum_{h_2=l-m+1}^N \sum_{h_3=k-l+1}^N (m+1)(l-m+1)(k-l+1) \\ \times \binom{h_1}{m+1} \binom{h_2}{l-m+1} \binom{h_3}{k-l+1} (-\delta_o)^{h_1+h_2+h_3-k-3} U(h_1)U(h_2)U(h_3) \quad (35)$$

Because of the same problem encountered in the second solution, the transformed functions at the previous sampling time (δ_o) are utilized. Mathematical transaction is the following order.

$f(\tau) = u'(\tau - \delta_o)u'(\tau - \delta_o)u'(\tau - \delta_o)$ is transformed to

$$F(k) = \sum_{l=0}^k \sum_{m=0}^l (m+1)(l-m+1)(k-l+1)U_{\tau-\delta_o}(m+1)U_{\tau-\delta_o}(l-m+1)U_{\tau-\delta_o}(k-l+1) \quad (36)$$

Expression of Eq. 14 for $q = 3$ is below.

$$0 = \sum_{h_1=k+1}^N \binom{h_1}{k} (-\delta_o)^{h_1-k} W(h_1) + \\ a_4 \sum_{l=0}^k \sum_{m=0}^l (m+1)(l-m+1)(k-l+1)U_{\tau-\delta_o}(m+1)U_{\tau-\delta_o}(l-m+1)U_{\tau-\delta_o}(k-l+1) \quad (37)$$

The linear equation system of Eq. 37 is the same way as the previous solution as follows.

$$\mathbf{A}_4 \mathbf{W} + \alpha_4 \mathbf{F} = \mathbf{0} \quad (38)$$

6. RESULTS AND DISCUSSION

Eqs. 13 and 14 are solved with the DDE23 function in MatLab[®] software and with MatLab[®]/Simulink software. The solutions of Eqs. 13 and 14 obtained with the Differential Transformation Method (Eqs. 25, 26, 33, 34 and 38) are also solved using MatLab[®] software. The parameter values used in the solutions are $a_1 = 0.05$, $a_2 = 0.6$, $a_3 = 0.001$, $a_4 = 0.001$, $N = 5$, $\delta = 6.4$ and $\delta = 6$.

The results obtained with four different methods, DTM, Multi-Step DTM, Simulink and DDE23, for $q = 3$ and $\delta = 6$ values are compared in Fig.1. The solution of the fundamental DTM which found by using the constant transformed functions values differs from other methods after a certain time. But the accuracy can be increased by selecting the higher N value. However, the result obtained with the transformed functions that take different values at each sampling time (Multi-Step DTM), gives very similar output to Simulink[®] and DDE23 solutions.

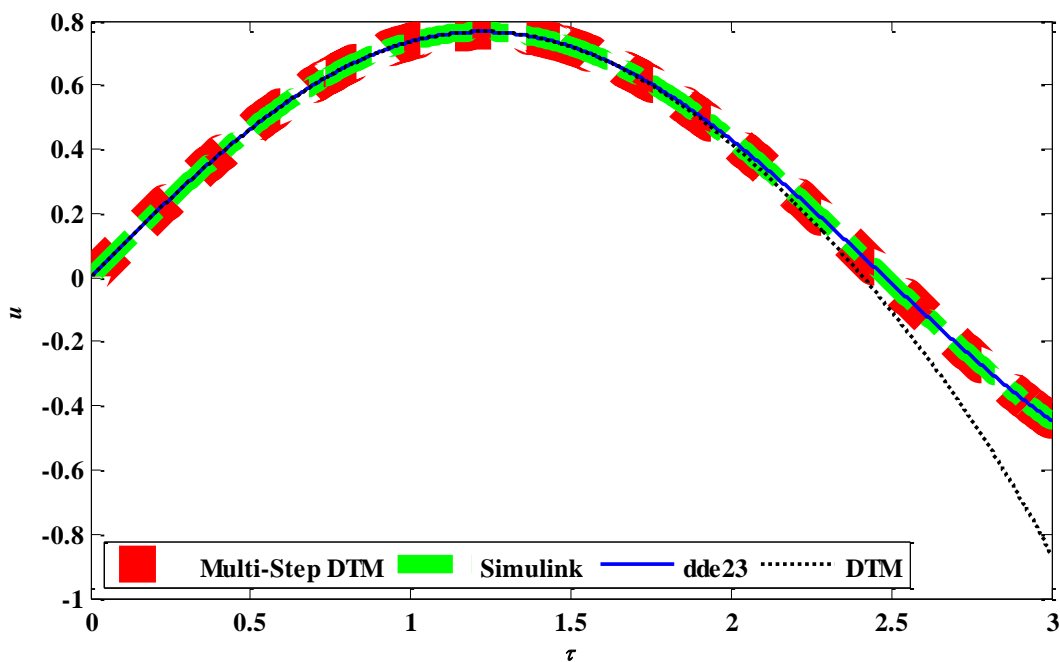


Figure 1. Comparison of Solutions for $q=3$ and $\delta=6$

A simulation for $q=1$ and $\delta=6.4$ values is executed by using Multi-Step DTM, Simulink[®] and DDE23 is shown in Fig. 2. As seen the system is damped depending on the selected parameters and carries on cutting without vibration. In this graph, the result obtained with Runge-Kutta based Simulink[®] is very close to the result obtained with Multi-Step DTM. DDE23 also gives close result to these two methods. Multi-Step DTM has higher values than that of the others when the direction of the motion changes.

u versus τ is demonstrated in Fig. 3. $q=2$ and $\delta=6.4$ values are taken in this solution. A similar interpretation in Fig. 2 can be made for Fig. 3. There can also be observed a damped oscillation. The difference from Fig. 2 is that damping occurs slowly. The reason for this is the q value in the nonlinear damping effect. Magnitude of derivative of u changes between 0 and 1. Consequently, taking the power of the damping term values with a larger q gives smaller values. This causes less damping effect.

The results of the simulation for $q=3$ and $\delta=6.4$ is plotted in Fig. 4. The basic difference of Fig. 4 from Figs. 2 and 3 is that the system is damped slowly which reason as mentioned above. The higher q value makes the magnitude of u' small. Therefore, the amplitude of u is higher than Figs. 2 and 3.

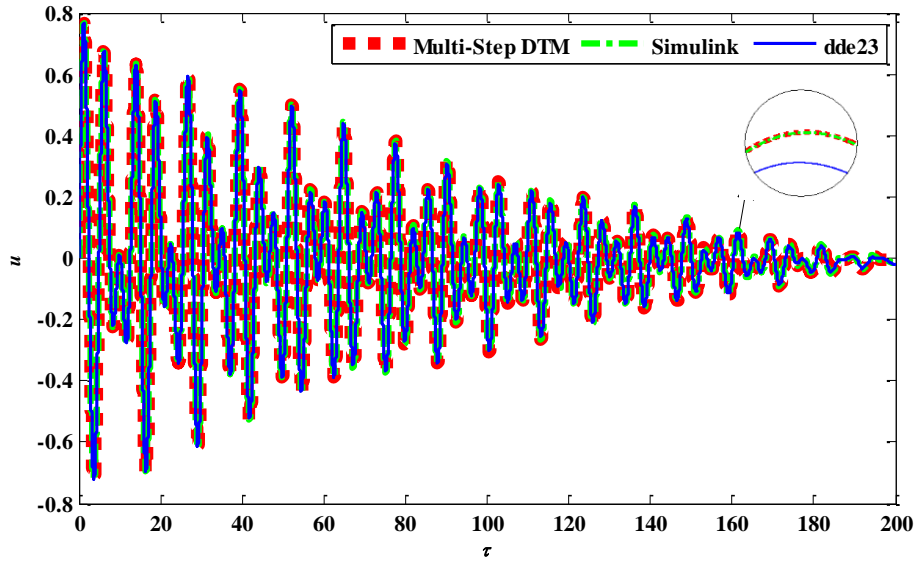


Figure 2. Time Histories for $q=1$ and $\delta=6.4$

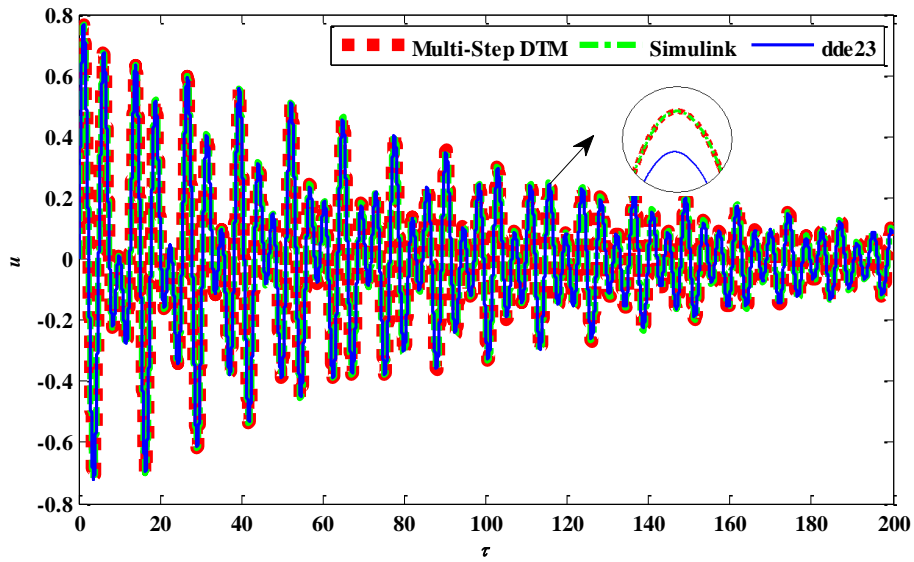


Figure 3. Time Histories for $q=2$ and $\delta=6.4$

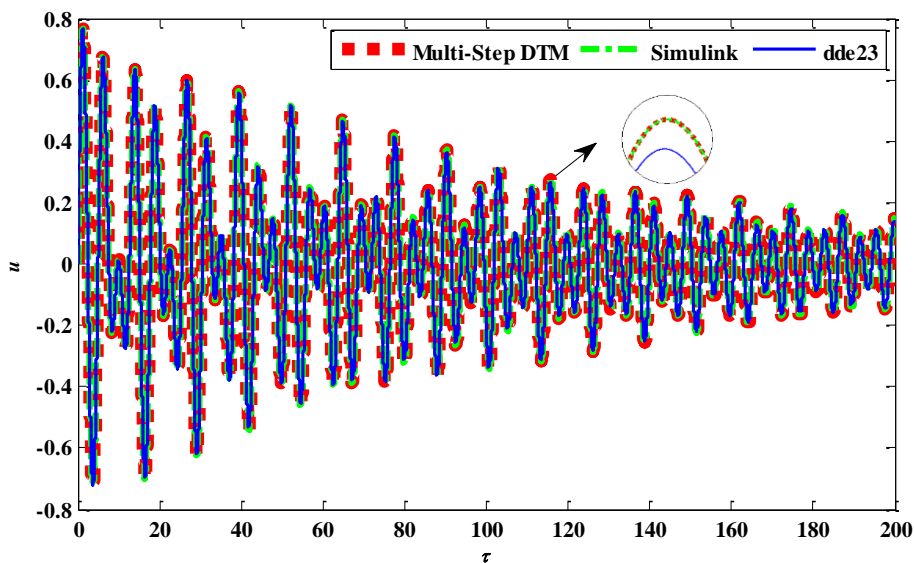


Figure 4. Time Histories for $q=3$ and $\delta=6.4$

The results for the value, $\delta = 6$, the dimensionless time delay, and three different q values are depicted in Fig. 5. Increasing of amplitude for all q values occurs because of the changing of dimensionless time delay. As seen in Fig. 5. (c), increment of amplitude is slower for larger q values. When taking the power of damping terms whose magnitude exceeds 1 with larger q values, larger damping values come out. This proves that the damping effect is higher. In this way, the amplitude rising is slower. In this solution, Multi-Step DTM and Simulink® methods give closer results than DDE23.

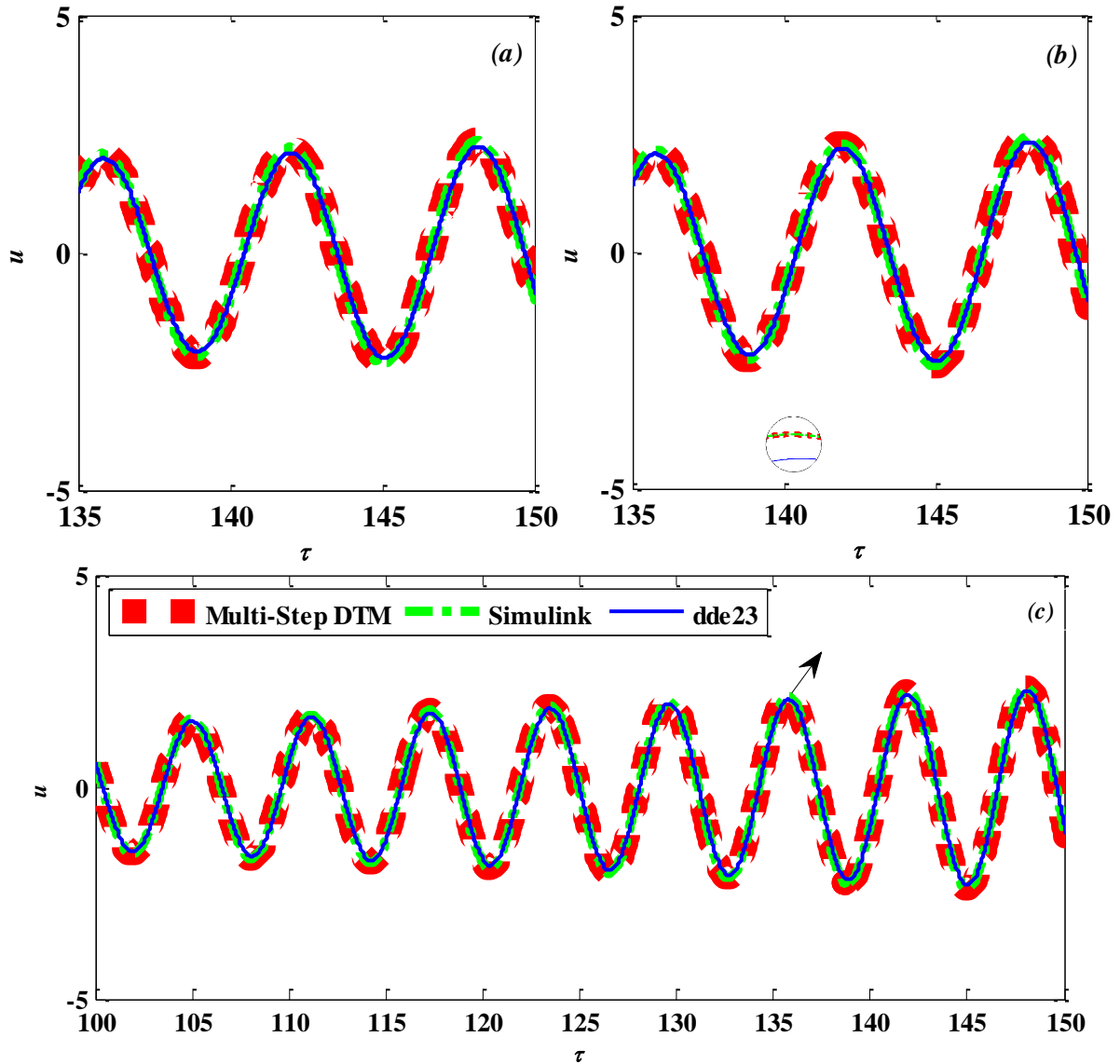


Figure 5. Time Histories for $\delta = 6$. a) $q=1$, b) $q=2$, c) $q=3$

7. CONCLUSIONS

In this paper, differential transformation method is used for solving the mathematical model that can be considered in cutting tool vibrations. The results are compared with that of Simulink® and DDE23. This study shows that the fundamental DTM is not giving valid results always. The study also proves that Multi-Step DTM gives competitive results with other methods. It is also a suitable method for the analysis of physical systems. This article offers a method to overcome the difficulty caused by nonlinear delay terms, by using the values of nonlinear delay terms that found before the delay time.

ACKNOWLEDGEMENT

The authors would like to thank The Scientific and Technological Research Council of Turkey (TUBITAK) for their support of the National Scholarships Programme (2211-A) for PhD Students.

CONFLICT OF INTEREST

No conflict of interest was declared by the authors.

REFERENCES

- Abdel, I. H., & Hassan, H. (2002). Different applications for the differential transformation in the differential equations. *Applied Mathematics and Computation*, 129(2-3), 183-201. doi:[10.1016/S0096-3003\(01\)00037-6](https://doi.org/10.1016/S0096-3003(01)00037-6)
- Altintas, Y. (2012). *Manufacturing Automation*. New York: Cambridge University Press.
- Arikoğlu, A., & Özkol, İ. (2005). Solution of boundary value problems for integro-differential equations by using differential transform method. *Applied Mathematics and Computation*, 168(2), 1145-1158. doi:[10.1016/j.amc.2004.10.009](https://doi.org/10.1016/j.amc.2004.10.009)
- Arikoğlu, A., & Özkol, İ. (2006a). Solution of difference equations by using differential transform method. *Applied Mathematics and Computation*, 174(2), 1216-1228. <https://doi.org/10.1016/j.amc.2005.06.013>
- Arikoğlu, A., & Özkol, İ. (2006b). Solution of differential-difference equations by using differential transformation method. *Applied Mathematics and Computation*, 181(1), 153-162. doi:[10.1016/j.amc.2006.01.022](https://doi.org/10.1016/j.amc.2006.01.022)
- Arikoğlu, A., & Özkol, İ. (2008). Solutions of integral and integro-differential equation systems by using differential transform method. *Computers and Mathematics with Applications*, 56(9), 2411-2417. doi:[10.1016/j.camwa.2008.05.017](https://doi.org/10.1016/j.camwa.2008.05.017)
- Astakhov, V. P. (2004). The assessment of cutting tool wear. *International Journal of Machine Tools and Manufacture*, 44(6), 637-647. doi:[10.1016/j.ijmactools.2003.11.006](https://doi.org/10.1016/j.ijmactools.2003.11.006)
- Ayaz, F. (2004). Solutions of the system of differential equations by differential transform method. *Applied Mathematics and Computation*, 147(2), 547-567. doi:[10.1016/S0096-3003\(02\)00794-4](https://doi.org/10.1016/S0096-3003(02)00794-4)
- Benhammouda, B., & Leal, H. V. (2016). A new multi-step technique with differential transform method for analytical solution of some nonlinear variable delay differential equations. SpringerPlus, 5, 1723. doi:[10.1186/s40064-016-3386-8](https://doi.org/10.1186/s40064-016-3386-8)
- Bozdogan, K. B., & Ozturk, D. (2014). Free vibration analysis of the tube-in-tube tall buildings with the differential transform method. *Advances in Structural Engineering*, 17(9), 1271-1279. doi:[10.1260/1369-4332.17.9.1271](https://doi.org/10.1260/1369-4332.17.9.1271)
- Bozdogan, K. B., & Aydin, S. (2016). Lateral stability analysis of multistory buildings using the differential transform method. *Structural Engineering and Mechanics*, 57(5), 861-876. doi:[10.12989/sem.2016.57.5.861](https://doi.org/10.12989/sem.2016.57.5.861)
- Chen, S-S., & Chen, C-K. (2009). Application of the differential transformation method to the free vibrations of strongly non-linear oscillators. *Nonlinear Analysis: Real World Applications*, 10(2), 881-888. doi:[10.1016/j.nonrwa.2005.06.010](https://doi.org/10.1016/j.nonrwa.2005.06.010)
- Chowdhury, M. A., Khalil, M. K., Nuruzzaman, D. M., & Rahaman, M. L. (2011). The effect of sliding speed and normal load on friction and wear property of aluminium. *International Journal of Mechanical & Mechatronics Engineering*, 11(1), 53-57.
- El-Shahed, M. (2008). Application of differential transformation method to non-linear oscillatory systems. *Communications in Nonlinear Science and Numerical Simulation*, 13(8), 1714-1720. doi:[10.1016/j.cnsns.2007.03.005](https://doi.org/10.1016/j.cnsns.2007.03.005)

- Gokdogan, A., Merdan, M., & Yıldırım, A. (2012). Differential transformation method for solving a neutral functional-differential equation with proportional delays. *Caspian Journal of Mathematical Sciences*, 1(1), 31-37.
- Hatami, M., Ganji, D. D., & Sheikholeslami, M. (2017). *Differential Transformation Method For Mechanical Engineering Problems*. Elsevier Academic Press. WOS:000409365500010
- Jang, M-J., Chen, C-L., & Liy, Y-C. (2000). On solving the initial-value problems using the differential transformation method. *Applied Mathematics and Computation*, 115(2-3), 145-160. doi:[10.1016/S0096-3003\(99\)00137-X](https://doi.org/10.1016/S0096-3003(99)00137-X)
- Karakoç, F., & Bereketoğlu, H. (2009). Solutions of delay differential equations by using differential transform method. *International Journal of Computer Mathematics*, 86(5), 914-923. doi:[10.1080/00207160701750575](https://doi.org/10.1080/00207160701750575)
- Kuo, B-L., & Lo, C-Y. (2009). Application of the differential transformation method to the solution of a damped system with high nonlinearity. *Nonlinear Analysis: Theory, Methods & Applications*, 70(4), 1732-1737. doi:[10.1016/j.na.2008.02.056](https://doi.org/10.1016/j.na.2008.02.056)
- Kurnaz, A., & Oturanç, G. (2005). The differential transform approximation for the system of ordinary differential equations. *International Journal of Computer Mathematics*, 82(6), 709-719. doi:[10.1080/00207160512331329050](https://doi.org/10.1080/00207160512331329050)
- Maekawa, K., Kitagawa, T., Shirakashi, T., & Usui, E. (1989). Analytical prediction of flank wear of carbide tools in turning plain carbon steels II: prediction of flank wear. *Bull. Japan. Soc. Prec. Eng*, 23(2), 126-133. WOS:A1989AN12800007
- Mirzaee, F. (2011). Differential transform method for solving linear and nonlinear systems of ordinary differential equations. *Applied Mathematical Sciences*, 5(70), 3465-3472.
- Momani, S., & Ertürk, V. S. (2008). Solutions of non-linear oscillators by the modified differential transform method. *Computers and Mathematics with Applications*, 55(4), 833-842. doi:[10.1016/j.camwa.2007.05.009](https://doi.org/10.1016/j.camwa.2007.05.009)
- Rebenda, J., & Šmarda, Z. (2017). A differential transformation approach for solving functional differential equations with multiple delays. *Commun Nonlinear Science and Numerical Simulation*, 48, 246-257. doi:[10.1016/j.cnsns.2016.12.027](https://doi.org/10.1016/j.cnsns.2016.12.027)
- Süngü, İ. Ç., & Demir, H. (2012). Diferansiyel Dönüşüm/Sonlu Fark Yöntemi İle Denklem Sistemlerinin Çözümleri. *e-Journal of New World Sciences Academy*, 7(2), 66-73.
- Šmarda, Z., Diblík, J., & Khan, Y. (2013). Extension of the differential transformation method to nonlinear differential and integro-differential equations with proportional delays. *Advances in Difference Equations*, 69. doi:[10.1186/1687-1847-2013-69](https://doi.org/10.1186/1687-1847-2013-69)
- Tabatabaei, K., & Gunerhan, E. (2014). Numerical solution of duffing equation by the differential transform method. *Applied Mathematics & Information Sciences Letters*, 2(1), 1-6. doi:[10.12785/amisl/020101](https://doi.org/10.12785/amisl/020101)
- Taylor, F. W. (1907). On the art of cutting metals. *Transactions of the ASME*, 28, 31-350.
- Thongmoon, M., & Pusjuso, S. (2010). The numerical solutions of differential transform method and the Laplace transform method for a system of differential equations. *Nonlinear Analysis: Hybrid Systems*, 4(3), 425-431. doi:[10.1016/j.nahs.2009.10.006](https://doi.org/10.1016/j.nahs.2009.10.006)
- Villafuerte, L., & Chen-Charpentier, B. M. (2012). A random differential transform method: Theory and applications. *Applied Mathematics Letters*, 25(10), 1490-1494. doi:[10.1016/j.aml.2011.12.033](https://doi.org/10.1016/j.aml.2011.12.033)
- Zanger, F., & Schulze, V. (2013). Investigations on mechanisms of tool wear in machining of Ti-6Al-4V using FEM simulation. *Procedia CIRP*, 8, 158-163. doi:[10.1016/j.procir.2013.06.082](https://doi.org/10.1016/j.procir.2013.06.082)
- Zhou, J. K. (1986) *Differential Transformation and its Application for Electrical Circuit*. Wuhan: Huazhong University Press.

APPENDIX

Transformed function of $u(\tau - \delta_o)$

$$U_1(k) = \sum_{h_1=k}^N \binom{h_1}{k} (-\delta_o)^{h_1-k} U(h_1) \quad (\text{A1})$$

Transformed function of $u'(\tau - \delta_o)$

$$U_2(k) = (k+1)U_1(k+1) \quad (\text{A2})$$

Transformed function of $h(\tau) = u'(\tau - \delta_o)^2$

$$H(k) = \sum_{l=0}^k U_2(l)U_2(k-l) \quad (\text{A3})$$

$$f(\tau) = u'(\tau - \delta_o)^3 \text{ is expressed as } f(\tau) = h(\tau)u'(\tau - \delta_o).$$

Transformed function of $f(\tau) = h(\tau)u'(\tau - \delta_o)$

$$F(k) = \sum_{l=0}^k H(l)U_2(k-l) \quad (\text{A4})$$

$H(k)$ in A3 is written in A4.

$$F(k) = \sum_{l=0}^k \sum_{m=0}^l U_2(m)U_2(l-m)U_2(k-l) \quad (\text{A5})$$

Using A1 and A2 equations, $U_2(k)$ in A2 is arranged as follows to be used in A5.

$$U_2(l) = (l+1) \sum_{h_1=l+1}^N \binom{h_1}{l+1} (-\delta_o)^{h_1-l-1} U(h_1) \quad (\text{A6})$$

$$U_2(k-l) = (k-l+1) \sum_{h_2=k-l+1}^N \binom{h_2}{k-l+1} (-\delta_o)^{h_2-k+l-1} U(h_2) \quad (\text{A7})$$

Transformed function of $f(\tau) = u'(\tau - \delta_o)^3$ is found as below.

$$F(k) = \sum_{l=0}^k \sum_{m=0}^l \sum_{h_1=m+1}^N \sum_{h_2=l-m+1}^N \sum_{h_3=k-l+1}^N (m+1)(l-m+1)(k-l+1) \times \binom{h_1}{m+1} \binom{h_2}{l-m+1} \binom{h_3}{k-l+1} (-\delta_o)^{h_1+h_2+h_3-k-3} U(h_1)U(h_2)U(h_3) \quad (\text{A8})$$



Failure Analysis of Hybrid Glass Reinforced Composites in Polymeric Industries

Dickson David OLODU^{1*}

¹Department of Mechanical Engineering, Faculty of Engineering, Benson Idahosa University, PMB 1100, Benin City, Edo State, Nigeria

Keywords	Abstract
Failure Analysis Fracture Modes Hybrid Glass Reinforced Composite Impact Load	This research deals with the failure analysis of hybrid glass reinforced composites in polymeric industries. In this research, fourteen specimens with different compositions were developed. The produced test specimens had a dimension of 210mm length, 150mm width and 50mm thickness which were in accordance with American Society for Testing and Materials (ASTM). The fourteen test specimens produced were subjected to impact test. The critical stress, shear stress and stress distribution for mode I and mode II were investigated and results were obtained. The results obtained shows that specimen A had an optimum critical and shear stress of 9.32 MPa and 25.1 MPa for mode I while specimen C had an optimum critical and shear stress of 2.49 MPa and 7.03 MPa for mode II respectively. It was also observed that specimen I which contained 12 plies of soft mat reinforcement required the least stress magnitude to grow the crack, while specimen C which contained 2 plies of woven roving and one ply of hat mat experienced the highest critical stress. Hence, adequate percentage composition of E-glass and polyester reduces failure in hybrid glass composites in polymeric industries.

Cite

Olodu D. D., (2021). Failure Analysis of Hybrid Glass Reinforced Composites in Polymeric Industries. *GU J Sci, Part A*, 8(1), 123-134.

Author ID / (ORCID Number)

Dickson David Olodu, 0000-0003-3383-2543

Article Process

Submission Date	14.11.2020
Revision Date	13.01.2021
Accepted Date	11.03.2021
Published Date	29.03.2021

1. INTRODUCTION

Failure of composite materials when subjected to impact load results to catastrophic failure which poses great challenges in polymeric industries. Mueller & Krobjilowski (2004) examined the fibre-reinforced hybrid composite laminates at different fraction volume of composite materials which involved epoxy resin, plain-woven glass fabric and textile satin fabric. According to Mueller & Krobjilowski (2004), fracture toughness of a material had immense importance in the determination of the resistance of the material to crack propagation. Therefore, in their research, impact behaviour and fracture toughness of the laminates were examined based on American Society for Testing and Materials (ASTM-D256), they analysed the specimen configuration which includes the selection of different notch depths, fibre proportion and orientations. Based on their study, the fracture toughness was found to increase continuously with increased volume of glass fabric and significantly depends on the notch size. The experimental results were validated using analysis of variance (ANOVA) technique, and it was found that the percentage of glass content was approximately 80%, while notch depth and orientation occupied 20% of the composition. Krueger (2006) in his investigation on computational fracture mechanics for composites found that, 'inter-laminar fracture mechanics proved useful for characterising the onset of delamination in composites'. The fracture toughness characterisation and inter-laminar fracture mechanics analysis tools were described demonstratively using applications on the structural level. Dhakal et al., (2006) experimentally investigated

*Corresponding Author E-mail: dolodu@biu.edu.ng

flax, hemp, and kenaf fibres in polypropylene binder for all hybrid fleeces in which the blending ratios were varied from 50/50 to 70/30 natural fibre/polymeric fibre composition. In their study, glass fibre/polypropylene mats were used as reference material. The influence of process temperature on the impact strength and tensile strength of the different composite materials reinforced by natural fibres and glass fibres were determined based on the fibre type. Williams (1978) in his analysis of the fracture mechanics of composites failure reviewed how fracture mechanism can be applied to the various fracture modes observed in composites. It was shown that conventional methods were used for short-fibre composites while the oriented laminates undergo delamination. The importance of delamination toughness in determining composite behaviour was emphasized and details of the various test methods and analysis techniques were given and finally, some discussions of the more complex failures seen in cross-ply laminates were also presented in his study. Pahizgar et al. (1982) applied linear elastic fracture mechanics for the study of orthotropic materials, it was shown that the fracture toughness of unidirectional composites was independent of the crack length but depends on crack-fibre orientation. To verify these claims, glass epoxy material was used. The fracture toughness for different crack-fibre orientations were obtained by utilising Solid Sap Finite Element Program and compact tension specimens. Hence, an empirical formula relating to the fracture toughness of the material for different crack-fibre orientation was found. Olodu & Osarenmwinda (2018) investigated the empirical model of injection moulded high density polyethylene-grass composite. In their study, they concluded that process parameter such as temperature and percentage by volume of the composite material contributes to the strength and failure of composite materials.

This study investigates the failure analysis of hybrid glass reinforced composites in polymeric industries.

2. MATERIALS AND METHODS

2.1. Materials

This research was carried out on samples fabricated by randomly varying plies of reinforcements in form of woven roving, hard and soft E-glass fibre mats, combined in unsaturated polyester resin (specific gravity 1.12, viscosity of 65cps and gel time of 25 min) matrix. The catalyst and accelerator used were methyl ethyl ketone peroxide (MEKP) and cobalt respectively due to their compatibility in polyester as curing agents at ambient temperature condition.

2.2. Reinforced Composite Specimen Manufacture and Preparation

The hand lay-up method was used for the production of 14 samples which consist of the randomly varied E-glass fibre reinforcement plies, neatly laid in an already prepared mould measuring $210\text{ mm} \times 150\text{ mm} \times 50\text{ mm}$. Hence, the reinforcement was impregnated with catalysed polyester resin, and allowed for a period of one month to completely cure at ambient condition. These tests samples were cut into 28 specimens, 14 of these samples were compact tension (CT) specimens used for fracture mechanics test and the other 14 specimens were for impact tests respectively. The developed test specimens were cut using the hack saw in accordance with the ASTM and ISO standard for fracture mechanics and impact tests respectively for composite materials (Figure 1).

2.3. Fracture Mechanics Assumptions in Reinforced Composite Analysis

The following assumptions were made in this study:

- i. Resin interlayer is isotropic and has uniform thickness.
- ii. The plies or layers are perfectly bonded in the laminate everywhere except in the region where a flaw is initiated or present from the surface notched tip.
- iii. There is perfect bonding between the resin and the fibre.
- iv. The resin and the fibres are experiencing the same stress due to the applied impact force.
- v. Crack tip have zero radius.

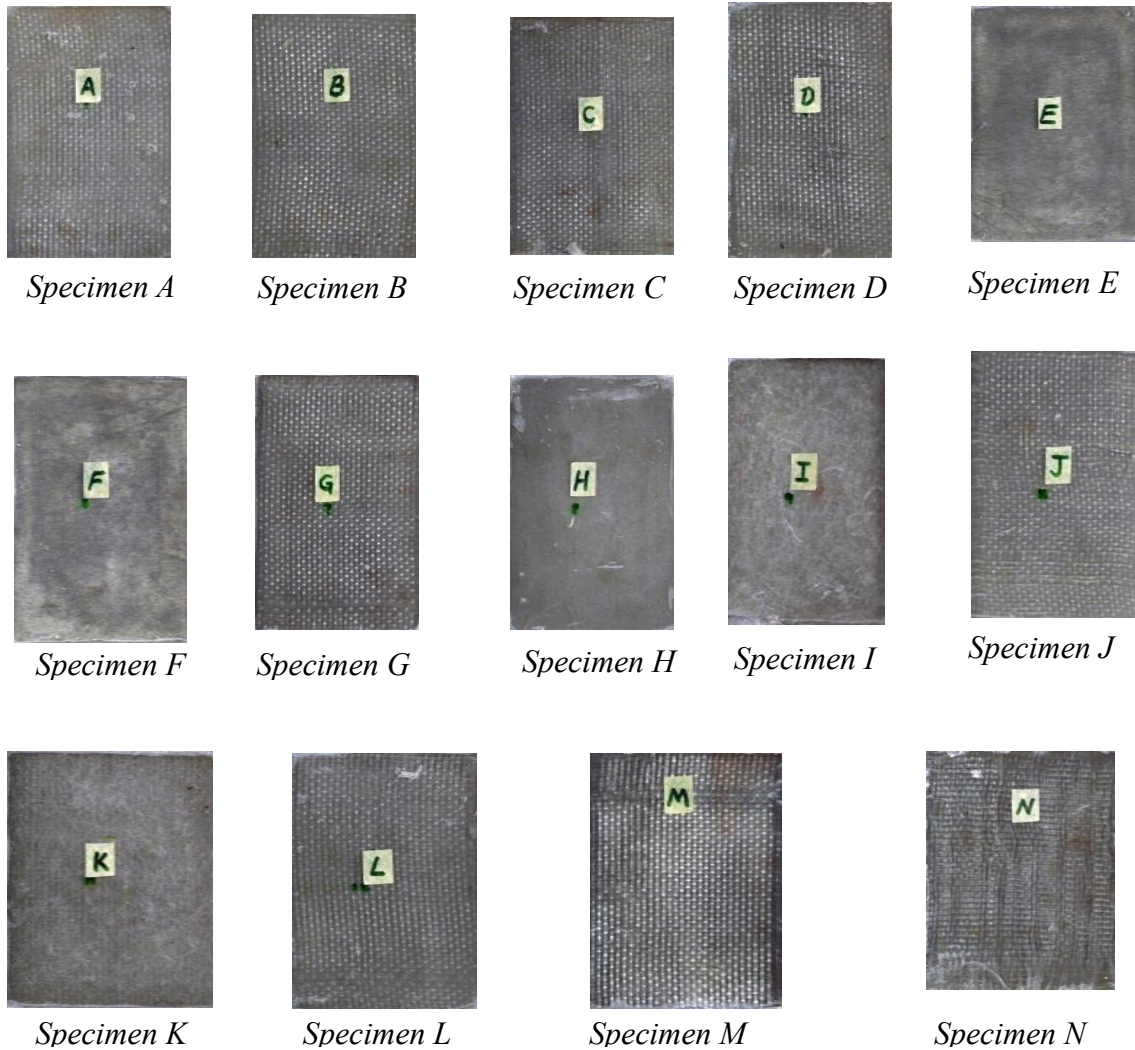


Figure 1. Samples of Reinforced Polyester Composite Plates Manufactured

2.4. Linear Elastic Fracture Mechanics

In the analysis of the fracture mechanics of reinforced polyester composite, the Linear Elastic Fracture Mechanics (LEFM) which according to Williams (1978), was used to analysed elastic stresses in the neighbourhood of pre-existent cracks of specified intensity, for which its purpose is to ascertain the level of applied stress, σ , at which pre-existent cracks of various sizes and geometries will propagate; and impact test approaches were used, where emphasis is focused on exploring the fracture mechanics at the crack tip of the fibre reinforced composite when subjected to impact force. The test was conducted under plane stress condition.

According to Pahizgar et al. (1982) the proper way to begin a study of fracture in orthotropic materials (reinforced composite material) is to compare their fracture with the fracture of isotropic materials and then model the fracture mechanism as homogeneous anisotropic materials. Based on the principle of LEFM, the following can be stated that:

- a) The crack will advance along the original crack direction.
- b) The crack tip displacements can be separated into three different modes: crack-opening mode (Mode I); edge or in-plane sliding mode (Mode II); and crack tearing or out-plane mode (Mode III).
- c) The crack tip stress and displacement equation for the above modes are given by Westergaard's equations (Equation 2).

2.5. Test Procedures for The Determination of Mode I Stress Intensity Factor, K_I

Before the determination of K_I , the CT specimen composition was manufactured as shown in Figure 2. The CT specimens were drilled to make provision for the pins through which loads were introduced on the test specimens using a U-bracket which is attached to the Universal Testing Mechanic. The loading brackets were properly aligned with the specimen to avoid twisting while the crack propagation takes place (Figure 3).

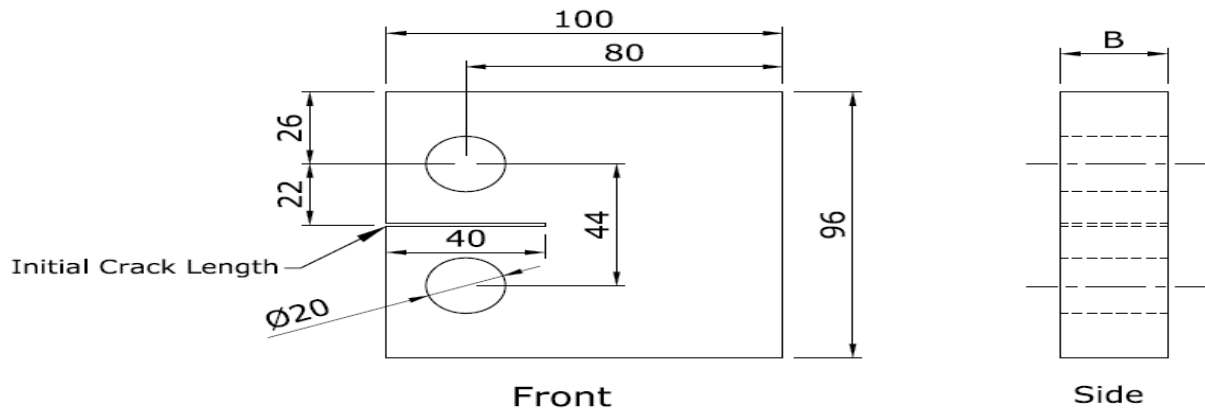


Figure 2. ASTM Standard Pre-Cracked Compact Tension (CT) Specimen

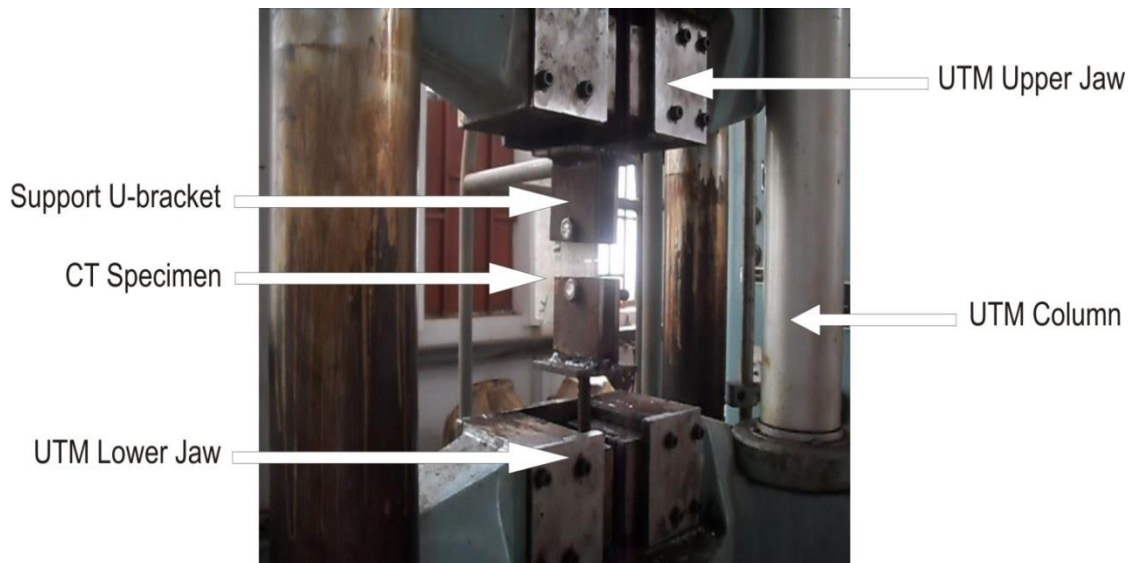


Figure 3. Fracture Test of CT Specimen on the UTM

2.6. The Test Machine Used for The Fracture Test

The test machine used for the fracture test was capable of being operated in displacement controlled mode with constant displacement rates in range of 0.55mm per minute. The load sensing device had accuracy over a load range of within $\pm 1\%$ of the indicated value. The crosshead separation was used to measure the CTOD of the specimen through the loading brackets attached. As the opening displacement increased, the crack growth front advancement along the ligament was marked on the specimen. The load, displacement and crack growth length along the ligament were continuously monitored, measured and recorded till the CT specimen could no longer sustain the loading and thus fractured. During the test, two replicate tests were done for every specimen containing an initial crack of length, 40mm which is $0.25W$ produced on the specimens. The advantage is to force the crack initiated to propagate along a straight line to comply with the Linear Elastic Fracture Mechanics (LEFM) requirements. Another purpose of notching and pre-cracking the test specimen is to simulate an ideal plane crack with essentially zero tip radius which agreed with the assumptions made in stress intensity analyses. Each specimen test record consisted of a plot of the

output of a load versus the displacement and the crack length extension measurement. The conventional plot of load along the y -axis and the displacement along the x -axis was maintained.

2.7 Analysis of Load-Displacement Records and Calculation of K_I

The failure analysis of hybrid glass reinforced composite in polymeric industries were carried out using Equation 1 to 4. The ASTM standards for the mode I stress intensity factor (SIF), K_I calibration for the CT specimen is given by Equation 1;

$$K_I = \frac{P}{BW^{3/2}} f(a_i/W) \quad (1)$$

Where P = maximum load

The expression for K_I determination is accurate to within 0.5%, over the entire range of a/W ($a/W < 1$) as presented in Janssen et al. (2004). The mode II stress intensity factor was obtained using Equation 2;

$$K_{II} = \tau_{n\theta} \sqrt{\pi a} \quad (2)$$

Hence, for a crack length of a , the critical stress, σ_c were determined according to the stress intensity factor criterion using Equation 3;

$$\sigma_c = \frac{K_{IC}}{\sqrt{\pi(a+\ell)}} \quad (3)$$

Where, ℓ = The damage zone at each crack tip which was determined from the experiment during failure along the crack ligament (Idicula et al., 2009).

2.8 Experimental Procedure for Impact Strength Determination

The specimens were cut, after which, the specimen was position in the anvil. The proper position of the impact head (striking edge) and the height of the pendulum were set. After securing the specimen, the pendulum was raised to position and allowed to freely swing towards the specimen to impact it to breaking, because the test was a destructive test similar to the fracture mechanics test (Figure 4).

The energy required to break the specimen was determined from the data recorded on the metering device on the machine. According to Radif & Ali (2001), one method of expressing the impact energy for a composite material by adopting a fracture mechanics approach is in terms of the relation (Equation 4);

$$U = \frac{E}{\phi b(d-c)} \quad (4)$$

Where U = Impact energy; E = Energy in KJ/m² which is registered for the test specimen; b = breadth; d = depth; c = notch; ϕ = a calibration factor which depends on specimen and crack dimension and compliance (Osarenmwinda & Nwachukwu, 2010; Orbulov & Ginzler, 2014; Romanova et al., 2009).



Figure 4. Charpy Impact Test Machine

3. RESULTS AND DISCUSSION

Table 1 shows the mode I stress intensity factor and critical stress for all 14 specimens while Table 2 shows the mode II stress intensity factor and shear stress for all 14 specimens. Furthermore, Figure 5 shows a quadratic relation of mode-I stress intensity factor curve at different critical stress level for all specimens; Figure 6 shows the linear relation of mode-II stress intensity factor at different shear stress level for all specimens; Figure 7 shows the stress distribution around locations ahead of crack for all specimens; Figure 8 shows the fractured compact test specimen after test while Figure 9 shows the impact energy versus impact strength curve. Table 1 shows the mode-I stress intensity factor and critical stress for all 14 specimens while Table 2 shows the mode II stress intensity factor and shear stress for all 14 specimens

Table 1. Mode I Stress Intensity Factor and Critical Stress for All 14 Specimens

Laminate Specimens	Stress Intensity Factor, K_I (MPa.m ^{1/2})	Critical Stress, σ_c (MPa)
A	9.32	25.1
B	6.57	18.31
C	9.49	25.82
D	6.41	17.44
E	6.59	18.36
F	6.59	18.36
G	6.65	18.2
H	4.47	12.19
I	3.02	8.36
J	4.87	13.57
K	4.68	12.88
L	6.17	16.88
M	6.7	18.23
N	4.86	13.22

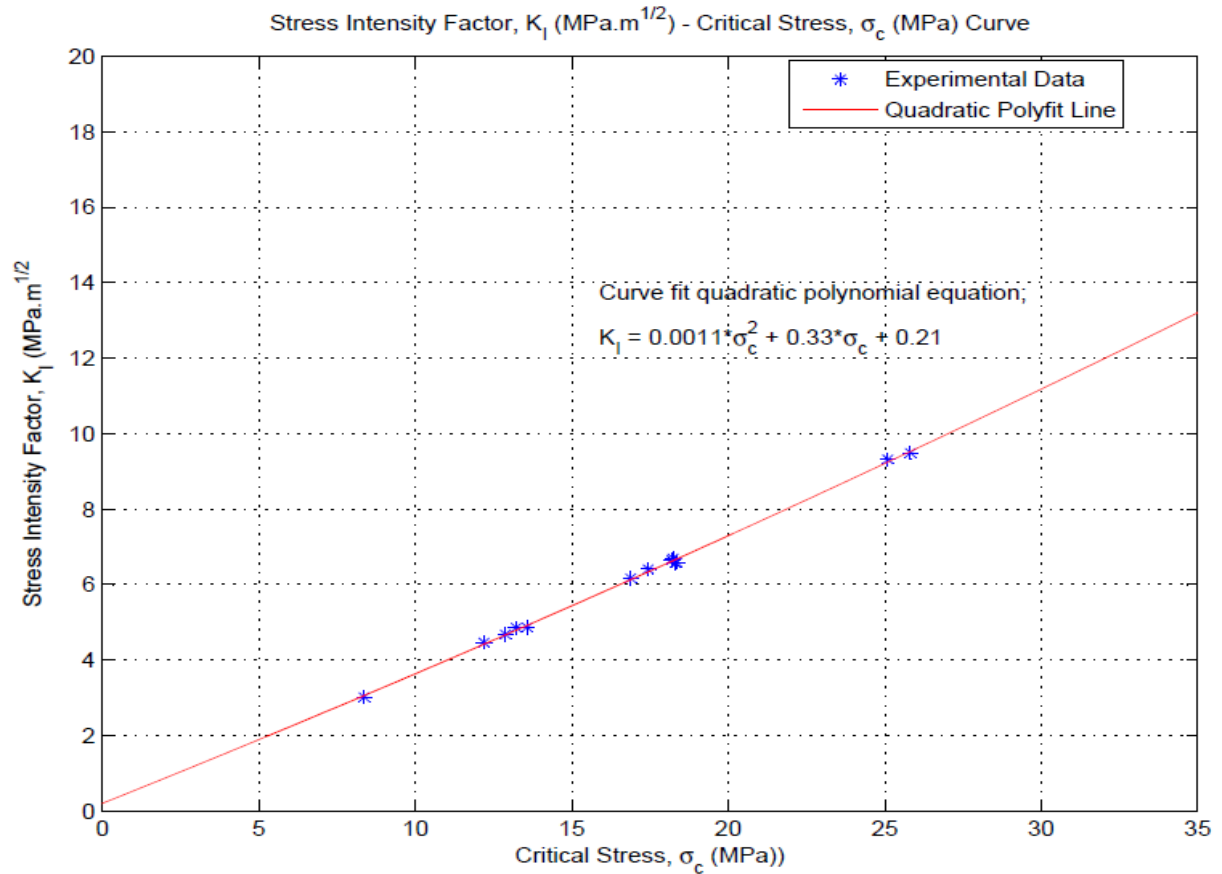


Figure 5. Quadratic Relation of Mode-I Stress Intensity Factor Curve at Different Critical Stress Level for All Specimens

Table 2. Mode II Stress Intensity Factor and Shear Stress for All 14 Specimens

Laminate Specimens	Stress Intensity Factor, K_{II} (MPa.m ^{1/2})	Shear Stress, $\tau_{n\theta}$ (MPa)
A	2.42	6.84
B	1.77	5.00
C	2.49	7.03
D	1.68	4.74
E	1.83	5.15
F	1.78	5.01
G	1.75	4.95
H	1.18	3.32
I	0.81	2.28
J	1.31	3.70
K	1.25	3.53
L	1.63	4.59
M	1.75	4.94
N	1.28	3.60

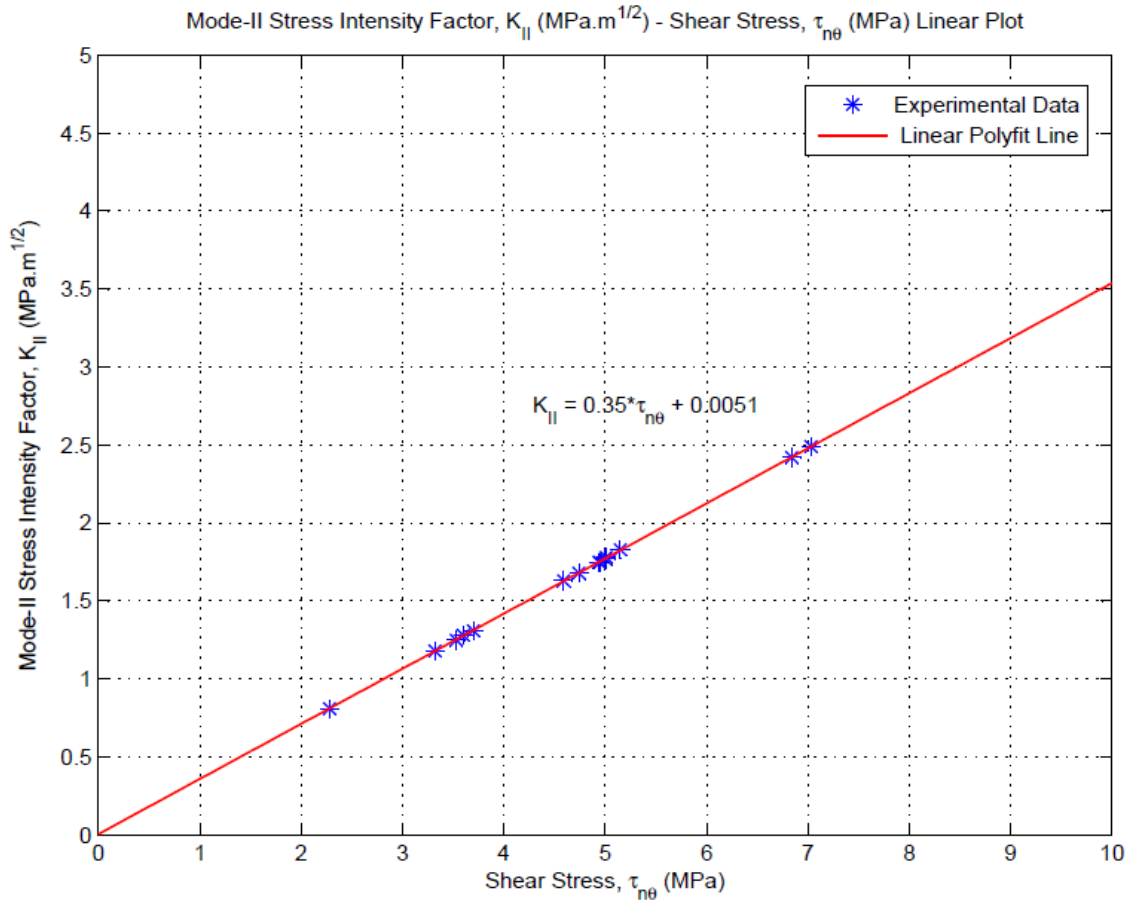


Figure 6. Linear relation of Mode-II Stress Intensity Factor, K_{II} Curve at Different Shear Stress Level for All Specimens

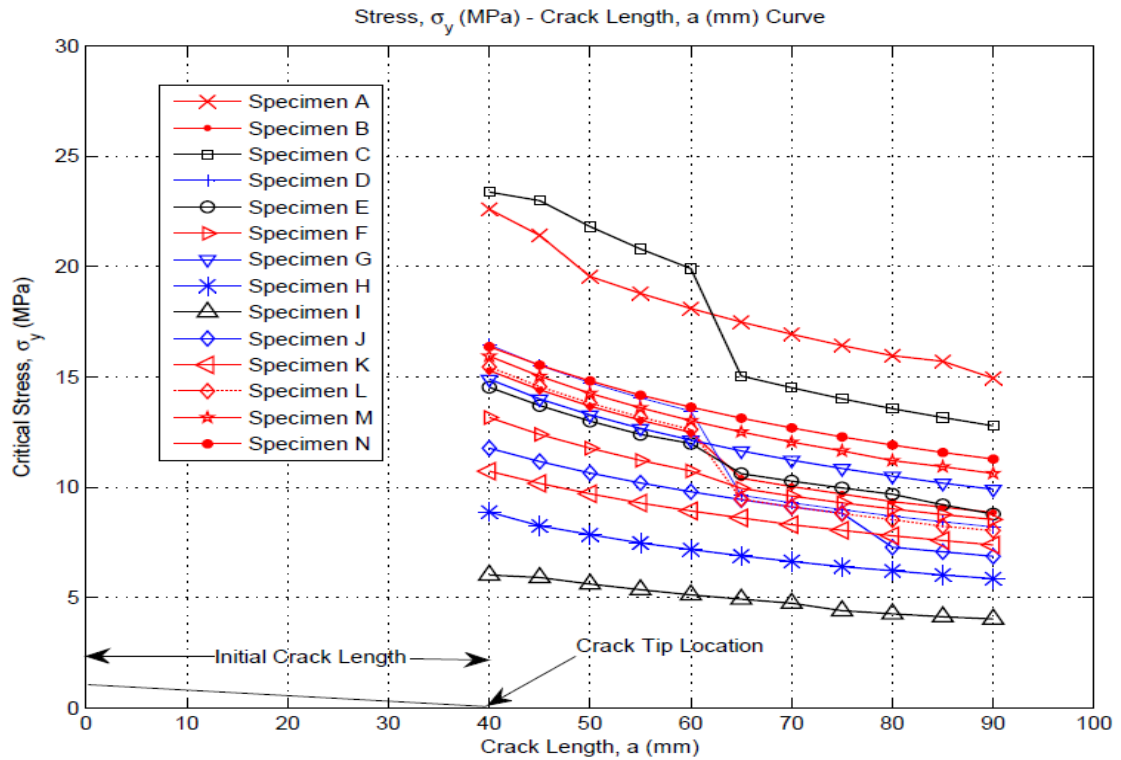


Figure 7. Stress Distribution Around Locations Ahead of Crack, a (mm) For All Specimens



Specimen A



Specimen B



Specimen C



Specimen D



Specimen E



Specimen F



Specimen G



Specimen H



Specimen I



Specimen J



Specimen K



Specimen L



Specimen M



Specimen N

Figure 8. *Fractured CT Test Specimen After Test*

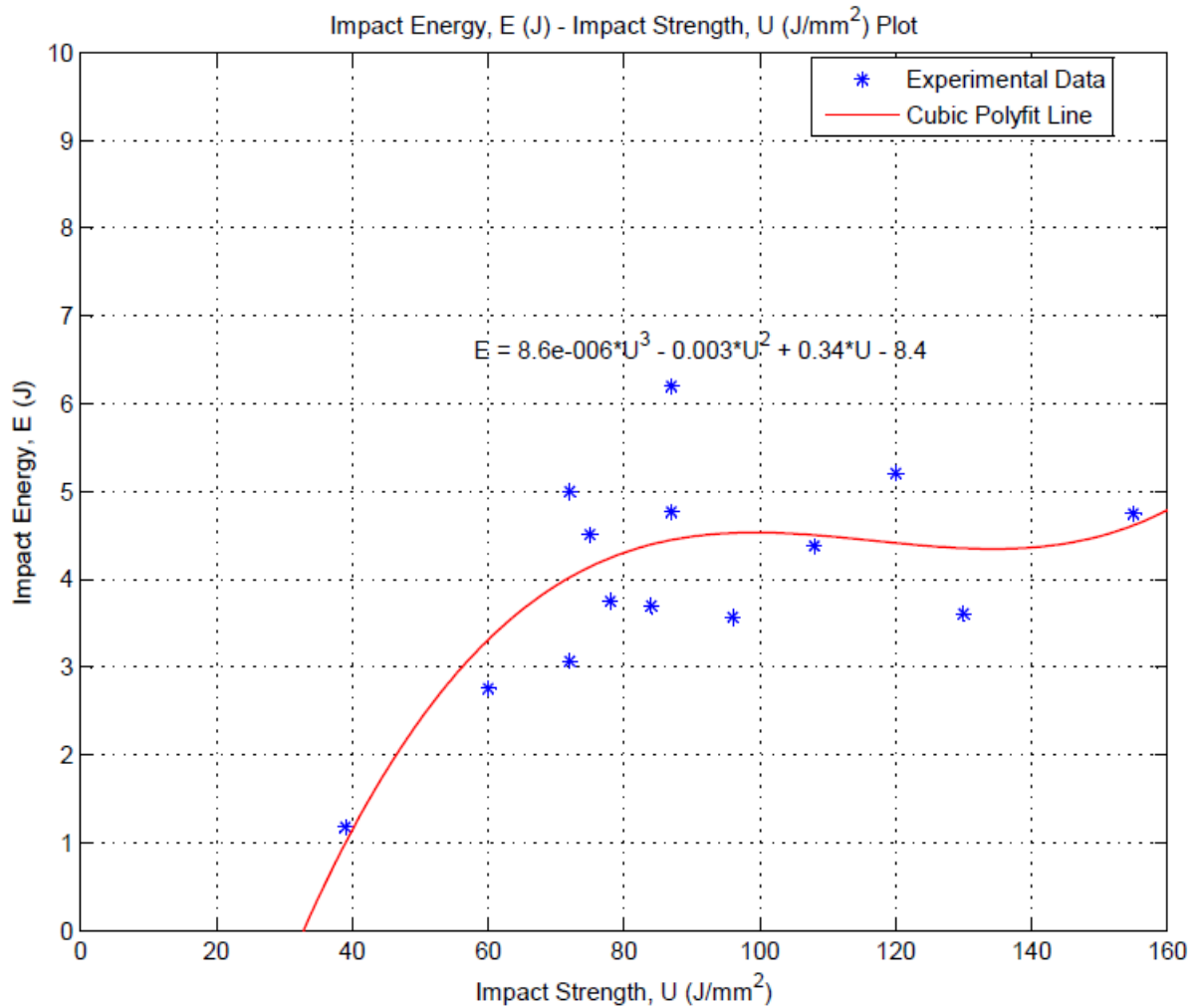


Figure 9. Impact Energy versus Impact Strength Curve

3.1. Discussion of Results

3.1.1. Stress Intensity Factor, K_I , and Critical Stress, σ_c Data Analysis

A factor that was found to be a major influence on the decreasing magnitude of K_I and K_{II} was the increase in thickness of the specimens. This means that the larger the thickness, the higher the volume of materials being subjected to the maximum stress along the point geometric discontinuity with a greater probability of finding a weakened region that cannot resist the maximum stress which will assist the crack growth. This is because; the size effect is related to the increased amount of surface area where cracks initiate. The observed increase of the stress intensity factor, K_I and K_{II} with respect to the critical stress, σ_c as shown in the Figure 5 and 6, having a linear relationship can be related to the above condition, of maximum stress being present at the point of geometric discontinuity in the neighbourhood of a flaw before degenerating into macroscopic crack. As the stress progressively increases, the crack continues to open and grow with ease, which sufficed that the principle of linear elastic fracture mechanics was upheld as indicated by Griffith criterion for the propagation of crack in that it states that; a crack will continue to propagate when the decrease in elastic strain energy is at least equal to the energy required to create the new crack surface (Mueller & Krobjilowski, 2004).

3.1.2. Critical Stress Distribution at Different Crack Length

Using Equation 3 to model the stress distribution near the crack tip, it could be shown that the region around the neighbourhood of the crack tip experienced higher stress state than other regions not around this vicinity. This was expressed in the stress distribution versus crack length curve as shown in Figure 7. Taking a look at the fracture mode of the CT specimens under mode I loading condition, it was observed that fracture of

specimens containing woven roving, namely; specimen A, B, C, D, G, J, K and M with the exception of specimen N, was not all along or in the direction of the original crack. The crack was observed to change direction as it propagates at an angle that was almost at 90° to the horizontal, without any crack growth in the initial crack direction, although this was not the case for all of them as some were seen to grow in the initial crack direction before change direction. The change in crack growth direction was a resistance posed by crack arrest from fibre bridging. This was also observed from the curves to result a decreased in the stress at the location. This could be explained as a change in direction as the crack grows will require a reduced stress level to grow the crack in that direction as the stress intensity at these locations are excessively higher. But for specimens E, F, H, I with the exception of specimen N contained soft and hard mat reinforcements. The cracks were observed to grow along the initial crack direction as a result of the reinforcement composition as this followed the LEFM principle. This could be traced to the form and mechanical properties of the fibre used which could not resist the crack growth efficiently. This shows that composites containing woven roving reinforcement were better fracture resistant composite material than soft and hard reinforcement mats. The weaving pattern of the woven roving was a key factor which contributed to its distinguished performance. From Figure 7, it be shown that specimen I which contained 12 plies of soft mat reinforcement required the least stress magnitude to grow the crack, while specimen C which contained 2 plies of woven roving and one ply of hat mat experienced the highest critical stress.

3.1.3. Failure Analysis of Hybrid Glass Reinforced Composites

Failure analysis was carried out by analysing the appearance of the fractured specimens and review of the slow video motion pictures and the photographs taken of the some samples selected. Figure 8 shows the appearance of fractured surface of specimens subjected to impact, two types of fractures were observed. In the first case laminate failed completely into two pieces, the fibres on the fractured surface were straight indicating minimal fibre pull-outs, and such failure were observed to occur in the case of laminates plies of either soft or hard mats reinforcements. The second type of failure was observed in specimens containing woven roving mats, used as reinforcement or had greater volume fraction of fibre. The fracture surface was characterised by fibre pull-outs and this was an indication that there was resistance from the fibre under the sudden impact force. The fracture appearance was same for all the laminates containing woven roving irrespective of percentage of glass content of either soft or hard mat. Figure 9 indicated an increase in impact strength as the impact energy absorbed by the specimen increased. This shows that the energy absorption capacity of a composite material is dependent on the fibre volume which in turn affects the thickness.

4. CONCLUSION

The research on the failure analysis of hybrid glass reinforced composite in polymeric industries had been achieved. It was observed from the experimental results that woven roving has been seen to possess exceeding resilience and resistance during sudden impact force compared to soft and hard mat reinforcement. It was also observed from the stress intensity and critical stress versus crack length curve, that the crack tip is where the maximum stress exists. It is also the location of the minimum stress intensity factor. This is an indication that glass reinforced polyester composites has the tendencies to resist damage and crack propagation when exposed to sudden impact force, if the internal structure and surface are void of defects and microcracks resulting from blisters, foreign particle, holes and fibre-matrix debonds, that is, the energy required to grow the crack will be inactivated or equal to zero. The mode I fracture toughness, K_{IC} was found to have a value of 2.5 MPa while the mode II fracture toughness, K_{IIC} was 1.3 MPa.

CONFLICT OF INTEREST

There is no conflict of interest in this research article.

REFERENCES

Dhakal, H. N., Zhang, Z. Y., Richardson, M. O. W., & Errajhi, O. A. Z. (2006). The Low Velocity Impact Response of Non-woven Hemp Fibre Reinforced Unsaturated Polyester Composites. Advanced Polymer and Composites (APC) Research Group, Department of Mechanical and Design Engineering, University of Portsmouth. Retrieved from www.elsevier.com.

- Idicula, M., Joseph, K., & Thomas, S. (2009). Mechanical Performance of Short Banana/Sisal Hybrid Fibre Polyester Composite. *Journal of Reinforced Plastics and Composites*, 29(1), 12– 29.
- Janssen, M., Zuidema, J., & Wanhill, R. J. H. (2004). *Fracture Mechanics*. (2nd Edition). New York: Spon Press.
- Krueger, R. (2006). *Fracture Mechanics for Composites: State-Of-The-Art and Its Challenges*. NAFEMS Nordic Seminar: Prediction and Modelling of Failure Using FEA, National Institute of Aerospace, USA. Retrieved from ntrs.nasa.gov
- Mueller, D. H., & Krobjilowski, A. (2004). Improving the Impact Strength of Natural Fibre Reinforced Composites By Specifically Designed Materials and Process Parameter. *International Nonwovens Journal*, 13(4), 31-38.
- Olodu, D. D., & Osarenmwinda, J. O. (2018). Emperical Modelling of Injection Moulded High Density Polyethylene-Grass Composite. *American Journal of Engineering Research (AJER)*, 7(12), 245-250.
- Orbulov, I. N., & Ginsztler, J. (2014). Compressive Behaviour of Metal Matrix Syntactic Foams. *Acta Polytechnica Hungarica*, 9(2), 43-56.
- Osarenmwinda, J. O., & Nwachukwu, J. C. (2010). Development of Composite Material from Agricultural Waste. *International Journal of Engineering Research in Africa*, 3, 42-48.
- Parhizgar, S., Zachary, L. W., & Sun, C. T. (1982). Application of the Principle of Linear Fracture Mechanics to the Composite Materials. *International Journal of Fracture Mechanics*, 20, 3-15.
- Radif, Z. S., & Ali, A. (2001). Fracture Toughness of Kenaf Mat Reinforced Polyester Composite. *Pertanika Journal of Science and Technology*, 99(1), 177-187.
- Romanova, V. A., Balokhonov, R. R., & Schmauder, S. (2009). The Influence of the Reinforcing Particle Shape and Interface Strength on the Fracture Behavior of a Metal Matrix Composite. *Acta Materialia*, 57(1), 97-107.
- Williams, J. G. (1978). Linear Fracture Mechanics. *Advances in Polymer Science*, 27, 69-82.



Case Study for Thermo Mechanical Performance of an Integrated Optic Device via Equation-Based Modelling

Seval DÖNERTAŞ^{1,2*}, Mutlu GÖKKAVAS², Ekmel ÖZBAY^{2,3}, Elif ÖZ ORHAN^{1,4}

¹Gazi University, Department of Advanced Technologies, 06560, Ankara, Turkey

²Bilkent University, Nanotechnology Research Center (NANOTAM), 06800, Ankara, Turkey

³Bilkent University, Department of Electrical and Electronics Engineering, 06800, Ankara, Turkey

⁴Gazi University, Department of Physics, 06560, Ankara, Turkey

Keywords	Abstract
<p><i>Integrated Optical Device</i> <i>Multiphysics</i> <i>Finite Element Analysis</i></p>	<p>An integrated optical device was modeled in the simulation environment via Comsol software. Model implementation, meshing analysis, the definition of material parameters, analyze and module type was introduced, respectively. At the end of this paper; it was understood that the connection of the bodies with different thermal expansion coefficients causes thermal stress accumulation and deformation. The acquired results reveal that fiber-based components can be analyzed with the contribution of the simulation interface. The literature researches were examined in detail and it was found that no study discusses the modeling of the full structure of the fiber optic integrated optic device. So; this study is crucial because it explains how to model an integrated optic device via simulations and leads the researchers about how to make complex meshing analysis in the presence of thin epoxy layers.</p>

Cite

Dönertaş, S., Gökkavas, M., Özbay, E., & Orhan Öz, E. (2021). Case Study for Thermo Mechanical Performance of an Integrated Optic Device via Equation-Based Modelling. *GU J Sci, Part A, 8(1)*, 135-145.

Author ID (ORCID Number)

S. Dönertaş, 0000-0002-3550-1281
M. Gökkavas, 0000-0002-9244-4201
E. Özbay, 0000-0003-2953-1828
E. Öz Orhan, 0000-0002-3949-6141

Article Process

Submission Date 21.12.2020
Revision Date 27.01.2021
Accepted Date 11.03.2021
Published Date 29.03.2021

1. INTRODUCTION

Integrated optics is an area combining fiber-optic and waveguiding technologies. Before signal transmission by light beams, electrical currents or radio waves were the preferred way to convey signals over long distances (Richter, 1989). With the development of fiber optics communication systems, advances in microfabrication technologies, integrated optical technology has emerged as an enabling technology. Low power consumption, smaller size, lower loss, and better reliability ensure that integrated optics is more preferable over competing technologies where available. Lightwave communications, control of microwave components, sensor systems, and data processing are a few application areas of integrated optics technology (John, 1997).

In general, electro-optic phase modulators are known as the simplest integrated optical devices which have applications in defense, navigation and space technologies. In these devices, the joint between an optical chip and input/output fiber is produced by the application of ultraviolet (UV) transparent epoxy. In this paper, we will study a Y-junction integrated optical device (Yang et al., 2014). Explicitly, it splits the incoming light signal into two arms at the end of the waveguide. The proposed integrated optical device is a lithium niobate (LiNbO₃) based component. Actually, in telecommunication applications, LiNbO₃ has high electro-optic coefficients in the near-infrared region of the spectrum, so this material is preferred in the fabrication process of the electro optic modulators (Wooten et al., 2000). Besides this; high Curie

*Corresponding Author, e-mail: sevaldonertas@gmail.com

temperature (1100°C-1180°C) of LiNbO₃ material enables it sufficient to produce low-loss waveguides via metal diffusion (Wooten et al., 2000). Especially; because LiNbO₃ has more than %80 optical transparency at the 1.55 µm telecommunication wavelength, it is a favorable material in optoelectronic applications. After the alignment of the waveguide arms of the LiNbO₃ based optical device and fiber optic pigtail carriers, input and output fibers are glued to both of the device arms. The final product is called a “fiber-coupled integrated optical device” (Tripathi et al., 2007).

Literature surveys about the mechanical behavior at the interface between the fiber-coupled device and optical fiber under thermal variations are investigated. In one research, the deformation was analyzed at the connection region between optical chip and fiber under temperature changes, so thermomechanical simulations at the coupling structure were progressed via finite element analysis (FEA) (Yao et al., 2018).

The reliability of the fiber optic current sensors was studied by conducting thermal tests (Lenner et al., 2017). Also; in this research, the effect of materials with different thermal expansion coefficients was considered to specify the failure modes.

According to another investigation, it is explained that stress is evaluated among basic factors of the mechanical breakdown between chip/epoxy junction (Suchoski and Boivin, 1992). Moreover, the failure of this coupling interface is extremely critical when considered other breakdown mechanisms for integrated optical chips.

Although several studies have been conducted about the mechanical strength of the integrated optical devices, it is clear that detailed investigations related to the theoretical analysis are relatively limited in the publications. So; this paper aims to examine the mechanical durability of the fiber-coupled devices via thermomechanical simulations by using three dimensional (3D) finite element analysis (FEA) method. In this context; the detailed expressions about simulation software, the construction of three-dimensional structural geometry, meshing types, material parameters, boundary conditions, analysis type, and module type were given, respectively. At the end of this study; it is obvious that the motivation related to the thermal simulation of fiber optic devices enhances.

2. MATERIAL AND METHOD

In this study, simulations were performed with COMSOL 5.5 Multiphysics commercial software by using FEA-based equations. COMSOL is a simulation program compatible with modeling experimental applications in a software environment. To solve complex physical problems comprehensively and scientifically, the “COMSOL multiphysics interface” was introduced to this software. Several different modules are combined in the “COMSOL multiphysics interface” such as acoustics, electromagnetics, chemical reactions, mechanics, fluid flow, and heat transfer (Anonymous, 2020a). Since the subject of this study is the investigation of thermomechanical performance, heat transfer, and solid mechanics software modules were utilized for the analysis.

The integrated fiberoptic device-under-study consists of three basic parts: fiber pigtail carriers, optical fibers, optical chip, and waveguide regions as shown in Figure 1. In addition to this, the electrodes which are shown in the figure are employed to create an electro-optic response while driving the device.

2.1. 3D Modelling

At the beginning of the simulation, the 3D geometrical structure of the integrated optical device was modeled with the actual dimensions. The main body of the configuration is an optical chip and its parameters are as follows: optical chip length along y-direction: 24 mm, width along x-direction: 2.6 mm, thickness along z-direction: 1 mm. The detailed structure is illustrated in Figure 2.

As shown in Figure 2; input/output fiber pigtail carriers incorporate two separate components: upper and bottom lower parts. Besides this, the optical fibers are sandwiched between upper and bottom pigtail carriers by sticking with a UV curable epoxy. Since there is a thickness difference between the optical chip

and pigtail carriers, two symmetric covers were attached to the input and output device ends. All of the device components are connected with UV curable epoxy.

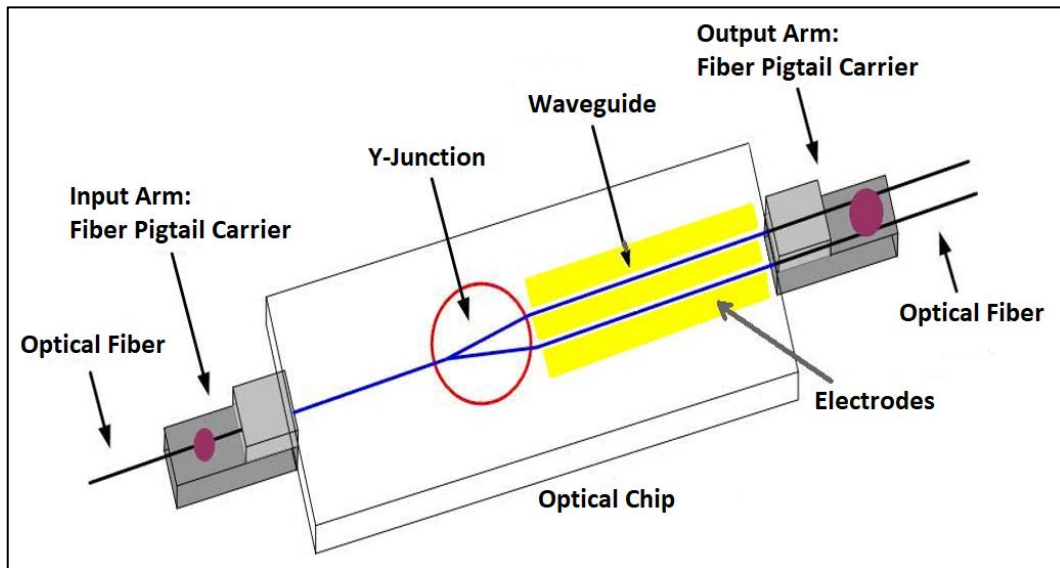


Figure 1. Schematic Configuration of the Integrated Optical Device

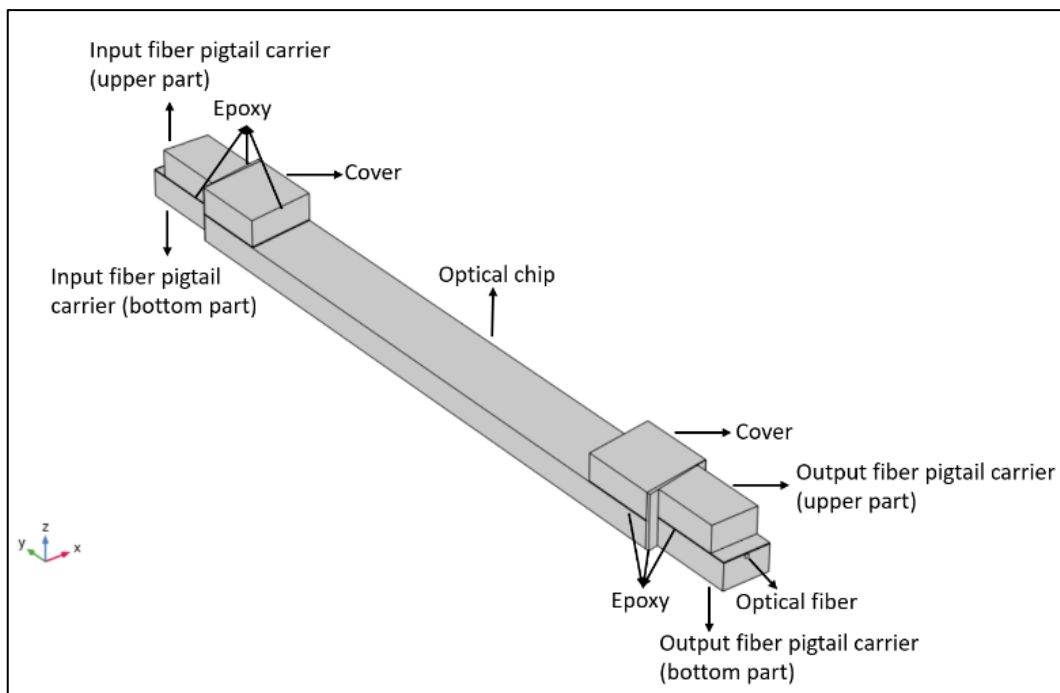


Figure 2. 3D Model of the Integrated Optical Device Structure

2.2. Meshing Analysis

Meshing analysis has a crucial effect on any simulation study. In COMSOL; there are two different meshing types: i) user-controlled, ii) physics-controlled. While physics controlled option enables automatic mesh construction, user-controlled mesh allows manual element size adjustments (Alvarado et al., 2013). The modeled integrated optical device includes a large number of parts with varying size and aspect ratio parameters. During the study, it was observed that physics-controlled mesh is not well suited for such structures due to the incompatibilities at the junction points. Although the default meshing sequence type for the simulation interface is a physics-controlled mesh type, different meshing element types can not be used with physics-controlled mesh and the usage of only one default element type is forced. As it is

mentioned before, the model structure in this paper includes many parts with different dimensions. Because of this reason, all of these parts can not be meshed with only one element type, otherwise, the discrepancies at the junction regions arise due to the aspect ratio incompatibilities and connection faults of the mesh nodes. On the other hand; user-controlled mesh type allows the operator to build and edit the meshing sequence manually. Also for this mesh type, mesh elements can be resized as required. Therefore, a user-controlled meshing type was chosen instead of physics controlled mesh. In Figure 3; the mesh construction of the whole geometry is shown.

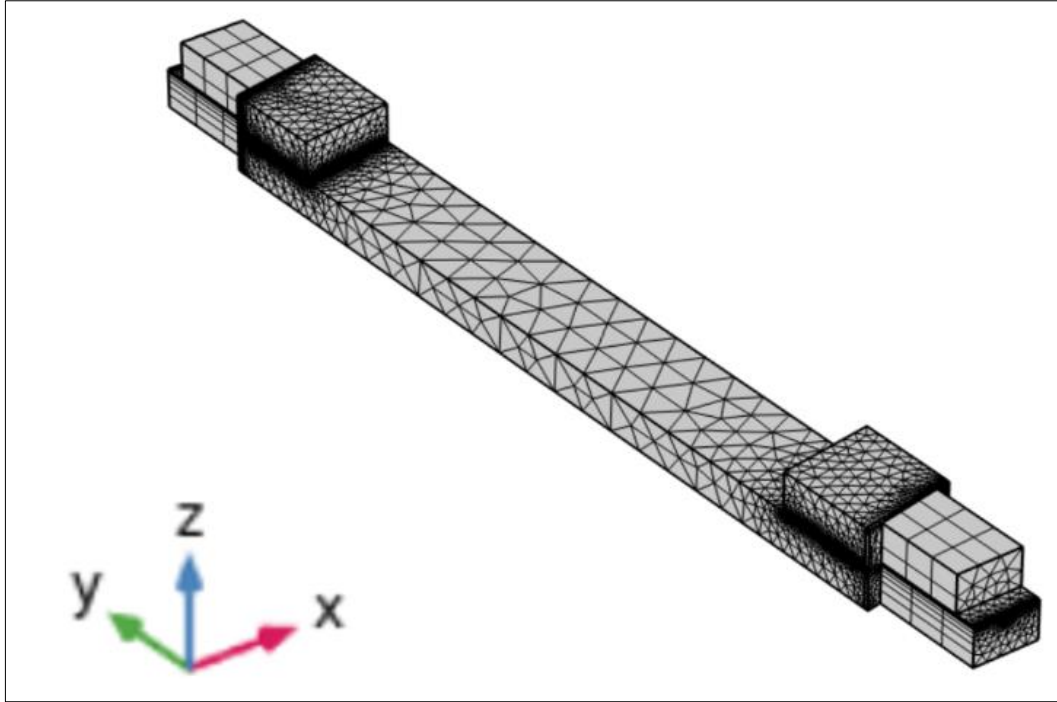


Figure 3. Meshed Model

It can be seen in Figure 3 that the densities, types, and sizes of the domains differ from each other. To make a comprehensive evaluation, the mesh parameters are listed in Table 1.

Table 1. Mesh Statistics for the Defined Geometry

Domain	Optical Chip	Fiber Pigtail Carrier	Cover	Epoxy	Optical Fiber
Mesh Type	Tetrahedral	Triangular/Swept	Tetrahedral	Tetrahedral	Triangular/Swept
Mesh Size	Extremely Fine	Extra Fine	Extremely Fine	Finer	Extra Fine
Mesh Element Number	35268	3621	28949	14678	198

Three different element types (tetrahedral, triangular, and swept) were preferred in the simulation. Especially, the variation of stress distribution on the epoxy domains at the fiber/optical chip joint requires a good discretization of these regions. While the thickness of the epoxy parts is approximately 40 μm , the rest of the parts are on the order of millimeters. Since the high aspect ratio between epoxy domains and the other parts makes the mesh solution challenges, the correct choice of mesh element type has a drastic influence on the stress calculation results. Below, we list a detailed description of the different mesh types:

The swept mesh type is known as a geometrical discretization technique in “Comsol Multiphysics” and is generally used for thin geometries and structures. It starts at a source boundary region and sweeps along a defined destination boundary (Anonymous, 2020b). Since fiber pigtail carriers are proven commercial products, these areas were not our major region of interest during our study. Application of the swept mesh type can be more convenient for such regions. Therefore, upper and bottom pigtail carrier parts, optical fibers, and the epoxy domains between upper and bottom parts were meshed with triangular and swept mesh types.

The tetrahedral element type is the basic and simplest one among others for most “Comsol Multiphysics” applications. Any domain can mesh with tetrahedral independent from the geometry (Anonymous, 2020c). The triangular element type can be used in some special circumstances. Since mesh algorithms generally need more input for this element type, it can not be used for every geometry. The primary cause of using triangular elements is that they can decrease mesh density (Anonymous, 2020c). There is a basic difference between tetrahedral and triangular mesh types. While triangular have high aspect ratios, the aspect ratio is limited to unity for tetrahedral mesh elements. In those cases where the analysis results are not crucial, it is favorable to use a triangular element type. In the context of this paper; since the fiber pigtail carriers, the epoxies between upper and bottom fiber pigtail carriers, and optical fibers results are not analyzed, swept and triangular mesh types were preferred for these components. The second reason for using these mesh types is that there is a high aspect ratio between optical fiber, epoxies, and the carriers. On the other hand, the tetrahedral mesh type is chosen for the rest of the domains due to the low aspect ratio.

2.3. Material Parameters

The material parameters defined for the integrated optical device are listed in Table 2. The materials of the constitutive parts are LiNbO₃ (Filatov et al., 2016), UV curable (Anonymous, 2021a) and SiO₂ (Anonymous, 2021b).

Table 2. Physical Parameters of the Materials

Domain	Material	ρ (kg/m ³)	E (GPa)	η	k (W/(m.K))	α (x10 ⁻⁶) (1/K)
Optical Chip/Cover/Pigtail Carriers	LiNbO ₃	4690	170	0.25	5.6	2.0 and 16.7
Epoxy	UV Curable	1290	1.03	0.48	0.15	65
Optical Fiber	SiO ₂	2170	66.3	0.15	1.30	0.55

A brief description of the parameters (ρ , density; E, Young's Modulus; η , Poisson's ratio; k, thermal conductivity, and α , coefficient of thermal expansion) listed in Table 2 is included below: These quantities are used in the heat transfer and solid mechanics calculations to solve the related equations. While Young's Modulus and Poisson's ratio terms are necessary parameters for the structural stability calculations, thermal conductivity, density, and coefficient of thermal expansion parameters belong to heat transfer calculations. According to the partial differential equation included in the heat transfer interface (Anonymous, 2020d), ρ and α are the parameters that are used in the related theoretical equation. Especially; the thermal expansion coefficient is one of the parameters which is incorporated in the derivation of thermoelastic damping. In Comsol Multiphysics; the expression of the heat flux by conduction is demonstrated with q and given as $k \cdot \nabla T$. In this equation; k is the thermal conductivity that accounts for the calculation of heat flux expression. Besides the heat transfer theory, the rest of the terms which are included in Table 2 are required to solve equations for solid mechanics interface. Young's Modulus and Poisson's Ratio are the basic characteristic parameters that are utilized to solve the structural deformation of the materials. In Comsol Multiphysics; these material parameters have importance to make structural analyses of the simulated model. Many of the stress calculations in Comsol Multiphysics are based on elastic strain equations

(Anonymous, 2020e). In general; strain means the deformation of a material because of the stress effect. Elastic strain tensor is derived after eliminating inelastic deformations from the displacements. For the linear analysis; elastic strain is given with the equation $\epsilon_e = \epsilon - \epsilon_{inel}$ (Anonymous, 2020e). Here; ϵ_e , ϵ and ϵ_{inel} are elastic, total, and inelastic strain tensor statements, respectively. There is a correlation between the Poisson's ratio and strain. Poisson's ratio; is the ratio of transverse contraction strain to longitudinal extension strain. Because the materials react to deform under thermal stress, particularly the Poisson's ratio is a crucial material parameter to calculate deformations in the structure. Just as strain, stress is another parameter to define geometrical changing of material. In a simulation environment; since Young's Modulus is essential to indicate how the material is bent or changes its shape under thermal or structural stresses, this property is a basic parameter for the related solid mechanics equations.

Besides, since LiNbO_3 is a uniaxial material, the properties along the x and y-axis are equal to each other, but the parameters along the z-axis are different. Thus, two different thermal expansion coefficients are defined for LiNbO_3 material.

2.4. Boundary Conditions

Thermal and boundary conditions were assigned to solve the equations in the heat transfer and solid mechanics environments. First of all; the temperature boundary condition was applied to the bottom surface of the optical chip and both of the fiber pigtail carriers, holding these surfaces at a temperature $T(t)$. In the solid mechanics section, a rigid motion suppression boundary condition is added to all of the domain parts. This constraint adds a minimum number of constraints to suppress rigid body motions (Anonymous, 2020e). Since all of the parts are bonded to each other by gluing, rigid motion suppression was applied to all of the domains. The motivation for the choice of this option can be explained as follows: in one simulation study (Anonymous, 2020f), rigid motion suppression was added to one of the two domains which were glued to each other, aiming the prevention of rigid body motion in at least one body. So, the reason why this boundary condition is preferred in our simulation study is that all of the domains are attached with some kind of epoxy. Moreover; in the referenced study, enabling structural stability for thermal expansion problems is proposed. Another boundary condition for solid mechanics is related to the anisotropic properties of LiNbO_3 which is a piezoelectric material. Since this kind of material is an anisotropic material, its physical properties are orientation-dependent (Zhang, 2012). In the fabrication process, x-cut y-propagation LiNbO_3 material was used. For the x-cut y-propagation material, while the waveguide is extended along the -y axis, the electrical field is applied along the z-axis to obtain maximum modulation coefficient, and also x-axis is normal to the crystal surface (Liu et al., 2019). In Figure 4; the x-cut LiNbO_3 substrated structure is demonstrated.

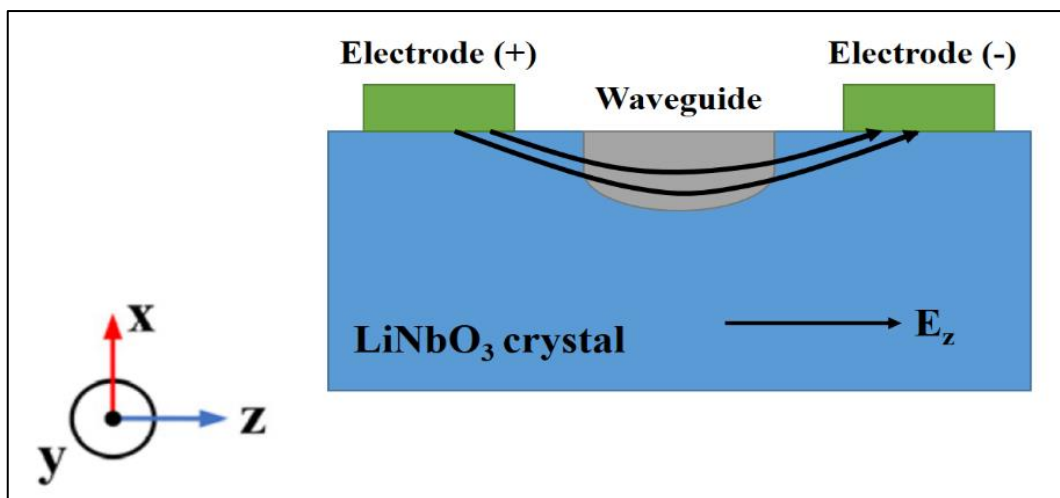


Figure 4. x-cut LiNbO_3 Crystal Orientation

A transformation vector set was specified to correspond to the crystal coordinate system with the material coordinate system, called a “base vector coordinate system”. This vector system allows creating an orthogonal coordinate system in Comsol as shown in Figure 5. In the left configuration; it is seen that the

x, y, z-axis were transformed as corresponding with their self colors. In the right notation; it is seen that the base vector coordinate system is expressed with the matrix form.

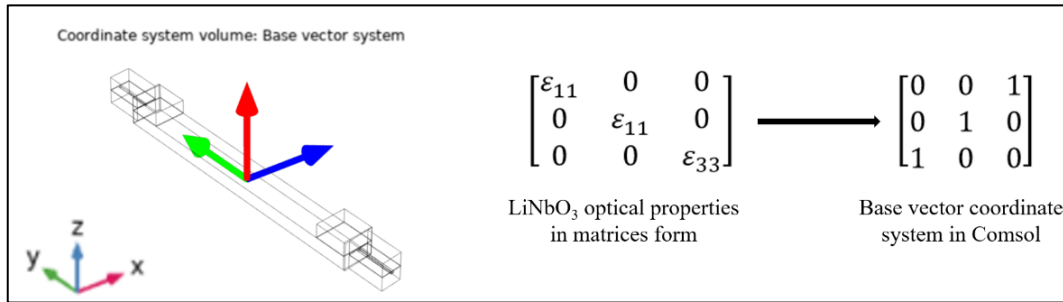


Figure 5. Base Vector Coordinate System and Matrix Form for the Crystal Orientation

2.5. Analyzation Type and Conditions

Thermomechanical simulations were carried out via time-dependent analysis. The time-dependent analysis is preferred when variables change in the time domain. For example; the heat transfer process can be used to calculate the temperature variations over time. Moreover; in solid mechanics applications, determination of the time-dependent deformation changes in the basic application area of this analysis method. In this paper; a temperature profile between -40°C and $+85^{\circ}\text{C}$ with $1^{\circ}\text{C}/\text{min}$. temperature rate was applied as shown in Figure 6. While at the heating process, the temperature is constant between 95.min-125.min time intervals, at the cooling process, it is constant between 255.min-285.min time intervals.

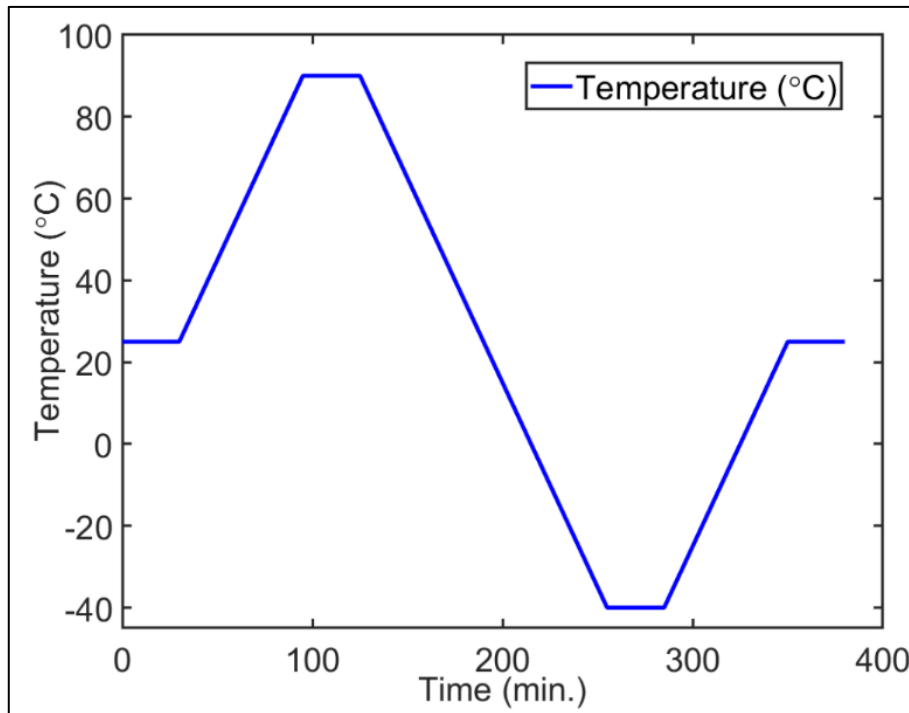


Figure 6. Time-Dependent Temperature Profile

2.6. Equation-Based Solutions for the Heat Transfer and Solid Mechanics Modules

The problems were solved using equation-based modeling. Basically; COMSOL operates according to the finite element model (FEM). FEM is a numerical technique to generate solutions that are defined by partial differential equations (PDE) (Nikishkov, 2004). The required model specifications can be created based on mathematical equations and they can be directly incorporated into the software's graphical interface (Anonymous, 2020g). These properties provide all of the models to be controlled. With equation-based modeling, expressions and mathematical terms can be introduced to the system. Some equation types such

as partial differential equations (PDE), algebraic equations, ordinary differential equations (ODE) can be solved using this modeling type. Especially, it is stated that a set of linear algebraic equations should be preferred for linear problems (Nikishkov, 2004).

In this study; temperature-dependent stress analysis was performed via equation-based modeling by associating heat transfer and solid mechanics interfaces. The solved equations are indicated in Equations 1 and 2.

$$\rho C_p \left(\frac{\partial T}{\partial t} \right) + \rho C_p \mathbf{u} \cdot \nabla T + \nabla \cdot (-k \nabla T) = Q + Q_{ted} \quad (1)$$

$$\boldsymbol{\sigma} = \boldsymbol{\sigma}_0 + \mathbf{C} : (\boldsymbol{\epsilon} - \boldsymbol{\epsilon}_0 - \boldsymbol{\alpha} \theta) \quad (2)$$

Equation 1 represents the heat transfer energy equation where the parameters (T, temperature; ρ , density; C_p , specific heat capacity at constant pressure; \mathbf{u} , the velocity vector of translational motion; k , thermal conductivity; Q , volumetric heat generation; Q_{ted} , thermoelastic damping) are defined. In this equation; the conservation of energy is explained in terms of temperature. Equation 2 is related to Hooke's law and explains the stress-strain relation of the material (Barbagallo et al., 2015). In the Equation 2; all given parameters ($\boldsymbol{\sigma}$, final stress tensor; $\boldsymbol{\sigma}_0$, initial stress tensor; \mathbf{C} , elasticity tensor; $\boldsymbol{\epsilon}$, total strain tensor; $\boldsymbol{\epsilon}_0$, initial strain tensor; $\boldsymbol{\alpha}$, volumetric thermal expansion coefficient; θ , the relationship between local temperature and strain reference temperature) are related to the mechanical properties of the materials. Moreover, Equation 2 was calculated to sense the stress-strain which is affected by thermal causes (Barbagallo et al., 2015). So; in this study, both solid mechanics and heat transfer equations are combined to solve equation-based simulations.

2.7. Evaluation of Temperature, Stress, and Deformation Fields

In this section; the following analyses were evaluated: i) temperature and ii) stress/deformation fields on the whole structure, iii) time-dependent Von-Mises stress distribution on the epoxy domain between optical chip/fiber pigtail carrier.

In Figure 7; the temperature field of an integrated optical component is shown. This figure describes the thermal distribution at 85°C over the whole system and obtained by solving the heat transfer module via time-dependent analysis. The thermal distribution of the epoxy domain between the optical chip/fiber pigtail carrier interface changes at most a few temperatures.

Besides the thermal performance, the stress and deformation field of the integrated optical device were investigated as depicted in Figure 8(a-b).

Apart from Figure 2, in Figure 8(a-b); the upper and bottom parts of the fiber pigtail carrier are at the same dimensions. It was seen during simulations that solving time was considerably longer when these pieces were at different dimensions, resulting in convergence problems due to the complex mesh construction. It is known that stress variations on the fiber pigtail carriers are ignored during analyses. So; while evaluating stress/deformation fields, both of the parts of the pigtails were modeled as equal sizes to save solution time, and actual geometric sizes were disregarded. To calculate stress variation along the x, y, and z-axis separately, the total stress change called Von-Mises stress was considered in the evaluation of the results as shown in Figure 8(a). As can be seen from the figure, the stress level is varying over the epoxy region between the optical chip/fiber pigtail carrier interface. This difference originates basically due to the use of the materials with different thermal expansion coefficients. Moreover, there is a bit more stress accumulation at the corner of the cover rather than the rest of the regions. From the literature researches, the stress at these regions may arise most likely because of the geometrical singularity (Petroni et al., 2015). We can say that although there are not enough investigations related to mechanical simulations of the fiber optic devices, we have utilized published papers concerning the thermo-mechanical performance of other model structures to take as a reference. Besides this; deformation on the same epoxy region was investigated via total displacement. According to Figure 8(b); while maximum deformation with nearly 5 μm originates in the area between optical chip and carrier, the rest of the structure senses weak deformation close to zero.

When the literature survey is examined (Yao et al., 2018), this displacement value is in the reasonable micrometers range.

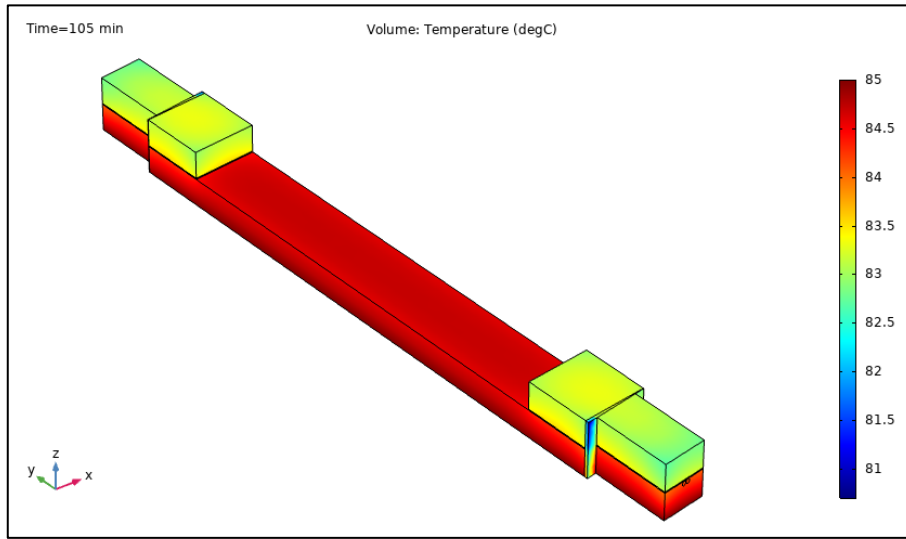


Figure 7. Temperature Field of the Integrated Optical Device at 85°C

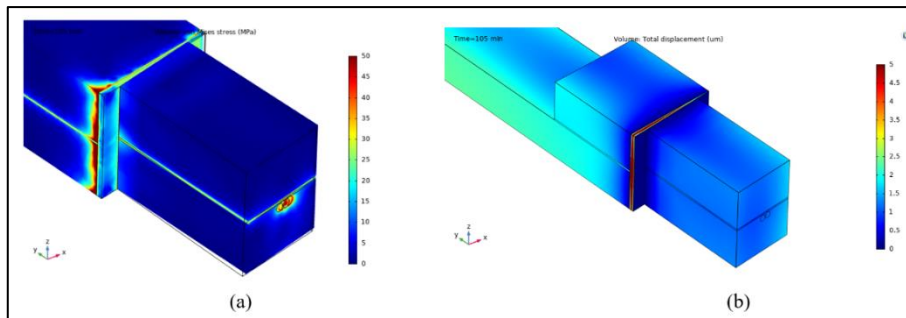


Figure 8. Stress and Deformation Field of the Integrated Optical Device, (a) Stress Field, (b) Deformation Field

A typical device structure produced in the laboratory environment and the components of the integrated optical device are shown in Figure 9(a), while the corresponding model structure in the simulation environment is given in Figure 9(b). To analyze the Von-Mises stress distribution on the epoxy between the chip/carrier interface, the region marked as epoxy 1 region was taken into consideration.

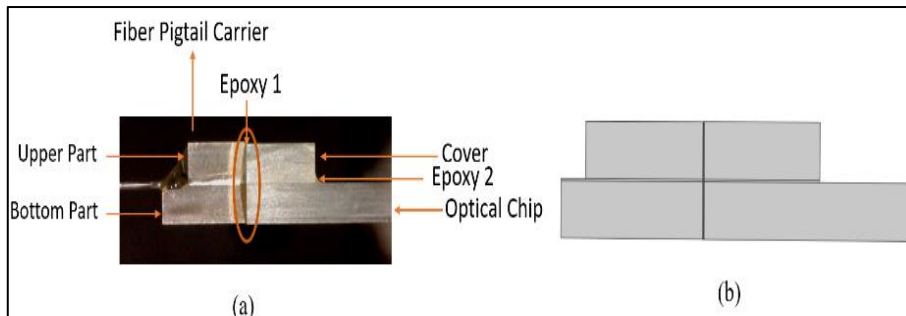


Figure 9. Components of the Integrated Optical Device, (a) In the Experimental Environment, (b) In the Simulation Environment

The Von-Mises stress distribution versus time (temperature) result for the aforementioned temperature-time profile is shown in Figure 10(a). From the analyses, it was observed that Von-Mises stress increases as temperature increased. This figure shows the stress analysis between 60. min-150. min at around 85°C.

Increase and decrease trends of the stress parameter resemble the time-dependent temperature profile. As the temperature rises, stress ascends and also at the constant temperature between 95. min – 125. min, stress level also becomes stable. Similarly; when the temperature decreases further 120 min., the stress level descends below 100 MPa. In Figure 10(b); the analysis was carried out at constant time interval of 400 min for the temperature profile. In this case; the stress level increases gradually up to 200 MPa. It can be deduced that; when the time duration lengthens out, the stress level also increases from nearly 160 MPa to 220 MPa as shown in Figure 10(a-b).

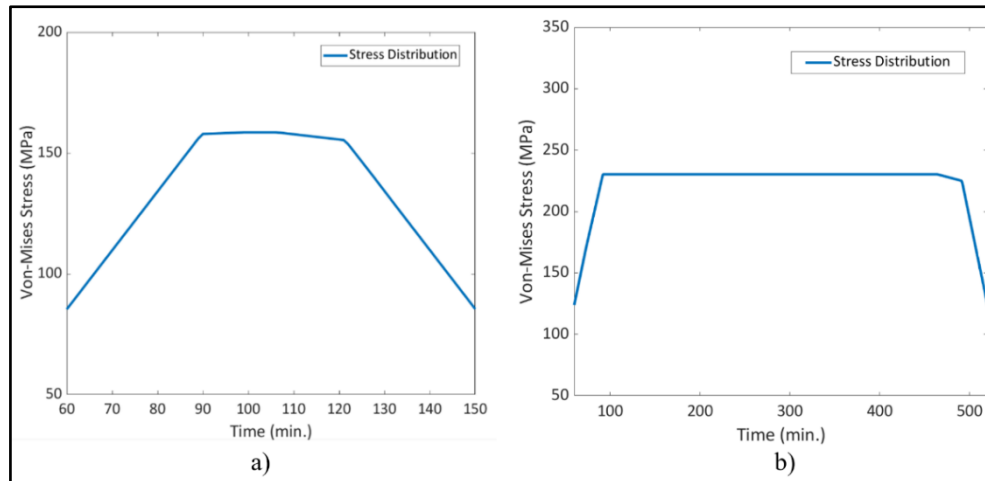


Figure 10. Stress Fields on the Epoxy Between the Optical Chip and Fiber Pigtail Carrier, (a) the Constant Time Interval is 30 min., (b) the Constant Time Interval is 400 min

3. CONCLUSIONS

In this study; a method for thermomechanical stress analysis for an integrated optical device was proposed. The main improvement of this study is that simulation methods of the integrated optical device structures were introduced and the instructions were given in detail. The absence of such a study in the literature encouraged and motivated us to write this paper. According to the analyses; firstly, it was understood that thermal performance analyses of the fiber optic components can be carried out via equation-based simulation tools. In addition to this, the material properties such as anisotropy of LiNbO_3 can be defined as a boundary condition. Since there is not much literature research related to thermal analysis of the integrated optical devices, this paper leads some guidelines in further researches and it showed that rather than stationary analysis, time-dependent solutions could be examined for this kind of structure.

In the future, simulation studies will be supported with experimental results. The results will be evaluated according to the changing of device geometry structures. These studies are currently in progression.

CONFLICT OF INTEREST

No conflict of interest was declared by the authors.

REFERENCES

- Alvarado, R., Barlett, M., Beski, R., Isaza, S., & Li, C. (2013). Analysis of the thermo-mechanical reliability of an SMT attachment. (E-project-042513-011426) Project, Worcester Polytechnic Institute.
- Barbagallo, C., Malgioglio, L. G., Petrone, G., & Cammarata, G. (2015). Thermo-mechanical analysis of a multi-chip power module. Conference on Thermal Energy Systems: Production, Storage, Utilization and the Environment.
- Filatov, V. Y., Kukaev, S. A., Shalymov, V. E., & Venediktov, Y. V. (2016). Multiphysical simulations of passive ring cavities. Proceedings of SPIE, Optical Sensing and Detection IV, 9899, 98992X. doi:[10.1117/12.2230223](https://doi.org/10.1117/12.2230223)

- John, F. (1997). Integrated optics. Industrial Applications of Lasers. Science Direct. Second Edition.
- Lenner, M., Yang, L., Frank, A., & Bohnert, K. (2017). Long-term reliability of fiber-optic sensor components in harsh industrial environments. Advanced Photonics Congress. doi:[10.1364/SENSORS.2017.SeW1E.3](https://doi.org/10.1364/SENSORS.2017.SeW1E.3)
- Liu, J., Zhang, C., Zheng, Y., Song, J., Gao, F., & Yang, D. (2019). Suppression of nonlinear residual intensity modulation in the multifunction integrated optic circuit for fiber-optic gyroscopes. *Journal of Lightwave Technology*, 38(6), 1572-1579. doi:[10.1109/JLT.2020.2968478](https://doi.org/10.1109/JLT.2020.2968478)
- Nikishkov, G. P. (2004). Introduction to the finite element method. [Lecture Notes] University of Aizu.
- Petrone, G., Barbagallo, C., & Scionti, M. (2015). Thermo-mechanical analysis and fatigue life prediction for an electronic surface-mount device (SMD). Proceedings of COMSOL Conference.
- Richter, P. (1989). Integrated optics: technology, devices and applications. *Periodica Polytechnica Chemical Engineering*, 34(1-3), 205-212.
- Suchoski, P.G., & Boivin, G.R. (1992). Reliability and accelerated aging of LiNbO₃ integrated optic fiber gyro circuits. *Fiber Optic and Laser Sensors X*, 1795, 38-47. doi:[10.1117/12.141273](https://doi.org/10.1117/12.141273)
- Tripathi, U.S., Dixit, N., Kaul, A. N., & Gupta, A.K. (2007). Multifunction integrated optic chip for FOG. Proceedings of the National Conference on Advances in Sensors for Aerospace Applications, Hyderabad.
- Wooten, E.L., Kissa, M.K., Yi-Yan, A., Murphy, J.E., Lafaw, A.D., Hallemeier, F.P., Maack, D., Attanasio, V.D., Fritz, J.D., McBrien, J.G., & Bossi, E. D. (2000). A review of lithium niobate modulators for fiber-optic communications systems. *IEEE Journal of Selected Topics In Quantum Electronics*, 6(1), 69-82. doi:[10.1109/2944.826874](https://doi.org/10.1109/2944.826874)
- Yang, J., Yuan, Y., Zhou, A., Cai, J., Li, C., Yan, D., Huang, S., Peng, F., Wu, B., Zhang, Y., Liu, Z., & Yuan, L. (2014). Full evaluation of polarization characteristics of the multifunctional integrated optic chip with high accuracy. *Journal of Lightwave Technology*, 32(22), 3641-3650. doi:[10.1109/JLT.2014.2342753](https://doi.org/10.1109/JLT.2014.2342753)
- Yao, J., Li, K., Li, B., Wang, C., Kan, C., She, X., & Shu, X. (2018). Study of wavelength temperature stability of multifunctional integrated optical chips applied on fiber-optic gyroscopes. *Journal of Lightwave Technology*, 36(23), 5528-5535. doi:[10.1109/JLT.2018.2875795](https://doi.org/10.1109/JLT.2018.2875795)
- Zhang, G. (2012). Orientation of piezoelectric crystals and acoustic wave propagation. Proceedings of Comsol Conference.
- Anonymous (2020a). (Accessed: 20/11/2020) www.comsol.com/blogs/what-is-comsol-multiphysics/
- Anonymous (2020b). (Accessed: 21/11/2020) www.comsol.com/blogs/meshing-sweep-your-meshes-with-ease/
- Anonymous (2020c). (Accessed: 22/11/2020) www.comsol.com/blogs/meshing-your-geometry-various-element-types/
- Anonymous (2020d). User's Guide Heat Transfer Module. (Accessed: 23/11/2020) doc.comsol.com/5.4/doc/com.comsol.help.heat/HeatTransferModuleUsersGuide.pdf
- Anonymous (2020e). User's Guide Structural Mechanics Module. (Accessed: 24/11/2020) doc.comsol.com/5.4/doc/com.comsol.help.sme/StructuralMechanicsModuleUsersGuide.pdf
- Anonymous (2020f). (Accessed: 25/11/2020) www.comsol.com/blogs/how-to-provide-structural-stability-in-thermal-expansion-simulations/
- Anonymous (2020g). (Accessed: 26/11/2020) <https://www.comsol.com/blogs/3-examples-of-equation-based-modeling-in-comsol-multiphysics/>
- Anonymous (2021a). (Accessed: 13/01/2021) www.norlandprod.com/adhesives/NOA%2061.html
- Anonymous (2021b). (Accessed: 14/01/2021) Comsol Material Library.



The Effects Welding Speed and Focal Length on Mechanical Characteristic of Fiber Laser-Welded Structures of DP600 Dual Phase Steel

Elif Selen ATMACA^{1*} , Adem KURT² 

¹Gazi University, Graduate School of Natural and Applied Sciences, Ankara, Turkey

²Gazi University, Faculty of Technology, Department of Metallurgical and Materials Engineering, Ankara, Turkey

Keywords	Abstract
DP600 DP Steels Fiber Laser Welding Welding Speed Focal Length	In this study, the effect of welding speed (3, 3.5, 4 m/min) and focal length (0, 1.4 mm) on the mechanical properties of the welded structure was investigated in the overlap type joining of 1.2 mm sheet thickness DP600 dual phase steel sheet material by fiber laser welding method. For this purpose, tensile-shear tests were performed on the samples joined by laser welding method, and the tensile strength and elongation amounts were determined. Microstructure investigation and microhardness measurements of the welded area were carried out. It is determined that weld joint shape and penetration depth changes according to focal length distance and welding speed, and with the maximum welding speed specimens has the minimum penetration depth. Tensile-shear strength values decreased depending on the increased welding speed for both focal length specimens. It is observed that the microhardness results were affected by welding speed and focal lengths. In 0 mm focal length distance specimens' hardness values increased according to the increased welding speed, but for -1.4 mm focal length distance the microhardness values decreased with an increased welding speed. The fracture zones and fracture surface morphology also affected by welding speed and focal distance. In 0 mm focal length, all the specimen fractured in base metal with a ductile fracture morphology, but in the -1.4 mm focal length, specimens fractured from the zones which are closer to HAZ and FZ with a brittle fracture morphology.

Cite

Atmaca, E. S., & Kurt, A. (2021). The Effects Welding Speed and Focal Length on Mechanical Characteristic of Fiber Laser-Welded Structures of DP600 Dual Phase Steel. *GU J Sci, Part A, 8(1)*, 146-156.

Author ID (ORCID Number)

E. S. Atmaca, 0000-0002-1892-9091
 A. Kurt, 0000-0002-1439-4683

Article Process

Submission Date 30.12.2020
Revision Date 14.03.2021
Accepted Date 25.03.2021
Published Date 29.03.2021

1. INTRODUCTION

The one of the purposes of the new generation materials used in the automotive industry is to reduce the fuel consumption and carbon emissions associated with it by reducing the vehicle weight. Therefore, the use of new generation materials that provide high strength in thinner sections is rapidly increasing (Gong et al., 2016).

Today, dual phase steels have an important place among the high strength steels and they are provided with superior mechanical properties such as high strength / weight ratio, low yield / ultimate strength ratio. These steels are produced with a sufficient cooling rate to convert the austenite to martensite phase after the ferrite + austenite structure is annealed between Ac_1 and Ac_3 temperatures. Thus, the martensite phase created in the material provides strength to the steel, while the soft ferrite matrix provides ductility (Fonstein, 2017; Çavuşoğlu et al., 2019; Dai et al., 2020).

Although different welding methods such as resistance spot welding, gas metal arc welding and friction stir welding are used for joining metallic materials, laser welding method is also preferred by automotive manufacturers considering the production speed and welding performance (Hong & Shin, 2017; Kancharla et al., 2018; Aktarer et al., 2019; Kuril et al., 2019; Zhao et al., 2019).

The studies on joining of steel sheets by laser welding method in the literature are abundant. Mitra et al. (2020a) determined that with increasing laser welding speed, the surface defects increased in the HAZ region and this situation facilitated the fracture in this region. Mitra et al. (2020b) showed in their study, which examines the relationship between welding speed and residual stress, concluded that a lower residual stresses occur at high welding speeds. Tuncel & Aydin (2020) investigated the laser weldability of DP600 double-phase steels in one sided and double sided forms and determined that as the pulse frequency of the laser beam increased, the tensile strength values increased depending on the increase in the area of weld zone. Alves et al. (2018) have optimized laser power and welding speed to minimize prior martensite softening and HAZ (Heat Affected Zone) in the laser weldability of DP1000 dual-phase steel. In the study of Wang et al. (2016), it was observed that DP1000 dual phase steel was subjected to coarse grain structure in laser welding with the increase of energy input and its mechanical properties were weakened. Zhao et al. (2013) determined that in the laser welding process of dual phase steels, the width of FZ (Fusion Zone) is decreased with the increase in welding speed, tensile-shear load decreases and maximum hardness values were obtained at FZ. According to Švec et al. (2015), due to the increase in welding speed, the amount of spatter around the weld seam increased, the weld pool width decreased, cap concavity and root sagging occurred, however, the highest hardness values were determined in FZ and the main material tensile strength was higher than the welded material. In the study by Xie et al. (2017) (3, 4, 5 m/min), no significant effect of laser welding speed on DP590 dual phase steel tensile strength was observed.

The studies in the literature showed that, laser power, pulse frequency, focus length and welding speed affect the mechanical properties of laser welded joining (Zhao et al., 2013; Švec et al., 2015; Wang et al., 2016; Fonstein, 2017; Hong & Shin, 2017; Xie et al., 2017; Alves et al., 2018; Kancharla et al., 2018; Aktarer et al., 2019; Çavuşoğlu et al., 2019; Kuril et al., 2019; Zhao et al., 2019; Dai et al., 2020; Mitra et al., 2020a; Tuncel & Aydin, 2020).

In this study, the effect of different welding speeds (3, 3.5, 4 m/min) and focal lengths (0 - 1.4 mm) on the mechanical and microstructural properties of DP600 dual phase steel sheet combined with fiber laser welding was examined in detail.

2. MATERIALS AND METHODS

2.1. Material

In this study, DP600 dual phase steel with a thickness of 1.2 mm was used. The full chemical composition was determined by spectral analysis. The chemical composition of DP600 is shown in Table 1. The coating mass determined according to ASTM E1659-12 (2012), and the Zn coating of DP600 was measured as 51 g/m²; Zn coating is present on the surface of DP600. Grinding and polishing processes were conducted for the metallographic imaging process of the base DP600 dual phase steel. Etching process was conducted with 2 % Nital solution for 3 sn. The light colored areas represent the ferrite and darker areas the martensite phases on the optical microstructural images of dual-phase steel in as received form given in Figure 1. Ultimate tensile strength determined according to ASTM E8 (2010) standard, and the average ultimate tensile strength was calculated as 691.31 MPa.

Table 1. Chemical Composition of DP600 Dual-Phase Steel (wt, %)

Steel	C	Mn	N	Cr	Si	Mo	Al
DP600	0.069	1.845	0.55	0.217	0.241	0.013	0.03

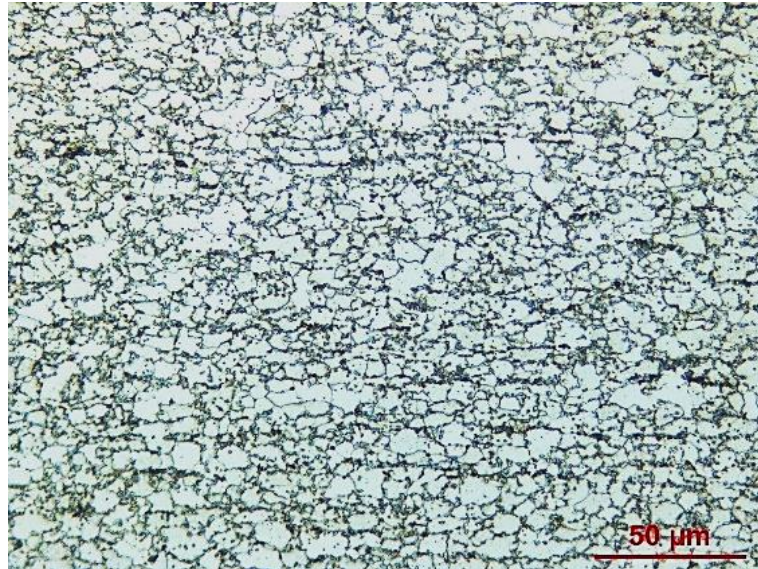


Figure 1. Optical Microstructure Image of DP600 Steel (as received)

2.2. Welding Procedure

Fiber laser welding operations carried out using IPG Photonics YLS 400 laser welding source. The fiber lasers with an emission wavelength of 1070 nm can deliver continuous wave mode through an output fiber core diameter of 100 μm . The focal diameter of the laser beam was 640 μm . The focus position during the welding was kept on the surface and -1.4 mm under the surface of samples. The fiber laser welding machine is shown in Figure 2.

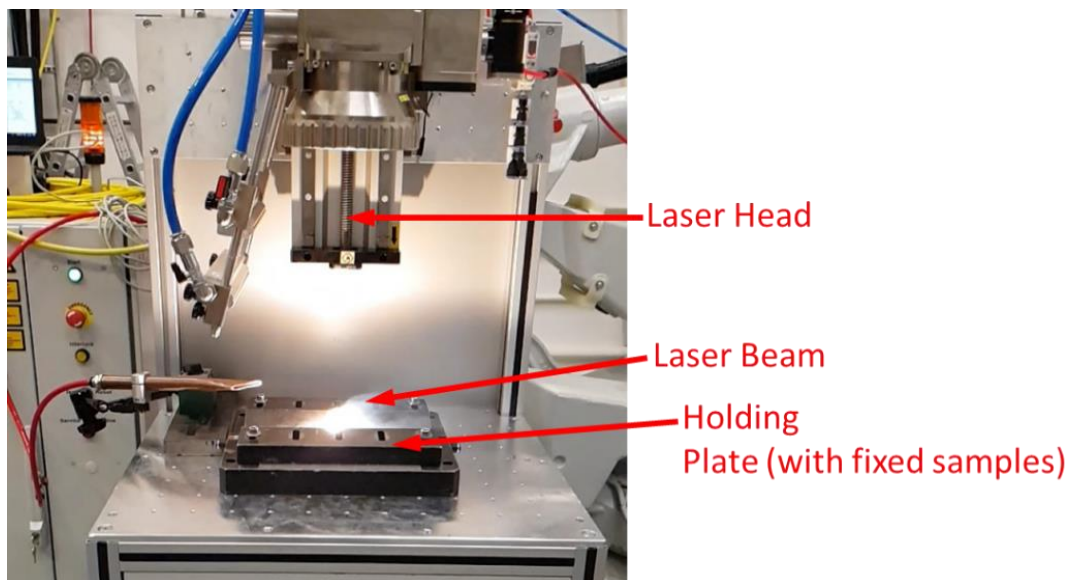


Figure 2. IPG Photonics YLS 400 Fiber Laser Welding Machine

To perform fiber laser welding processes, sheet plates were prepared on the rolling direction in the dimension 221 x 105 mm and steel-on-steel overlap joint of two samples with the overlap length of 35 mm. Schematic representation of the placement of the sheets to the fiber welding laser device is given in Figure 3. Before welding, the surface of all samples were cleaned with acetone to remove grease and residues. The joints were produced by keyhole welding method without filler metal and shielding gas. 0.2 mm shim plates were located between two sheets. Welding parameters and specimen codes were given in Table 2. Laser beam geometry regarding to focal length is also shown in Figure 4. As it stated in Figure 4, when the focal length sets as 0 mm, laser beam focus on the top of the upper sheet; but when the focal length sets as -1.4 mm, laser beam focus on the top of the lower sheet.

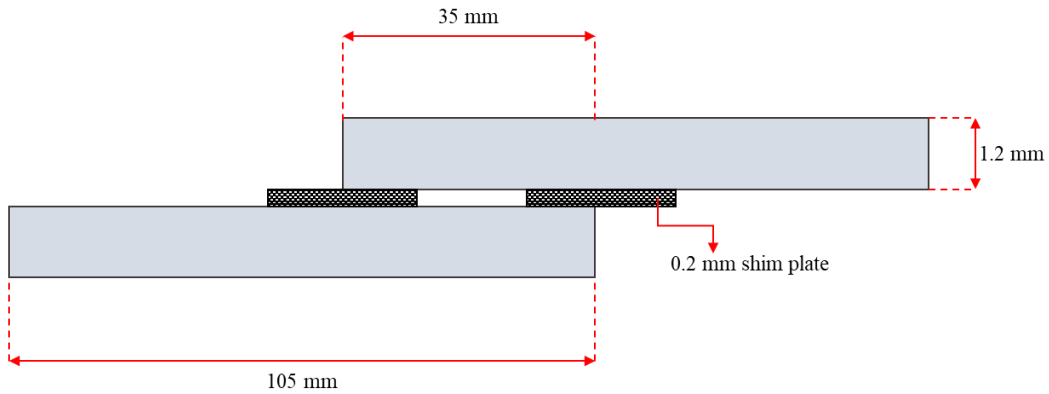


Figure 3. Placement of Sheets into the Fiber Laser Welding Machine

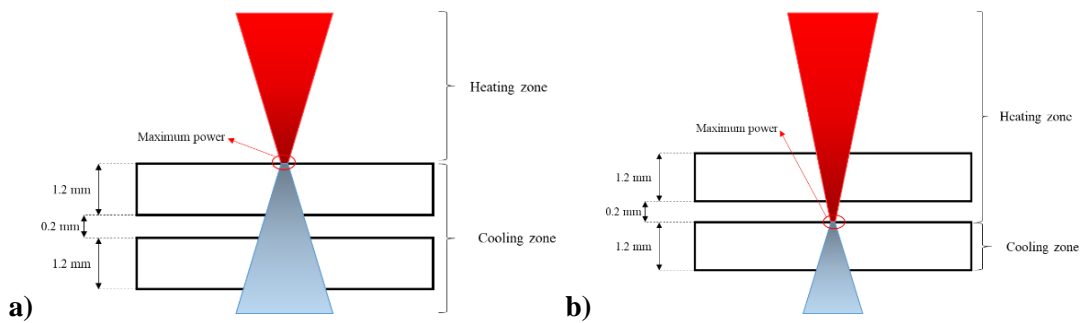


Figure 4. Laser Beam Geometry Differences According to Focal Length,
a) Focal Length: 0 mm, b) Focal Length: -1.4 mm

Table 2. Welding Parameters and Specimen Codes

Laser Power (kW)	Focal Length (mm)	Wave Length (nm)	Spot Size (μm)	Welding Speed (m/min)	Specimen Codes
4	0	1070	640	3	D1
				3.5	D2
				4	D3
4	-1.4	1070	640	3	D4
				3.5	D5
				4	D6

From the welded samples, the tensile-shear test samples were machined with water jet cutting method in the size of 30 x 175 mm according to EN ISO 14273 (ISO, 2016). The tests were performed on the INSTRON 3369 universal testing machine. All tensile-shear tests were carried out perpendicular to the welding direction. The strain rate was chosen as 0.0067s^{-1} according to EN ISO 6892-1 (ISO, 2019). In order to minimize error margin, three tests were performed for each parameter and average results were considered.

The Vickers hardness measurement across the weld zone and base metal were carried out on polished and etched samples using 4.903 N ($\text{HV}_{0.5}$) with a 10 second dwelling time. Average micro hardness value of base metal is measured as $210 \text{HV}_{0.5}$.

The microstructural investigation of welding was performed on the Leica optical microscope and the fracture surface investigation of the tensile-shear tested samples were carried out on the JEOL JEM 6060 scanning electron microscope.

3. RESULTS AND DISCUSSION

3.1. Mechanical Properties

Tensile-shear tests were performed to determine the effect of welding speed and focal length parameters on DP600 dual phase steel sheets. Maximum tensile-shear load – crosshead displacement results for both focal length and different welding speed parameters are shown in Figure 5.

When the Figure 5 is examined, it is seen that there is a decrease in the crosshead displacement values due to the increase in welding speed, and tensile-shear load values were determined as 24.52 kN, 23.82 kN and 23.66 kN for D1, D2 and D3 (Figure 5a), respectively. While for D4, D5 and D6, tensile-shear load values were determined as 246.37 kN, 24.39 kN and 24.15 kN (Figure 5b), respectively. The difference of tensile-shear load between D1 and D3 is almost 4 %, meanwhile 2 % for D4 and D6. The crosshead displacement values showed a similar tendency to the tensile-shear load values. Crosshead displacement values were measured for D1, D2, D3 as 28.63 mm, 26.91 mm and 16.23 mm (Figure 5a), respectively. Crosshead displacement values were also measured for D4, D5, D6 as 29.20 mm, 20.02 mm and 18.44 mm (Figure 5b), respectively. As the welding speed at 0 mm focal length increases, the crosshead displacement decreases approximately 43.5 %, while this ratio is calculated to be 36.83 % at -1.4 mm focal length.

Lakshminarayana et al. (2018) also determined that with the increase in the welding speed caused the incomplete penetration. For this reason, incomplete penetration occurs due to the increase in the welding speed at both focal lengths (Table 3) and thus a decrease in the maximum tensile-shear load and crosshead displacement values occurs.

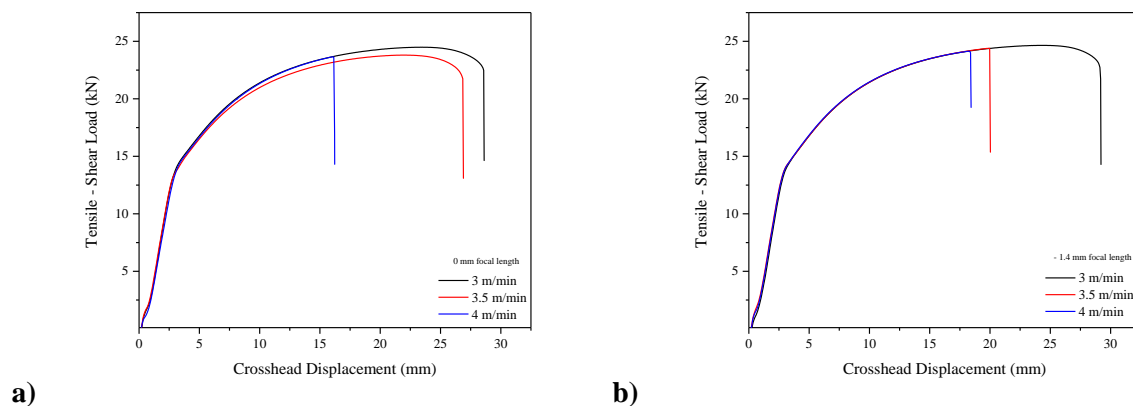


Figure 5. Tensile-Shear Load - Crosshead Displacement curves,
a) Focal Length: 0 mm, b) Focal Length: -1.4 mm

In Figure 6, lap joint fiber laser welded DP600 macrostructure and weld zones have been showed. Base material zones were not affected by heat input and cooling rates and the microstructure is the same as-received material. HAZ were partially affected by heat input and cooling rates. Because of this, the phase transformations and grain size differences can be detected clearly. Since the highest heat input and the highest cooling rate occur in FZ, the fundamental changes can be seen in this region.

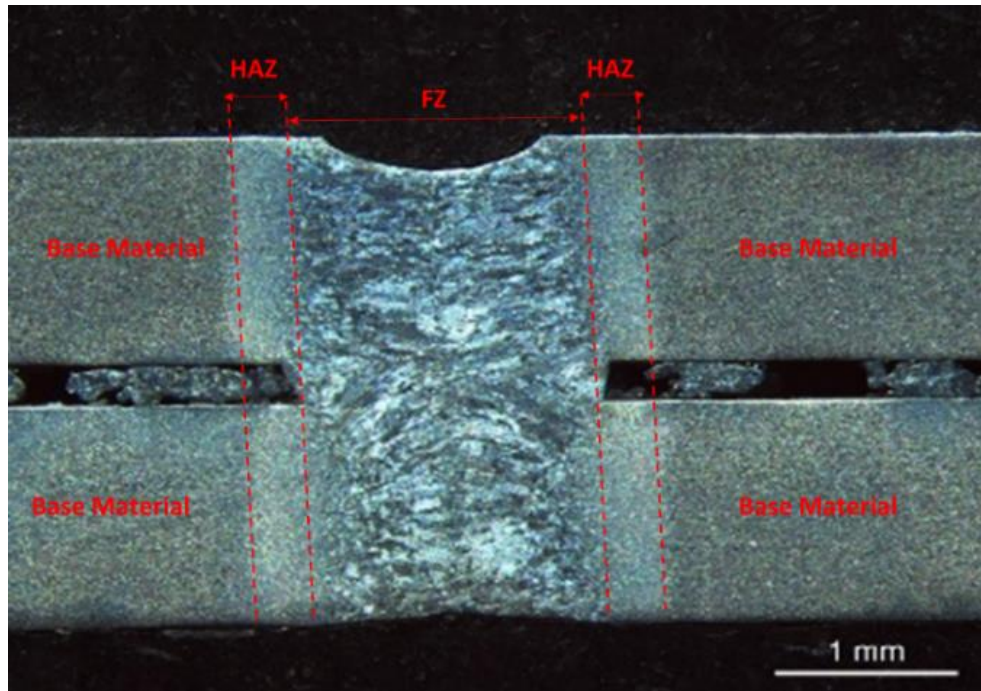


Figure 6. Zone of Welding Structure: Base Material (BM), Heat Affected Zone (HAZ), Fusion zone (FZ)

In Figure 7, microhardness values are shown depending on the welding speed and focal distance conditions. When Figure 7 is examined, a higher hardness value in weld zone (FZ) was observed than HAZ and base material, due to the fact that the cooling rate in the FZ region is the highest at both focal distances. The base metal hardness values, which were not exposed to any thermal effects, have the lowest hardness values. During the welding process, due to the heat input and cooling rate, regions such as HAZ or FZ formed where phase transformations occur.

For 0 mm focal length, FZ and HAZ hardness values measured. According to measurement results, hardness values of HAZ for D1 sample are 316 and 325 $HV_{0.5}$, and FZ hardness value is 329 $HV_{0.5}$; hardness values of HAZ for D2 sample are 322 and 338 $HV_{0.5}$, and FZ hardness value is 347 $HV_{0.5}$; hardness values of HAZ for D3 sample are 339 and 350 $HV_{0.5}$, and FZ hardness value is 355 $HV_{0.5}$.

During the optical analysis, the base metal consists of ferrite matrix and embedded martensite phases (Figure 1). Also Farabi et al. (2011), Gong et al. (2016) and Ferreira et al. (2020) determined fully lath martensitic structure in FZ, and ferrite, lath martensite, tempered bainite in HAZ and according to Sun et al. (2016) during these phase transformations, it is thought that the hardness value increases due to the decrease in the ferrite amount in the HAZ due to the heat input and cooling rates, but the hardness values are lower than FZ due to the tempered phases occurring in this region.

As seen in Figure 7, for -1.4 mm focal length specimens, the micro hardness values decrease as the welding speed increased. Hardness values of HAZ for D4 sample are 381 and 386 $HV_{0.5}$, and FZ hardness value is 422 $HV_{0.5}$; hardness values of HAZ for D5 sample are 367 and 363 $HV_{0.5}$, and FZ hardness value is 400 $HV_{0.5}$; hardness values of HAZ for D6 sample are 330 and 337 $HV_{0.5}$, and FZ hardness value is 367 $HV_{0.5}$.

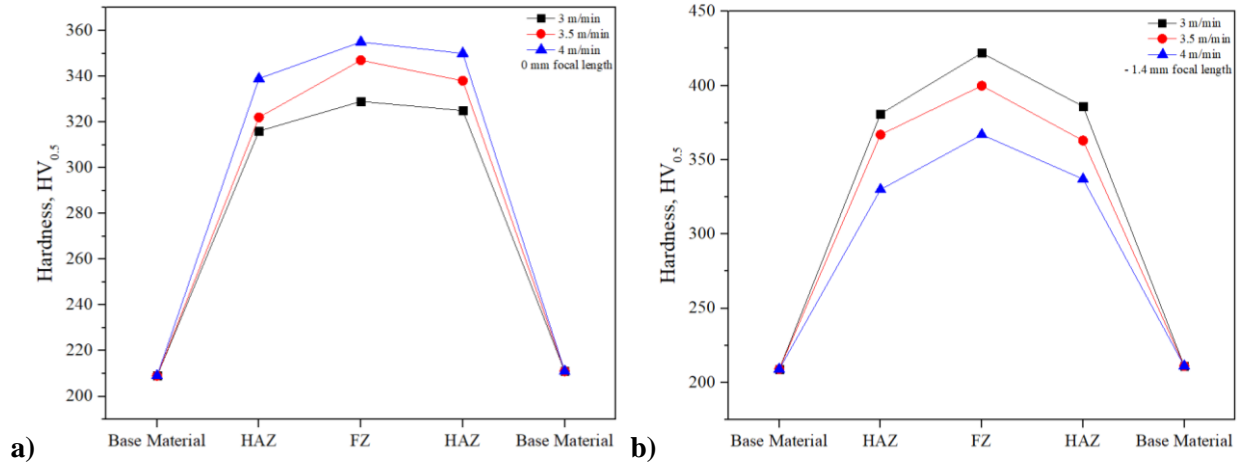


Figure 7. Hardness Distribution on Welded Structure,
a) Focal Length: 0 mm, b) Focal Length: -1.4 mm

It was calculated that the cooling rates increased due to the increase in the welding speed, but the values at this negative focal distance decreased by approximately 21.3 % in all welding speeds compared to the cooling rates of 0 mm focal length samples. Considering the weld regions, the base material consists of ferrite and martensite, and the average hardness values obtained in these regions were considered the same in both focal length samples. When the HAZ and FZ were examined, it was observed that the hardness values decreased due to the increase in the welding speed. When the weld pool where the most prominent transformation (ferrite to lath martensite transformations) occurs in all samples are examined, it is thought that carbide formation occurs besides lath martensite (Figure 8). Although there is an increase in the cooling rate, it is thought that this cooling rate is not enough to keep the structure completely in the martensite phase, the dissolution starts to form carbide and therefore a decrease in hardness values occurs. A similar situation has been observed in HAZ. Tempered martensite phase was observed in the fine-grained region forming the HAZ, different from the sample realized by using 0 mm focal length (Sun et al., 2016; Kundu et al., 2019). For this reason, the hardness values obtained in this region are lower than those of the 0 mm focal distance sample and it is thought that due to the relative decrease in the cooling rate, the tempered martensite phase formed in this region causes a decrease in the hardness values as the welding speed increases, due to the formation of a higher amount. The similar results were also determined in some experimental studies (Kundu et al., 2019; Ferreira et al., 2020; Palanivel et al., 2020).

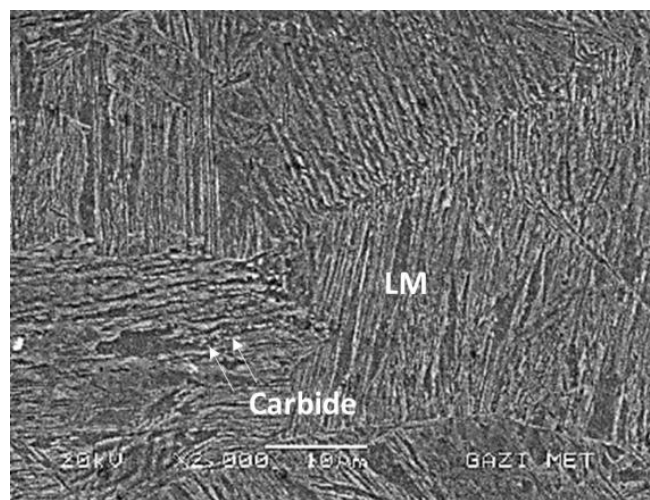
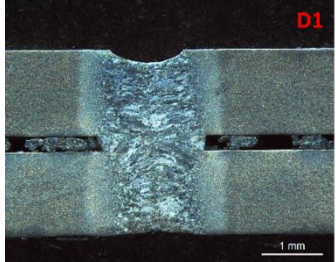
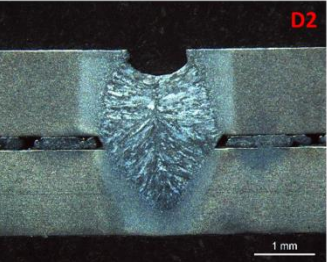
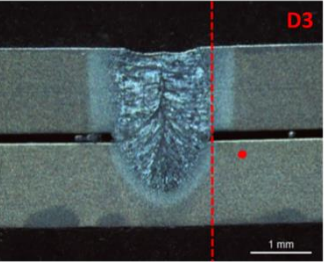
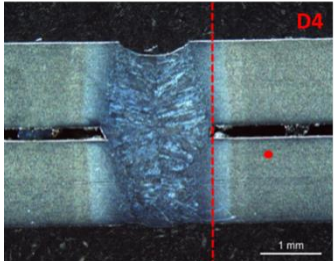
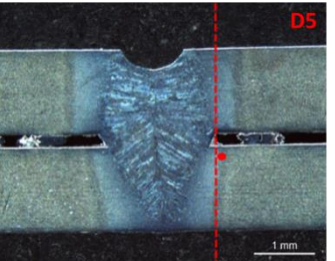
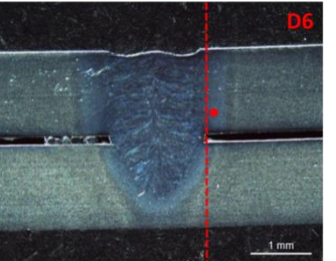


Figure 8. SEM Image of Lath Martensite (LM) and Carbide in FZ

Optical macro structure images depending on welding speed and focal distance parameters and fracture zones of the samples after the tensile-shear tests are shown in Table 3, and reference lines to measure the distances to fracture zone is indicated as red line and fracturing points of samples are marked with red dots.

Fusion zones of D1 and D4 are almost hourglass shaped (Palanivel et al., 2020) and it is seen that the penetration depth in the bottom sheet decreases due to the increase in the welding speed at both focal lengths. Although shrinkage cavity is also observed in D1 and D4, this indication is observed to have the highest depth in D2 and D5 samples.

Table 3. Macro Images and Fracture Zones of Samples

		Welding Speed		
		3 m/min	3.5 m/min	4 m/min
Focal length	0 mm			
	-1.4 mm			

In Figure 9, the distances of the fracture zones of the samples to the Heat Affected Zone (HAZ) are given. Although the fracture approached towards the weld pool as the welding speed increased in the samples with 0 mm focal length, it was still observed that it broke off from the base material. D1, D2 and D3 Fracture Zone-HAZ distances at 0 mm focal length are 30710 μm , 18220 μm and 341 μm , respectively. In D3 sample, it is seen that the fraction is very close to HAZ. When the SEM images were examined, ductile fracture morphology was observed for D1 and D2 (Figure 10a and Figure 10b). Therefore, as expected, fractures in the base material have ductile fracture morphology and similar dimple sizes (Wang et al., 2017). As supported by tensile-shear load – crosshead displacement data, the lowest tensile-shear load – crosshead displacement value is in the D3 sample. The main reason for this situation is that the depth of penetration in the lower sheet is in this sample as seen in Table 3. Because of lack of penetration, the fracture zone got closer to the HAZ and so the D3 fracture surface has brittle fracture morphology (Figure 10c).

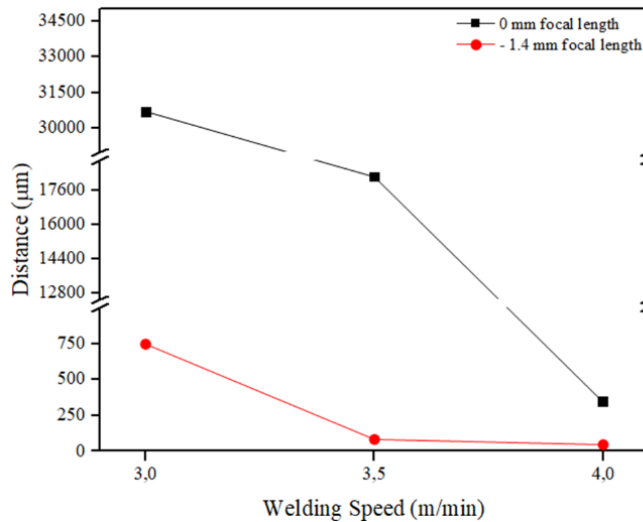


Figure 9. Fracture Distance to Heat-Affected Zone (HAZ)

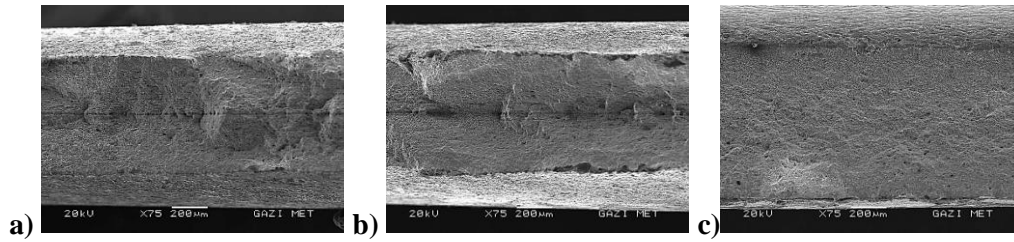


Figure 10. Fracture Surface of 0 mm Focal Length Specimens After Tensile - Shear Load Test, a) D1 Sample, b) D2 Sample, c) D3 Sample

In the samples produced with – 1.4 mm focal length, D4 is fractured from the base material, D5 from the partially transformed region and D6 from the coarse grained region. Also fracture zone and fusion zone distances were measured as 745 μm , 82 μm , and 45 μm respectively. When the SEM images are examined (Figure 11), D4 was fractured from the base material with a ductile morphology (Figure 11a), and this result can be supported with tensile-shear load – crosshead displacement values. The rupture region of the D5 sample is considered to be the partially transformed region. As a result of the SEM analysis, it is thought that the ferrite, martensite and temper martensite phases that are likely to occur in this region cause a decrease in tensile-shear load – crosshead displacement values and also the brittle fracture areas in the SEM analysis of the fractured surfaces (Figure 11b). It is estimated that the D6 sample broke off from the coarse-grained region, which is thought to be composed of ferrite, tempered martensite and tempered bainite phases. Due to the increase in welding speed, the depth of penetration in this sample also decreased and at the same time, this grain coarsening was the basis of the brittle fracture morphology in the examination of the fracture surface (Figure 11c).

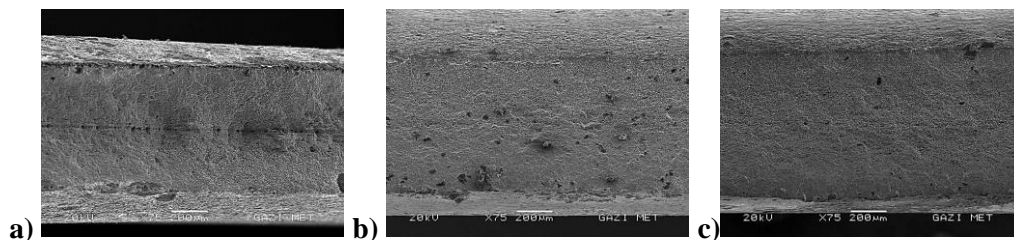


Figure 11. Fracture Surface of –1.4 mm Focal Length Specimens After Tensile - Shear Load Test, a) D4 Sample, b) D5 Sample, c) D6 Sample

4. CONCLUSION

In this study 4 kW laser power, 3, 3.5, 4 m/min welding speed and two different focal length distances (0 and –1.4 mm) parameters were used as welding parameters. Tensile-shear strength, microhardness, and fracture surfaces were examined and the influences of welding speed and focal length distances on the result of mechanical properties of the welded joints have been discussed. The following conclusions were drawn:

1. Weld joint shape is completely related to the heat input and the Lorentz forces, Marangoni and plasma shear forces. For both focal lengths, bottom penetration depths decreased when the welding speeds increased. From samples welded using different focal lengths, the FZ geometries of samples using the same welding speed are similar. Since Lorentz forces occurring due to arc pressure in the keyhole during welding are higher than Marangoni and plasma shear forces, the shrinkage cavity is at most 3.5 m/min occurred in samples with welding speed.
2. Tensile-shear strength values decreased depending on the increased welding speed for both focal length specimens. Since penetration depth and especially phase transformations has changed according to the welding speed, heating and cooling characteristics.
3. The microhardness results were affected by welding speed and focal lengths. In 0 mm focal length distance specimens' hardness values increased according to the increased welding speed and high cooling rate. But in negative focal length, cooling rate is slower than 0 mm focal length, so it is

thinking that the tempering process is occur in the bottom plate because of the laser beam geometry and this tempering process cause tempered martensite and tempered bainite especially in the bottom plate and finally these issues cause the decreasing the hardness values when the welding speed increased.

4. All specimens were fractured from BM in 0 mm focal length and so, in SEM investigations, ductile fracture morphology and similar dimple size were observed in fracture surfaces. Since penetration depth, grain coarsening and also phase transformation, fracture zones changed according to the welding speed in negative focal length. But the specimens which are welded in -1.4 mm focal length, fracture zones got closer to the FZ when the welding speed increased.

ACKNOWLEDGEMENT

This study is supported by IPG Photonics Eurasia – Tuzla, İstanbul, Turkey.

CONFLICT OF INTEREST

The authors declares that there is no conflict of interest regarding the publication of this paper.






REFERENCES

- Aktarer, S. M., Küçükömeroğlu, T., & Davut, K. (2019). Friction stir processing of dual phase steel: Microstructural evolution and mechanical properties. *Materials Characterization*, 155, 109787. doi:[10.1016/j.matchar.2019.109787](https://doi.org/10.1016/j.matchar.2019.109787)
- ASTM International. (2010). *Standard Test Methods for Tension Testing of Metallic Materials* (ASTM E8/E8M-21) doi:[10.1520/E0008_E0008M-16A](https://doi.org/10.1520/E0008_E0008M-16A)
- ASTM International. (2012). *Standard Test Methods for Coating Mass and Chemical Analysis of Zinc-Nickel Alloy Electrolytically Coated on Steel Sheet* (ASTM E1659-12) doi:[10.1520/E1659-12](https://doi.org/10.1520/E1659-12)
- Alves, P. H. O. M., Lima, M. S. F., Raabe, D., & Sandim, H. R. Z. (2018). Laser beam welding of dual-phase DP1000 steel. *Journal of Materials Processing Technology*, 252, 498-510. doi:[10.1016/j.jmatprotec.2017.10.008](https://doi.org/10.1016/j.jmatprotec.2017.10.008)
- Çavuşoğlu, O., Toros, S., & Gürün, H. (2019). Microstructure based modelling of stress-strain relationship on dual phase steels. *Ironmaking & Steelmaking*, 46(4), 313-319. doi:[10.1080/03019233.2017.1371959](https://doi.org/10.1080/03019233.2017.1371959)
- Dai, J., Meng, Q., & Zheng, H. (2020). High-strength dual-phase steel produced through fast-heating annealing method. *Results in Materials*, 5, 100069. doi:[10.1016/j.rinma.2020.100069](https://doi.org/10.1016/j.rinma.2020.100069)
- Farabi, N., Chen, D. L., & Zhou, Y. (2011). Microstructure and mechanical properties of laser welded dissimilar DP600/DP980 dual-phase steel joints. *Journal of Alloys and Compounds*, 509(3), 982-989. doi:[10.1016/j.jallcom.2010.08.158](https://doi.org/10.1016/j.jallcom.2010.08.158)
- Ferreira, C. C. de A., Braga, V., de Siqueira, R. H. M., de Carvalho, S. M., & de Lima, M. S. F. (2020). Laser beam welding of DP980 dual phase steel at high temperatures. *Optics and Laser Technology*, 124, 105964. doi:[10.1016/j.optlastec.2019.105964](https://doi.org/10.1016/j.optlastec.2019.105964)
- Fonstein, N. (2017). 7 - Dual-phase steels. In: R. Rana & S. B. Singh (Eds.), *Automotive Steels* (pp. 169-216). Woodhead Publishing. doi:[10.1016/B978-0-08-100638-2.00007-9](https://doi.org/10.1016/B978-0-08-100638-2.00007-9)
- Gong, H., Wang, S., Knysh, P., & Korkolis, Y. P. (2016). Experimental investigation of the mechanical response of laser-welded dissimilar blanks from advanced- and ultra-high-strength steels. *Materials & Design*, 90, 1115-1123. doi:[10.1016/j.matdes.2015.11.057](https://doi.org/10.1016/j.matdes.2015.11.057)
- Hong, K., & Shin, Y. C. (2017). Prospects of laser welding technology in the automotive industry : A review. *Journal of Materials Processing Technology*, 245, 46-69. doi:[10.1016/j.jmatprotec.2017.02.008](https://doi.org/10.1016/j.jmatprotec.2017.02.008)
- ISO (2016). *Resistance welding - Destructive testing of welds - Specimen dimensions and procedure for cross tension testing of resistance spot and embossed projection welds* (ISO 14273:2016) www.iso.org/standard/61273.html

- ISO (2019). *Metallic materials - Tensile testing - Part 1: Method of test at room temperature* (ISO 6892-1:2019) www.iso.org/standard/78322.html
- Kundu, J., Ray, T., Kundu, A., & Shome, M. (2019). Effect of the laser power on the mechanical performance of the laser spot welds in dual phase steels. *Journal of Materials Processing Technology*, 267, 114-123. doi:[10.1016/j.jmatprotec.2018.12.014](https://doi.org/10.1016/j.jmatprotec.2018.12.014)
- Kuril, A. A., Jagannatham, M., Janaki Ram, G. D., & Bakshi, S. R. (2019). Effect of Post - Weld Heat Treatment on the Microstructure of Plasma Arc Welded DP600 Steel. *Metallography, Microstructure, and Analysis*, 8(6), 848-860. doi:[10.1007/s13632-019-00590-9](https://doi.org/10.1007/s13632-019-00590-9)
- Lakshminarayana, P., Gautam, J. P., Mastanaiah, P., Reddy, G. M., Rao, K. B. S. (2018). Influence of beam power and Traverse speed in Fibre Laser welding of dual Phase steel (590) on depth of WELD zone penetration, microstructure and hardness. *Materials Today: Proceedings*, 5(9), 17132-17138. doi:[10.1016/j.matpr.2018.04.121](https://doi.org/10.1016/j.matpr.2018.04.121)
- Mitra, S., Arora, K. S., Bhattacharya, B., & Singh, S. B. (2020a). Effect of Welding Speed on Texture in Laser-Welded Dual-Phase Steel. *Metallurgical and Materials Transactions A*, 51(6), 2915-2926. doi:[10.1007/s11661-020-05747-8](https://doi.org/10.1007/s11661-020-05747-8)
- Mitra, S., Arora, K. S., Bhattacharya, B., & Singh, S. B. (2020b). Effect of Welding Speed on the Prediction Accuracy of Residual Stress in Laser Welded 1.2 mm Thick Dual Phase Steel. *Lasers in Manufacturing and Materials Processing*, 7(1), 74-87. doi:[10.1007/s40516-019-00107-w](https://doi.org/10.1007/s40516-019-00107-w)
- Palanivel, R., Dinaharan, I., & Laubscher, R. F. (2020). Microstructure and mechanical behavior of Nd:YAG laser beam welded high strength low alloy steel joints. *Optik*, 208, 164050. doi:[10.1016/j.ijleo.2019.164050](https://doi.org/10.1016/j.ijleo.2019.164050)
- Sun, Q., Di, H. S., Li, J. C., & Wang, X. N. (2016). Effect of pulse frequency on microstructure and properties of welded joints for dual phase steel by pulsed laser welding. *Materials & Design*, 105, 201-211. doi:[10.1016/j.matdes.2016.05.071](https://doi.org/10.1016/j.matdes.2016.05.071)
- Švec, P., Schrek, A., Hrnčiar, V., & Csicsó, T. (2015). Fibre Laser Welding of Dual Phase Steels. *Acta Metallurgica Slovaca*, 21(4), 311-320. doi:[10.12776/ams.v21i4.626](https://doi.org/10.12776/ams.v21i4.626)
- Tuncel, O., & Aydın, H. (2020). A Comparison of Tensile Properties of Single-Sided and Double-Sided Laser Welded DP600 Steel Sheets. *Materials Science*, 26(2), 173-178. doi:[10.5755/j01.ms.26.2.21374](https://doi.org/10.5755/j01.ms.26.2.21374)
- Kancharla, V., Mendes, M., Grupp, M., & Baird B. (2018, May 1). Recent advances in fiber laser welding. *Industrial Laser Solutions*. www.industrial-lasers.com/welding/article/16485184/recent-advances-in-fiber-laser-welding
- Wang, J., Yang, L., Sun, M., Liu, T., & Li, H. (2016). Effect of energy input on the microstructure and properties of butt joints in DP1000 steel laser welding. *Materials & Design*, 90, 642-649. doi:[10.1016/j.matdes.2015.11.006](https://doi.org/10.1016/j.matdes.2015.11.006)
- Wang, X., Sun, Q., Zheng, Z., & Di, H. (2017). Microstructure and fracture behavior of laser welded joints of DP steels with different heat inputs. *Materials Science & Engineering A*, 699, 18-25. doi:[10.1016/j.msea.2017.05.078](https://doi.org/10.1016/j.msea.2017.05.078)
- Xie, C., Yang, S., Liu, H., Zhang, Q., Cao, Y., & Wang, Y. (2017). Microstructure and Fatigue Properties of Laser Welded DP590 Dual-Phase Steel Joints. *Journal of Materials Engineering and Performance*, 26(8), 3794-3801. doi:[10.1007/s11665-017-2848-7](https://doi.org/10.1007/s11665-017-2848-7)
- Zhao, D., Wang, Y., Zhang, P., & Liang, D. (2019). Modeling and Experimental Research on Resistance Spot Welded Joints for Dual-Phase Steel. *Materials*, 12(7), 1108. doi:[10.3390/ma12071108](https://doi.org/10.3390/ma12071108)
- Zhao, Y. Y., Zhang, Y. S., Hu, W. (2013). Effect of welding speed on microstructure, hardness and tensile properties in laser welding of advanced high strength steel. *Science and Technology of Welding and Joining*, 18(7), 581-590. doi:[10.1179/1362171813Y.0000000140](https://doi.org/10.1179/1362171813Y.0000000140)



The Dependence of The Nickel Concentration of ZnO Thin Films for Gas Sensors Applications

Baktiyar SOLTABAYEV¹ , Irmak KARADUMAN ER^{2*} , Memet Ali YILDIRIM³ , Aytunç ATEŞ⁴ , Selim ACAR⁵ 

¹National Laboratoty Astana, Nazarbayev University, Nur-Sultan, Kazakistan

²Department of Medical Services and Techniques, Eldivan Medical Services Vocational School, Çankırı Karatekin University, Çankırı, Turkey

³Department of Electric and Electronic Engineering, Engineering Faculty, Erzincan Binali Yıldırım University, Erzincan, Turkey

⁴Department of Material Engineering, Engineering and Natural Sciences Faculty, Yıldırım Beyazıt University, Ankara, Turkey

⁵Department of Physics, Science Faculty, Gazi University, Ankara, Turkey

Keywords

Gas Sensor
ZnO
Low Temperature Range
NO
SILAR Method

Abstract

Undoped ZnO and Ni-doped ZnO thin films were synthesized on glass substrate using the SILAR method. The aim of this work is the analysis of NO gases using Zn_{1-x}Ni_xO sensors concentrations in the range from 100 ppb to 25 ppm. The gas sensing properties of the films for low NO gas concentrations were carefully investigated within a temperature range from 35 to 135°C. The gas measurement results revealed that the doping process was strongly affected by the response of Ni-doped ZnO thin films. The Zn_{0.75}Ni_{0.25}O sensor exhibited higher sensitivity, faster response, and recovery times for NO gas at low (100 ppb) concentration. It was concluded that the Ni dopant enhanced the properties of ZnO films for gas sensor applications by changing the microstructure, morphology, and bandgap of ZnO material.

Cite

Soltabayev, B., Karaduman Er, I., Yıldırım, M. A., Ateş, A., & Acar, S. (2021). The Dependence of The Nickel Concentration of ZnO Thin Films for Gas Sensors Applications. *GU J Sci, Part A*, 8(1), 157-165.

Author ID (ORCID Number)

B. Soltabayev, 0000-0002-5320-2576
I. Karaduman Er, 0000-0003-3786-3865
M. A. Yıldırım, 0000-0002-6175-1807
A. Ateş, 0000-0002-5802-9207
S. Acar, 0000-0003-4014-7800

Article Process

Submission Date 09.02.2021
Revision Date 01.03.2021
Accepted Date 17.03.2021
Published Date 29.03.2021

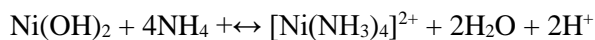
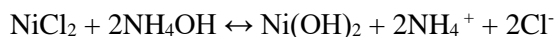
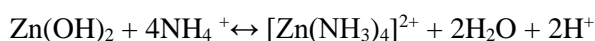
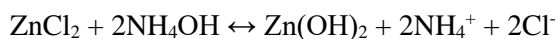
1. INTRODUCTION

Nowadays, there is two basic ways to improve the properties of metal oxide semiconductor-based (MOS) sensors, which widely used in the development of gas sensors. The first one is the using of thin ZnO and the second is doping with transition or noble metals into ZnO. The first method based on that the response of MOS-based sensors depends on the surface area, grain size, morphology, and structural properties of sensing material (Moon et al., 2010). These properties can be tuned via choosing the suitable synthesis method and conditions, thus the properties of gas sensing material with different structures and morphologies have been studied intensively in (Wang et al., 2016). Also, low-temperature synthesis in an aqueous solution is convenient and is considered to be a chemical alternative with practical advantages (Nwanya et al., 2015). The synthesis of ZnO thin films using the SILAR method in low temperature is preferred in recent years because it is cheaper, simpler, and less time-consuming in semiconductor film synthesis than expensive vacuum equipment. The SILAR is an aqueous solution method involving a series of successive reactions between a substrate and a solution, in which the compound semiconductor to be grown on the underlying material is submerged in a series of aqueous solutions containing ions of each species (Salunkhe & Lokhande, 2008; Yıldırım et al., 2016). It is possible that the number of the SILAR cycles can be determined for the control of the thickness of the material and this is one of the

most important parameters in the SILAR method. As the number of cycles increases, the thin film thickness increases and a more stable structure is obtained. However, too many SILAR cycles are not suitable because when the thin film thickness reaches a certain value, the ions will now accumulate on the surface in the form of sediment, and as a result, the breaks will become easier and the thin film quality will decrease (Çorlu et al., 2018). The second method, the doped MOS thinsensors have become an attractive subject in the various fields (Chen et al., 2016). The physical and structural properties of MOS sensors have been studied and enhanced by doping with either the noble metals (Pt, Pd, Ag and Au) or by the transition metals (Mn, Al, Cu, and Ni) (Sun et al., 2017). Transition metal-doped MOS-based sensors have intrinsic donor defects which effect the electrical and optical properties of gas sensors (Keskenler et al., 2012). Besides, it also improves the ferromagnetic and sensor properties (sensitivity and selectivity). Thus, transition metal-doped MOS-based nanostructure material is an important role in the gas sensing application and other optoelectronic devices. Nickel (Ni) is one of the transition metals, which shows higher response and better selectivity for the gas at low concentrations (~0.1-100 ppm). Ni doped ZnO nanostructure material for gas-sensing applications enhances the parameters of sensor such as sensitivity and selectivity. Due to the similarities between the valence of Zn^{2+} and Ni^{2+} , the effective ionic radii of Ni^{2+} (0.69 Å) is closer to that of Zn^{2+} (0.74 Å), thus there becomes the possibility of exchanging Zn^{2+} in ZnO lattice by Ni^{2+} . The exchanging of Zn^{2+} by Ni^{2+} produces high donor defect and makes the charge separation and transport in the ZnO easy (Cheng et al., 2008; Gao et al., 2017; Gu et al., 2017; Wang et al., 2017). So, Ni can be used as the efficient doping transition metal into host ZnO nanostructure. Therefore, Ni doped ZnO nanostructures may be an appropriate candidate for MOS-based gas sensors. In this study, Ni doped ZnO thinfilms were synthesized on glass substrate by the SILAR method at room temperature. The sensitivity changes of gas sensors were observed depending on the concentrations of Ni dopant and gas-sensing properties to NO gas for low gas concentrations were carefully investigated.

2. MATERIAL AND METHOD

Zn_{1-x}Ni_xO thinfilms (pure ZnO, Zn_{0.75}Ni_{0.25}O, Zn_{0.50}Ni_{0.50}O, Zn_{0.25}Ni_{0.75}O and NiO) were synthesized on glass substrate using the SILAR method. To synthesize thin films, aqueous $[Zn(NH_3)_4]^{2+}$ and $[Ni(NH_3)_4]^{2+}$ complexes were chosen for the cation precursors, in which ZnCl₂ (99.9%) of 0.1M, NiCl₂ (99.9%) of 0.1M and NH₃ (28%) were used. The obtained complexes were mixed in appropriate proportions according to the composition for Zn_{1-x}Ni_xO. Glass substrates were prepared and cleaned to growing Zn_{1-x}Ni_xO thin films. After cleaning, solutions were prepared at the desired doping rate. Zn_{1-x}Ni_xO thin films were growth by the SILAR method. The chemical reactions taking place during the growing process are given below;



When ZnCl₂, NiCl₂ and NH₃ solutions are mixed, the above reactions take place and $[Zn(NH_3)_4]^{2+}$ and $[Ni(NH_3)_4]^{2+}$ (pH≈10) complex is formed. The glass substrate was kept in a solution of $[Zn(NH_3)_4]^{2+}$ and $[Ni(NH_3)_4]^{2+}$ for 20 seconds and the aqueous thin film was coated on the glass substrate surface. The glass substrate was removed from the solution and kept in distilled water at 90°C for 7 seconds. the main goal here is to achieve the Ni(OH)₂ → NiO transformation. substrates taken out of hot water were kept in air environment for 60 seconds. It was then kept in pure water at room temperature for 30 seconds. Thus, a SILAR cycle was completed.

After the preparation of Zn_{1-x}Ni_xO thin films by the SILAR method, the morphological and structural analyses were analyzed and investigated with XRD, SEM and UV absorbance analysis. The gas sensing performance of prepared the Zn_{1-x}Ni_xO thin films via a computer-controlled gas measurement system was included a Keithley 2400 sourceter, a LakeShore 325 temperature controller, mass flow controllers and

a humidity sensor. The gas measurements of sensors were carried out to NO gas at low concentrations (100 ppb - 25 ppm) and different temperatures range (35 to 135°C) by observing the resistance changes of samples. During all gas measurements, the relative humidity (RH) was kept stable about 25%.

3. RESULTS AND DISCUSSION

Figure 1 shows the SEM results of $Zn_{1-x}Ni_xO$ thin films. All thin films have dense surface morphology and very well covered on the glass substrates. The uniformity and smoothness of the films decreased with increasing Ni doping as seen in Figure 1 (b, c, d). $Zn_{0.75}Ni_{0.25}O$ have nameplates structure and localized clusters on the surface morphology (Figure 1b). Also, $Zn_{0.75}Ni_{0.25}O$ film has interconnected nano-network structure and smoothness very high compared with other films. Due to the increase of concentration of Ni ions in the solution, the nucleation in the ZnO structure becomes easier to the lower activation energy barrier of heterogeneous nucleation. This assists to grow ZnO in a different direction as a result to form nano-network structure morphology (Kumar Rana et al., 2016).

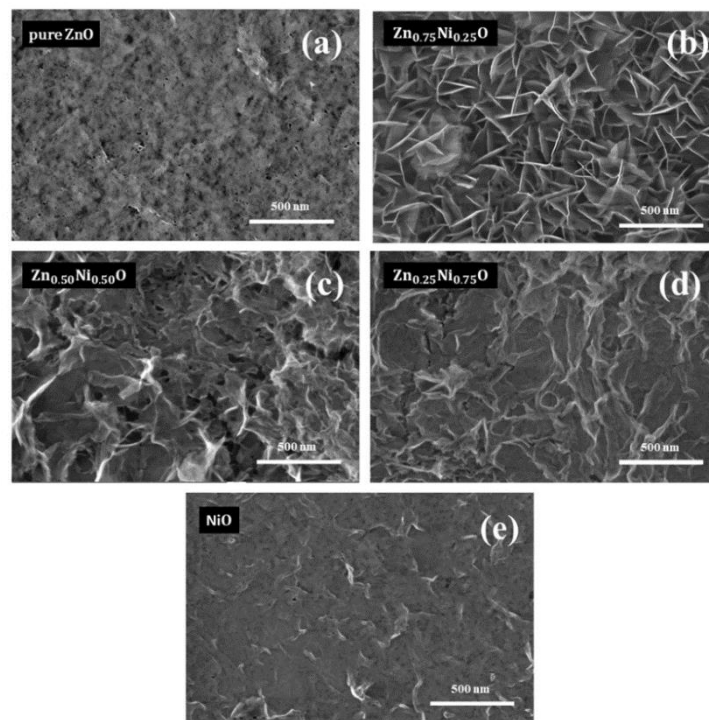


Figure 1. The SEM Images of (a) Pure ZnO, (b) $Zn_{0.75}Ni_{0.25}O$, (c) $Zn_{0.5}Ni_{0.5}O$, (d) $Zn_{0.25}Ni_{0.75}O$, (e) NiO

Figure 2a shows XRD patterns of pure ZnO, $Zn_{0.75}Ni_{0.25}O$, $Zn_{0.5}Ni_{0.5}O$, $Zn_{0.25}Ni_{0.75}O$, and NiO thin films. The films have well-defined peaks belonging to ZnO and NiO, as well as polycrystalline nature. As shown in Figure 2a, ZnO film has a hexagonal wurtzite phase (Çorlu et al., 2017), when the pure NiO film has a cubic phase (Karaduman et al., 2017). The diffraction peaks of pure ZnO corresponding to (100), (002), (101), (102), (110), (103) and (112) are in good agreement with the standard JCPDS data (Card No. 36-1451). The intensity of the diffraction peaks of pure ZnO decreased, as well as (100), (002), and (101) peaks start disappeared in high Ni dopant ($Zn_{0.5}Ni_{0.5}O$, $Zn_{0.25}Ni_{0.75}O$), whereas the diffraction peaks of NiO began to appear and the intensity of (200) and (111) peaks increased with increasing Ni doping concentration. This change of the parameters can be attributed to the replacement of larger Zn^{2+} (0.60 Å) ions with smaller Ni^{2+} ions (0.55 Å). The exchanging of Zn^{2+} by Ni^{2+} produces high donor defect and makes the charge separation and transport in the ZnO easy. Ni doping within ZnO films caused the crystallinity to degenerate (Cheng et al., 2008). Therefore, the change from hexagonal wurtzite structure to cubic structure with increasing Ni dopant was seen from Figure 2a. The bandgap energy values of thin films increased from 3.14 to 3.48 eV according to the doping rate, as shown in Figure 2b. The bandgap energy of pure ZnO was 3.37 eV and NiO was 3.6 eV. So, with the increase of Ni contribution, the rising bandgap can be associated with this difference (Akaltun & Çayır, 2015). Moreover, an increase in the

bandgap energy with the doping element is explained by changes in morphological, crystallinity, atomic distances, and grain sizes of the base material (ZnO, in an actual case).

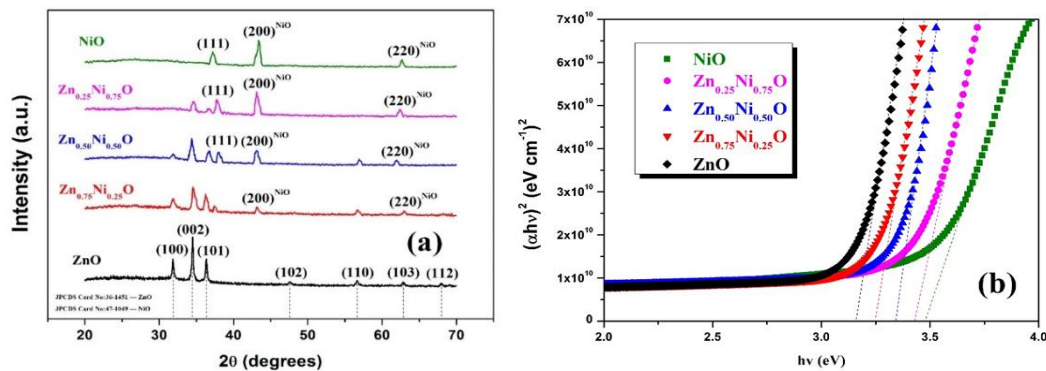


Figure 2. XRD Patterns (a) and $(\alpha h\nu)^2$ Versus Light ($h\nu$) Energy Plots (b) of $Zn_{1-x}Ni_xO$

Generally, the sensing performance of MOS-based gas sensors depends on operating temperature. The operation temperature is the temperature at which MOS-based gas sensors obtain an optimal response, the response will increase first and decrease next with the increase of the temperature (Wang et al., 2008). Starting from the accepted oxygen adsorption theory, modulating the operating temperature is a possible way to realize the dual gas selectivity of MOS, because during the gas sensing process, the gas diffusion and adsorption, the formation of chemisorbed oxygen, and the surface redox reaction are all closely related with the operating temperature. In order to estimate the optimum operating temperature of the gas sensor, the sensing response of $Zn_{1-x}Ni_xO$ gas sensors for 25 ppm NO was measured at different temperatures range (35-135°C). The operating temperature of $Zn_{1-x}Ni_xO$ gas sensors was found at 85°C. As seen in Figure 3, the gas sensing responses of $Zn_{1-x}Ni_xO$ gas sensors began to fall when the operating temperature exceeded 85°C. Maximum response has been achieved in the $Zn_{0.75}Ni_{0.25}O$ sensor. While 40% response was achieved in the $Zn_{0.75}Ni_{0.25}O$ sensor, the responses of $Zn_{0.50}Ni_{0.50}O$, $Zn_{0.25}Ni_{0.75}O$ and NiO sensors 31%, 24% and 33% were achieved, respectively. This phenomenon has been attributed the distribution and the adsorption of oxygen species (O^- , O_2^- and O^{2-}) on the sensor surface which depends on the operating temperature (Wang et al., 2008). For operating temperatures less than 50°C, the response of the sensor is very low because the adsorbed target gas is not activated enough to react with the adsorbed oxygens on the sensor surface. An increase in operating temperature by 85°C contributes to overcoming the activation energy barrier of the reaction and an increase in the response of the sensor. However, above 85°C the decrease in target gas adsorption is not compensated by the increase of surface reaction, and the response of the sensor decreases.

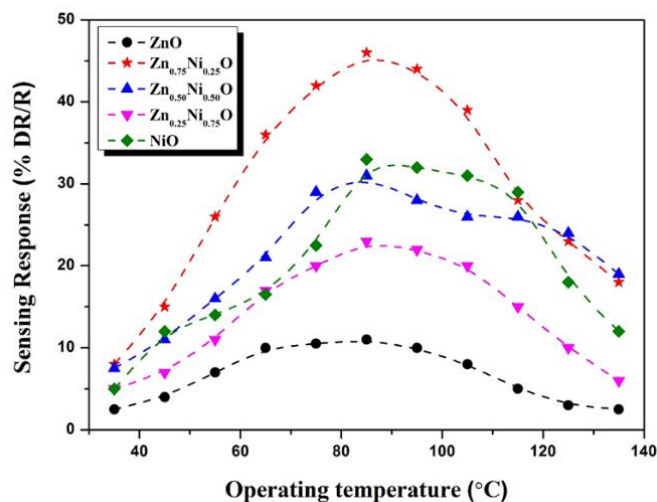


Figure 3. The Sensing Responses of the Sensors versus Operating Temperature at Constant 25 ppm NO Gas Concentrations

The dynamic gas measurements were carried out at 85°C. Figure 4 (a-e) shows the sensing responses of $Zn_{1-x}Ni_xO$ sensors as a function of gas concentrations from 100 ppb to 25 ppm NO gas. It is not difficult to deduce that $Zn_{0.75}Ni_{0.25}O$ have the maximum responses. Each measurement exhibits different response when the target gas is exposed, the sensors can distinguish each gas concentration. The sensing responses at 25 ppm NO gas were calculated 14%, 40%, 31%, 24% and 34% for ZnO, $Zn_{0.75}Ni_{0.25}O$, $Zn_{0.50}Ni_{0.50}O$, $Zn_{0.25}Ni_{0.75}O$ and NiO, respectively. ZnO sensor showed no response to 100 ppb NO gas. The responses of 100 ppb NO gas were calculated 7%, 5%, 4% and 5% for $Zn_{0.75}Ni_{0.25}O$, $Zn_{0.50}Ni_{0.50}O$, $Zn_{0.25}Ni_{0.75}O$ and NiO, respectively. For very low gas concentration like 100 ppb, maximum response was obtained for $Zn_{0.75}Ni_{0.25}O$. As seen in Figure 5, the gas responses increased with increasing NO gas concentrations. It can be seen that Ni content considerably affects the response of sensor. In the absence of Ni doping, the ZnO sensor showed no response to 100 ppb NO gas. With Ni doping of 25%, the response of the sensor increased and exhibited a high response to NO gas. As Ni doping increased to 75%, the sensor response decreased. It can be related to the morphology of NiO.

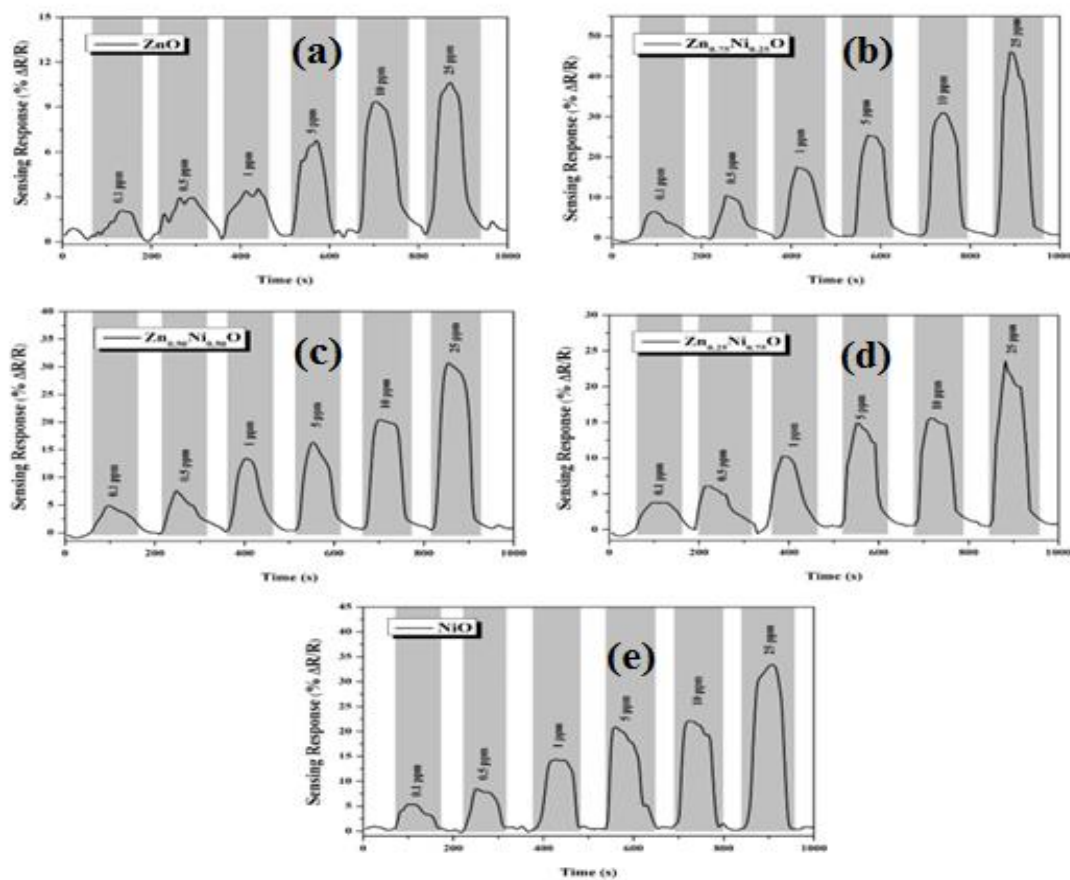


Figure 4. The Dynamic Sensing Responses of $Zn_{1-x}Ni_xO$ for Different NO Gas Concentrations from 100 ppb to 25 ppm at 85 °C

The response and recovery times were calculated and were shown in Figure 6 (a-b). $Zn_{0.75}Ni_{0.25}O$ sensor has the fast response and recovery times compared to other sensors. The response and recovery times of 100 ppb NO gas were obtained 21 s and 17 s for $Zn_{0.75}Ni_{0.25}O$ sensor. As seen in Figure 6, the recovery time were faster than response time. The response and recovery times of 25 ppm NO gas were obtained 13 s and 10 s for $Zn_{0.75}Ni_{0.25}O$ sensor.

The gas sensing selectivity is another important parameter to evaluate the gas-sensing properties of the gas sensors and greatly desired in practical application. The selectivity of the sensors was analyzed for CO, NO, NH_3 , H_2 and CO_2 at 85°C because the operating temperature was found 85°C from the previous measurements. The gas concentrations were taken from 100 ppb to 25 ppm, as shown in Figure 7. The responses were shown differences according to the doping concentrations. The responses of NH_3 and CO

gases increased with increasing Ni concentrations, whereas the response of NO decreased. No response was shown to the H₂ and CO₂ gases. Lin et al. (2017) showed that different nickel concentrations exhibit different responses to target gases. Ganesh Sanker et al. (2017) reported that there was an increase in response up to a certain nickel concentration and a decrease in response above optimal concentration. Shen et al. (2017) showed that optimal nickel concentrations exhibited higher response, have lower detection limit and better selectivity compared to other doping concentrations.

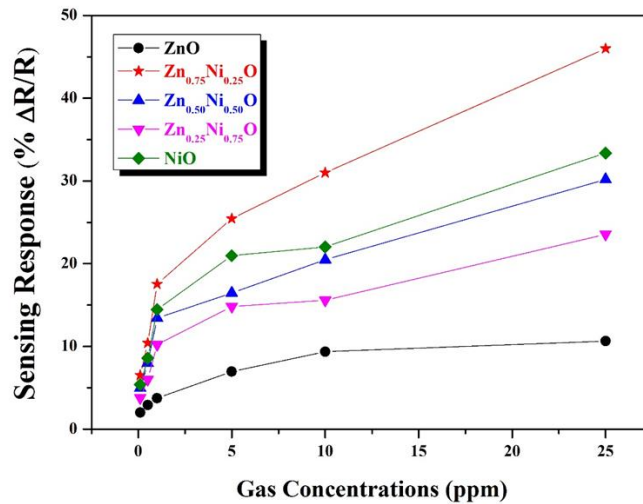


Figure 5. The Sensing Responses of Zn_{1-x}Ni_xO for Different Gas Concentrations from 100 ppb to 25 ppm at 85 °C

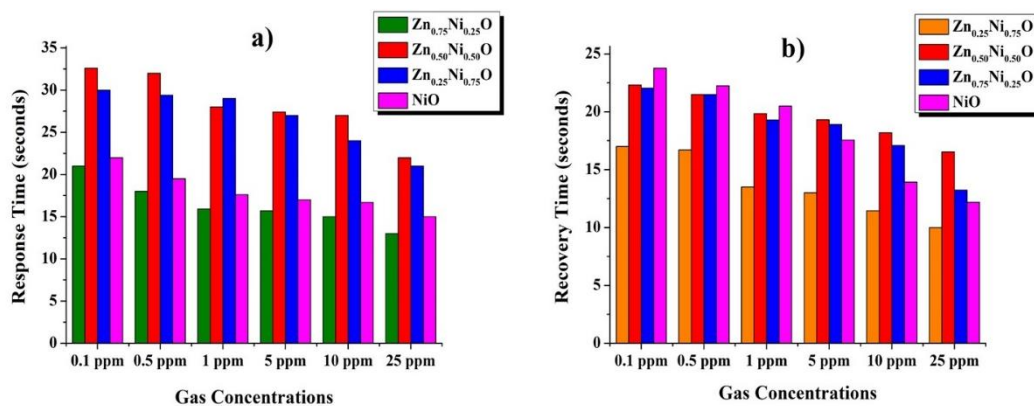


Figure 6. The Response and Recovery Times of Zn_{1-x}Ni_xO for 20 ppb-25 ppm

The gas detection mechanism in metal oxide materials is based on the chemical reactions that occur between the surface of the metal oxide and the gas molecules in the atmosphere that cause changes in the electrical conductivity of the metal oxide (Rambu et al., 2013). The chemical absorption of oxygen plays an important role when examining the sensing mechanism in metal oxide gas sensors. Molecular oxygen is captured by the electron in the conductivity band of the metal oxide and clings to the surface. The charge transfer between chemically absorbed oxygen and the target gas changes the conductivity of the metal oxide (Karaduman Er, 2021). During this charge transfer, receiving or giving away electrons; differs according to whether the target gas is oxidizing or reducing and whether the metal oxide used as the sensing layer is p-type or n-type. Reactions may also differ, as the gas sent to the surface is reducing and oxidizing. After the oxygen adsorption reaction on the outer surfaces of the metal oxides sensor, an electron with higher resistance at the sensor surface depletion layer occurs (Karaduman Er, 2021). NO molecules, as a highly reactive species showing an oxidizing character, can be directly chemisorbed on the surface active sites and abstract electrons from the surface. When sensor exposed to NO gas, NO molecules capture electrons from the sensing surface and increasing the resistance.

In addition, nickel doping is a prominent effect on gas sensing. It accelerates the reactions and can drop the operating temperature (Rambu et al., 2013). Rambu et.al. (2013) showed that Ni-doped ZnO films exhibited high response and faster response-recovery times at low operating temperature. They found that the gas sensitivity was depend on the Ni concentration in ZnO films (Rambu et al., 2013). Wang et.al. (2013) reported that gas sensing properties of Ni-doped ZnO nanofibers were effectively improved by Ni doping.

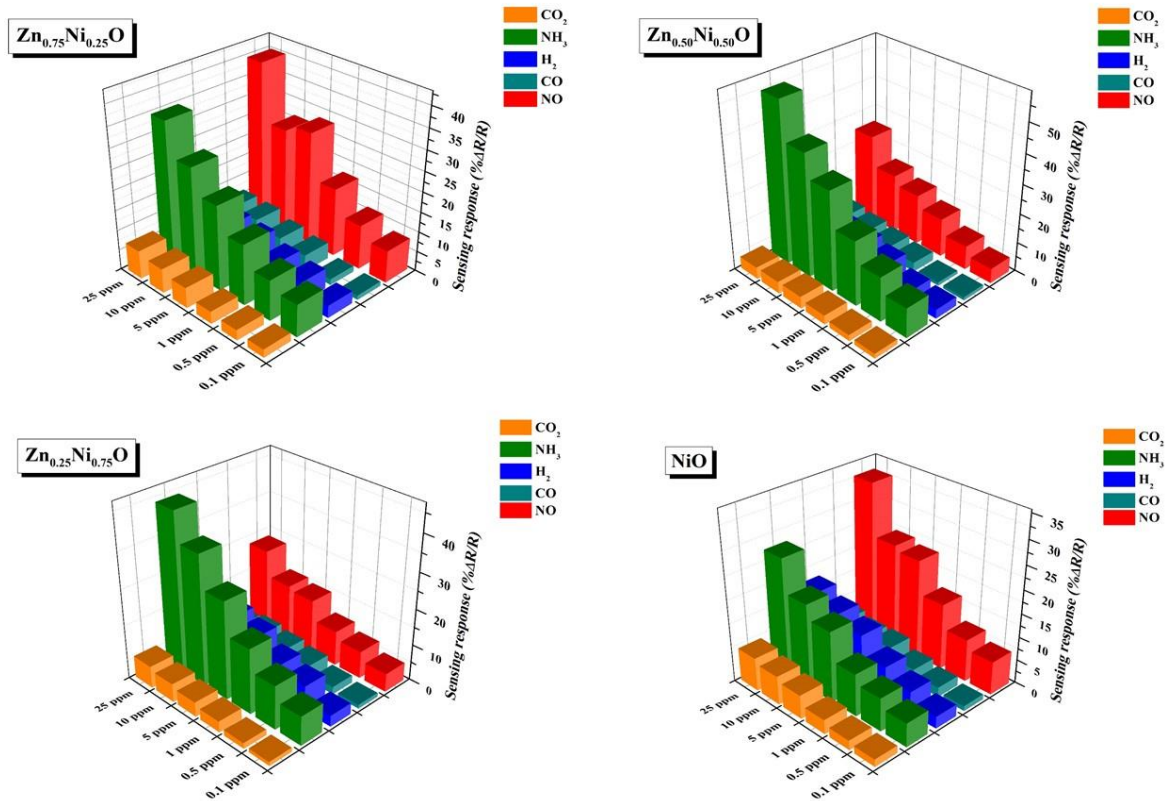


Figure 7. The Selectivity of the Sensors Exposed to NO , CO , NH_3 , H_2 and CO_2 Gases for Different Gas Concentrations at $85^\circ C$

4. CONCLUSION

$Zn_{1-x}Ni_xO$ based sensors were synthesized by SILAR method and the gas sensing properties of the films were studied with the effect of operating temperature and doping concentrations. The maximum sensing response of $Zn_{0.75}Ni_{0.25}O$ sensor to 100 ppb NO gas was 7% at $85^\circ C$. The responses began to decrease as concentration increased. It was proposed that the catalytic effect of Ni, the concentration of Ni doping, and also the morphology of thin films affected the response of gas sensors. ZnO based gas sensors have exhibited high gas sensing performance through Ni doping and this modification seems very encouraging to develop high performance, low cost, compact NO gas sensors.

ACKNOWLEDGEMENT

This work was supported by TUBITAK with Project No: 115M658 and Gazi University Scientific Research Fund Project No: 05/2016-21.

CONFLICT OF INTEREST

This manuscript has been written by the stated authors who are all aware of its content and approve its submission. There is no conflict of interest exists about this submission.

REFERENCES

- Akaltun, Y., & Çayır, T. (2015). Fabrication and characterization of NiO thin films prepared by SILAR method. *Journal of Alloys and Compounds*, 625, 144-148. doi:[10.1016/j.jallcom.2014.10.194](https://doi.org/10.1016/j.jallcom.2014.10.194)
- Chen, Z., Lin, Z., Xu, M., Hong, Y., Li, N., Fu, P., & Chen, Z., (2016). Effect of gas sensing properties by Sn-Rh codoped ZnO nanosheets. *Electronic Materials Letters*, 12(3), 343-349. doi:[10.1007/s13391-016-6053-x](https://doi.org/10.1007/s13391-016-6053-x)
- Cheng, C., Xu, G., Zhang, H., & Luo, Y. (2008). Hydrothermal synthesis Ni-doped ZnO nanorods with room-temperature ferromagnetism. *Materials Letters*, 62(10-11), 1617-1620. doi:[10.1016/j.matlet.2007.09.035](https://doi.org/10.1016/j.matlet.2007.09.035)
- Çorlu, T., Karaduman, I., Yıldırım, M. A., Ateş, A., & Acar, S. (2017). Effect of Doping Materials on the Low-Level NO Gas Sensing Properties of ZnO Thin Films. *Journal of Electronic Materials*, 46(7), 3995-4002. doi:[10.1007/s11664-017-5503-z](https://doi.org/10.1007/s11664-017-5503-z)
- Çorlu, T., Karaduman, I., Galioglu, S., Akata, B., Yıldırım, M. A., Ates, A., & Acar, S. (2018). Low level NO gas sensing properties of Cu doped ZnO thin films prepared by SILAR method. *Materials Letters*, 212, 292-295. doi:[10.1016/j.matlet.2017.10.121](https://doi.org/10.1016/j.matlet.2017.10.121)
- Ganesh Sankar, R., Durgadevi, E., Navaneethan, M., Patil, V. L., Ponnusamy, S., Muthamizhchelvan, C., Kawasaki, S., Patil, P. S., & Hayakawa, Y. (2017). Controlled synthesis of Ni-doped ZnO hexagonal microdiscs and their gas sensing properties at low temperature. *Chemical Physics Letters*, 689, 92-99. doi:[10.1016/j.cplett.2017.09.057](https://doi.org/10.1016/j.cplett.2017.09.057)
- Gao, H., Wei, D., Lin, P., Liu, C., Sun, P., Shimano, K., Yamazoe, N., & Lu, G. (2017). The design of excellent xylene gas sensor using Sn-doped NiO hierarchical nanostructure. *Sensors and Actuators B: Chemical*, 253, 1152-1162. doi:[10.1016/j.snb.2017.06.177](https://doi.org/10.1016/j.snb.2017.06.177)
- Gu, C., Guan, W., Liu, X., Gao, L., Wang, L., Shim J-J., & Huang J., (2017). Controlled synthesis of porous Ni-doped SnO₂ microstructures and their enhanced gas sensing properties. *Journal of Alloys and Compounds*, 692, 855-864. doi:[10.1016/j.jallcom.2016.09.103](https://doi.org/10.1016/j.jallcom.2016.09.103)
- Karaduman, I., Çorlu, T., Yıldırım, M. A., Ateş, A., & Acar, S. (2017). Hydrogen Gas Sensing Characteristics of Nanostructured NiO Thin Films Synthesized by SILAR Method. *Journal of Electronic Materials*, 46(7), 4017-4023. doi:[10.1007/s11664-017-5400-5](https://doi.org/10.1007/s11664-017-5400-5)
- Karaduman Er, I. (2021). Development of ZnO sensors via succession ionic layer adsorption and reaction (SILAR) method for ppb level NO gas sensing. *Research on Engineering Structures & Materials*. doi:[10.17515/resm2020.212ma0901](https://doi.org/10.17515/resm2020.212ma0901)
- Keskenler, E. F., Doğan, S., Turgut, G., & Gürbulak, B., (2012). Evaluation of Structural and Optical Properties of Mn-Doped ZnO Thin Films Synthesized by Sol-Gel Technique. *Metallurgical and Materials Transactions A*, 43(13), 5088-5095. doi:[10.1007/s11661-012-1365-4](https://doi.org/10.1007/s11661-012-1365-4)
- Kumar Rana, A., Bankar, P., Kumar, Y., More, M. A., Late, D. J., & Shirage, P. M. (2016). Synthesis of Ni doped ZnO nanostructures by low temperature wet chemical method and their enhanced field emission properties. *RSC Advances*, 6(106), 104318-104324. doi:[10.1039/C6RA21190A](https://doi.org/10.1039/C6RA21190A)
- Moon, H. G., Jang, H. W., Kim, J-S., Park, H.-H., & Yoon S-J. (2010). Size effects in the CO sensing properties of nanostructured TiO₂ thin films fabricated by colloidal templating. *Electronic Materials Letters*, 6(1), 31-34. doi:[10.3365/eml.2010.03.031](https://doi.org/10.3365/eml.2010.03.031)
- Lin, Z., Li, N., Chen, Z., & Fu, P. (2017). The effect of Ni doping concentration on the gas sensing properties of Ni doped SnO₂. *Sensors and Actuators B: Chemical*, 239, 501-510. doi:[10.1016/j.snb.2016.08.053](https://doi.org/10.1016/j.snb.2016.08.053)
- Nwanya, A. C., Deshmukh, P. R., Osuji, R. U., Maaza, M., Lokhande, C. D., & Ezema F. I. (2015). Synthesis, characterization and gas-sensing properties of SILAR deposited ZnO-CdO nano-composite thin film. *Sensors and Actuators B: Chemical*, 206, 671-678. doi:[10.1016/j.snb.2014.09.111](https://doi.org/10.1016/j.snb.2014.09.111)

- Rambu, A. P., Ursu, L., Iftimie, N., Nica, V., Dobromir, M., & Iacomi, F. (2013). Study on Ni-doped ZnO films as gas sensors. *Applied Surface Science*, 280, 598-604. doi:[10.1016/j.apsusc.2013.05.033](https://doi.org/10.1016/j.apsusc.2013.05.033)
- Salunkhe, R. R., & Lokhande, C. D. (2008). Effect of film thickness on liquefied petroleum gas (LPG) sensing properties of SILAR deposited CdO thin films. *Sensors and Actuators B: Chemical*, 129(1), 345-351. doi:[10.1016/j.snb.2007.08.035](https://doi.org/10.1016/j.snb.2007.08.035)
- Shen, J., Guo, S., Chen, C., Sun, L., Wen, S., Chen, Y., & Ruan, S. (2017). Synthesis of Ni-doped α -MoO₃ nanolamella and their improved gas sensing properties. *Sensors and Actuators B: Chemical*, 252, 757-763. doi:[10.1016/j.snb.2017.06.040](https://doi.org/10.1016/j.snb.2017.06.040)
- Sun, G.-J., Kyung Lee, J., Lee, W. I., Prakash Dwivedi, R., Lee, C., & Ko, T. (2017). Ethanol sensing properties and dominant sensing mechanism of NiO-decorated SnO₂ nanorod sensors. *Electronic Materials Letters*, 13(3), 260-269. doi:[10.1007/s13391-017-1719-6](https://doi.org/10.1007/s13391-017-1719-6)
- Wang, B., Yuan, Y., Wang, C., Huang, J., Li, X., Zhang, H., Xia, F., & Xiao, J. (2017). Effects of Ni addition on the response of La₂CuO₄ sensing electrode for NO sensor. *Sensors and Actuators B: Chemical*, 252, 37-43. doi:[10.1016/j.snb.2017.05.123](https://doi.org/10.1016/j.snb.2017.05.123)
- Wang, L., Zhou, T., Zhang, R., Lou, Z., Deng, J., & Zhang T., (2016). Comparison of toluene sensing performances of zinc stannate with different morphology-based gas sensors. *Sensors and Actuators B: Chemical*, 227, 448-455. doi:[10.1016/j.snb.2015.12.097](https://doi.org/10.1016/j.snb.2015.12.097)
- Wang, X., Zhao, M., Liu, F., Jia, J., Li, X., & Cao, L. (2013). C₂H₂ gas sensor based on Ni-doped ZnO electrospun nanofibers. *Ceramics International*, 39(3), 2883-2887. doi:[10.1016/j.ceramint.2012.09.062](https://doi.org/10.1016/j.ceramint.2012.09.062)
- Wang, Y., Wang, Y., Cao, J., Kong, F., Xia, H., Zhang, J., Zhu, B., Wan, S., & Wu, S. (2008). Low-temperature H₂S sensors based on Ag-doped α -Fe₂O₃ nanoparticles. *Sensors and Actuators B: Chemical*, 131(1), 183-189. doi:[10.1016/j.snb.2007.11.002](https://doi.org/10.1016/j.snb.2007.11.002)
- Yıldırım, M. A., Yıldırım, S. T., Cavanmirza, I., & Ateş, A. (2016). Chemically synthesis and characterization of MnS thin films by SILAR method. *Chemical Physics Letters*, 647, 73-78. doi:[10.1016/j.cplett.2016.01.048](https://doi.org/10.1016/j.cplett.2016.01.048)



Gümüşler (Niğde) Antimon (Sb) Cevherleşmesinin Mineralojik ve Jeokimyasal Araştırılması

Mineralogy and Geochemistry Investigations of Gümüşler (Nigde) Antimony (Sb) Mineralization

Ali TÜMÜKLÜ^{1*}, Okan TOSUNBAŞ²

¹Niğde Ömer Halisdemir Üniversitesi, Mühendislik Fakültesi, Jeoloji Mühendisliği Bölümü, 51240, Niğde

²Niğde Ömer Halisdemir Üniversitesi, Fen Bilimleri Enstitüsü, Jeoloji Mühendisliği ABD, 51240, Niğde

Anahtar Kelimeler

Gümüşler
Jeokimya
Stibnit
Zinober
Metazinober
Nabit Altın

Özet

Gümüşler Sb cevherleşmesi Niğde metamorfikleri içerisinde yapısal kontrollü olarak iki farklı tipte cevherleşme sunmaktadır. Birinci tip cevherleşme metamorfiklerin şistozite yüzeyine paralel konumda kuvars bantları içerisinde. İkinci tip cevherleşme fay düzlemleri içerisinde breşik zonda yer almaktadır. Her iki cevher tipinin ana gang minerali kuvars olup, baritt minerali de bulunmaktadır. Antimon cevherinin ana minerali stibnit olup, süperjen ortamlarda alterasyonu sonucu ikincil antimon oksit minerallerine dönüşmüştür. Şistozite yüzeylerinin arasındaki cevherleşme süt kuvars içerisinde. Breşik zondaki cevherler ise Niğde metamorfiklerine ait breş parçaları ile birlikte bulunmaktadır. Antimon cevheri ile birlikte Hg cevherleşmesinin ana cevher minerali zinoberdir. Zinoberler yüzey sularının introzyondan kaynaklanan ısınması sonucu metazinobere dönüşmüştür. Kuvars kristalleri içerisinde nabit altın taneleri bulunmaktadır. Jeokimyasal analiz sonuçlarının ikili diyagramlarında Sb-Cu, Sb-Zn ve Sb-Mo element çiftlerinin arasında negatif ve Sb-As, Sb-Pb ve Sb-Ba arasında pozitif bir bağlantı bulunmaktadır. Elementler arasındaki bu ilişki korelasyon matriksinde de tespit edilmiştir.

Keywords

Gumusler
Geochemistry
Stibnite
Cinnober
Metacinnober
Native Gold

Abstract

Gümüşler Sb mineralization represents two different types of structurally controlled mineralization within the Niğde metamorphics. The first type of mineralization is in quartz bands parallel to the schistosity surface of metamorphics. The second type of mineralization is located in the brecciated zone within the fault planes. The main gangue mineral of both ore types is quartz and barite is also present. The main mineral of antimony ore is stibnite and it has been transformed into secondary antimony oxide minerals as a result of alteration in supergene environments. The mineralization between the schistosity surfaces coexists with milk quartz. The ores as a result of the heating of surface waters due to intrusion. There are native gold grains in quartz crystals. In the binary diagrams of the geochemical analysis results, there is a negative correlation between Sb-Cu, Sb-Zn and Sb-Mo element pairs and a positive correlation between Sb-As, Sb-Pb and Sb-Ba. This relationship between elements was also found in the correlation matrix.

Alıntı / Cite

Tümüklü, A., & Tosunbaş, O. (2021). Gümüşler (Niğde) Antimon (Sb) Cevherleşmesinin Mineralojik ve Jeokimyasal Araştırılması. *GU J Sci, Part A*, 8(1), 166-188.

Yazar Kimliği / Author ID (ORCID Number)

A. Tumuklu, 0000-0003-1215-8748
O. Tosunbas, 0000-0001-5313-2435

Makale Süreci / Article Process

Başvuru Tarihi / Submission Date 28.02.2021
Revizyon Tarihi / Revision Date 09.03.2021
Kabul Tarihi / Accepted Date 25.03.2021
Yayın Tarihi / Published Date 29.03.2021

1. GİRİŞ

Antimon (Sb) cevherleşmesinin yatak oluşum modellemesi, mineraloji-petrografi ve jeokimyasal özelliklerinin araştırma çalışmaları, Au, Hg, W ve Bi gibi kıymetli metallerin kökenleri ve yataklanma şekilleri ile benzer olan hidrotermal sistemlerde bulunması ve benzer parajenez göstermesi ile son yıllarda bilim insanlarının önem verdiği cevherleşmelerdir. Antimon rezervleri Dünya üzerinde başta Çin olmak üzere Bolıvyaya, Kanada, Meksika, Rusya, Güney Afrika, Tacikistan ve Türkiye’de bulunmaktadır (Seal vd., 2017). Türkiye’de; Balıkesir, Hatay, İzmir, Kütahya, Manisa, Niğde, Tokat illerinde antimon rezervleri bulunmaktadır (Yücel, 2020). Günümüzde bu yatakların önemli bir bölümünde Sb cevheri olan stibnit (Sb_2S_3) üretimi yapılmaktadır. Niğde ili güneydoğusunda yer alan Çamardı ilçeleri arasında birçok Sb, Au, Sn, Hg, Cu, W, Pb/Zn ve Fe yatak ve mostraları yer almaktadır. Bunlardan Celaller Sn (kasiterit, SnO_2) yatağının işletme tarihleri Bronz çağına kadar tarihlenebilmektedir. Bölgedeki diğer birçok yatak (Üçkapılı Au, Tandırlı Sırtı Pb/Zn, Gümüşler Sb ve Hg) ise Osmanlı imparatorluğu ve daha önceki uygarlıklar tarafından işletildiği ile ilgili bazı veriler eski ocak kalıntılarında rastlanılmaktadır. Bölgede birçok eski madencilik çalışmaları ile ilgili galeri, yarma, kuyu ve açık ocak işletme alanı gibi kalıntılar mevcuttur. Gümüşler (Niğde) Sb işletme kalıntıları da bunlardan birisidir. Cevherleşmeler yaklaşık doğu-batı uzanımlı olan aplitik ve mikropegmatitik daykılarla yakın bir ilişki gösterir (Akçay, 1995). Günümüzde Çamardı (Niğde) ilçesinin batı ve kuzey kesiminde Pb/Zn ve Sb üretimi yapılmasına rağmen bazı ocaklar terk edilmiş durumda bulunmaktadır.

Niğde masifini konu alan birçok akademik çalışma bulunmaktadır. Bu çalışmalar genel jeoloji ve mineraloji-petrografi ağırlıklı olup, maden yatakları ile ilgili olanları ise daha az sayıdadır. Blumenthal (1941; 1963), Tromp (1942), Okay (1955), Kleyn (1970), Dennis (1970) ve İleri’nin (1975) çalışmalarında Niğde masifinin temel jeolojik unsurları ortaya konulmuştur. Daha sonraki süreçte Göncüoğlu (1977; 1981a, b; 1986), Özgüneyli (1978) ve Oygür vd.’nin (1984) çalışmaları yer almıştır. Son 20 yılda ise bölge özellikle yabancı araştırmacıların ilgisini çekmiştir. Bunlar arasında Whitney & Dilek (1998), Whitney vd. (2001; 2003), Gautier vd. (2002), Fayon & Whitney (2007) ve Çinku vd. (2016) sayılabilir. Bu çalışmalarda Niğde masifini oluşturan Gümüşler, Kaleboynu ve Aşığediği litodemlerini oluşturan mika ve granatlı şist, amfibolit ve kuvarsitlerin ayrıntılı mineralojik-petrografik, tektonizma ve metramorfizma ilişkilerini açıklamışlardır. Bölgedeki maden yatakları ve jeokimya ile ilgili olarak, Kuşçu vd. (1993), Akçay (1995), Yalçın & Yaman (1996), Yalçın (1998), Altuncu vd. (2018a, b) ve Tmkl vd. (2018) çalışmaları sayılabilir. Yapılan bu çalışmalarda cevherleşmelerin mineraloji-petrografi ve jeokimyasal özellikleri birlikte incelenmemiştir.

Bu araştırmada Niğde ili ve Çamardı (Niğde) ilçesi arasında yer alan Niğde Masifinin kuzeybatısındaki Gümüşler bölgesi Sb cevherleşmesi konu edilmiştir. Bu kapsamda inceleme alanındaki eski işletme kalıntıları olan yarmalar ile mostralardan alınan örnekler üzerinde mineraloji-petrografi ve jeokimya ile maden jeolojisi özellikleri incelenmiştir.

2. MATERYAL VE METOT

Gümüşler (Niğde) güney bölgesinde bulunan eski işletme alanlarındaki cevher ve yan kayaçlardan toplamda 25 adet örnek alımı yapılmıştır. Alınan kayaç örneklerinden ince kesit ve cevher örneklerinden ise parlak kesitleri yapılmıştır. Kesitler Niğde Ömer Halisdemir Üniversitesi Mühendislik Fakültesi Jeoloji mühendisliği bölümü mineraloji-petrografi laboratuvarında incelenerek mikroskobik yapı, dokuları ile cevher parajenezleri belirlenmiştir.

Mikroskop çalışmaları sonucu 6 adet örnek jeokimyasal analiz amaçlı belirlenmiştir. Jeokimyasal analiz için, cevher numuneleri Niğde Ömer Halisdemir Üniversitesi Mühendislik Fakültesi Jeoloji Mühendisliği laboratuvarlarında pulverizatörle 80 mesh (177 μ) boyutunda öğütülmüştür. Homojen öğütülemeyen örnekler agat havan kullanılarak homojenleştirilmiş ve 15 gramlık kilitli plastik poşetlere konulup analize hazır hale getirilmiştir. Örnekler 950°C’de ısıtılarak kızdırma kayıpları tespit edilmiştir. Jeokimyasal analizler Aksaray Üniversitesi Bilimsel ve Teknolojik Uygulama ve Araştırma Merkezi’nde dalga boyu dağılımlı X Işını Floresans Spektrometersi (WD-XRF) yöntemi ana oksit ve iz element oranları belirlenmiştir.

3. BULGULAR VE TARTIMA

3.1. Genel Jeoloji

alıma alanı ve civarında tabandan tavana doęru Nięde metamorfik Masifi, kaplı Granodiyoriti, ofiyolitik ve volkanik kayalar ile tm bu birimlerden treyen gncel tutturulmamı alvyal birimler yer almaktadır. Nięde Metamorfik masifindeki metamorfik kayalar topluca Nięde grubu olarak adlandırılır ve litolojik özelliklerine gre Gmler, Kaleboynu ve Aıęedięi Litodemlerinden olumaktadır (ekil 1). Masif ve üzerindeki ofiyolitik kayaları Alt Senomiyen yalı kaplı granodiyoriti pegmatitik daykları ve apitleri tarafından kesilmi ve kontakt metamorfizmaya uęratılmıtır (Gncoęlu, 1977; 1981a, b). alıma alanı ierisindeki Miyosen-Erken Pliyosen yalı (4,9-5,5±0,2 milyon yıl) (Ercan, 1986) volkanik kayalar ile alvyonlarda dayk sistemi gzlenmemitir.

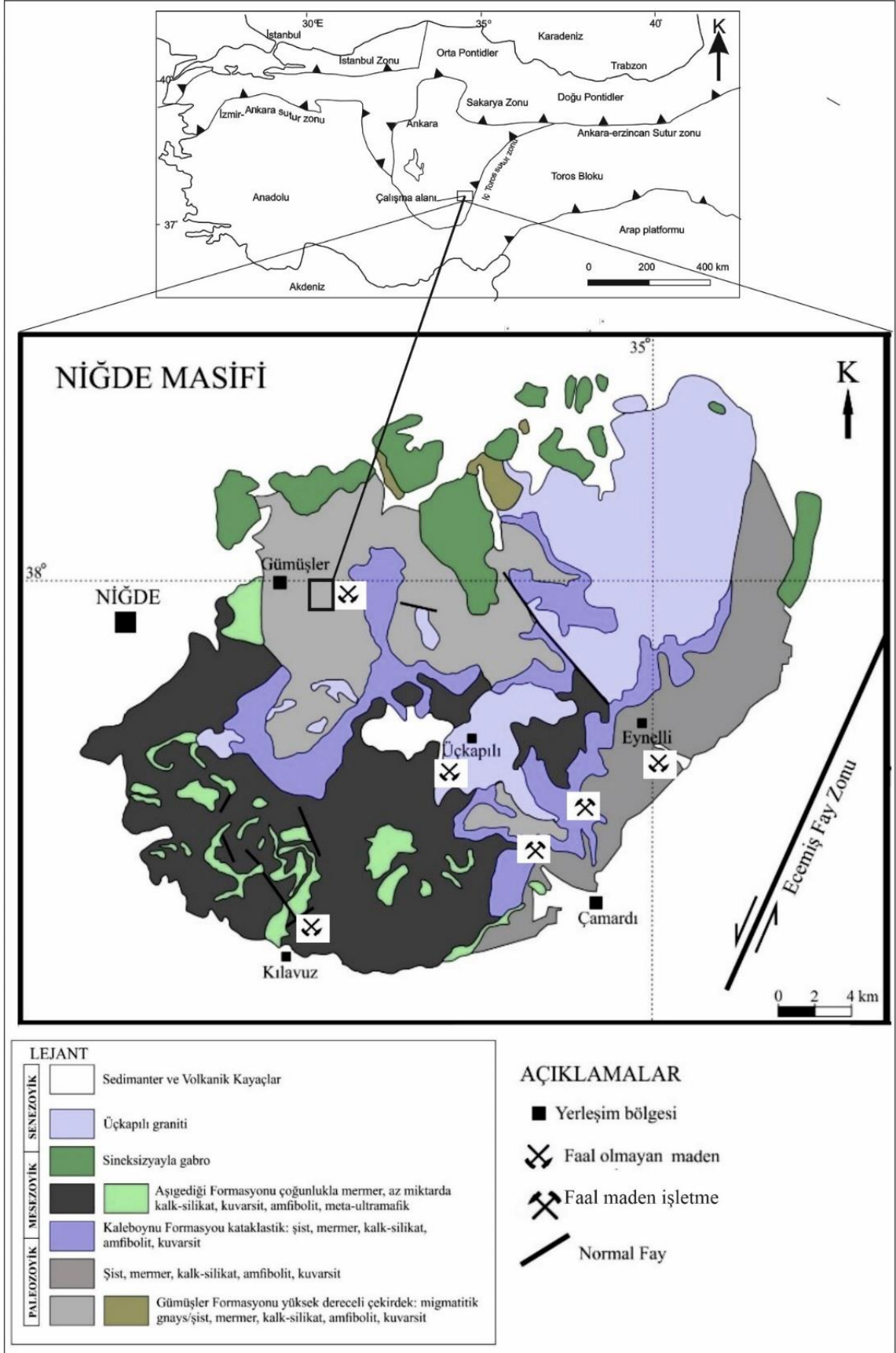
alıma alanı ierisinde Gmler Litodemi, kaplı Granodiyoritine ait pegmatitik dayklar apitler, volkanik kayalar ve ukur alanları dolduran tutturulmamı alvyonlar yer almaktadır (ekil 2). Nięde masifinin temelini oluturan Gmler Litodemi, Gmler kynn doęu ve gneydoęusunda yzeylenir ve Gmler domunun ekirdeęini oluturur, tabanı grlmez ve grnen kalınlıęı 600 metredir (Viljoen & İleri, 1973). Litodem Paleozik yalı olup iinde biri doęu, biri gneydoęu ve bir dięeri de merkez (Gmler civarı) olmak zere 3 dilimden olumaktadır. Her bir dilimin metamorfizma derecesi ve ierdięi mineraller birbirinden farklıdır. Doęu ve merkez dilimlerde migmatitlemi kayalar gzlenirken gneydoęu dilimde migmatitleme gzlenmez (Gautier vd., 2002).

Bu litodemin %70'ten fazlasını eitli gnayslar oluturmaktadır. Gnayslar iinde amfibolit, mermer, kuvarsit ve migmatitik kayalar arabantlı olarak gzlenir. Geri kalan kısımları ise, merceksel konumlu mermerler, kuvarsitler ve amfibolitler oluturmaktadır (Atabey & Ayhan, 1986). Kaleboynu Litodemi, tarafından uyumlu olarak rtlr.

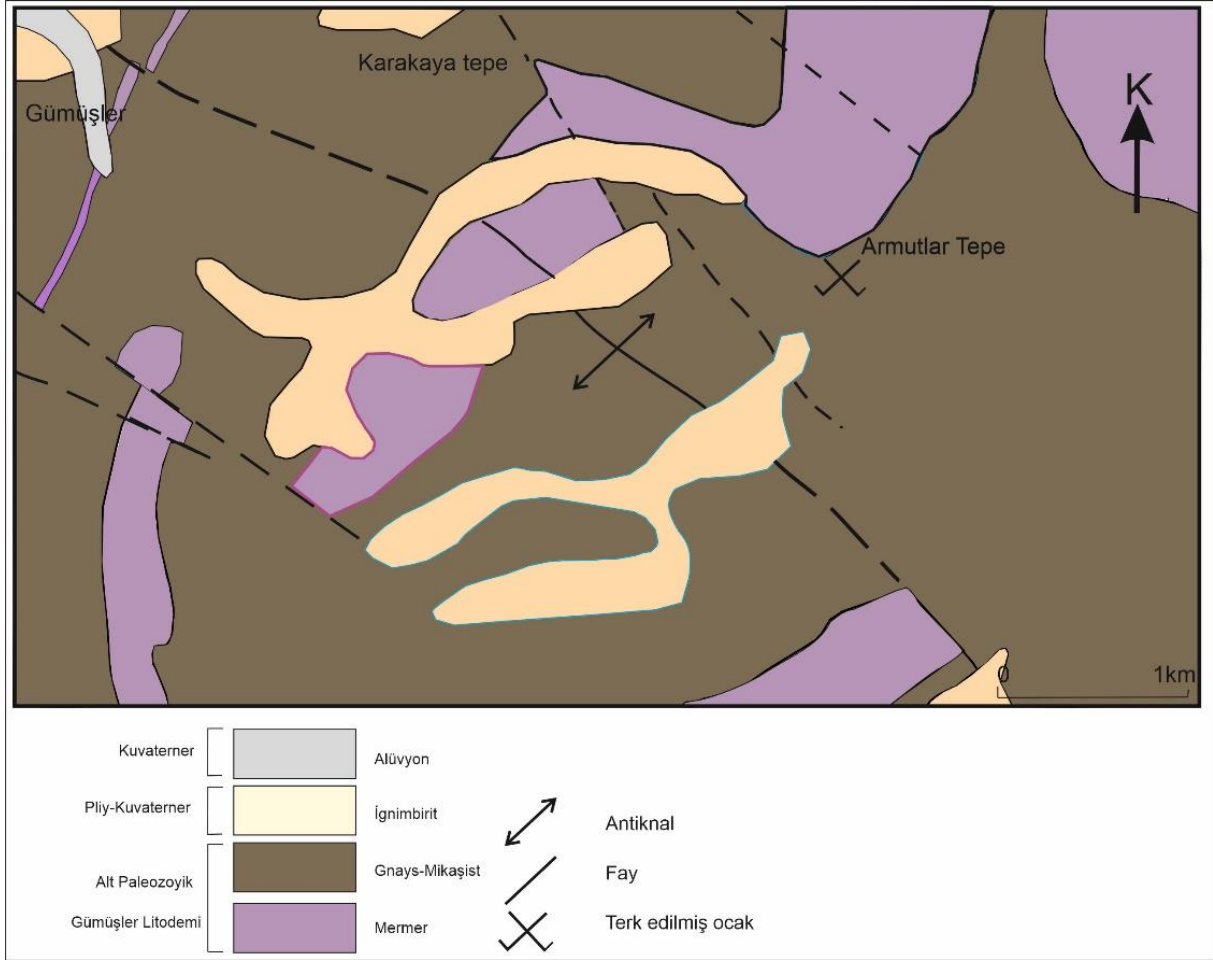
Blgede ok sayıda pegmatitik dayk ve apitleri bulunmaktadır. Dayklar 0,5-10 m kalınlıęında olup mostra uzunlukları 500 metreye yaklaanları mevcuttur. Dayklar Gmler Litodemeine ait kayalar guruplarını farklı aılarla keserler (ekil 3a) Antimon cevherlemesi Gautier vd. (2002) tarafından adlandırılan merkez dilim ierisinde yer alır. Gmler kynn gneydoęusunda yer alan bir antiknalın zirve blmleri ile antiknal etrafında meydana gelmi kayma dzlemlerine baęlı sreksizlik zonlarında cevherleme grlr. Cevherlemeler Őistozite dzlemleri arasında, mermer-Őist-gnays tabaka dzlemlerinde ve tektonik sreksizliklerde yer almaktadır. Metamorfik kayaların Őistozite dzlemleri arasındaki cevherlemeler genel olarak 5-10 cm ile 50 cm arasında kalınlıęa sahip kuvars damarları ierisinde yer almaktadır. Cevherli kuvars damarları ile metamorfik kayalar arasındaki sınır net olarak ayırt edilmekte olup, ok az kesimde Őistler ierisinde 25-30 cm uzunluk ve birka mm kalınlıęa sahip damarlar da grlmektedir. Mermer-gnays-Őist tabaka dzlemleri arasında da Őistler ierisindeki kuvarslı cevher damarları benzer özelliktedir.

3.2. Eski İletme ve Ocaklar

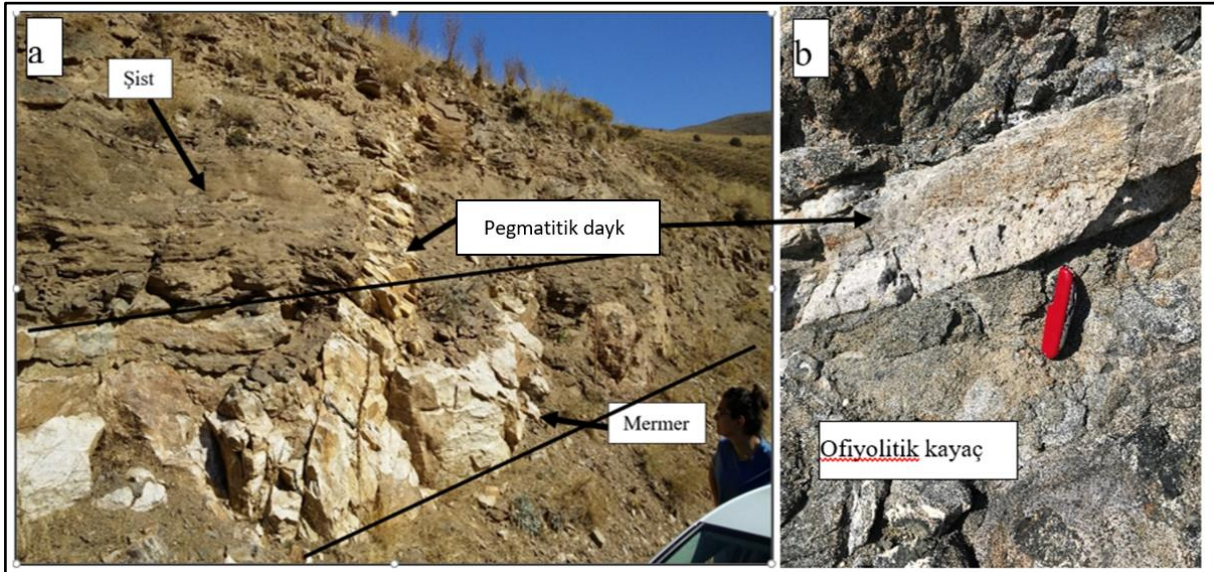
Gmler kasabası civarında 1970'li yılların sonuna kadar Gmler Litodemeine ait Őist, mermer ve fay zonlarında yer alan Sb cevheri (stibnit) ve Hg (zinober) cevheri retimi yapılmıtır. Blgede bulunan yer altı ve yer st ocaklarından ıkarılan yksek tenrl Sb cevheri tvenan olarak deęerlendirilmitir. ıkarılan cevherde zinober tenr yksek olanlar ise damıtma tesisinde cıva retimi iin kullanılmıtır. Blgedeki cıva madencilięin tarihi Romalılar dnemine kadar uzanmaktadır. 1965'in sonlarına doęru, %0,5-1,0 tenrl ayrılmı cıva cevheri paralarını ilemek iin  ift eęimli imbik yntemi kullanılarak cıva retimi yapılmıtır (Yıldız & Bailey, 1978). Blgedeki eski tesis kalıntıları ve resimlerinden elde edilen sonulara gre, yksek tenrl (%0,5<) tvenan cıva cevherinin (zinober) ısıtılması yntemi ile hızlıca buhar fazına gemesi saęlanmakta, sonraki srete imbikten geirilerek soęuması nedeniyle cıva elementi sıvı fazda elde edilmitir. Blgede ok sayıda eski retim galerisi bulunmaktadır. Eski retim tesis civarında ısıtma ilem grm atıklar (cruf) ve az miktarda dk tenrl cevher stoku bulunmaktadır (ekil 4a-f).



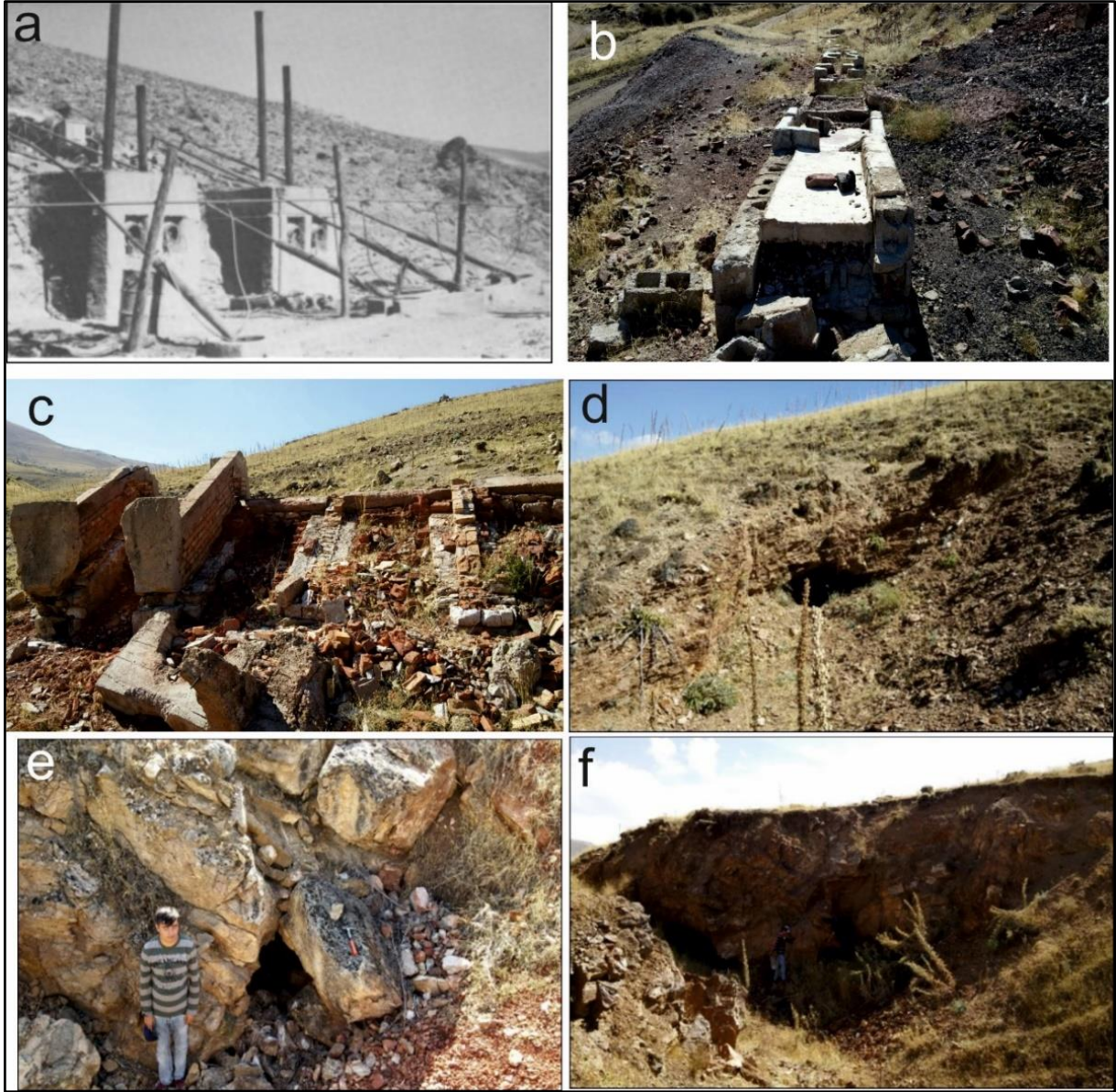
Őekil 1. ÇalıŐma Alanı Yer Bulduru ve Genel Jeoloji Haritası (Whitney vd., 2003'ten deđiŐikle)



Őekil 2. alıŐma Alanı Genel Jeoloji Haritası



Őekil 3. kapılı Granodiyoritine ait Dayklar,
a) GmŐler DoĐu Kesimi Mermer ve Őistleri Kesen Pegmatitik Dayk,
b) Ofiyolitik Kayaları Kesen Aplit (GmŐler Barajı Civarı, alıŐma Alanı Batı Kesimi)



Őekil 4. GmŐler Blgesinde 1970'li Yıllara Kadar alıŐmıŐ Olan Ocaklar ve Hg ZenginleŐtirme (Damıtma) Tesisinin Grnm,
a) Tesisin alıŐma Zamanına ait Grnm (Fotoğraf: Yıldız & Bailey'den (1978) alınmıŐtır),
b), c) Tesisin Gnmzdeki Atıl Durumu, d), e), f) Eski retim Galerileri

3.3. CevherleŐme

GmŐler blgesi cevherleŐmeleri GmŐler Litodemine ait mermer, gnays ve Őistler ierisinde, Őistoziye paralel staratabaound damar ile ve fay dzlemlerindeki breŐik yapı ierisindeki cevher olmak zere iki farklı yapısal zellikte bulunmaktadır. Eski ocakların ierisindeki cevherli zonlar ile mostraların takibinde cevherli zonlar 1 km mesafeye kadar takip edilebilmektedir. Bu zonlar genel anlamda D-B ynnde uzanmakta ve 35-45° ile K ve KB ynnde eĐimleri mevcuttur. Kalınlıkları ise birkaç cm leĐinden yer yer 1 metreye kadar ıkabilmektedir. BreŐik zonda bulunan birincil cevher mineralleri, stibnit, zinober, hematit ve realgar'dan oluŐmaktadır. Stibnit mineralleri 2-3 mm boyutunda kmeler veya izole iĐnemsı kristaller Őeklinindedir. Zinoberler 2-3 mm boyutunda yuvarlaĐımsı yapıda izole kristal kmeleri veya iĐnemsı ubuklar Őeklinindedir. Hematit, breŐ ierisinde en ok bulunan cevher mineralleŐmesini oluŐurmaktadır. Hematitler mm leĐinden baŐlayarak 20 cm'ye ulaŐan yuvarlak kmeler veya bantlar Őeklinindedir. Realgar, kremite-kırmızımsı renklerde, breŐik zonda genelde 3-5 mm leĐinde kçük kmeler Őeklinde bulunmaktadır. Birincil cevher mineralleri alterasyon sonucu, stibnitler antimon oksite, hematit limonite ve realgar ise orpimente dnŐmŐtr. BreŐik zonda gang minerallerini, GmŐler litodemine

ait mermer, ist, kuvarsit ve amfibolit paraları oluturmaktadır. Bre paraları mm boyutundan 20-25 cm boyutuna kadar ıkabilmektedir. Brein tamamına yakını kseli kenarlara sahiptir (ekil 5a-f).

Staratabaound stibnit cevheri Gmler litodemine ait istler ierisinde kuvars damarları ile birlikte yer almaktadır. Kuvars ve stibnitlerden oluan damarlar istlerin yapraklanma dzeyine paralel bir yapıda 2-3 cm ile 20-25 cm arasında deęien kalınlıęa sahip damarlar ekindedir. Cevherin (stibnit) taze yzeyi, parlak elik grisi ve daha az oranda parlak mavimsi rengi ve ięnemsiz yapısıyla karakteristiktir. Ana cevher minerali olarak stibnit ve ok az oranda (yaklaık %1-2) pirit ve kalkopirit mineralleri iermektedir. Stibnit cevherlemesi kuvars damarları ierisinde mm leęinde kılcal ve 8-10 cm kalındıęında devamsız damarlar veya yıęıımlar ekindedir. Bu stibnit damarları ve yıęıımları kendi ierisinde masif yapıya sahiptir. Masif yapıda bulunan bu tip cevher ierisinde cm boyutlarında, pudramsı yapıda ve sarı rengiyle karakteristik realgar minerallemesi mevcuttur. Kuvars damarlarının yan kaya ile olan dokunaęına yakın bantların taban ve tavan kesimlerinde stibnitler kuvarslar ierisinde saımsı cevher tipine benzer yapıdadır. Breik zonda yaygın olarak grlen hematit, zinober ve realgar minerallemesi masif yapıdaki cevherleme ierisinde yaygınlıęı kısıtlıdır. Gang minerali olarak ierisinde yer aldıęı kuvars bulunmaktadır. Kuvars kristalleri st beyazı rengindedir. Stibnit minerallemesinin alterasyon rengi tipik topraęımsı renkte ve alterasyonun yoęun olduęu alanlarda koyu kırmızı-algam renkli okr'lar meydana gelmitir. Yzeyde veya kırıklar boyunca oksitlenerek oluan antimon oksitler-okr'lar 2-3 mm kalınlıęına ıkabilmektedir (ekil 6a-e, ekil 7a, b).

3.4. Mineraloji-Petrografi

alıma alanı ierisinde mostra, eski aık ve kapalı ocak iletme alanlarından alınan cevher rneklerinden yapılan parlak kesitlerinin incelenmesi sonucunda parajenezde ana cevher minerali stibnittir. Stibnite elik eden elik eden dięer cevher mineralleri ise orpiment, zinober, metazinober, pirit, kalkopirit, malahit, hematit, limonit ve nabit altın'dır. Cevherlemenin ana gang minerali kuvars olup, barit ve kalsit de bulunmaktadır.

Stibnit (Sb_2S_3), mineralleri anizotrop zellikte olup genelde ubuksu bir yapıda z ekilli ve yarı z ekilli olarak, kuvars kristalleri arasını ve kristal ierisinde yer alan kırık, atlak ve bolukları doldurmutur. Yer yer kuvarsların arasında atlak dolgusu amorf yapıda da rastlanır. z ekilli kristaller zellikle masif cevher yapısında sık olarak rastlanır ve kristalleri oluturan ubukları 2,5-3 mm uzunluęunda ve 25-30 μm kadar genilięindedir. Bu ubuklar birbirine paralel yapıda olup ubuk demetleri eklinde bir arada bulunmaktadır. ubuklardan tekil olanına rastlanılmamıtır. Kristal ubuk demetleri ile gang minerali olan kuvars dokanıkları keskin bir sınıra sahip olmayıp girinti-ıkıntılı olarak kristaller birbirine kenetlidir. Stibnitler, kk ($>0,1$ mm) kuvars tanelerinin evreler konumudur. Kristaller ierisinde 0,1-0,2 mm aplarında dzensiz yapıda kaya yapıcı mineraller, apları 50 μm 'yi gemeyen orpiment yıęıım/kristal minerallemesi bulunmaktadır. Stibnit kristal kmeleri ierisinde gl portakal renkli i yansıması ile orpiment minerallemesi yaygın olarak bulunmaktadır. Ayrıca kristaller ierisinde pirit ve kalkopirit minerallerine rastlanılmaktadır. Masif cevherde greceli olarak kuvars kristallerinin daha az bulunduęu kesitlerde stibnit kristal kmelerinin arasını zinober doldurmutur. Bazı kesitlerde stibnit kristallerini arasını mikro lekte breik zonlu yapıya benzer yapılar tespit edilmitir. Bu breik yapıya benzeyen yapı ierisinde byklkleri 0,1 mm'den kk kristal ve/veya amorf yapıda oluumlar bulunmaktadır. Bunlardan cevher mikroskopunda tespit edilenler barit ve malahittir. Bunun ile birlikte mikroskop tayini net olamayan kristal ve/veya amorf yapılar mevcuttur. Stibnit kristallerin arasını kriptonkristalin veya amorf yapıda Sb_2S_3 'nin alterasyonu (oksitlenmesi) sonucu ikincil alterasyon minerallemesi bulunmaktadır. Bunların tayini mikroskopta yapılamamıtır. Fakat bu alterasyon minerallerinin servanit ($Sb^{+3}Sb^{+5}O_4$) ve seramonit (Sb_2O_3) kriptonkristalinleri olduęu dnlmektedir. Bu alterasyon mineralleri makro cevher rneklerinde de net olarak tespit edilmitir. Bazı kesitlerde stibnit kristallerinde eęilme-bklme gsteren basın ikizlenmesi mevcuttur. Basın sonucu eęilme-bklme gsteren ubukların eęilme-bklme aıları 5-20 derece arasında deęimektedir. Basınların iki farklı ynde, yaklaık birbirine paralel ve zıt ynde ubukları etkiledięi tespit edilmitir. Basın sonucu stibnit ubuklarında kırılma ve kamburumsu yapılar olumutur (ekil 8 ve 9).

Orpiment (As_2S_3), mineralleşmesi, boyutları maksimum 150-200 µm civarında saçınımlar şeklinde stibnit ve zinober minerallerinin içinde, kenar kısımlarında ve boşluklarda yer almaktadır. Mikroskop altında belirlenen stibnit içindeki tüm orpimentlerin kenarları boyunca 20 µm kadar izotropik koyu renkli kuşak şeklinde altere kil/minerallere dönüşmüştür. Bu yapının cevher mikroskopunda tespiti mümkün olmamıştır. Orpimentler, makro cevher örneklerinde cm bazında tespit edilen realgar kümelerinin alterasyonu sonucu ikincil olarak oluşmuştur (Şekil 9).

Zinober (HgS), kan kırmızı rengiyle karakteristik olan zinober mineralleri kuvars ve amorf silika içerisinde yaygındır. Breşik zonda bulunan cevherleşmede yaygın olarak bulunur. Fakat stratarabound masif cevherleşme de ise yaygınlığı breşik zona göre fazla değildir. Her iki tip cevherleşme içerisinde zinober mineralleri iki farklı yapısal özelliktedir. Birincisi 2-3 mm boyutunda yuvarlak saçınım kütleleri şeklindedir. Zinoberlerin ikinci bulunuş şekli, ince uzun boru biçimli şekillendirme olarak adlandırılabilir. İkinci tip bu zinober minerallerinin uzunlukları 1 mm'ye kadar çıkabilmektedir. Cevher mikroskopunda 10x ve daha büyük mercekte altında bu boru yapısındaki zinober minerallerinin uzun eksenleri boyunca homojen bir yapıda bulunmayıp orta kesimlerin boşluklu olduğu belirlenmiştir. Yuvarlak kütleli zinoberler içerisinde 0,1 mm kadar çapında realgarlar bulunmaktadır (Şekil 10a-e).

Metazinober (HgS), zinober minerallerin kenarları boyunca grimsi siyah anizotropik yapısı, grimsi siyah rengi ve lamelli yapısıyla yer almaktadır. Metazinoberleri oluşturan lameller 50 µm civarında kalınlığa ve 0,4-0,5 mm kadar uzunluğa sahiptirler. Metazinoberi oluşturan lameller zinober haricinde diğer cevher minerallerinde rastlanılmamıştır. (Şekil 10a).

Hematit (Fe_2O_3), breşik yapıda cevherleşmenin ana cevher mineralidir. Kırık ve çatlaklar boyunca düzensiz yapı ve ana gang minerali olan kuvars içerisinde kapanımlar olarak bulunur. Kenarların itibaren limonite dönüşmüştür (Şekil 11a).

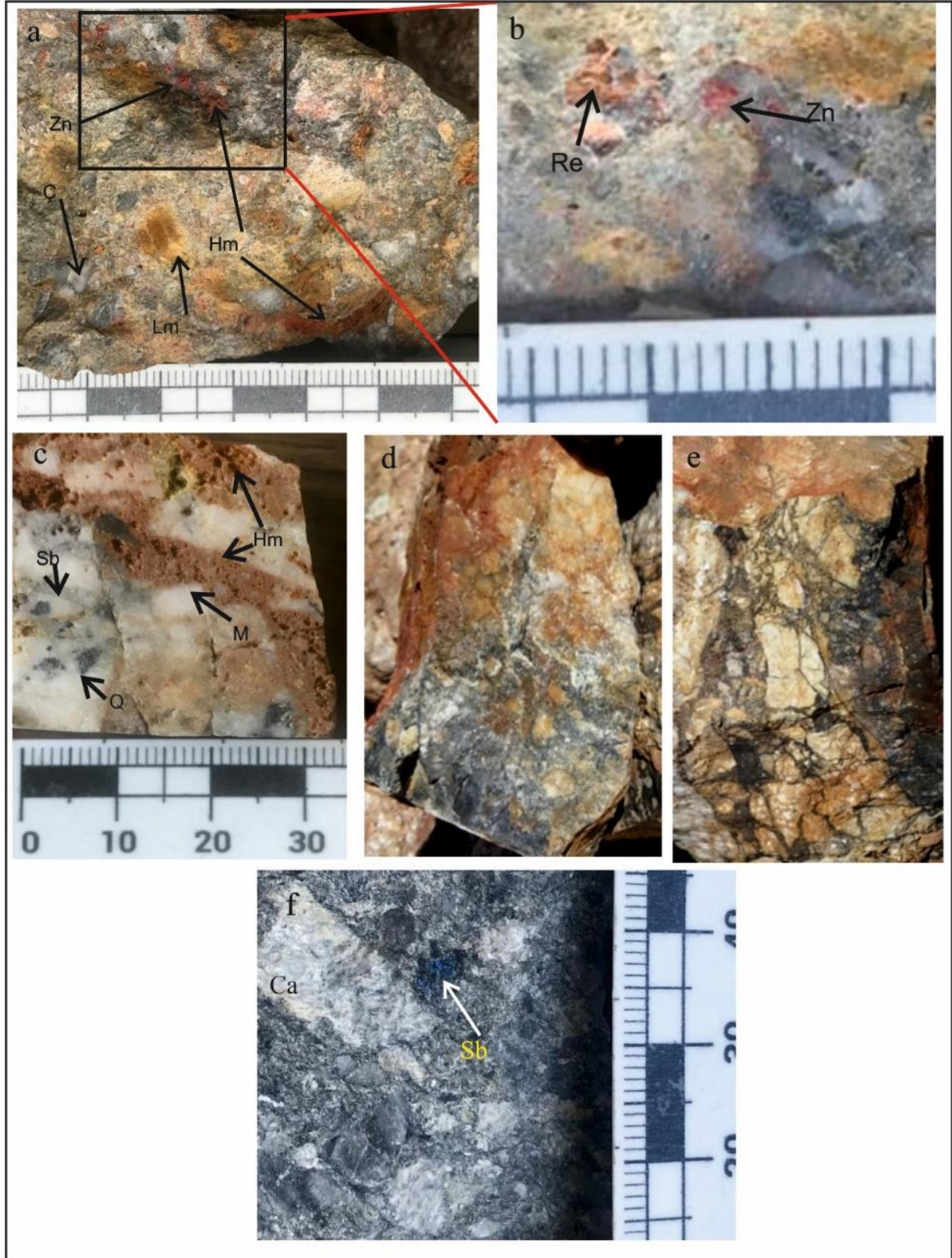
Limonit [$FeO(OH) \cdot nH_2O$], kırık ve çatlaklar boyunca yaygın olarak düzensiz iç yapısı ve limon sarısı rengiyle yer almaktadır. Hematitlerin alterasyonu sonucu oluşmuştur. Limonitler genel olarak diğer alterasyon minerali olan malahit ile birlikte bulunmaktadır. Limonit kümelerinin içerisinde yer yer hematit kalıntıları bulunmaktadır (Şekil 11b).

Pirit (FeS_2), yapılan tüm kesitlerde yaklaşık 0,1 mm'den küçük saçınımlar olarak bulunmaktadır. En fazla stibnit kristalleri içerisinde tespit edilmiştir. Kristalleri yarı özşekilli ve özşekilsiz olarak bulunmaktadır (Şekil 11c).

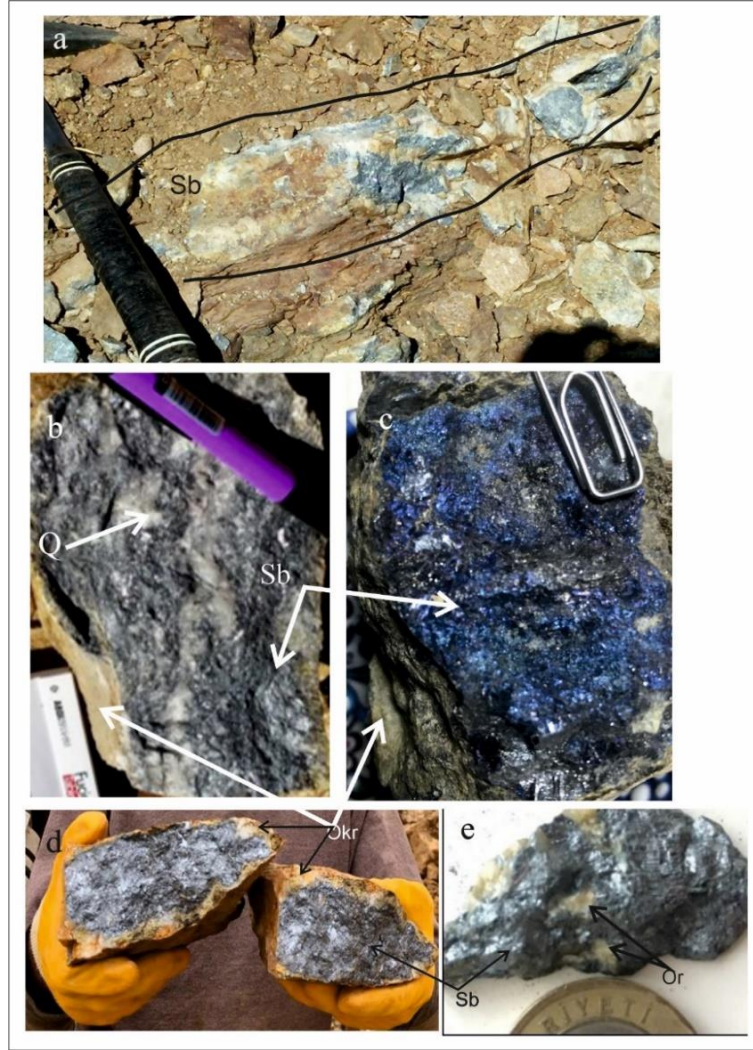
Kalkopirit ($CuFeS_2$), yeşilimsi sarı rengi ve mavimsi anizotropik rengiyle malahitlerin içerisinde çok az olarak da izole taneler olarak tespit edilmiştir. Kalkopiritler alterasyon sonucu malahite dönüşmüştür (Şekil 11d).

Malahit (Cu_2CO_3), lifsi kümeler düzensiz iç yapısı ve tipik yeşil rengiyle karakteristiktir. Malahit kalkopiritin alterasyonu sonucu oluşmuştur. Bazı kesitlerde malahit kümeleri içerisinde kalkopirit kalıntıları yer almaktadır. Alterasyonun yoğun olduğu kesitlerde Cu elementi hareketlilik kazanarak kırık ve çatlaklarda malahite dönüşmüş ve limonit ile birlikte görülür (Şekil 11a, b, d).

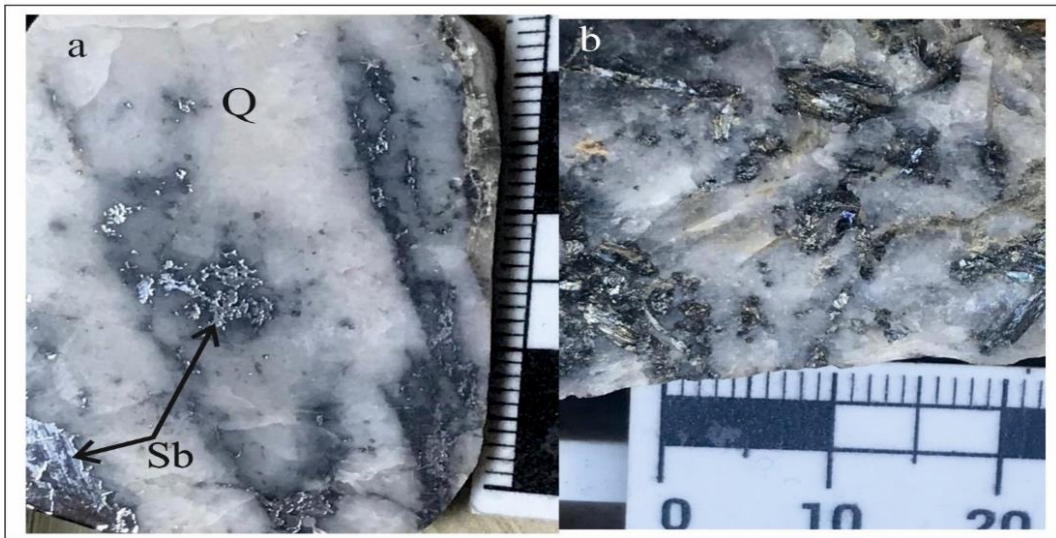
Nabit Altın (Au), yüksek iç yansıması ve kenarları boyunca oksitlenme göstermemesi ile karakteristiktir. Nabit altın taneleri 70 µm boyutuna ulaşan izole taneler şeklinde kuvars içerisinde yer almaktadır. Cevher mineralleri içerisinde altın tanesine rastlanılmamıştır (Şekil 12a, b).



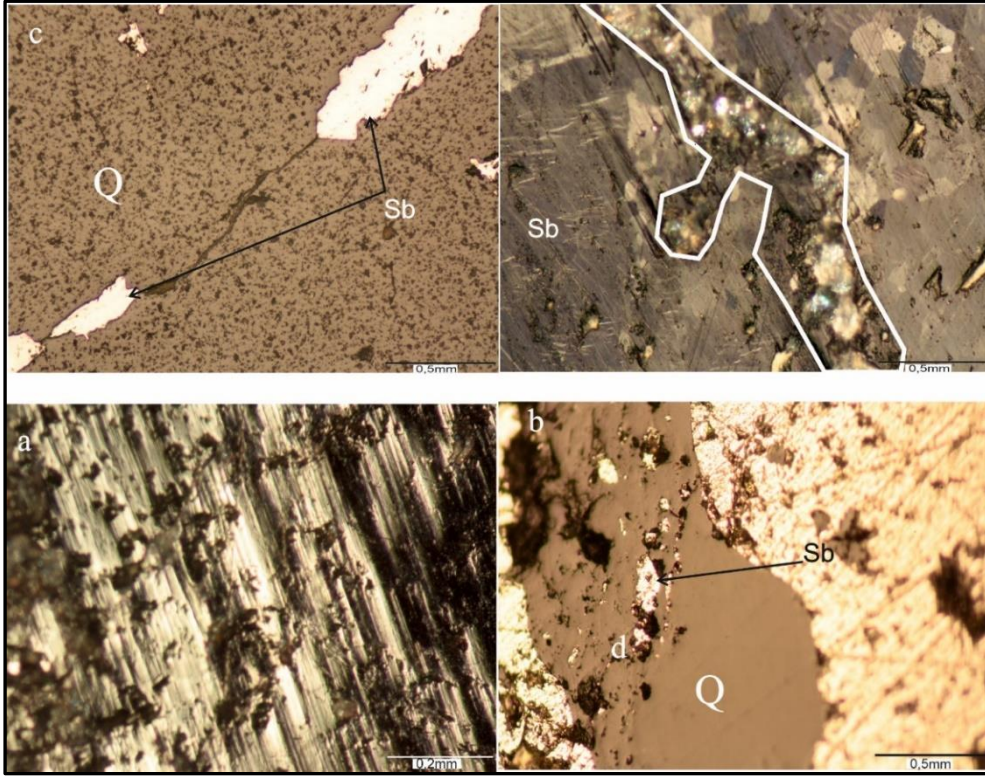
Őekil 5. Fay Dzlemleri İerisinde BreŐik CevherleŐmeler,
a) BreŐik Yapı İerisinde Zinober, Hematit, Limonit MineralleŐmesi ve akıl Paraları,
b) a'nın Detay Grnmnde Realgar ve Zinober MineralleŐmesi,
c) BreŐik Yapı İerisinde Stibnit ve Hematit, **d), e)** KŐeli BreŐlerin Genel Grnm,
f) BreŐik Yapı İerisinde Mavi Renkli Stibnit



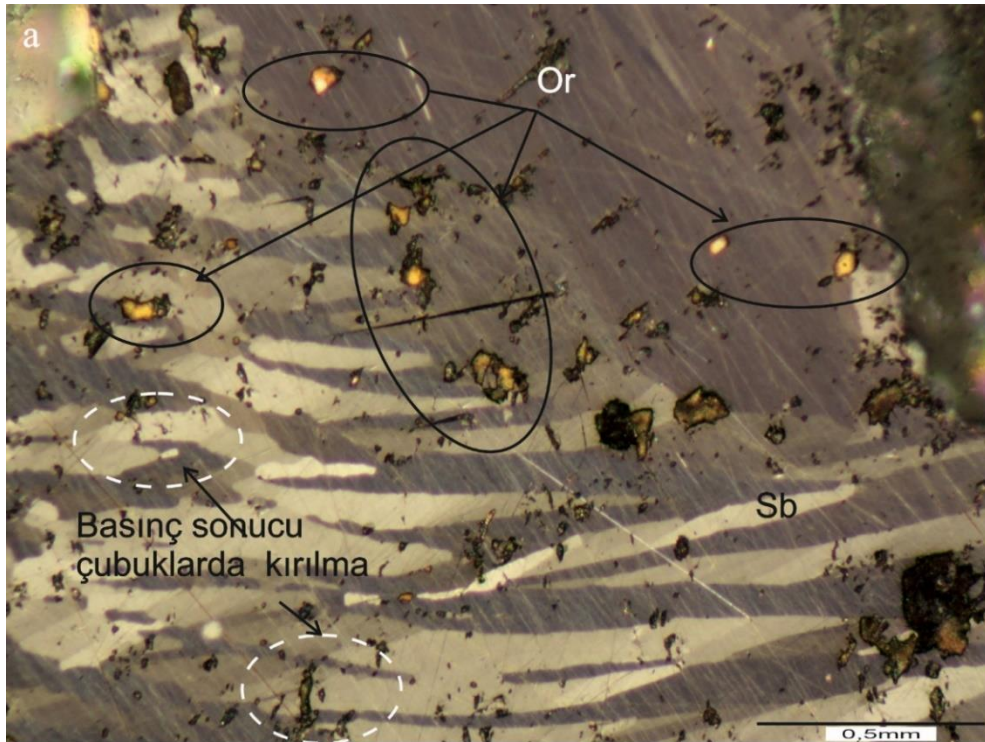
Şekil 6. Staratabaound Tipte Stibnit Cevherleşmesi,
a) Şistler İçerisinde Şistoziteye Paralel Kuvars Damarları ve Stibnit Cevherleşmesi,
b) Kuvars ile birlikte Stibnit, **c)** Mavi Stibnit, **d)** Stibnitlerin Dış Kesimlerinde Meydana Gelen Alterasyon,
e) Stibnit İçerisinde Orpiment (Sb:Stibnit, Or:Orpiment, Q:Kuvars)



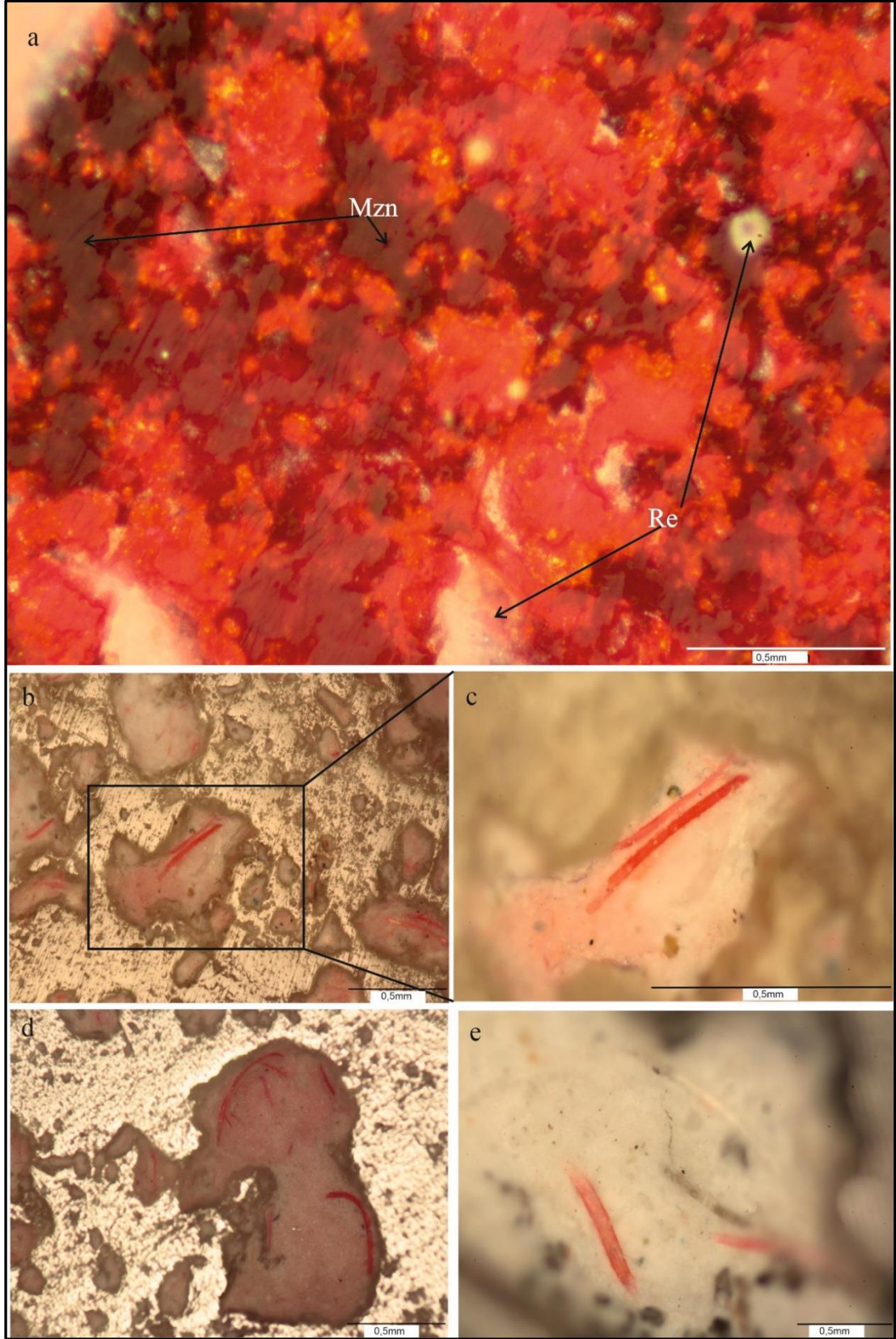
Şekil 7. a, b) Süt Kuvars İçerisinde Stibnit Kristalleri (Q:Kuvars, Sb:Stibnit)



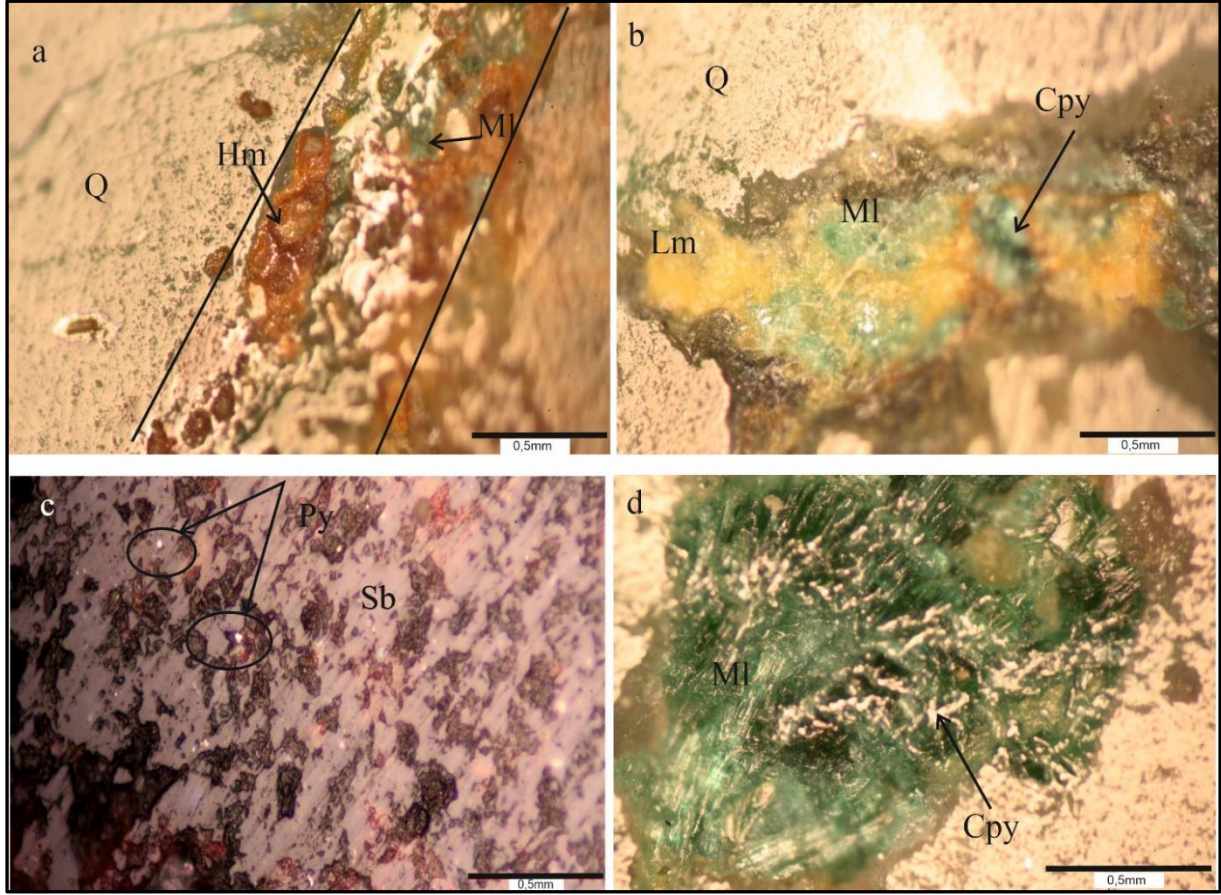
ekil 8. *alıma Alanı İerisindeki Stibnit Cevher Mikroskop Grntleri, a) Anizotrop Stibnitleri Oluturan ubuklar, b) Ana Gang Mineralini Oluturan Kuvars Kristalleri İerisinde, Kırık ve atlak ile Boluklarda Bulunan Stibnit, c) Kırıklarda Grlen Amorf Yapıda Stibnit, d) Stibnitler Arasını Dolduran Breik Yapı (Q:Kuvars, Sb:Stibnit)*



ekil 9. *Stibnit İerisinde Orpiment Minerallemesi ve Stibnit ubuklarında Meydana Gelen Eđilme-Bklme ve Kırıklar (Sb: Stibnit, Or:Orpiment)*



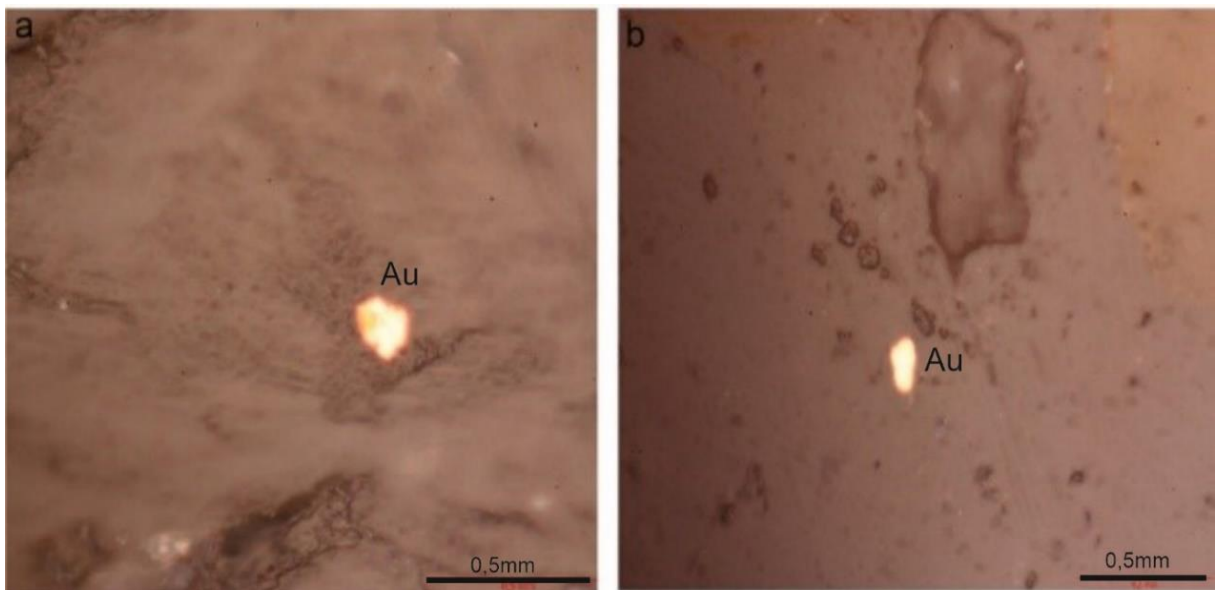
Őekil 10. alıma Alanı İerisindeki Zinoberlerin Cevher Mikropkopik Grnmleri,
a) Kan Kırmızı Rengiyle Karakteristik Zinober, İerisinde Lamelli Metazinober ve Canlı Sarı Rengiyle
 Orpiment, **b), c), d), e)** Amorf Silika İerisinde Boru Őekil Yapısında Zinober, (c resmi b'nin ayrıntısıdır)



ekil 11. Cevherlemenin Ana Gang Minerali İerisindeki Malahit, Hematit, Limonit, Kalkopirit ve Pirit,

- a) Kuvars Kristalleri Arasında Hematit ve Limonit,
 b) Kristaller Arasının Dolduran Limonit, Malahit ve Kalkopirit,
 c) Özeklisiz Stibnit İerisinde Pirit Taneleri,
 d) Kuvars Kristalleri Arasında Malahite Dnm Kalkopirit

(Hm:Hematit, Lm:Limonit, Ml: Malahit,Sb:Xstibnit, Cpy: Kalkopirit.Py: Pirit, Q: Kuvars)



ekil 12. a), b) Gang Minerali Olan Kuvars İerisinde Nabit Au

3.5. Jeokimyasal Analizler

Toplam 6 adet antimon cevher rneęinin ana oksit ve iz element deęerleri tespit edilmitir. Elde edilen deęerler Tablo 1’de grlmektedir. Analiz sonularından elde edilen minimum ve maksimum ana oksit deęerleri (%); SiO₂: 6,21-53,47; SO₃: 18,61-29,97; Fe₂O₃: 0,5-1,61; Al₂O₃: 0,31-4,37; P₂O₅: 0,1-0,13; K₂O: 0,02-1,93; CaO: 0,19-0,44; Cr₂O₃: 0,03-0,09; Na₂O: 0,01-0,1; MgO: 0,01-0,29; TiO₂: 0-0,31’dir. Analiz sonularından elde edilen minimum ve maksimum iz element deęerleri (ppm) ise; Sb (%): 23,02-43,13; Pb (%): 0,27-0,57; Cl: 39,1-72,1; Sc: 85,7-658,8; Ba: 15369-15824,2; Th: 999,4-1442,8; Ni: 21-98,3; Cu: 83,8-290,1; Zn: 18,8-1141,8; Ga: 9,3-11,6; Ge: 0-1,2; As: 346,1-823,4; Y: 307,1-497,7; Zr: 5,2-18,3; Nb: 4,4-5,7; Mo: 23,1-39,3; Gd: 0,8-3,7; V: 0-8,9; Co: 0,2-3,4; Sm: 0-0,2 ve Hf: 0-3,9 deęerindedir. rnekler de kızırdırma kaybı %1,7-20,4 arasında deęimektedir. Kızırdırma kaybının yksek ıkan rneklerde yksek ısıda buharlaan ierięinde H₂O ve uuu mineral ierięinden kaynaklanmaktadır.

Tm kaya jeokimyasına ait sonular ikili diyagramlarda karılatırılmıtır. İkilili diyagramlarda Sb-Cu, Sb-Zn, Sb-Mo arasında negatif bir iliki bulunmaktadır. Negatif ilikilerin R² deęerleri Sb-Cu: 0,685, Sb-Zn: 0,6605 ve Sb-Mo: 0,5419 olarak tespit edilmitir. Negatif ilikilerin R² deęerleri olduka birbirine yakındır. İkilili diyagramlarda Sb-As, Sb-Pb ve Sb-Ba arasında pozitif ynde iliki bulunmaktadır. Pozitif ilikilerin R² deęerleri Sb-As:0,2591, Sb-Pb:0,0486, Sb-Ba: 0,9242 olarak tespit edilmitir. İkilili diyagramlarda en anlamlı deęer pozitif ilikide Sb-Ba arasında olarak tespit edilmitir (ekil 13a-f).

İstatistiksel analiz yapmak iin, ncelikle kimyasal analiz sonularında normallik testinin yapılması gerekmektedir. Bu kapsamda ‘‘Shapiro-Wilk’’ ve ‘‘Kolmogorov-Smirnov’’ analizleri kontrol edilmelidir. Ayrıca, basıklık- arpıklık (skewness- kurtosis) deęerleri de incelenmelidir. Bu deęerlendirmelerden sonra, ok deęikenli istatistik yntemler uygulanmalıdır (Yalın & İlhan, 2008; Yalın vd., 2013; 2019; Yalın vd., 2016). Kimyasal analiz sonularına uygulanan ‘‘Kolmogorov-Smirnov’’ ve ‘‘Shapiro-Wilk’’ testleri uygulanmıtır. Bazı deęerlerin ‘‘0’’ ıkması nedeniyle kimyasal analiz sonularına ‘‘Spearman’’ korelasyon uygulanmıtır. Jeokimyasal analiz sonularına, tanımlayıcı istatistiksel analiz ile birlikte ok deęikenli istatistiksel analizlerden ‘‘korelasyon’’ (Spearman) analizi uygulanmıtır (Tablo 2 ve Tablo 3). arpıklık analizi sonularına gre elde edilen deęerler (- 1, +1) deęerlerinden daha farklı sonular verdięi iin, normal daęılımlı deęildir. rneklerden pozitif olanlar sivri ve negatif olanlar basıktır. alıma konusu olan Sb ile Ba, Y arasında yksek pozitif korelasyon ilikisi vardır. Ancak, Sb ile Sc arasında yksek negative korelasyon ilikisi vardır (Tablo 2). İkilili korelasyon ilikileri ile SPSS korelasyon ilikisi ile benzer ıkmıtır. ok deęikenli istatistiksel analizlerden korelasyon analizi, seilmi elementler arasındaki ikili korelasyon ilikilerinin ıkarılmasına gre, incelenen elementlerin tamamının grlmesi aısından daha avantajlı olmutur.

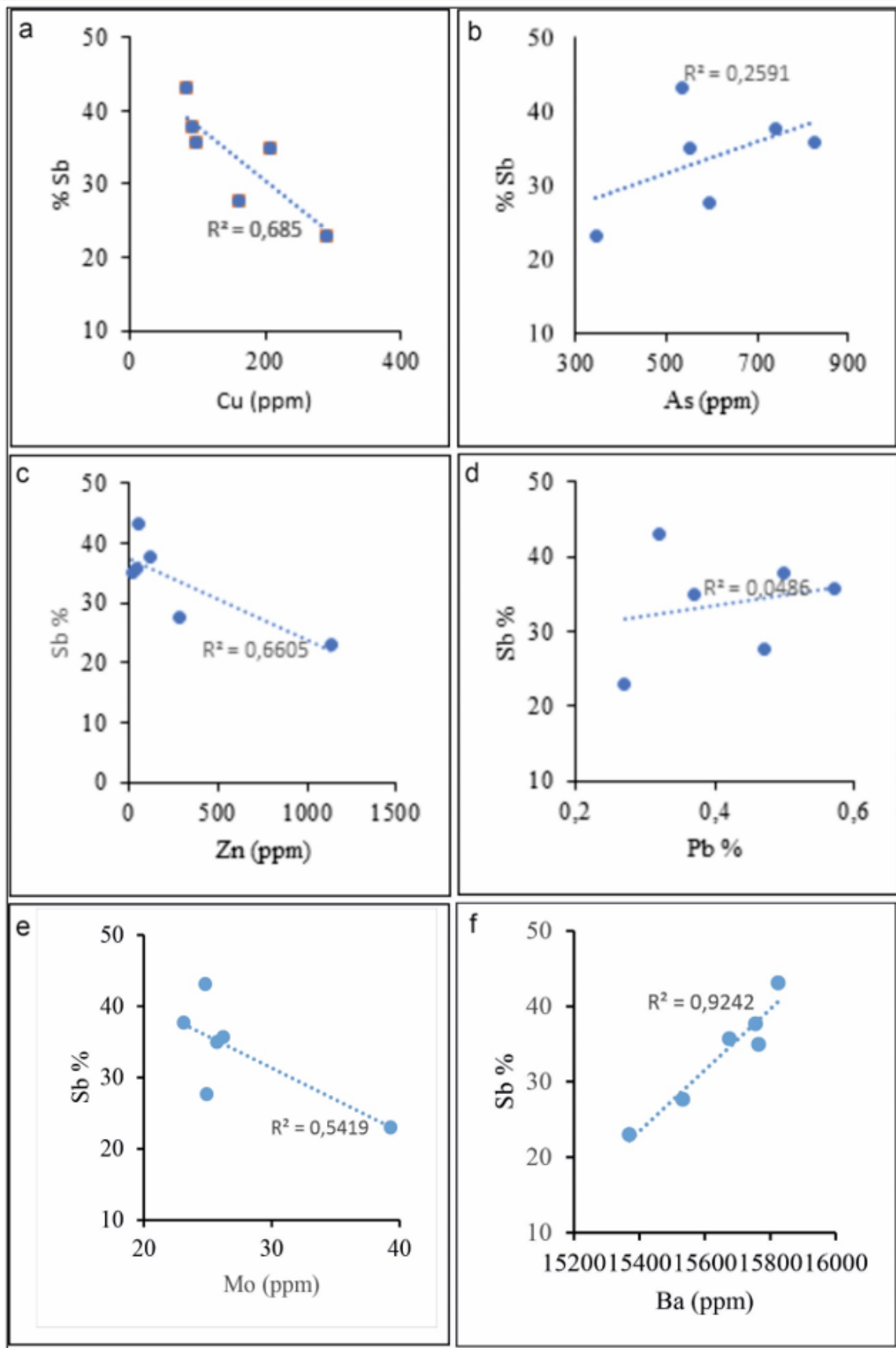
4. TARTIMA

alıma alanı olan Gmler (Nięde) kasabası civarında birok eski madencilik alımasına ait terk edilmi ocak ve tesis kalıntıları ile mostralar mevcuttur. Bu tesis kalıntıları ve ocaklarda yapılan gzlemler sonucu bu alanlarda 1980’li yılların balarına kadar nemli miktarda Sb ve Hg cevher retimi yapılmıtır. Blgede tespit edilen cevher mineralleri Akay (1995) ve Yalın & Yaman (1996) alımalarındaki mineralleri ile birlikte Tablo 4’te verilmitir. Tablo 4’te grleceęi zere Gmler blgesinde tespit edilen cevher mineralleri slfrler: stibnit, orpiment, zinober, metazinober, Őeelit, arsenopirit, sfalerit, galen ve markazit, oksitler; hematit, limonit, Sb-oksitler (okr), ve Zn oksit, karbonatlar; malahit ve Zn-karbonat, nabit; Altın, amorf Sb ve slfo tzlerdir.

Gmler blgesi cevherlemesinin ana cevher minerali stibnittir. Stibnit cevherlemesi, tipik olarak epitermal sistemlerin evresel kısımlarında okelir (Morteani vd., 2011; Schwarz-Schampera, 2014). Epitermal sistemlerin genel karakteristik mineral topluęunda; nabit Au (genellikle Ag elementi yksek), nabit Ag, Cu, Bi, pirit, markazit, sfalerit, galen, kalkopirit, zinober, jamesonit, stibnit, realgar, orpiment, yakut gm (ruby silvers), argentit, selenidler ve telluridler oluurmaktadır (Evans, 1993).

Tablo 1. Jeokimyasal Analiz Sonuları

Element/No	13A1	14B	H2	H1	14A	13A2
Ana Oksitler (%)						
SiO₂	42,47	18,56	20,5	6,21	15,51	53,47
SO₃	21,73	25,19	26,39	29,39	29,97	18,61
Sb	27,68	37,71	34,98	43,13	37,72	23,02
Fe₂O₃	0,77	1,61	0,58	0,8	0,72	0,5
Al₂O₃	1,14	4,37	0,34	0,31	1,52	0,57
P₂O₅	0,11	0,13	0,11	0,12	0,13	0,1
K₂O	0,26	1,93	0,02	0,05	0,63	0,03
CaO	0,4	0,44	0,19	0,19	0,2	0,34
Pb	0,47	0,57	0,37	0,32	0,5	0,27
Cr₂O₃	0,05	0,07	0,09	0,09	0,03	0,07
Na₂O	0,01	0,01	nd	nd	0,01	0,1
MgO	nd	0,29	nd	nd	0,01	nd
TiO₂	0,04	0,31	nd	nd	0,08	nd
Kız. K.	3,7	8,9	17,3	20,4	13,4	1,7
Toplam	98,83	100,09	100,87	101,01	100,43	98,78
İz elementler (ppm)						
Cl	72,1	39,1	64,9	59,4	42,4	65,8
Sc	563,5	275,2	338,1	85,7	270,1	658,8
Ba	15532,3	15674,4	15763,8	15824,2	15754,3	15369
Th	1164,9	1442,8	1231,4	1242,2	1390	999,4
Ni	40,8	98,3	29	26,2	21	64,4
Cu	160,4	89,4	208,3	83,8	90,8	290,1
Zn	279,1	38	18,8	57,1	120,7	1141,8
Ga	10,1	11,6	9,3	10,2	10,1	9,4
Ge	1,2	0,5	0,6	nd	1	0,8
As	596,1	823,4	552,1	535,8	741,5	346,1
Y	332	450,4	401,3	497,7	458,6	307,1
Zr	10	18,3	5,9	5,2	8	7,7
Nb	4,4	5,7	4,7	4,7	4,5	4,7
Mo	24,9	26,2	25,7	24,8	23,1	39,3
Gd	2,7	1,4	3,4	3,7	2,8	0,8
Co	1,3	nd	nd	0,2	nd	3,4
Sm	0,2	nd	nd	nd	nd	0,1
Hf	1,1	2,3	nd	3,9	3,9	nd



Őekil 13. Jeokimyasal Analizlerde Elde Edilen SonuŐların İkili Diyagramdaki DeĐerlendirmeleri

Tablo 2. Ayrımcı İstatistik Özellikler

	Ortalama	Medyan	Mod	Std. Sapma	arpıklık	Basıklık	Minimum	Maksimum
SiO₂	26,12 ± 7,33	19,53	6,21 ^a	17,96	0,78	-0,84	6,21	53,47
SO₃	25,21 ± 1, 80	25,79	18,61 ^a	4,41	-0,52	-0,94	18,61	29,97
Sb	34,04 ± 3,01	36,35	23,02 ^a	7,38	-0,56	-0,69	23,02	43,13
Fe₂O₃	0,83 ± 0,16	0,75	0,50 ^a	0,40	1,99	4,40	0,50	1,61
Al₂O₃	1,38 ± 0,63	0,86	0,31 ^a	1,54	1,96	4,05	0,31	4,37
P₂O₅	0,12 ± 05	0,12	0,11 ^a	0,01	-0,08	-1,55	0,10	0,13
K₂O	0,49 ± 0,30	0,16	0,02 ^a	0,74	1,98	3,93	0,02	1,93
CaO	0,29 ± 0,05	0,27	0,19	0,11	0,29	-2,53	0,19	0,44
Pb	0,42 ± 0,05	0,42	0,27 ^a	0,12	0,03	-1,62	0,27	0,57
Cr₂O₃	0,07 ± 0,01	0,07	0,07 ^a	0,02	-0,67	-0,45	0,03	0,09
Na₂O	0,02 ± 0,02	0,01	0,01	0,04	2,36	5,67	0	0,10
MgO	0,05 ± 0,05	0	0	0,12	2,44	5,98	0	0,29
TiO₂	0,07 ± 0,05	0,02	0	0,12	2,10	4,53	0	0,31
Cl	57,28 ± 5,50	62,15	39,10 ^a	13,47	-0,61	-1,67	39,10	72,10
Sc	365,23 ± 85,93	306,65	85,70 ^a	210,49	0,31	-0,82	85,70	658,80
Ba	15653 ± 70,13	15714,35	15369 ^a	171,77	-1,02	0,05	15369	15824,20
Th	1245,12 ± 65,08	1236,80	999,40 ^a	159,42	-0,34	-0,12	999,4	1442,80
Ni	46,62 ± 12,12	34,90	21,00 ^a	29,68	1,29	0,91	21	98,30
Cu	153,80 ± 33,96	125,60	83,80 ^a	83,20	0,96	-0,25	83,80	290,10
Zn	275,92 ± 177,43	88,90	18,80 ^a	434,61	2,21	4,98	18,80	1141,80
Ga	10,12 ± 0,34	10,10	10,10	0,82	1,27	2,21	9,30	11,60
Ge	0,68 ± 0,17	0,70	,00 ^a	0,42	-0,62	0,42	0	1,20
As	599,17 ± 68,51	574,10	346,10 ^a	167,82	-0,15	-0,02	346,10	823,40
Y	407,85 ± 30,77	425,85	307,10 ^a	75,37	-0,37	-1,67	307,10	497,70
Zr	9,18 ± 1,95	7,85	5,20 ^a	4,78	1,80	3,55	5,20	18,30
Nb	4,78 ± 0,19	4,70	4,70	0,47	2,04	4,60	4,40	5,70
Mo	27,33 ± 2,43	25,30	23,10 ^a	5,96	2,27	5,38	23,10	39,30
Gd	2,47 ± 0,46	2,75	,80 ^a	1,14	-0,63	-1,20	0,80	3,70
Co	0,82 ± 0,56	0,10	0	1,36	1,84	3,10	0	3,40
Sm	0,05 ± 0,03	0	0	0,08	1,54	1,43	0	0,20
Hf	1,87 ± 0,73	1,70	0	1,79	0,18	-2,23	0	3,90

Tablo 3. Korelasyon Analizi

	SiO ₂	SO ₃	Sb	Fe ₂ O ₃	Al ₂ O ₃	P ₂ O ₅	K ₂ O	CaO	Pb	Cr ₂ O ₃	Na ₂ O	MgO	TiO ₂	Cl	Sc	Ba	Th	Ni	Cu	Zn	Ga	Ge	As	Y	Zr	Nb	Mo	Gd	Co	Sm	Hf	
SiO ₂	1																															
SO ₃	-.954**	1																														
Sb	-.993**	.931**	1																													
Fe ₂ O ₃	-.355	.162	.405	1																												
Al ₂ O ₃	-.166	.032	.197	.939**	1																											
P ₂ O ₅	-.769	.758	.779	.679	.644	1																										
K ₂ O	-.259	.127	.287	.945**	.995**	.708	1																									
CaO	.540	-.668	-.483	.579	.659	-.063	.579	1																								
Pb	-.290	.282	.288	.741	.820*	.750	.821*	.432	1																							
Cr ₂ O ₃	-.197	-.026	.209	.000	-.239	-.330	-.221	-.190	-.540	1																						
Na ₂ O	.782	-.760	-.765	-.348	-.172	-.626	-.223	.284	-.528	-.037	1																					
MgO	-.218	.016	.254	.959**	.959**	.562	.959**	.620	.669	.044	-.154	1																				
TiO ₂	-.253	.088	.264	.955**	.997**	.673	.998**	.612	.808	-.181	-.214	.972**	1																			
Cl	.567	-.540	-.570	-.678	-.742	-.890*	-.800	-.040	-.651	.314	.257	-.684	-.765	1																		
Sc	.988**	.922**	.997**	.365	-.148	-.740	-.240	.518	-.214	-.256	.724	-.219	-.217	.543	1																	
Ba	-.973**	.957**	.948**	.215	.029	.674	.119	-.628	.255	.199	-.854*	.071	.095	-.423	.939**	1																
Th	-.763	.728	.754	.716	.689	.961**	.748	-.031	.818*	-.243	-.712	.627	.722	-.852*	.706	.704	1															
Ni	.292	-.499	-.243	.720	.778	.078	.735	.833*	.332	.110	.345	.844*	.765	-.336	.257	-.443	.123	1														
Cu	.814*	-.790	-.846*	-.604	-.460	-.915*	-.518	.107	-.637	.214	.772	-.395	-.491	.649	.813*	-.745	-.851*	.092	1													
Zn	.845*	-.801	-.825*	-.442	-.279	-.711	-.338	.280	-.572	-.066	.984**	-.276	-.327	.398	.785	-.892*	-.804	.249	.799	1												
Ga	-.378	.224	.440	.973**	.910*	.749	.918**	.553	.760	-.142	-.359	.888*	.919**	-.706	-.400	.225	.730	.631	-.708	-.436	1											
Ge	.627	-.432	-.667	-.245	.029	-.209	-.033	.346	.324	-.778	.223	-.202	-.042	.183	.713	-.535	-.171	-.050	.311	.293	-.207	1										
As	-.574	.550	.571	.766	.782	.908*	.816*	.197	.947**	-.400	-.668	.673	.795	-.787	-.508	.523	.958**	.224	-.803	-.737	.789	.057	1									
Y	-.976**	.925**	.987**	.428	.249	.826*	.341	-.463	.302	.131	-.679	.290	.312	-.664	.986**	.903*	.773	-.194	-.855*	-.754	.479	-.652	.587	1								
Zr	.033	-.184	.005	.905*	.971**	.462	.942**	.813*	.763	-.205	-.066	.937**	.956**	-.566	.044	-.158	.522	.860*	-.307	-.149	.862*	.119	.663	.044	1							
Nb	-.247	.007	.281	.881*	.844*	.448	.854*	.501	.449	.287	-.065	.958**	.872*	-.626	-.266	.093	.518	.846*	-.277	-.205	.777	-.409	.502	.314	.818*	1						
Mo	.749	-.786	-.731	-.314	-.189	-.700	-.238	.282	-.609	.193	.971**	-.106	-.218	.328	.684	-.816*	-.748	.404	.824*	.368	.070	-.728	-.669	-.068	.032	1						
Gd	-.656	.720	.626	-.266	-.472	.208	-.415	-.715	-.064	.190	-.780	-.457	-.428	.175	-.625	.789	.234	-.807	-.451	-.708	-.226	-.289	.112	.528	-.568	-.453	-.748	1				
Co	.901*	-.870*	-.873*	-.443	-.310	-.784	-.381	.356	-.572	-.036	.936**	-.306	-.363	.530	.837*	-.930**	-.865*	.241	.808	.981**	-.435	.324	-.767	-.824*	-.147	-.251	.912*	-.660	1			
Sm	.799	-.736	-.769	-.270	-.198	-.592	-.292	.545	-.083	-.307	.340	-.305	-.267	.677	.784	-.731	-.609	-.050	.430	-.480	-.218	.652	-.369	-.801	.008	-.436	.285	-.252	.623	1		
Hf	-.737	.785	.776	.331	.220	.815*	.289	-.306	.349	-.300	-.490	.139	.246	-.625	-.770	.637	.645	-.252	-.886*	-.515	.496	-.340	.546	.834*	.040	-.061	-.594	.384	-.569	-.454	1	

** . Correlation is significant at the 0.01 level (2-tailed); * . Correlation is significant at the 0.05 level (2-tailed).

Tablo 4. Gmler Cevherlemesinin Parajenezi

	Blgede Tespit Edilen Mineraller			
	Mineraller	Bu alımada	Akay (1995)	Yalın & Yaman (1996)
Slfrler	Stibnit	x	x	x
	Orpiment	x	x	
	Zinober	x		x
	Metazinober	x		
	Pirit	x	x	x
	Kalkopirit	x	x	x
	eelit		x	x
	Arsenopirit			x
	Sfalerit		x	x
	Galen		x	x
	Markazit		x	
	Realgar	x	x	
Oksitler	Hematit	x		
	Limonit	x		x
	Servantit	x		x
	Seramonit	x		x
	Zn Oksit		x	
Karbonat	Malahit	x		
	Zn Karbonat		x	
Nabit	Altın	x	x	x
S. Tuzlar				x
Amorf Sb			x	
Gang	Kuvars	x	x	x
	Barit	x	x	x

Stibnit, ortamın basın ve sıcaklıėındaki herhangi bir deėiikliėe karı ok hassastır ve oėu mineralin yaptığı gibi, deėiikliklerin etkilerini ortadan kaldırmak iin i yapısını yeniden ynlendirerek yanıt verme eėilimindedir. İlk tepki, basın lamellerinin ortaya ıkmasıyla sonulanır. Bir numune sıkıtırıldıėında, genellikle birbirine neredeyse paralel ve sıkıtırma eksenine neredeyse dik olan iyi tanımlanmı bantlar geliir (Stanton, 1972). Stibnit kristallerinde tespit edilen kırık, atlak, eėilme bklme yapıları ve mikro boyutta breik yapının bulunması cevher oluum srelerinin tamamlanmasından sonra basın, ortam sıcaklıėının deėiimi, sıkıma ve gerileme kuvvetleri gibi deformasyon srelerinin etkisi altında kaldığını gstermektedir.

Antimon cevherinin sperjen ortama maruz kalması sonucu oksitlenerek ikincil valentinit (orthorombik Sb_2O_3), senarmontit (kubik Sb_2O_3), servantit (Sb_2O_4), kermesit (Sb_2S_2O), ve stibiikonit

[(Ca,Sb)₂Sb₂O₆(O,OH)] mineraller oluur ve bu mineraller yzey artlarında znmezler (Laurence, 2004). Gmler antimon cevherlemesi kırık ve atlaklar boyunca altere olarak ikincil Sb-oksit (okr) minerallerine dnmtr. Bu mineraller masif cevherin etrafında yer yer 1cm kalınlıa ulamaktadır. Sperjen ortamda gelien bu minerallerin boyutları maksimum 20-25 µm civarında olmasından dolayı optik olarak belirlenememitir.

Cevherleme ierisinde slfrlerin bulunması (Tablo 1) ve aynı zamanda slfat mineralinin (barit) bulunması greceli olarak yksek fO₂ ve SO₄ bakımından yksek sıvılardan kaynaklandığını gstermektedir (Ohmoto, 1972).

alıma alanı ierisinde ikinci tespit edilen nemli cevherleme Hg (zinober) yataklanmasıdır. En nemli cıva cevheri olan zinober [HgS], dk sıcaklıkta termodinamik aıdan en kararlı formudur (Barnett vd., 2001). Zinnobar, 345°C'de polimorf'u olan metazinober'a dnr (Dickson & Tunell, 1959). Epitermal sistemler yzeyeye yakın kesimlerde (<1,5 km) oluurlar ve gl bir oranda meteorik suların etkilenirler (Henley & Ellis, 1983; Taylor, 2007). Cevher mikroskop alımasında tespit edilen zinober ve metazinoberin birliktelii, Hg cevherinin yzeyden kaynaklanan meteorik suların dolaımı ile intrzyondan ısınarak zinober minerallerinin bir kısmını metazinobere dntrmtr.

Yapısal kontroll epitermal sistemlerde gml intrzyondan kaynaklanan cevherli akıkanların souyarak ykseldii alanlarda maden yatak oluumuna imkn verirler. Ykselen cevherli akıkanlar yzeyeye yakın alanlarda oksitlenerek Au kelmesine neden olurlar (Corbett, 2012.) Mehmetler Yurdu Sivrisi Tepe (Gmler gney kesimi) cevherlemesinde 37,3 ppm'e kadar ulaan altın, yerel olarak yzeyeye yakın zonlarda oluur (Kucu & Erler, 1993). ren Dere (Gmler GD) ierisinde dere kumu bate neklerinde 18 adet nabit altın tanesi tespit edilmitir (Yalın & opurolu, 2001). Bu veriler, alıma alanı ierisinde alınan neklerde 70 µm'ye boyuta ıkan nabit altın tanelerin varlıı ile uyumludur.

5. SONULAR

Gmler (Nide) cevherlemesinin ana cevher minerali stibnittir. Jeokimyasal analizlerde maksimum %43,13 Sb elementi tespit edilmitir. Sb elementinin sadece stibnit (Sb₂S₃) mineralinin ierisinde olduu kabul edilirse (alterasyon sonucu oluan ikincil mineraller ihmal edilmesi durumunda) analizi yapılan nek (nek no:H1) ierisinde molekl aılıı yntemine gre; %60,25 Sb₂S₃ minerali bulunmaktadır. Elde edilen bu oran Gmler Sb cevherlemesinin nemli bir konuma sahip maden yataı olduunu gstermektedir. Stibnit ile birlikte Hg (zinber ve metazinober) cevherlemesinin mineralojik-petrografik zelliklerine maden yataı olarak tanımlanabilir. Stibnit ve Hg yatakları, Nide metamorfik kayaları ile gl bir konumsal iliki gstermektedir. Cevherlemeler sadece Gmler litodemi ierisinde bulunmaktadır. Ana cevher minerali olan stibnit cevherlemesi sonrası tektonizmadan etkilenmitir. Tektonizma sonucu deformasyon yapıları olan kırık ve atlaklar ile ikizlenme yapıları meydana gelmitir. Cıva cevherinin ana cevher minerali zinober olup, sperjen ortamda meteorik suların dngsnde intrzyondan kaynaklanan ısınma sonucu metazinobere dntr. Dier bir nemli cevherleme nabit Au tespit edilmitir. Nabit altın sadece kuvars damarlarında ve kuvars minerali ierisinde tespit edilmitir. ok deikenli istatistiksel analizlerden korelasyon analiz ve ikili element analiz sonularına gre antimon (Sb) elementi ile As, Pb ve Ba arasında pozitif bir birliktelik bulunurken, Cu, Zn ve Mo elementleri arasında negatif bir birliktelik bulunmaktadır. Tespit edilen pozitif ve negatif birliktelikleri gml cevherlerin tespiti iin kullanılabilir.

IKAR ATIMASI

Yazarlar ıkar atiması beyan etmemektedir.

KAYNAKLAR

Akay, M. (1995). Gmler (Nide) yresi Sb±Hg±W cevherlemelerinin jeolojik, mineralojik ve altın potansiyeli ynnden incelenmesi. *Trkiye Jeoloji Blteni*, 38(2), 23-34.

- Altuncu, S., Tmkl, A., & zgr, F. Z. (2018a). Nide masifi metalik cevherlemelerinin mineralojisi ve jeokimyası. *Nide mer Halisdemir n. Mhendislik Bilimleri Dergisi*, 7(3), 1101-1106. doi:[10.28948/ngumuh.502269](https://doi.org/10.28948/ngumuh.502269)
- Altuncu, A. Tmkl, A., & zgr, F. Z. (2018b). Trace Elements Geochemistry of Nigde (Turkey) Antimony Deposits. *Journal of Scientific and Engineering Research*, 5(5), 622-631.
- Atabey, E., & Ayhan A. (1986). Nide-Ulukıla-amardı-iftehan Yresinin Jeolojisi. MTA Raporu, No: 8064.
- Barnett, M. O., Turner, R., & Singer, P. C. (2001). Oxidative dissolution of metacinnabar (β -HgS) by dissolved oxygen. *Applied Geochemistry*, 16(13), 1499-1512. doi:[10.1016/S0883-2927\(01\)00026-9](https://doi.org/10.1016/S0883-2927(01)00026-9)
- Blumenthal, M. (1941). Un aperu de la Gologie du Taurus dans les vilayets des Nide et d'Adana: Maden Tetkik Arama Enstits Yayınları, B. 6, 195 s.
- Blumenthal, M. (1963). Le Systme structural du Taurus Sud - Anadolien: in Livre à mmoire du Prof. Fallat, Mm hs-sr. Gol. France, t. II, S. 611-682.
- inku, M. C., Hisarlı, Z. M., Yılmaz, Y., lker, B., Kaya, N., ksm, E., Orbay, N., & ta zbey, Z. (2016). The tectonic history of the Nide-Kırehir Massif and the Taurides since the Late Mesozoic: Paleomagnetic evidence for two-phase orogenic curvature in Central Anatolia. *Tectonics*, 35, 772-811. doi:[10.1002/2015TC003956](https://doi.org/10.1002/2015TC003956)
- Corbett, G. J. (2012). Structural Controls to, and Exploration for, Epithermal Au-Ag Deposits Structural controls to, and exploration for, epithermal Au-Ag deposits. *Australian Institute of Geoscientists Bulletin*, 56, 43-47.
- Dennis, R. A. (1970). The Mineralization at the Hg-Sb-W Mine near Nigde, South-Central Turkey. M.Sc Thesis, Swansea University. (unpublished)
- Dickson, F. W., & Tunell, G. (1959). Stability relations of cinnabar and metacinnabar. *American Mineralogist*, 44(5-6), 471-488.
- Ercan, T. (1986). Cenozoic volcaismm of central Anatolia. *Maden Tektik ve Arama Dergisi*, 107,107-114.
- Evans, A. H. (1993). Ore Geology and Industrial Minerals, third edition, Blackwell Scientific, Oxford, 390 s.
- Fayon, A. K., & Whitney, D. L. (2007). Interpretation of tectonic versus magmatic processes for resetting apatite fission track ages in the Nide Massif, Turkey. *Tectonophysics*, 434(1-4), 1-13. doi:[10.1016/j.tecto.2007.01.003](https://doi.org/10.1016/j.tecto.2007.01.003)
- Gautier, P. E., Bozkurt, E., Hallot, E., & Dirik, K. (2002). Dating the exhumation of a metamorphic dome: Geological evidence for pre-Eocene unroofing of the Nide Massif (central Anatolia, Turkey), *Geol. Mag.*, 139, 559-576.
- Gncolu, M. C. (1977). Geologie des Westlichen Nigde Massivs. PhD Thesis, Borm. (unpublished)
- Gncolu, M. C. (1981a). Nide Masifinin Jeolojisi. İ Anadolu'nun Jeolojisi Sempozyumu, TJK 35. Bilimsel ve Teknik Kurultayı, Bildiriler Kitabı: 16-19.
- Gncolu, M. C. (1981b). Nide Masifinde viridin-gnaysın kkeni. *Trkiye Jeoloji Kurumu Blteni*, 24(1), 45-51.
- Gncolu, M. C. (1986). Geochronological data from the southern part (Nigde area) of the Central Anatolian Massif. *Bulletin of the Mineral Research and Exploration Institute of Turkey*, 105-106, 83-96.
- Henley, R. W., & Ellis, A. J. (1983). Geothermal systems ancient and modern: A geochemical review. *Earth-Science Reviews*, 19, 1-50. doi:[10.1016/0012-8252\(83\)90075-2](https://doi.org/10.1016/0012-8252(83)90075-2)
- İleri, S. (1975) Antimon yataklarında jeolojik konum. *Trkiye Jeoloji Kurumu Blteni*, 18(1-2,) 41-47.
- Kleyn, V. D. (1970). Recommendation of Exploration for Mineralization in the South western Part of Nide-amardi Massif. MTA Report, Ankara. (unpublished)

- Kucu, İ., Erler, A., & Gncođlu, M. C. (1993). Geology of The amardı (Niđe-Turkey) Region. *Geosound*, 23, 1-16.
- Laurence, R. (2004). Introduction to ore-forming processes, New York, Blackwell Science, 382 s.
- Morteani, G. Ruggieri, G. Mller, P., & Preinfalk, C. (2011). Geothermal mineralized scale in the pipe system of the geothermal Piancastagnaio power plant (Mt. Amiata geothermal area): a key to understand the stibnite, cinnabarite and gold mineralization of Tuscany (central Italy). *Mineralium Deposita*, 46, 197-210.
- Ohmoto, H. (1972). Systematics of sulfur and carbon isotopes in hydrothermal ore deposits. *Econ. Geol.*, 67(5), 551-578.
- Okay, A. C. (1955). Niđe amardı ve Ulukıla arasındaki blgenin jeolojisi. MTA Raporu, No:2381.
- Oygr, V., Er kale, H. E., Erkan, N. & Karabalık, N. (1984). Niđe Masifi Demir Cevherlemeleri Maden Jeolojisi Raporu. MTA Raporu, No:7521.
- zgneyli, A. (1978). Niđe-amardı kristalin masifi genel prospeksiyon alıması ve demir-baz metal-wolfram ve altın cevherlemeleri hakkında alıma raporu. MTA Raporu, No:6851.
- Schwarz-Schampera, U. (2014). Antimony. In: G. Gunn (Eds.) Critical Metals Handbook (pp. 70-98). UK, John Wiley & Sons, Ltd.
- Seal II, R. R, Schulz, K. J., & DeYoung, J. H. (2017). Critical Mineral Resource of the United States-Economic and Enviromental Geology and Prospects for Future Supply. Professional Paper 1802-C doi:[10.3133/pp1802C](https://doi.org/10.3133/pp1802C)
- Stanton, R. L. (1972). Ore petrology. McGraw-Hill, New York, 713 p.
- Taylor, B. E. (2007) Epithermal gold deposits. In: Goodfellow W. D. (Eds) Mineral Deposits of Canada-a synthesis of major deposit types, district metallogeny, the evolution of geological provinces and exploration methods. Geological Association of Canada, Mineral Deposit Division, Special Publication, No. 5, pp 113-139.
- Tromp, S. W. (1942). Niđe-İncesu, Kızılırmak ve Tuz Gl arasında bulunan mıntıkların jeolojik etd. MTA Raporu, No:1456.
- Tmkl, A., Altuncu S., & zgr, F. Z. (2018) Niđe masifinin maden yatakları ynnden deđerlendirilmesi. *Niđe mer Halisdemir niversitesi Mhendislik Bilimleri Dergisi*, 7(3), 1119-1123.
- Viljoen, R. P., & İleri, S. (1973). Mineralization The Geology and of Portions in the Pozantı Dađı (Niđe) Massif of South Central Turkey, Johannesburg Consol. Invest. Co. Ltd. Geol. Res. Dept., Rep. No:39, 59p. (unpublished)
- Whitney, D. L., & Dilek, Y. (1998). Metamorphism during crustal thickening and extension in central Anatolia: The Niđe metamorphic core complex. *Journal of Petrology*, 39(7), 1385-1403.
- Whitney, D. L., Teyssier, C., Dilek, Y., & Fayon, A. K. (2001). Metamorphism of the Central Anatolian Crystalline Complex, Turkey: Influence of orogen-normal collision vs. wrench dominated tectonics on P-T-t paths. *Journal of Metamorphic Geology*, 19(4), 411-432. doi:[10.1046/j.0263-4929.2001.00319.x](https://doi.org/10.1046/j.0263-4929.2001.00319.x)
- Whitney, D. L., Teyssier, C., Fayon, A. K., Hamilton, M. A., & Heizler, M. (2003). Tectonic controls on metamorphism, partial melting, and intrusion: Timing of regional metamorphism and magmatism of the Niđe Massif, Turkey. *Tectonophysics*, 376(1-2), 37-60. doi:[10.1016/j.tecto.2003.08.009](https://doi.org/10.1016/j.tecto.2003.08.009)
- Yalın, F., Kılı, S., Nyamsari, D. G., Yalın, M. G., & Kılı, M. (2016). Principal Component Analysis of Integrated Metal Concentrations of Bogacayı Riverbank Sediments in Turkey. *Pol. J. Environ. Stud.*, 25(2), 471-485. doi:[10.15244/pjoes/61009](https://doi.org/10.15244/pjoes/61009)
- Yalın, M. G. (1998). Ecemi fay kuađı batı blođundaki amardı ve gmler antımuan yataklarının morfolojik yapısal ve jenetik ynden karılatırılması. Niđe ni. Jeo. Mh. Workshop I, Niđe, Trkiye, 5-8 Nisan, 150-162.

- Yaln, M. G., & opurolu, İ. (2001). Nide Masifi Metalik Maden Yataklarının Mineralojisi ve Jenezi. *Geosound*, 38, 49-65.
- Yaln, M. G., & İlhan, S. (2008). Major and trace element geochemistry of Terra Rossa soil in the Kucukkoras region, Karaman, Turkey. *Geochemistry International*, 46(10), 1038-1054. doi:[10.1134/S001670290810008X](https://doi.org/10.1134/S001670290810008X)
- Yaln, M. G., & Yaman, S. (1996). Gmler (Nide) Antimuan-Cıva Cevherlemesinin Mineralojik İncelenmesi, *Geosound*, 28, 189-201.
- Yaln, M. G., imsek, G., Ocak, S. B., Yaln, F., Kalaycı, Y., & Karaman, M. E. (2013). Multivariate statistics and heavy metals contamination in beach sediments from the Sakarya Canyon, Turkey. *Asian Journal of Chemistry*, 25(4), 2059-2066. doi:[10.14233/ajchem.2013.13309](https://doi.org/10.14233/ajchem.2013.13309)
- Yaln, M. G., Cokun, B., Nyamsari, D. G., & Yaln, F. (2019). Geomedical, ecological risk, and statistical assessment of hazardous elements in shore sediments of the Iskenderun Gulf, Eastern Mediterranean, Turkey. *Environmental Earth Sciences*, 78(15), 1-28. doi:[10.1007/s12665-019-8435-5](https://doi.org/10.1007/s12665-019-8435-5)
- Yıldız, M., & Bailey, E. H. (1978). Mercury Deposits in Turkey. *Geological Survey Bulletin*.1456. doi:[10.3133/b1456](https://doi.org/10.3133/b1456)
- Ycel, B. M. (2020). Antik dnemden gnmze bir serven: Antimuan. *MTA Doal Kaynaklar ve Ekonomi Blteni*, 29: 79-100.